INFORMATION TO USERS

This manuscript has been reproduced from the microfilm master. UMI films the text directly from the original or copy submitted. Thus, some thesis and dissertation copies are in typewriter face, while others may be from any type of computer printer.

The quality of this reproduction is dependent upon the quality of the copy submitted. Broken or indistinct print, colored or poor quality illustrations and photographs, print bleedthrough, substandard margins, and improper alignment can adversely affect reproduction.

In the unlikely event that the author did not send UMI a complete manuscript and there are missing pages, these will be noted. Also, if unauthorized copyright material had to be removed, a note will indicate the deletion.

Oversize materials (e.g., maps, drawings, charts) are reproduced by sectioning the original, beginning at the upper left-hand corner and continuing from left to right in equal sections with small overlaps.

Photographs included in the original manuscript have been reproduced xerographically in this copy. Higher quality 6" x 9" black and white photographic prints are available for any photographs or illustrations appearing in this copy for an additional charge. Contact UMI directly to order.

Bell & Howell Information and Learning
300 North Zeeb Road, Ann Arbor, MI 48106-1346 USA

UMI®
800-521-0600

SINGLE- AND MULTIPHOTON INFRARED LASER SPECTROSCOPY OF ATOMIC NEGATIVE IONS

By

MICHAEL SCHEER, Dipl. Phys.

A Thesis

Submitted to the School of Graduate Studies

in Partial Fulfillment of the Requirements

for the Degree

Doctor of Philosophy.

McMaster University

INFRARED LASER SPECTROSCOPY OF ATOMIC NEGATIVE IONS

DOCTOR OF PHILOSOPHY (1998)
(Physics)

McMaster University
Hamilton, Ontario

TITLE: Single- and multiphoton infrared laser spectroscopy of atomic negative ions

AUTHOR: Michael Scheer, Dipl. Phys. (University of Göttingen, Germany)

SUPERVISOR: Dr. Harold K. Haugen

NUMBER OF PAGES: xv, 115

Abstract

A pulsed, tunable infrared laser source (0.6–5.2 μm) has been developed on the basis of a commercial dye laser and non-linear optical conversion techniques. This laser source was combined with a keV negative ion beam apparatus in a crossed-beam geometry, with the aim to systematically study several atomic negative ions through a variety of single- and multiphoton detachment experiments.

Photodetachment threshold spectra of 21 ionic species (B^-, C^-, O^-, Al^-, Si^-, Cr^-, Co^-, Ni^-, Cu^-, Ge^-, Mo^-, Rh^-, Pd^-, Ag^-, Sn^-, Sb^-, Te^-, Cs^-, Ir^-, Pt^-, and Bi^-) have been recorded, in most cases resulting in very accurate determinations of ionic binding energies, marking substantial improvements over previous experimental values. In fact, several ionic states investigated here had not been observed previously.

Different schemes for resonant multiphoton detachment of atomic negative ions were demonstrated for the first time. These studies were conducted with several anions (Si^-, Sn^-, Sb^-, Te^-, Ir^-, and Pt^-) providing highly accurate ionic energy level splittings and clearly demonstrating that multiphoton probes are generally applicable to negative ion structure.

Acknowledgements

I would like to thank Dr. Harold Haugen, the supervisor of this Thesis, for the insight and knowledge that he has shared with me in the many discussions that we have had over the past four years. I am grateful to the committee members, Dr. Adam Hitchcock and Dr. Peter Sutherland, for their guidance and helpful suggestions throughout this work. Thanks are also extended to the past and present members of the negative ion group, in particular to Dr. Jan Thogersen and René Bilodeau, and to the various collaborators of the individual research projects.

I wish to express my deepest gratitude to my friends and family whose constant support has made the completion of this Thesis possible.

Preface

The work presented in this Thesis has been previously published in the form of several refereed journal articles. I am the first author of the seven articles listed below, and as such, I have been the primary contributor to the experimental realisation, data analysis, and writing of these works.

1. **Single- and Multiphoton Infrared Laser Spectroscopy of Sb^-: A Case Study.**

   Michael Scheer, Harold K. Haugen, and Donald R. Beck.

   Physical Review Letters **79**, 4101 (1997).

2. **Experimental Evidence that the $6s6p\ ^3P_J$ States of Cs^- are Shape Resonances.**

   M. Scheer, J. Thogersen, R.C. Bilodeau, C.A. Brodie, H.K. Haugen, H.H. Andersen, P. Kristensen, and T. Andersen.

   Physical Review Letters **80**, 684 (1998).

3. **Negative Ion of Boron: An Experimental Study of the ^3P Ground State.**

   Michael Scheer, René C. Bilodeau, and Harold K. Haugen.

   Physical Review Letters **80**, 2562 (1998).

1. **Threshold photodetachment of Al^-: Electron affinity and fine structure.**

   Michael Scheer, René C. Bilodeau, Jan Thogersen, and Harold K. Haugen.

Physical Review A **57**, R1493 (1998).

5. **Systematic study of the stable states of C^-, Si^-, Ge^-, and Sn^- via infrared laser spectroscopy.**

   Michael Scheer, René C. Bilodeau, Cicely A. Brodie, and Harold K. Haugen.

   Physical Review A **58**, issue 4 (October 1998).

6. **Laser Spectroscopic Measurements of Binding Energies and Fine Structure Splittings of Co^-, Ni^-, Rh^-, and Pd^-.**

   Michael Scheer, Cicely A. Brodie, René C. Bilodeau, and Harold K. Haugen.

   Physical Review A **58**, issue 3 (September 1998).

7. **Observation of the magnetic-dipole fine-structure transition in the tellurium negative ion.**

   Michael Scheer, René C Bilodeau and Harold K Haugen.

   Journal of Physics B **31**, L11 (1998).

In addition, I have participated in the experimental realisation and data analysis of other related research projects which have resulted in the following publications:

8. **Two-Photon Detachment of Negative Ions via Magnetic Dipole Transitions.**

   J. Thogersen, M. Scheer, L. D. Steele, H. K. Haugen, and W. P. Wijesundera.

   Physical Review Letters **76**, 2870 (1996).

9. **Fine-structure measurements for negative ions: Studies on Se^- and Te^-.**

   J. Thogersen, L. D. Steele, M. Scheer, H. K. Haugen, P. Kristensen, P. Balling, H. Stapelfeldt, and T. Andersen.

   Physical Review A **53**, 3023 (1996).

10. **Electron affinities of Si, Ge, Sn and Pt by tunable laser photodetachment studies.**

    J. Thogersen, L. D. Steele, M. Scheer, C. A. Brodie, and H. K. Haugen.

    Journal of Physics B **29**, 1323 (1996).

11. **Infrared laser photodetachment of transition metal negative ions: Studies on Cr^-, Mo^-, Cu^- and Ag^-.**

    René C Bilodeau, Michael Scheer and Harold K Haugen.

    Journal of Physics B **31**, 3885 (1998).

The outline of the Thesis is as follows:

After a brief introduction to the history and various aspects of negative ion research in Chapter 1, a more detailed description of the quantum mechanics of atomic negative ions and their interactions with photons will be given in Chapter 2. Chapter 3 then discusses the experimental setup and procedures utilized at McMaster University. A summary of the results that were obtained in photodetachment threshold studies of negative ions which detach into *s*-wave continua is given in Chapter 4, including a detailed discussion of some sample cases. Similarly, our efforts with ions detaching

into p-wave continua are described in Chapter 5. Finally, Chapter 6 discusses and summarizes the results that were obtained in studies of various negative ions by means of resonant multiphoton detachment, a technique that has been largely pioneered by the McMaster group. The Thesis concludes with a summary and an outlook to future perspectives of the field.

This Thesis provides a self consistent and comprehensive compilation of the experimental work that I have conducted during my PhD program at McMaster University. Nevertheless, for the convenience of the reader who might be interested in more specific details of a particular experiment, copies of the 11 journal articles on which the Thesis is based are included as an appendix.

Contents

List of Figures

List of Tables

Chapter 1

Introduction

The existence of atomic negative ions, i.e. atomic systems in which the number of electrons in the shell exceeds the number of protons in the nucleus, may at first seem surprising. A neutral atom possesses no permanent electric monopole or dipole moments, and as such exerts no forces on a free (distant) electron. This conclusion is based on the assumption that the electron itself has no influence on the atom, which is the approximation made in the so-called independent-particle model. Within this model, the electron would feel the electrostatic attraction of the nucleus only at very short distances, as the electron begins to penetrate the electron shell of the atom. However, even the Hartree-Fock model, the most sophisticated independent-particle model, which is very successful in the calculation of neutral and positively charged atomic systems, generally fails at predicting stable negative ions. On the other hand, most atoms form stable anions† [1], hence, the stability of negative ions must be largely due to a correlated rather than independent motion of the electrons. The implementation of such electron correlations into numerical models is rather challenging and yet fundamentally important to atomic theory. Accurate experimental data on

†Notable exceptions are the noble gases and many of the elements with closed outer subshells. In these cases, the extra electron would have to occupy a higher shell resulting in a reduced correlation energy, insufficient to overcome the electrostatic repulsion between the electrons.

negative ions, the atomic systems with the strongest correlation effects, is therefore crucial for an evaluation of different theoretical approaches.

The absence of a long-range Coulombic attraction between the atomic core and the extra electron is also responsible for the most characteristic structural features of negative ions. The longest-range electrostatic interaction between the electron and the atomic core is an induced dipole interaction which results from a polarization of the electronic shell by the distant electron (this is the classical limit of electron correlations). Such an induced-dipole potential is too short ranged to support Rydberg states, hence the number of stable ionic states must be finite. In fact, atomic negative ions possess only very few or even no bound excited states in addition to the ionic ground state [1]. Even the ground state binding energies, which define the electron affinities (EA) of the corresponding atoms, are typically small ($\sim$1 eV), Cl being the most strongly bound atomic ion with 3.6 eV. Photon-anion interactions therefore generally result in bound-free rather than bound-bound transitions, i.e. in a removal of the extra electron, so-called photodetachment. Hence, negative ion spectroscopy often reduces to a study of (relative) photodetachment cross-sections. The shape of detachment cross sections at threshold differs substantially from thresholds of ionization spectra, but the phenomenon is well understood theoretically. In fact, negative ion detachment constitutes an important example for Wigner's threshold law, which applies here since the induced dipole potential falls off more rapidly than a centrifugal potential [2]. The shape of the photodetachment continuum above the first threshold, particularly in the proximity of excited atomic states, is often strongly influenced by the presence of unstable (excited) ionic states. Such states are manifested as resonance structures in photodetachment as well as electron-atom scattering cross sections. The shape, width and strength of a particular resonance depends on

whether the ionic state is metastable or rapidly autodetaching, and whether it is located above or below its atomic parent state.†

Despite their exotic nature, negative ions have long been recognized to play an important role in a variety of physical phenomena. As early as 1939 Wildt suggested that the presence of H^- in the solar photosphere may be a major contributor to the opacity in the near infrared [1]. Similarly, negative ions are known to contribute to the photochemistry of the earth's ionosphere. Furthermore, more recent simulations of the chemistry of interstellar gas clouds indicate that of all charged particles negative ions play the dominating role. Negative ions are also relevant to various plasma phenomena that are accessible on a laboratory scale. For example, in thermonuclear fusion research negative ions are used to produce intense atomic beams for injection heating of tokamak fusion plasmas. Similarly, ultra-sensitive isotope detection through accelerator mass spectrometry is a branch of applied physics that depends on accurate knowledge of negative ion structure. Last but not least, some biochemical processes, certain chemical reactions, and the electrolytic properties of solutions rely on the presence of anions as well as cations.

Nevertheless, the experimental investigation of negative ions, particularly in the gas phase, remains challenging. Available production schemes such as molecular dissociation or electron attachment are rather delicate, and high ionic concentrations are difficult to obtain. Furthermore, negative ions are very fragile and are easily destroyed in collisions with other particles. Hence, in was not until the 1950's, when ultra-high vacuum (UHV) and negative ion-beam technologies were developed, that negative ion experiments were attempted (largely pioneered by Branscomb's

†The study of continuum resonances constitutes an important branch of negative ion physics of which an exhaustive review was recently given by Buckman and Clark [3]. A further discussion of continuum resonances, which would be relevant to only one of the many ions investigated in this thesis, is therefore omitted.

group [5]). Technological improvements that have advanced the field since then include high-intensity sputter sources, charge exchange cells, ion traps, and collinear laser-ion beam apparatuses.

However, even with the availability of powerful ion sources, probes of negative ion structure are significantly different from those utilized in the study of neutral or positively charged atomic or molecular species. The traditional techniques of emission and absorption spectroscopy are not applicable to negative ions due to the general lack of stable electronically excited states. Information on negative ion structure, bound relative to the atomic ground state, is therefore largely derived from photodetachment spectra. Although some early investigations were based on conventional light sources, accurate and systematic studies were not possible until commercial laser sources became available. Two laser-based techniques are particularly noteworthy here, laser photodetached electron spectrometry (LPES) and laser photodetachment threshold (LPT) spectroscopy. LPES employs a fixed-wavelength laser with photon energies well above the threshold for photodetachment. Ionic binding energies are then derived from energy-resolved measurements of the detached electrons, according to $E_{i,n} = E_{photon} - E_{e,i,\ to\ n}$. LPES is a powerful technique, as it can be applied to virtually any stable negative ion, irrespective of the binding energy to be measured. The accuracy of measured energy values is, however, limited to the resolution of the electron spectrometer, which is typically a few meV [1]. LPT measurements, on the other hand, utilize tunable laser sources in order to locate the actual photodetachment thresholds. Accuracies range from 0.1 to 0.001 meV, as they are often only limited by the laser bandwidth. The constraint on LPT studies involving detachment to the atomic ground state is that the tunable photon energies have to match the ionic binding energies. Most previous LPT studies have utilized visible laser light

and have therefore been restricted to systems with electron affinities larger than 1.4 eV.[†]. This major constraint on LPT studies can be removed if infrared laser sources are utilized. However, such sources are not readily available, and only very few infrared LPT measurements are reported in the literature.[‡] Therefore, a large portion of the work described in this thesis was devoted to the development of an infrared LPT system and its systematic application to a large number of atomic negative ions. Similarly, the great potential of multiphoton probes of anionic structure was recognized [11] early on, but resonant multiphoton detachment of atomic negative ions, again largely depending on intense infared laser sources, was not attempted prior to the collaborative efforts of the McMaster and Aarhus groups described in this thesis.

[†]Notable exceptions are the alkali and alkaline earth negative ions, where detachment to excited states of the respective atoms and state selective detection schemes were employed. [7, 6]

[‡]These are Feldmann's study of Li^-, C^-, and P^- using an optical parametric oscillator [8, 9] and Lykke *et al.*'s investigation of H^- based on an F-center laser [10].

6

Chapter 2

Theory of Atomic Negative Ions

2.1 A semi-classical negative ion model

A qualitative understanding of the existence of atomic negative ions can be gained from semi-classical considerations. In a crude model, the atom may be viewed as composed of a nucleus with positive charge Z surrounded by a spherically symmetric cloud of electrons of equal negative charge. Such an atom has a net charge of zero and no permanent electrostatic multipole moments, but it will have a non-vanishing polarizability, α. Hence, a free electron would induce a dipole moment of magnitude $P \propto \alpha E$ in the atom, where E is the magnitude of the electron's electric field at the position of the atom, $E \propto 1/r^2$. Due to this induced dipole potential, $\Phi \propto P/r^2 \propto \alpha/r^4$, the electron would experience a weak attraction by the atom resulting in a positive binding energy and thus a stable negative ion. Of course, as this simple negative ion model is based on classical monopole-dipole interactions, it is only valid in the classical limit, i.e. at large distances. At short distances, where the extra electron begins to penetrate the atom's electron cloud, the quantum-mechanical nature of the system can no longer be neglected. A quantitative negative ion model therefore has to consider the (correlated) motion of the $Z+1$ electrons simultaneously, as discussed

below. However, some characteristic negative ion features can be understood on the basis of the present model. The quantum-mechanical treatment of a particle bound by a $1/r^n$ potential shows that an infinite number of bound states only exists in the cases $n = 1$ and 2. Shorter ranged potentials such as the induced-dipole potential ($n = 4$) support only a finite number of bound states. In particular, there is no series of bound states converging towards the continuum, the onset of free-particle states. Hence, the cross section for negative ion photodetachment must be zero just below threshold and furthermore obeys the Wigner threshold law, as discussed in detail in Sec. 2.4.

2.2 Quantum mechanics of atomic systems

A quantitative model of atomic systems, including negative ions, is provided within the framework of nonrelativistic quantum mechanics.[†] Here, particles such as electrons are described as waves and the dynamic evolution of a particular system is determined by the Schrödinger equation,

$$H\Psi(X,t) = i\hbar\frac{\partial}{\partial t}\Psi(X,t) \ , \tag{2.1}$$

which is shown here in coordinate representation with X standing for a full set of system coordinates. Ψ denotes the wave function of the system and the Hamilton operator H represents its total energy. For an atom or ion consisting of N electrons and a nucleus with charge Z the Hamiltonian is given by

$$H = \frac{\vec{p}_n^{\,2}}{2m_n} + \sum_{i=1}^{N}\left(\frac{\vec{p}_i^{\,2}}{2m_e} - \frac{Ze^2}{|\vec{r}_i - \vec{r}_n|}\right) + \sum_{i<j}\frac{e^2}{|\vec{r}_i - \vec{r}_j|} \ , \tag{2.2}$$

[†]Only a brief summary of the most relevant concepts of quantum mechanics shall be given here. The reader should refer to standard text books on quantum mechanics or atomic physics for details, e.g. Refs. [12, 13, 14].

where the subscripts n and i of the momenta $\vec{p}$ and position coordinates $\vec{r}$ stand for 'nucleus' and 'i-th electron' respectively [12]. As this Hamiltonian has no explicit time dependence,

$$\Psi(\vec{r}_1, \ldots, \vec{r}_N, t) = \psi(\vec{r}_1, \ldots, \vec{r}_N) e^{-iEt/\hbar} \tag{2.3}$$

is a solution of the time dependent Schrödinger equation (2.1) if ψ is a solution of the time independent Schrödinger equation,

$$H\psi(\vec{r}_1, \ldots, \vec{r}_N) = E\psi(\vec{r}_1, \ldots, \vec{r}_N) . \tag{2.4}$$

Hence, the possible states of the system are given by the eigenstates of the Hamilton operator (2.2) with energy eigenvalues E. However, solving this eigenvalue problem, i.e. diagonalizing the Hamilton operator remains a great challenge.

2.2.1 One-electron systems

Analytic solutions of Eq. (2.4) are only possible for one electron systems (N=1 in Eq. 2.2), namely atomic hydrogen and hydrogenic ions. In this case, the most problematic term in the Hamiltonian (2.2), the dielectronic interaction term which represents the mutual repulsion of pairs of electrons, does not exist, and the remaining terms can be simplified by going over to spherical centre-of mass coordinates. The Hamiltonian then reduces to that of a point particle in a radially symmetric potential for which the angular momentum operator $\vec{l} = \vec{r} \cdot \vec{p}$ commutes with H. The eigenstates of H are then of the form

$$\psi(\vec{r}) = \frac{\phi_{n,l}(r)}{r} Y_{l,m}(\theta, \varphi) , \tag{2.5}$$

where the spherical harmonics $Y_{l,m}(\theta, \varphi)$ are the eigenstates of the angular momentum operators $\vec{l}^2$ and l_z (with eigenvalues $l(l+1)\hbar^2$ and $m\hbar$ respectively) and where the

radial wave functions $\varphi_{n,l}(r)$, which are basically generalized Laguerre polynomials, are solutions of the radial Schrodinger equation

$$\left(-\frac{\hbar^2}{2\mu}\frac{d^2}{dr^2}+\frac{l(l+1)\hbar^2}{2\mu r^2}-\frac{1}{r}\right)\varphi_{n,l}(r)=E_{n,l}\varphi_{n,l}(r)\,. \tag{2.6}$$

It is important to note that even the radial motion of the electron is affected by its angular momentum, which appears here in the form of a repulsive centrifugal potential $l(l+1)\hbar^2/2\mu r^2$. The three quantum numbers $n' = 2n + l$, l, and m are traditionally used (and are sufficient) to identify the spatial state of a one-electron atomic system.[7] A state is labelled $n'lm$, where letters are used for l (i.e. $s, p, d, f, g, h, \ldots$ for $0,1,2,\ldots$) and numbers for for n' and m (although m is most often omitted).

2.2.2 Electron spin

Electrons possess an additional, purely intrinsic property, the so-called spin $\vec{s}$, which obeys the commutation relations of an angular momentum operator. A rigorous theoretical treatment of the electron spin has to take the (fully relativistic) Dirac equation rather than the non-relativistic Schrödinger equation as its starting point. The algebra of the Dirac equation is fairly involved, but in the weakly relativistic case the equation can be expanded to yield the Schrödinger equation with correction terms in the Hamiltonian [12]. The lowest-order terms are a relativistic correction term to the kinetic energy, the so-called Darwin term, and the spin-orbit term

$$H_{ls}=\frac{1}{2m_e^2c^2}\frac{1}{r}\frac{dV(r)}{dr}\vec{l}\cdot\vec{s}\,. \tag{2.7}$$

The contributions of the spin-orbit interaction, which is magnetic in nature, and of the other correction terms are usually small and can therefore be calculated with

[7] The use of the principal quantum number $n' = 2n + l$ instead of the radial (or nodal) quantum number n is advantageous, as the energy eigenvalues are then only dependent on n'.

perturbative methods after the eigenstates of the non-relativistic Hamiltonian (2.2) are found.

2.2.3 Many-electron systems

Due to the presence of the dielectronic interaction term in Eq. (2.2) the eigenstates of many electron systems can only be found with numerical methods involving certain approximations. Most common is the independent particle approximation which considers each electron as moving independently in the attractive Coulomb field of the nucleus and the repulsive radial mean field due to the average charge distribution constituted by the other electrons. This mean-field approach is the lowest-order approximation to electron interactions and does not take account of residual two body interactions [12]. However, the N-electron Hamiltonian (2.2) is now reduced to N coupled one-electron Hamiltonians whose eigenstates can be found with an iterative method developed by Hartree. The wave function of the N-electron system is therefore given as a direct product of one-electron wave functions which are similar to hydrogenic wave functions. An N-electron state is consequently denoted as a configuration of one-electron states (e.g. $1s^2 2s^2 2p^4$ for the ground state of oxygen).

Pauli principle and angular momentum coupling

The Hartree method is very successful in predicting the energetic order of different configurations, i.e. the shell and subshell structure of atoms, but it cannot calculate the next level of substructure, the so-called terms, as the electron spin and the angular part of the spatial wave function are ignored. Electrons are fermions and as such obey the Pauli principle which states that the total wave function of a system consisting of fermions must be antisymmetric with respect to an exchange of any two electrons. Hence, within the independent particle model the N-electron system

should be represented as a properly antisymmetrized direct product of one-electron wave functions including the spin and angular parts (Such a representation has the algebraic form of a Slater determinant). This is the important modification of the Hartree method leading to the Hartree-Fock method. However, the effects of including angular momentum and spin via antisymmetric wave functions can also be understood qualitatively. If one electron spin-orbit interactions (Eq. 2.7) are ignored the total orbital angular momentum and the total spin,

$$\vec{L} = \sum_{i=1}^{N} \vec{l}_i \quad , \quad \vec{S} = \sum_{i=1}^{N} \vec{s}_i \quad , \tag{2.8}$$

provide good quantum numbers, L and S respectively. A single configuration may then give rise to several terms, denoted as ^{2S+1}L, depending on how the individual angular momenta and spins couple together. The energetic order of different terms is expressed in Hund's rules: Of all terms belonging to one configuration those with the largest value of S (or largest multiplicity $2S + 1$) are lowest in energy, and of the terms with the same multiplicity the term with the largest value of L is the energetically lowest [12]. This energetic order is a result of the so-called exchange interaction which in turn originates from antisymmetrisation. For example, maximum S means parallel individual spins and a symmetric spin wave function. The spatial wave function must then be antisymmetric, which gives rise to an increased average separation between electrons, which in turn lowers the electrostatic repulsion. Hence, the forces behind the exchange interaction and the formation of $\vec{L}$ and $\vec{S}$ are primarily electrostatic in nature and are in most cases much stronger than the (magnetic) spin-orbit interaction [15]. The effect of the N individual spin-orbit interaction terms (which are of the form shown in Eq. (2.7)) can then be treated approximately by considering only the coupling between $\vec{L}$ and $\vec{S}$ (through an interaction term similar to Eq. 2.7) resulting in a total momentum $\vec{J} = \vec{L} + \vec{S}$. As a result of this so-called

LS-coupling[†] a ^{2S+1}L term will split up into $(L+S-|L-S|+1)$ fine-structure levels differing in their value for J and labelled as $^{2S+1}L_J$. Each fine structure level finally consists of $2J+1$ states which are degenerate in the absence of external fields and are labelled with the quantum number M_J.[‡]

Electron correlations

The quantum mechanical many electron model presented so far is very successful in calculating ground states as well as singly excited states of atoms and positive ions, but it fails in the case of negative ions. This is due to the fact that negative ions owe their stability largely to electron correlations, i.e. the residual two-body interactions between electrons, that are ignored in the independent-particle approximation. Hence, a negative ion quantum state is not well described by a single electron configuration (or a single Slater determinant). It may, however, be represented as a linear combination of different configurations (with the same values for the good quantum numbers), since the (one-electron) Slater determinants form a complete basis set of the full Hilbert space of an N-electron atomic system [12]. Hence, the problem of including electron correlations reduces to the task of finding the correct coefficients in this linear combination of configurations. This can be done with the multiconfiguration Hartree-Fock method (MCHF) where a subset of configurations is chosen and where the coefficients and one-electron wave functions are optimized simultaneously through variational methods. Alternatively, diagonalization of the Hamiltonian (2.2) with respect to a sufficiently large basis set of configurations may also provide accurate energy eigenvalues and states. This approach is called configuration interaction

[†] The LS-coupling approximation breaks down for atomic systems with large Z for which other coupling schemes such as jj-coupling may be a more appropriate description.

[‡] Analogously, if a nuclear spin $\vec{I}$ is present, it will couple weakly to $\vec{J}$ resulting in a total momentum $\vec{F} = \vec{J} + \vec{I}$ and a hyperfine splitting of each fine structure level J.

calculation (CI).†

2.3 Interaction between atomic systems and light

In the classical theory of electromagnetism a radiation field is represented by a vector potential $\vec{A}$ which solves the wave equation

$$\vec{\nabla}^2 \vec{A} - \frac{1}{c^2}\frac{\partial^2 \vec{A}}{\partial t^2} = 0 \tag{2.9}$$

and which relates to the electric and magnetic field through the equations

$$\vec{E} = -\frac{1}{c}\frac{\partial \vec{A}}{\partial t}, \quad \vec{B} = \vec{\nabla} \times \vec{A}, \tag{2.10}$$

where the Coulomb gauge is assumed. The plane wave solutions for $\vec{A}$ are of the form

$$\vec{A}(\vec{r}, t) = \vec{A}_0 e^{\pm i(\vec{k}\cdot\vec{r} - \omega t)} \tag{2.11}$$

with $\vec{A}_0 \cdot \vec{k} = 0$ for transversality. The electromagnetic field is then introduced into the Hamiltonian of a system of charged particles by replacing the individual particle momenta $\vec{p}_i$ with $\vec{p}_i + (q/c)\vec{A}(\vec{r}_i, t)$. Performing this replacement on the Hamiltonian of an N-electron atomic system (2.2) and dropping terms quadratic in $\vec{A}$ will yield the original Hamiltonian plus an interaction term H_I:

$$H_I = -\frac{e}{mc}\sum_{i=1}^{N} \vec{A}(\vec{r}_i) \cdot \vec{p}_i \,. \tag{2.12}$$

Before the effect of H_I on the atomic system can be evaluated quantitatively, the classical vector potential $\vec{A}$ must be converted into a quantum mechanical operator. This requires quantization of the radiation field which is the subject of the theory of quantum electrodynamics. Only the result shall be given here:

$$\vec{A}(\vec{r}_i, t) \mapsto cF_k\sqrt{\frac{h}{\omega V}}\vec{\pi}_{k\ell}\, e^{\pm i(\vec{k}\cdot\vec{r}_i - \omega t)} \,. \tag{2.13}$$

†Examples for electron affinity calculations with these two methods are given in Sec. 4.3.

Here $\vec{\pi}_k$ is the polarization vector of photons with wave vector $\vec{k}$ and the factor F_k equals $\sqrt{n_k + 1}$ and $\sqrt{n_k}$ in emission and absorption respectively, where n_k is the number photons with wave vector $\vec{k}$ in a volume V.†

Now, if the contribution of H_I is small, i.e. if the interaction between atom and light field is weak the dynamic evolution of the atomic system due to the presence of H_I is well described by time-dependent perturbation theory. In this framework first order effects are evaluated with Fermi's Golden Rule,

$$P_{i\to f} = \frac{2\pi}{\hbar}|\langle o_f|H_I|o_i\rangle|^2 \rho_f \,, \tag{2.14}$$

which gives the probability per unit time for a transition between the (unperturbed) states o_i and o_f caused by a perturbing operator H_I, where ρ_f is the density of final states.

In order to evaluate this equation it is advantageous to expand the exponential term in the expression for H_I into a power series of $\vec{k}\cdot\vec{r}$: $\exp(\pm i\vec{k}\cdot\vec{r}) = 1 \pm i\vec{k}\cdot\vec{r} - (\vec{k}\cdot\vec{r})^2 \pm \ldots$. For optical transitions in atoms wavelengths ($\sim 1/k$) are much larger than atomic dimensions ($\sim r$) and the so-called dipole approximation, $\exp(\vec{k}\cdot\vec{r}) \approx 1$, is valid. Using the commutator identity $\vec{p} = \frac{m}{i\hbar}[\vec{p}^2, \vec{r}] = \frac{m}{i\hbar}[H, \vec{r}]$ the matrix element $\langle o_f|H_I|o_i\rangle$ in equation (2.14) is then found to be

$$\langle o_f|H_I|o_i\rangle = -iF_k\sqrt{\frac{2\pi}{\hbar\omega V}}(E_f - E_i)\vec{\pi}\cdot\langle o_f|\vec{D}|o_i\rangle \,, \tag{2.15}$$

where the energy difference between initial and final state, $E_f - E_i$, must equal the photon energy $\hbar\omega$, and where

$$\vec{D} = -e\sum_{i=1}^{N}\vec{r}_i \tag{2.16}$$

† An operator describing the interaction between an atomic system and a radiation field must be the product of two terms, one operating on the atomic wave function, the other operating on the wave function of the quantized field. In the expression given here, the latter operation has already been carried out. The field operator is a one-photon creation (emission) or annihilation (absorption) operator, hence the factors $\sqrt{n_k + 1}$ and $\sqrt{n_k}$ respectively.

denotes the electric dipole operator. With these equations and an appropriate choice for ρ_f (e.g. $\rho d\Omega = \frac{\lambda^2}{4\pi^2} d\Omega$) the probability for specific transition processes such as spontaneous emission, stimulated emission, or absorption are easily derived. For example, the probability for spontaneous emission (in any direction Ω and with arbitrary polarization $\vec{\epsilon}$), the so-called Einstein A coefficient, is found to be

$$A_{E1} = \frac{4}{3}\frac{\omega^3}{\hbar c^3} |\langle o_f | \vec{D} | o_i \rangle|^2 , \tag{2.17}$$

where the subscript $E1$ stands for 'electric dipole' [12]. Similarly, most electric dipole selection rules, which are summarized in Table 2.1, are easily derived from the fundamental properties of the operator: $\vec{D}$ has odd parity, hence the two atomic states must be of opposite parity; $\vec{D}$ can be expressed as a rank-1 tensor operator in spherical coordinates to which the Wigner-Eckart theorem applies, hence the selection rules regarding J and M_J [13].

In cases where electric dipole transitions are forbidden, higher-order terms in the expansion of the interaction term H_I become relevant. The derivation of the resulting operators is more involved than in the electric dipole case. The matrix element of the first order term can be transformed into a sum of matrix elements of the magnetic dipole and electric quadrupole operators,

$$\vec{\mu} = \mu_B (\vec{L} + 2\vec{S}) , \quad \mathbf{Q} = -e \sum_{i=1}^{N} \sum_{r,s} 3 r_{i,r} r_{i,s} - \delta_{r,s} \vec{r}_i^{\,2} , \tag{2.18}$$

respectively, which are vector (i.e. rank-1 tensor) and rank-2 tensor operators respectively (r_r and r_s denote cartesian components of $\vec{r}$). Expressions for transition probabilities are again derived utilizing Fermi's Golden Rule. For example, the probabilities for spontaneous emission via magnetic dipole (M1) and electric quadrupole (E2) transitions are

$$A_{M1} = \frac{4}{3}\frac{\omega^3}{\hbar c^5} |\langle o_f | \vec{\mu} | o_i \rangle|^2 , \quad A_{E2} = \frac{1}{90}\frac{\omega^5}{\hbar c^5} |\langle o_f | \mathbf{Q} | o_i \rangle|^2 , \tag{2.19}$$

respectively [14]. As for E1 transitions most selection rules for M1 and E2 transitions, which are given in Table 2.1, are easily derived from the fundamental properties of the respective operators. Finally, based on Eqs. (2.17) and (2.19) order-of-magnitude estimates for relative transition probabilities can be derived: $A_{M1}:A_{E1} \sim 10^{-5}$ and $A_{E2}:A_{E1} \sim 10^{-6}$ [14]. Hence, M1 and E2 transitions are of comparable strength, but both are significantly weaker than E1 transitions. Optical atomic transitions due to higher multipole moments (M2, E3, etc.), which arise if even higher terms in the expansion of H_I are considered, would be several orders of magnitude weaker than M1 and E2 transitions and are almost[†] impossible to observe.

The photon-atom interactions described by H_I are one-photon processes. Transition probabilities derived on the basis of first order perturbation theory (2.14) therefore always refer to single-photon transitions. Multiphoton transition probabilities are obtained if the higher-order terms in the time-dependent perturbation series are evaluated. This task is rather involved, so only the result most relevant to the present work, the probability for a stimulated two-color (ω_1, ω_2) two-photon transition shall be given here [17]:

$$P^{(2)}_{i\to f} \propto \left| \sum_n \frac{\langle o_f|\vec{\varepsilon}_2\cdot\vec{D}|o_n\rangle\langle o_n|\vec{\varepsilon}_1\cdot\vec{D}|o_i\rangle}{E_n - E_i - \hbar\omega_1 + i\Gamma_n/2} + \frac{\langle o_f|\vec{\varepsilon}_1\cdot\vec{D}|o_n\rangle\langle o_n|\vec{\varepsilon}_2\cdot\vec{D}|o_i\rangle}{E_n - E_i - \hbar\omega_2 + i\Gamma_n/2} \right|^2 \cdot I(\omega_1)I(\omega_2)\frac{(\Gamma_i+\Gamma_f)/2}{(E_f - E_i - \omega_1 - \omega_2)^2 + (\Gamma_i+\Gamma_f)^2/4} . \qquad (2.20)$$

Here, Γ denotes the natural width of a state, and the summation goes over all possible intermediate states o_n. For two-photon transitions in negative ions intermediate states would be primarily continuum states. With the convention that ω_i is positive if a photon is absorbed and negative if it is emitted, equation (2.20) may represent two-photon absorption, stimulated emission, as well as Raman processes. The most

[†]The first successful observations of atomic octupole transitions were only recently reported [16]. However, multipole transitions play an important role in nuclear physics [15].

important selection rules for two-photon transitions are listed in Table 2.1.

Table 2.1: Selection rules for radiative transitions in atoms (with unpolarized light) [14, 17]. The rules for J, M_J, and parity apply rigorously, the other rules apply only if the atomic system is well described by a single configuration and LS-coupling.

Rule	one-photon			two-photon
	E1	M1	E2	E1
$\Delta J =$	$0, \pm 1$	$0, \pm 1$	$0, \pm 1, \pm 2$	$0, \pm 1, \pm 2$
$(J \nleftrightarrow J')$	$(0 \nleftrightarrow 0)$	$(0 \nleftrightarrow 0)$	$(0 \nleftrightarrow 0, \frac{1}{2} \nleftrightarrow \frac{1}{2}, 0 \nleftrightarrow 1)$	$(0 \nleftrightarrow 1)$
$\Delta M_J =$	$0, \pm 1$	$0, \pm 1$	$0, \pm 1, \pm 2$	$0, \pm 1, \pm 2$
Parity change	Yes	No	No	No
Electron jumps	1	0	0,1	0,1,2
$\Delta l =$	± 1	0	$0, \pm 2$	$0, \pm 2$
$\Delta L =$	$0, \pm 1$	0	$0, \pm 1, \pm 2$	$0, \pm 1, \pm 2$
$(L \nleftrightarrow L')$	$(0 \nleftrightarrow 0)$		$(0 \nleftrightarrow 0, 0 \nleftrightarrow 1)$	$(0 \nleftrightarrow 1)$
$\Delta M_L =$	$0, \pm 1$	0	$0, \pm 1, \pm 2$	$0, \pm 1, \pm 2$
$\Delta S =$	0	0	0	0

2.4 Photodetachment thresholds

An analytic expression for the photodetachment cross section[1] close to threshold may be obtained from Fermi's Golden Rule (Eq. 2.11). Due to the absence of a converging Rydberg series of states the final state density is zero below threshold and the transition probability vanishes. The density of continuum states above threshold

[1] In absorption the transition probability P depends on the photon density ρ and thus on the photon flux $\Phi = \rho c$. Therefore, the cross section $\sigma = P/\Phi$ is a more appropriate quantity to characterize absorption.

is given by the free-electron density of states $\rho(k)dk \propto k^2 dk$ where k denotes the magnitude of the free-electron wave vector. With $E \propto k^2$ and $\rho(k)dk = \rho(E)dE$ this gives $\rho(E) \propto \sqrt{E}$, the state density as a function of the energy above threshold, $E = E_{photon} - E_{threshold}$.

Close to threshold E is small and hence the final state wavelength ($\lambda \propto 1/\sqrt{E}$) is large compared to the extent of the initial (bound) state wave function. Apart from a normalization factor $N(E)$ of the final state wave function, the matrix element in Eq. (2.11) is then only weakly dependent on E and may be expanded into a series of E. Hence the photodetachment cross section close to threshold may be written as

$$\sigma \propto \sqrt{E} N(E) [1 + O(E)] . \tag{2.21}$$

The factor $N(E)$ is derived on the basis that final state interactions between the detached electron and the atomic core must vanish (at least) assymptotically as their separation increases. In other words, normalization is achieved by demanding that the final state wave function approaches a free electron wave function at large distances. The longest-range interaction between detached electron and atomic core is therefore responsible for the leading term in the expression for $N(E)$.

In atomic negative ion detachment the longest-range interactions are given by the repulsive centrifugal potential, $l(l+1)\hbar^2/2\mu r^2$, which the detached electron feels if it carries l units of angular momentum with respect to the atomic core. In this case, the leading term in the expression for $N(E)$ is found to be E^l. Inserting this result in Eq. (2.21) and dropping higher order terms finally yields

$$\sigma \propto E^{l+1/2} \tag{2.22}$$

for the photodetachment cross section at threshold, as first derived by Wigner [18]. Eq. (2.22) is plotted in Fig. 2.1 for $l = 0, 1, 2$, i.e. for detachment into s-, p-, and

d-wave continua, respectively. As can be seen, the onset of an s-wave threshold is sharp and sudden (infinite derivative) whereas the onset of p-wave and higher order thresholds is smooth and slow (zero derivative). This result is easily understood qualitatively: While the s-wave cross section is solely determined by the density of states available to the free electron ($\rho(E) \propto \sqrt{E}$), the cross section for detachment into $l = 1,2,\ldots$ continua also includes the probability for the electron to tunnel through the centrifugal barrier. This probability is zero for $E = 0$ where the barrier is infinitely wide and increases only slowly with increasing energy E.

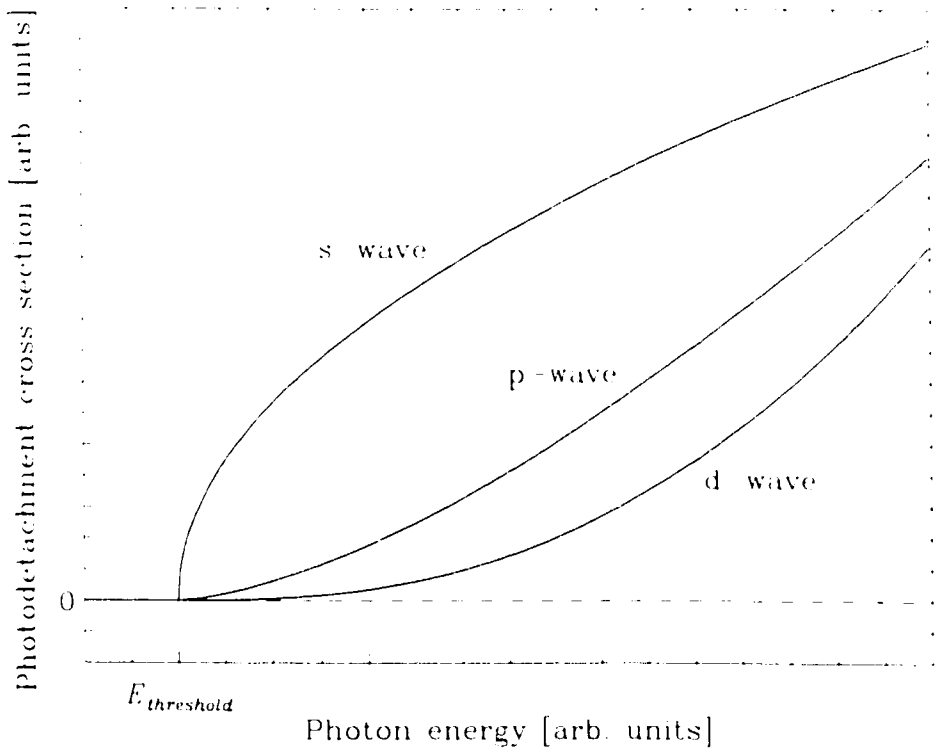

Figure 2.1: Schematic diagram of the cross section for photodetachment into s-, p-, and d-wave continua.

The approximations made in the derivation of the Wigner threshold law (Eq. 2.22) restrict its validity to the region very close to threshold. A quantitative analysis of the cross section higher above threshold requires the inclusion of higher-

order terms. An analytic expression for the first order term in Eq. (2.21), $O(E)$, was recently derived by Farley [19]. Earlier, O'Malley had obtained the leading correction term in the expression for $N(E)$ by including the effect of the induced dipole potential ($\propto \alpha/r^4$) in the normalization of the final state wave function [20]. This term is particularly relevant if the polarizability α of the atomic core is large.

2.5 Multiple detachment thresholds

For any particular negative ion more than one photodetachment channel may be present due to the existence of different electronic configurations, terms, or fine structure levels in either the ion or the atom. The relative strengths of different detachment channels at threshold vary significantly depending on the statistical weights of the energy levels involved and also the geometric properties of the respective angular wavefunctions. For an ionic electron configuration with only one open shell the intensity for photodetachment from an ionic ^{2S+1}L term to an atomic $^{2S'+1}L'$ term is given by

$$I(LS, L'S') \propto n_l |SL\{|S'L'\}l\rangle|^2 \sum_{l'=|l-1|}^{l+1} |\langle l\|\vec{D}\|l'\rangle|^2. \tag{2.23}$$

Here, n_l is the number of electrons in the open shell of the ion, $SL\{|S'L'\}l\rangle$ is the fractional parentage coefficient (see e.g. Ref. [13]) for the decomposition of the ionic ^{2S+1}L term into an atomic $^{2S'+1}L'$ term and an l-electron, and $\langle l\|\vec{D}\|l'\rangle$ is the reduced matrix element of the electric dipole operator for the photodetachment of a bound l-electron into the $\varepsilon l'$ continuum [21, 22]. This $^{2S+1}L \rightarrow {}^{2S'+1}L'$ photodetachment transition is further composed of up to $(2S+1)(2S'+1)$ fine structure transitions. In the case that the spin-orbit coupling of the electrons can be approximated by

LS-coupling, the relative intensity of a fine structure transition $J \rightarrow J'$ is given by

$$I(J,J') \propto \sum_{l=|l-1/2|}^{l+1/2} (2j+1)(2J+1)(2J'+1) \cdot \left\{ \begin{array}{ccc} S & L & J \\ \frac{1}{2} & l & j \\ S' & L' & J' \end{array} \right\}^2 \exp\left(\frac{-E(J)}{kT}\right) , \qquad (2.24)$$

where l and j denote orbital and total angular momentum of the bound electron that is to be detached. (Note that the angular momentum l' of the detached electron, which determines the shape of the threshold, is not relevant here.) The properties of the 9J-symbol in Eq. (2.24) determine the selection rules for photodetachment:

$$|\Delta S| = \frac{1}{2}, \quad |\Delta L| \leq l, \quad \Delta J = -l + \frac{1}{2}. \qquad (2.25)$$

The Boltzmann factor $\exp(-E(J)/kT)$ in Eq. (2.24) accounts for a thermal population of the different ionic energy levels and must be included unless the level splittings are much smaller than kT, where T is the effective ion source temperature (see Sec. 3.1). T can be evaluated from Eq. (2.24) if it is possible to experimentally determine two fine structure thresholds for a given ionic term. If the relative intensities of more than two thresholds are measured, a comparison with the theoretical predictions of Eq. (2.24) will indicate the validity of the LS-coupling approximation for the particular ion.

2.6 Photodetachment in static electric fields

In the presence of a static electric field the cross section for photodetachment (Eq. 2.22) is altered. This phenomenon has been discussed in the literature for both s-wave [23] and p-wave thresholds [21]. However, since the effect is more pronounced for s-wave thresholds and since the theoretical description of the p-wave case is complicated due to the anisotropy of p-wave detachment, only the s-wave case shall be considered

here.[†] In this case, an accurate quantitative description of the phenomenon can be obtained from a very simple model. In this model the extra electron is bound in a short range potential (approximated by a δ-function) to which the sloping potential of a constant electric field is added. Hence, for photon energies below the zero-field threshold there now exists a finite probability for electron detachment through tunneling. For photon energies above the zero field threshold, on the other hand, an interference occurs between the free electron wave packets that travel in the downward direction of the potential hill and those that initially travel upward and are then reflected. This interference gives rise to an oscillatory modulation of the cross section as a function of energy.

An analytic expression for the modified cross section may again be obtained from an integral version of Fermi's golden rule (Eq. 2.11):

$$P_{i\to f} = \frac{2\pi}{\hbar}\int |\langle\phi_f(\epsilon)|H_I|\phi_i\rangle|^2\delta(E_f - E_i)\rho(E_f)d\epsilon \ , \tag{2.26}$$

which allows the use of a convenient representation for the final state. In the present case, the final state $|\phi_f(\epsilon)|$ in Eq. (2.26) is the wave function of a free electron in a static electric field which, in cartesian coordinates, is proportional to

$$\phi_f \propto \cos(k_x x)\cos(k_y y)\mathrm{Ai}(-\zeta) \ , \tag{2.27}$$

where Ai is the Airy function and ζ is defined by $\zeta = (z + \epsilon_z/eF)(2meF/\hbar^2)^{1/3}$, with F as the electric field strength and ϵ_z as the electron's kinetic energy in the direction of the field [25]. Close to threshold the final state wavelength is large compared to the extent of the initial state. Within this limit the term $H_I|\phi_i\rangle$ in Eq. (2.26) may be approximated with the δ-function, i.e. $H_I\phi(x,y,z) \propto \delta(x)\delta(y)\delta(z)$, which leads

[†]A consideration of static field effects was originally not intended, but became necessary in the analysis of some high-resolution s-wave thresholds due to the presence of weak stray fields in the laser-ion interaction region.

to $\langle \phi_f | H_I | \phi_i \rangle \propto \mathrm{Ai}[-\kappa(\epsilon_z, z=0)]$. Finally, Eq. (2.26) must be integrated over all possible values of ϵ_z, i.e. from $-\infty$ to $E = E_{ph,tot} - E_{bind,H}$, yielding

$$\sigma \propto \int_{-\infty}^{E} \mathrm{Ai}^2[-\kappa(\epsilon_z, z=0)]\mathrm{d}\epsilon_z \tag{2.28}$$

for the photodetachment cross section in the presence of a static electric field.

Chapter 3

Experimental Setup

Fig. 3.1 gives a schematic overview of the experimental apparatus that was used in the photodetachment studies described in this thesis. The setup consists of a negative ion beam apparatus and an infrared laser source, arranged in a crossed beam geometry. The beam apparatus is comprised of a cesium sputter source, a bending magnet, an interaction chamber, and detection electronics. The infrared laser source includes a Nd:YAG laser, a dye laser, and various optical components for wavelength conversion and filtering.

3.1 The ion beam apparatus

The ion source is a home-built version of the high-intensity cesium sputter source developed by Middleton. The principle of operation of this type of negative ion source is described in detail elsewhere [26]. In brief, a continuous flow of cesium vapor is admitted into the evacuated (pressure $\leq 10^{-6}$ mbar) source chamber where some of the cesium atoms condense on the cooled surface of the sputter target while others are ionized by a heated tantalum coil. The target is negatively biased with respect to the ionizer such that the Cs^+ ions are accelerated and electrostatically focused

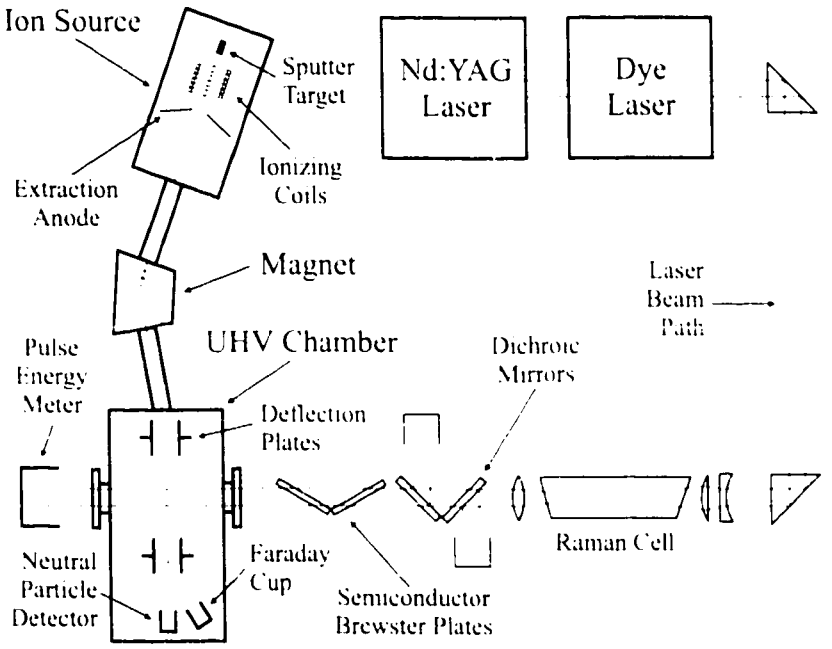

Figure 3.1: Schematic diagram of the experimental setup. See text for details.

onto the target. The cesium layer on the target reduces the effective work function of the sputter surface and thereby greatly enhances the probability that an atom (or molecule) of the target material picks up an extra electron as it is sputtered from the surface. Once formed, the negative ions are accelerated through the ionizer and a subsequent extraction anode. Typical voltage settings in the experiments described here were 1 kV for the target bias and 10 kV for the extraction anode. The extracted ion beam is collimated with the aid of an electrostatic Einzel-lens (not shown in Fig. 3.1) and then magnetically deflected through 30°. The magnet is operated at fields of $\leq$ 0.52 T which enables a reasonable mass separation of the various ion beam components ($\Delta M/M \approx 5\%$). Since cesium sputter sources operate with solid targets the beam composition can indeed be manifold. In addition to atomic negative ions, the ions of dimers and trimers are often present, as well as the ions of oxides and various compounds which result from target impurities or from reactions of the

target with the background gas of the source. In cases where the masses of atomic and molecular ions cannot be separated, the problem is often alleviated by the fact that most prolific molecular ions are too strongly bound to be photodetached by infrared light [27].

While the various source parameters are generally optimized to yield maximum beam currents of the ion species of interest, studies of ions with bound excited states also have to be concerned with the fractional population of the different ionic levels. The temperature of the sputter area gives rise to a Boltzmann population of the ionic energy levels, based on the assumption that the negative ions are able to thermalize before leaving the sputter surface. This temperature should depend on the energy and current of the sputter beam [26] but also on the size of the sputter area. The latter can be easily varied by moving the target back or forth. It was found that this has only a small effect on the total beam current but a significant effect on the population of excited ion levels. As expected, large excited level populations are obtained with the sputter target on focus, whereas the excited ion beam currents are up to two orders of magnitude smaller with the target off focus. These tests indicate a range of 500–1500 K for the effective temperature of the sputter source.

Negative ions from a keV ion beam are easily detached in collisions with rest gas molecules, hence the background signal in a measurement of photodetachment events strongly depends on the collisional detachment rate. As this rate is proportional to the rest gas pressure, the photon-ion interaction is carried out in an ultrahigh vacuum (UHV) chamber at pressures of less than 10^{-8} mbar. The ion beam is fed into the interaction chamber through a differential pressure tube. Although the transmitted beam current is typically reduced by a factor of two to five, the reduction in rest gas pressure of over two orders of magnitude still warrants a significant net im-

provement in the signal-to-background ratio. In the UHV chamber the ion beam is deflected through 10° by a pair of electrostatic deflection plates which removes any neutral particles from the beam and brings the beam on axis with the detector. The ion beam then passes through the interaction region where it is crossed at 90° by a pulsed laser beam. A second pair of electrostatic deflection plates located behind the interaction region deflects the residual ion beam into a Faraday cup, while neutral particles that were produced in the photon-ion interaction remain unaffected and finally impinge on the open cathode of a discrete-dynode electron multiplier. The signal from the electron multiplier is passed through a fast preamplifier to minimize electronic noise and is then fed into a gated integrator and boxcar averager. The gate is typically set to 50 ns which provides a sufficiently large window for the detection of all photodetachment events resulting from a ≈8 ns laser pulse, and at the same time facilitates a substantial suppression of the collisional background count, down to ∼0.1 events for a typical beam current of 100 nA.† The data acquisition window is delayed by 1–2 μs relative to the laser pulse in order to accomodate the flight time of the photodetached neutral particles from the interaction region to the detector. The time-of-flight difference between species of slightly different mass in fact enables a factor of two improvement in mass separation ($\Delta M/M \approx 2\%$) if narrow gates and a tightly collimated (or focused) laser beam are used. In the experiments described here, the number of photodetachment events per pulse was usually larger than one, which is the reason the data acquisition was conducted via analog signal integration rather than digital pulse counting. Consequently, special care had to be taken that the electron multiplier would operate in a linear regime. The data are finally read from the boxcar averager by a personal computer for further processing.

†In experiments with a collimated laser beam the minimum gate width is dictated by the ion transfer time through the laser beam, which is of the order of a few tens of nanoseconds.

3.2 The infrared laser source

The generation of tunable infrared light is based on a Nd:YAG (neodymium:yttrium-aluminium-garnet) laser, a Lumonics YM-800. The laser is operated with a Q-switched cavity, i.e. in a pulsed mode with a 10 Hz repetition rate. It is optimized to provide maximum output at 532 nm, the second harmonic of the fundamental YAG wavelength, with up to 400 mJ of energy in a ≈8 ns pulse. The pulse energy is stabilized against temperature drifts by purging the laser housing with cool nitrogen gas. The 532 nm laser pulse is used to pump a Lumonics HD-300 dye laser. This laser is operated with a 1800 lines/mm grating rather than the more common 2400 lines/mm grating in order to enable tunability over the 680–980 nm range. For this tuning range the spectral bandwidth of the laser ranges from 0.1 to 0.06 cm^{-1}. Accurate dye laser wavelength calibrations are routinely performed with a hollow cathode discharge lamp (see Sec. 3.4.2 below).

The dye laser is optimized to achieve maximum pulse energies which results in a somewhat reduced quality of the spatial pulse profile. Typical pulse energies are 50 mJ at 700 nm and 25 mJ at 950 nm. The associated peak powers of $\sim 10^7$ W are sufficient to achieve frequency conversion through the non-linear optical properties of various media. In the present case, conversion of the dye laser pulses further into the infrared was tested with two different methods, difference-frequency-mixing in non-linear optical crystals, and stimulated Raman scattering in a single-pass high-pressure hydrogen cell. The latter approach was finally chosen as it provides a broader infrared tuning range with a simpler and less delicate optical setup. A 120 cm long, 8 mm diameter cell is used, filled with H_2 at a pressure of ≈22 bar. Good conversion of the dye laser pulse into first Stokes radiation (with quantum efficiencies of up to 40%) is achieved by focusing the ≈3 mm diameter beam into the center of the cell.

A Galilean telescope (f_1=-5 cm, f_2=10 cm) with an effective focal length of ≈90 cm was utilized for this purpose. As stimulated Raman scattering is a coherent optical process, spatial, spectral, and temporal properties of the dye laser pulse are generally adopted by the first Stokes pulse (with allowance for the nonlinear aspects). For a measured cell pressure of 22(1) bar a Raman shift of 4155.187(5) cm^{-1} is expected,† based on accurate studies of the pressure dependence of the fundamental Raman band in H_2 [29]. In addition, for first Stokes wavelengths shorter than 1150 nm the optogalvanic lamp could be used for a direct calibration of the Raman shifted light. This yielded a shift of 4155.197(20) cm^{-1}, in excellent agreement with the literature value. The dye laser tuning range of 680-980 nm translates into a 950-1650 nm tuning range for the first Stokes light, although the use of different dyes is required for different regions of the tuning range. This is illustrated in Fig. 3.2 which shows pulse energy curves for the different dyes and their first and second Stokes conversions.

Conversion to second Stokes radiation becomes necessary whenever tunability beyond 1650 nm is required. Raman scattering of the first Stokes radiation, i.e. *sequential* stimulated Raman scattering would appear to be the most likely process for the generation of second Stokes radiation. However, the sequential scattering process has to compete against another non-linear process, namely parametric four-wave mixing, where the nonlinear susceptibility $\chi^{(3)}$ of the medium acts as the mixing parameter. Parametric four-wave mixing exhibits a somewhat different intensity and wavelength dependence than stimulated Raman scattering. As a result, it has been shown that Raman cells of sophisticated design are capable of suppressing the para-

†Wave numbers, cm^{-1}, are the energy units traditionally used in spectroscopy, whereas it is customary to give ionic binding energies and electron affinities in electron volts, eV, where 1 eV ≡ 8065.5410(24) cm^{-1} [28].

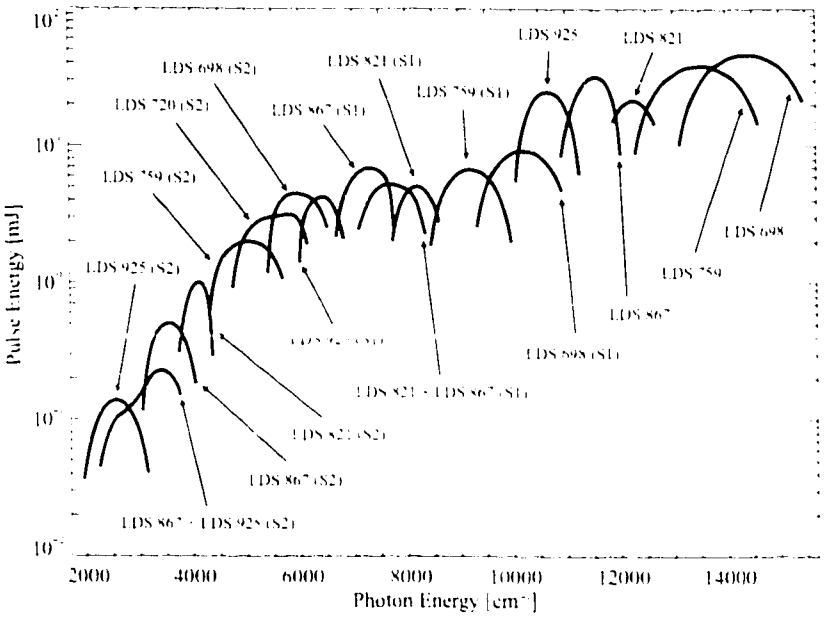

Figure 3.2: Measured pulse energy curves for selected laser dyes and for the associated first and second Stokes conversions (indicated with the labels (S1) and (S2) respectively).

metric process or at least some of its undesired properties. Such cells are Herriott type multi-pass cells with refocusing geometry [30] or single pass cells with capillary confinement of the focused laser beam [31]. Both these designs rely on a significant extension of the focused path length, which cannot be achieved with a simple single-pass cell. Hence, with the present setup second Stokes generation has to proceed via parametric four-wave mixing. The disadvantages of this process are an inevitable generation of various anti-Stokes orders, a lower theoretically achievable conversion efficiency, and the requirement of phase-matching between the mixed waves. Despite the small dispersion of H_2 gas, the phase-matching requirement noticeably affects the spatial beam profiles; in contrast to the essentially Gaussian profiles of the dye laser and first Stokes beams, the second Stokes and anti-Stokes beam profiles are donut-shaped, with almost zero intensity at the center. Commensurate with its high order of nonlinearity the four-wave mixing process is found to be strongly dependent on the

laser pulse energy, the beam quality, and the focusing geometry, but only moderately dependent on the cell pressure, in agreement with other studies [32]. For the 3 mm diameter dye laser beam used here, best results are obtained with 'soft focusing', namely a focal length around 120 cm and a focal position close to the exit window of the cell. The increased path length before the focus is believed to enhance the generation of first Stokes photons before the focus is reached, which then results in a more effective seeding of the four wave mixing process [32]. For a dye laser tuning range of 680–980 nm a second Stokes wavelength range of 1.6–5.2 μm is obtained as shown in Fig. 3.2. Quantum conversion efficiencies of up to 25% are realised at shorter wavelengths, which is only a factor of two less than the efficiency achieved with multipass cells [30]. Although the conversion efficiency drops for longer wavelengths (down to 2% at 5 μm) it was still found to be sufficient in most of the photodetachment studies.

Further Raman conversion, i.e. the generation of third Stokes radiation is expected to be rather inefficient in a single-pass cell. In fact, we found no evidence for the presence of a third Stokes component in the Raman cell output, even for the most energetic pulses at 680 nm. Hence, the use of laser dyes that operate in the near infrared rather than the visible regime is of great advantage whenever a single-pass cell is utilized.

Various combinations of optical filters are employed to eliminate the unwanted wavelength components from the Raman cell output. In experiments that require the use of first Stokes radiation long-pass filters made from Schott glass are often sufficient to remove the dye laser and anti-Stokes wavelengths. Two rectangular filters are used, tilted in opposite directions, and arranged at Brewster's angle. This minimises reflection losses without introducing a lateral beam displacement. In cases where the second Stokes wavelength falls within the transmission range of the glass filter,

no further filtering is deemed necessary, as the presence of second Stokes radiation should not affect an experiment that uses the first Stokes beam. Whenever dye laser wavelengths beyond 800 nm or first Stokes radiation have to be suppressed, pairs of 45° dichroic mirrors are utilized to attenuate the unwanted beam components by ≈90%. The final filtering is then achieved with a Brewster angle pair of semiconductor plates, made from either silicon or germanium. In all cases, a CaF_2 lens with an appropriate focal length is used to recollimate the Raman cell output such that the desired wavelength component would have a beam diameter of 3–5 mm. The infrared laser beam is finally transmitted via CaF_2 viewports through the interaction chamber, where it crosses the ion beam perpendicularly. The alignment of the crossing angle is crucial but had to be carried out only once (as described in Sec. 3.4.2 below). This is a major advantage of using filters rather than dispersing prisms or gratings as wavelength selective components; the laser beam alignment becomes wavelength independent. A pyroelectric energy meter located behind the exit window is utilized to monitor the energy of the laser pulses. The energy meter as well as the entire infrared optics table are sealed off and purged with dry nitrogen gas, as infrared absorption bands of atmospheric molecules such as CO_2 or H_2O would otherwise lead to a substantial laser beam attenuation.

3.3 Data acquisition

A region of interest in the photodetachment cross section of a negative ion is typically investigated with a slow (20–30 min) dye laser scan. Depending on the signal-to-noise ratio, the scan procedure is repeated up to ten times, and individual scans are summed. Poor signal-to-noise can be due to a large photodetachment background, small ion beam currents, and/or low infrared pulse energies. Beam current and pulse

energy are always recorded parallel to the neutral particle signal and are utilized to normalise the photodetachment data. Depending on the type of data (s-wave thresholds, p-wave thresholds, or resonances) different analyses and fitting procedures are utilized. These methods are described in Chapters 4, 5, and 6 respectively.

3.4 Experimental uncertainties

Statistical uncertainties in fitted parameters such as threshold or resonance position naturally arise from statistical fluctuations in the photodetachment data. In addition, the accuracy of crossed beam photodetachment experiments is ultimately limited by a number of factors such as the calibration uncertainty, the laser bandwidth, Doppler broadening, and possible Doppler shifts or thermal wavelength drifts. These various contributions to the experimental uncertainty are described in this section. The uncertainties of the final experimental results given in this thesis always include the various systematic errors in addition to the standard deviations obtained from the numerical fits to the data.

3.4.1 Energy resolution

The finite bandwidth of the infrared laser source ($\approx$0.08 cm^{-1}) gives rise to a predominantly Lorentzian broadening of all spectroscopic features. Doppler effects may cause an additional Gaussian broadening. For the crossed-beam setup used here the angular divergence of the ion beam is the major source of Doppler broadening. Geometric considerations of the interaction chamber suggest that the beam divergence angle should not be more than 0.5°. In the case of photodetachment with visible light this angle may very well cause a Doppler broadening larger than the laser bandwidth, but for a typical infrared photodetachment experiment (2 μm light, 15 keV beam en-

ergy, atomic mass of 60) a broadening of only 0.03 cm^{-1} results. Doppler broadening due to a (thermal) tangential velocity spread in the ion beam is even smaller and can therefore be neglected.

In principle, the finite interaction time between the fast ion beam and the pulsed laser beam constitutes an additional source of broadening. In practice, for a collimated laser beam this time is given by the duration of the laser pulse ($\approx$8 ns) and the resulting broadening is negligible. It is only for a tightly focused laser beam, as may be used in multiphoton detachment studies, that ion transfer times reach the sub-nanosecond regime and then cause broadenings of $\approx$0.1 cm^{-1}.

3.4.2 Systematic errors

In an attempt to minimize potential sources of systematic errors we have performed various tests with the infrared laser setup prior to the actual photodetachment experiments.

Calibration uncertainty

Very well known transitions in argon [33] in the 670–1150 nm range were used as a calibration standard for the tuning control unit of the dye laser. The calibrations were conducted with the aid of an argon-filled hollow cathode discharge lamp (Hamamatsu). Discharge lamps yield an optogalvanic effect, i.e. a measurable change in the discharge impedance whenever the laser wavelength is in resonance with certain atomic transitions of the filler gas [31]. Discharge lamps constitute a very convenient and quick means of wavelength calibration, but provide only relatively few calibration lines. There are 25 optogalvanically active transitions available within the 680–980 nm dye laser tuning range, with gaps between consecutive lines of up to 45 nm. Hence, the wavelength calibration of most photodetachment experiments would have to rely

on an extrapolation from the nearest argon lines, i.e. the calibration accuracy would strongly depend on the degree of nonlinearity in the tuning mechanism. Fig. 3.3 shows differences between tabulated [33] and measured argon line positions in units of wave numbers. The lines span a wavelength range of 60 nm and were measured after the tuning control unit had been calibrated using only two lines. The data in Fig. 3.3 appear to fluctuate randomly about the zero line by small amounts of less than 0.05 cm^{-1}. However, the deviation of any particular line is reproducible in different measurements to within ± 0.01 cm^{-1}.[†] The fluctuations are therefore believed to be the result of small 'local' nonlinearities in the tuning mechanism. In order to determine an upper limit for this effect an etalon was employed to monitor the laser tuning over small regions ($\approx$2 nm) at different wavelengths within the full tuning range. Deviations from linearity were very small, similar to those found for the argon lines. Therefore, a dye laser calibration uncertainty of 0.05 cm^{-1} is assumed for all experiments.

In addition, the uncertainty in the Raman shift has to be accounted for whenever first or second Stokes radiation is employed. Values of 0.02 and 0.04 cm^{-1} are used respectively, based on the uncertainty of our experimentally determined Raman shift (see Sec. 3.2).

Temperature drifts

In addition to nonlinearities, possible temperature drifts are of some concern as certain threshold or resonance scans can take several hours. The dye laser was found to require a two hour warm-up period before a drift of less than 0.01 cm^{-1} per hour is established. In addition to the water cooling of the laser dye, temperature gradients are minimized by continuously flushing the laser housing with cool nitrogen gas.

[†]The residual fluctuations of ± 0.01 cm^{-1} are likely due to a small jitter in the tuning mechanism.

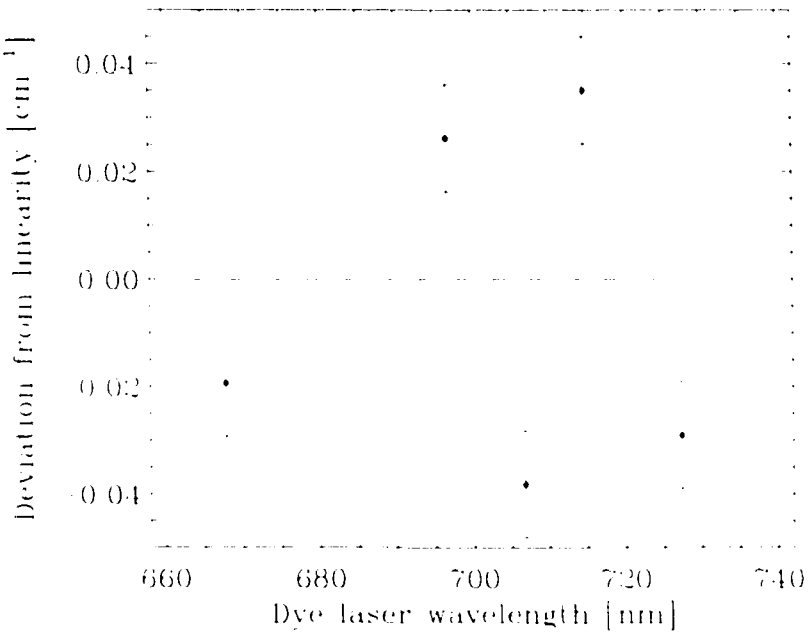

Figure 3.3: Differences between measured and tabulated optogalvanic transitions in argon as a function of transition wavelength.

A calibration performed on the temperature-stabilized laser would therefore remain valid throughout the experiment. The laser is recalibrated for each experiment to eliminate the possibility of small day-to-day fluctuations. In very long experiments that require the highest accuracy, laser calibrations are carried out before as well as after the detachment scans. This enables a correction of the data for possible wavelength drifts.

Intensity shifts

As a pulsed laser source is utilized, with peak intensities of $\sim 10^7$ and $\sim 10^{10}$ W/cm^2 for a collimated or focused beam respectively, the possibility of intensity shifts has to be considered. The threshold for photodetachment in strong laser fields is shifted to higher energies due to the ponderomotive energy of a free electron in an electromagnetic field [35]. We have therefore investigated the $^1S_{3/2} \rightarrow {}^3P_0$ thresholds of C^- and

Ge^- with a collimated laser beam (≈3 mm diameter), a cylindrically focused beam (25 cm focal length), and a spherically focused beam (20 cm focal length). While identical threshold values were obtained in the first two cases, a threshold shift of ≈1 cm^{-1} resulted in the third case. To with certainty avoid possible intensity shifts, all photodetachment threshold experiments are conducted with collimated laser light.

The bound-bound transition of a multiphoton detachment scheme, on the other hand, may be shifted in the presence of a strong laser field as a result of an *ac* Stark shift of the negative ion levels involved. However, for the transitions investigated here the ion levels belong to the same electronic configuration and should therefore exhibit very similar Stark shifts. Hence, the transition energy should remain largely unshifted. To be certain of this, we have measured the $Sn^-(^1S_{1/2} \rightarrow {}^2D_{3/2})$ resonance (see Paper 5) with the three aforementioned focusing geometries. No shifts in the resonance position were apparent.

Doppler shifts

A particular problem with the crossed-beam geometry of the present experimental setup is its susceptibility to linear Doppler shifts. In the rest frame of the fast ion beam the laser frequency will appear shifted whenever the crossing angle deviates from 90°. An alignment of this angle based on the geometry of the interaction chamber alone has an uncertainty of ≈2°, necessitating further alignment checks. For a typical ion beam energy of 15 keV and a light element such as oxygen with an electron affinity of 11784.648(6) cm^{-1} [36, 37] a misalignment of 2° would result in a Doppler shift of 0.6 cm^{-1}. In addition to its extremely well known binding energy, O^- is also a very prolific ion from a Cs sputter source for almost any oxide cathode, and furthermore detaches with a sharp *s*-wave threshold. Hence, a detachment experiment with O^- provides a sensitive test for Doppler effects. A careful measurement of the

$O^-(^2P_{3/2} \rightarrow {}^3P_2)$ detachment threshold which is presented in detail in the following chapter yielded a threshold value of 11784.6203(3) cm^{-1}. The uncertainty given here represents the standard deviation obtained from the fitting routine and the calibration uncertainty for this particular wavelength range. Our value agrees with the more accurate literature value within one standard deviation. We therefore deduce an upper limit of 0.03 cm^{-1} for possible Doppler shifts due to laser beam misalignment. While the laser beam alignment is easily maintained between experiments, some uncertainty remains regarding small deviations in the beam path for different ions. Again, geometric considerations of the interaction chamber suggest that this uncertainty should not be more than 0.5°. Hence, residual Doppler uncertainties are calculated on the basis of this value and the 0.03 cm^{-1} uncertainty from the O^- experiment. Final values range from 0.05 to 0.13 cm^{-1} depending on atomic mass and photon energy.

10

Chapter 4

Threshold Photodetachment into s-wave Continua

As outlined in Sec. 2.1, the photodetachment cross section is proportional to the reduced matrix element of the (single-electron) electric dipole operator. For detachment into an s wave continuum this matrix element is approximately constant, and the energy dependence of the cross section near threshold is proportional to the final state density. Hence, a detachment threshold with a sharp onset (infinite derivative) is expected, as the cross section is zero for photon energies (ε) below the threshold energy (ε_0) and proportional to $\sqrt{\varepsilon - \varepsilon_0}$ for $\varepsilon > \varepsilon_0$. However, the electric dipole operator has odd parity; hence, detachment into the (even) s-wave continuum can only occur if the bound electron to be detached occupies an odd parity orbital, e.g. a p- or f-orbital, but only the p-orbital is allowed by the $\Delta l = \pm 1$ selection rule (Table 2.1).

Nevertheless, atoms with valence f-electrons, namely the lanthanides and actinides could possess stable negative ions that detach into s-wave continua. The theoretically predicted binding energies of these ions are small ($\lesssim$0.5 eV) and their production is rather challenging, particularly for sputter-type ion sources. LPT studies of these systems have not yet been attempted, but recent theoretical works [38]

indicate that the extra electron might be bound in a p- or d- rather than an f-orbital, which would result in s-wave or p-wave thresholds respectively. A similar anomaly exists for the anions of scandium and yttrium which are predicted to be stable in the $(n-1)dns^2np$ configuration, but not in the $(n-1)d^2ns^2$ configuration of the respective isoelectronic atoms, titanium and zirconium.[†] Hence, these ions should exhibit s-wave instead of p-wave detachment thresholds. While Sc^- and Y^- have been studied via LPES, no data from LPI studies is yet available to confirm the assigned electron configurations.

Apart from the somewhat 'exotic' s-wave detaching ions discussed thus far, the vast majority of the ions belonging to this class is provided by main group elements, namely groups IIIA to VIIA. The atoms of these groups possess only valence p-electrons, the other outer subshells being full. Hence, stable negative ions can only arise from attachment of an extra p-electron. Core-excited ionic configurations might be bound relative to the respective core-excited configuration of the atom, but would be embedded in the detachment continuum above the atomic ground state due to the large difference between core-excitation energies and ionic binding energies for these systems. Despite the lack of stable electronically excited states, the ions of groups IIIA to VIA provide very prominent examples of anions possessing more than one stable state. The excited states arise from the different terms and fine structure levels that are associated with p^k electron configurations. The ions of the B- and N-group elements exhibit ^3P and ^1D terms, ^4S, ^2D, and ^2P terms are found in the C-group ions, and the ions of the O-group exist in a single term, ^2P.

[†] The very weakly bound ground states of Ca^-, Sr^-, and Ba^- also result from p-electron attachment.

4.1 Threshold fit

The different ionic as well as atomic terms associated with p^k configurations are well separated in energy. The thresholds of the various photodetachment channels are therefore found at very different photon energies. Fine structure splittings in both atom and ion, on the other hand, are small and give rise to series of closely-spaced cascaded thresholds. Hence, for an accurate fit to any particular threshold ε_0 it is necessary to account for the effect of the other photodetachment channels. The contribution of these other channels to the total cross section in the vicinity of ε_0 will be smooth and can be represented by a linear term, as long as the respective thresholds are not too close to ε_0. In this case, the function that is fitted to an individual s-wave threshold is given by

$$\sigma_0 = \begin{cases} a + b(\varepsilon - \varepsilon_0) + c_0\sqrt{\varepsilon - \varepsilon_0}, & \text{for } \varepsilon > \varepsilon_0 \\ a + b(\varepsilon - \varepsilon_0), & \text{for } \varepsilon \leq \varepsilon_0 \end{cases} . \qquad (4.1)$$

The fitting routine that is utilised here performs a non-linear least squares fit via a multi-parameter gradient-expansion algorithm. The fitting parameters a, b, c_0, and ε_0 are optimized simultaneously.

For a series of closely-spaced thresholds the linear background approximation is not valid. In this case, all thresholds are fitted simultaneously. The fitted function is then defined recursively:

$$\sigma_n = \sigma_{n-1} + \begin{cases} c_n\sqrt{\varepsilon - \varepsilon_n}, & \text{for } \varepsilon > \varepsilon_n \\ 0 & \text{for } \varepsilon \leq \varepsilon_n \end{cases} . \qquad (4.2)$$

Here, n=0,1,2,... labels the individual thresholds in the series. Such a simultaneous fit is found to work well if only two or three thresholds are present and if their relative intensities are not too different. However, if several thresholds or thresholds with largely differing intensities have to be fitted, this fitting routine may fail to

converge properly. In such a case, a sequential threshold fit is performed by fitting Eq. (4.1) to the lowest energy threshold first, subtracting the fit from the data, then fitting the second threshold, again subtracting the fit from the data, and so on. This method is less rigorous than the simultaneous fit as the coupling between the fitting parameters is reduced. This may result in over-optimistic standard deviations in the fitted parameters, which are therefore verified on a case to case basis.

The range of validity of the Wigner law (Eq. 2.22) is limited to the photodetachment cross section close to threshold. For a theoretical description of the cross section higher above threshold, correction terms have to be taken into account (as discussed in Sec. 2.1). However, in cases where a deviation from the Wigner law is observed, an inclusion of higher-order terms to the fitting function (Eq. 4.1) can be avoided by restricting the final scan range to a region over which the Wigner law is valid. Generally, this does not result in an increased uncertainty of the fitted threshold value as the onset of an s-wave threshold is steep and well pronounced. In contrast, for p-wave detachment the cross section higher above threshold is often essential for a determination of the threshold value from a fit to the data (see Chapter 5).

Systematic deviations from the Wigner threshold behavior may also result from a (partial) saturation of the detachment process by the intense laser pulse (although cross sections close to threshold are typically very small, $\sim 10^{-19}$ cm^2). Partial saturation should not affect the near threshold data, i.e. the fitted threshold value, but it may have an effect on the measured relative threshold intensities, particularly if different thresholds are observed that originate from the same ionic level. In measurements of threshold strengths the linearity of detachment signal versus pulse energy is therefore checked at the high energy end of the scan range.

4.2 The oxygen anion: a sample case

A schematic energy level diagram of O^- and the the ground state of O is shown in Fig. 4.1. The photodetachment cross section is composed of six cascaded thresholds, indicated by arrows in the figure. The relative strengths of these six thresholds can be evaluated with Eq. (2.24) yielding (from low to high energies) 5 : 9 : 25 : 1 : 9 : 2 for a statistical level population ($I \to \infty$). The third threshold, $^2P_{3/2} \to {}^3P_2$, which defines the electron affinity of oxygen is particularly strong.

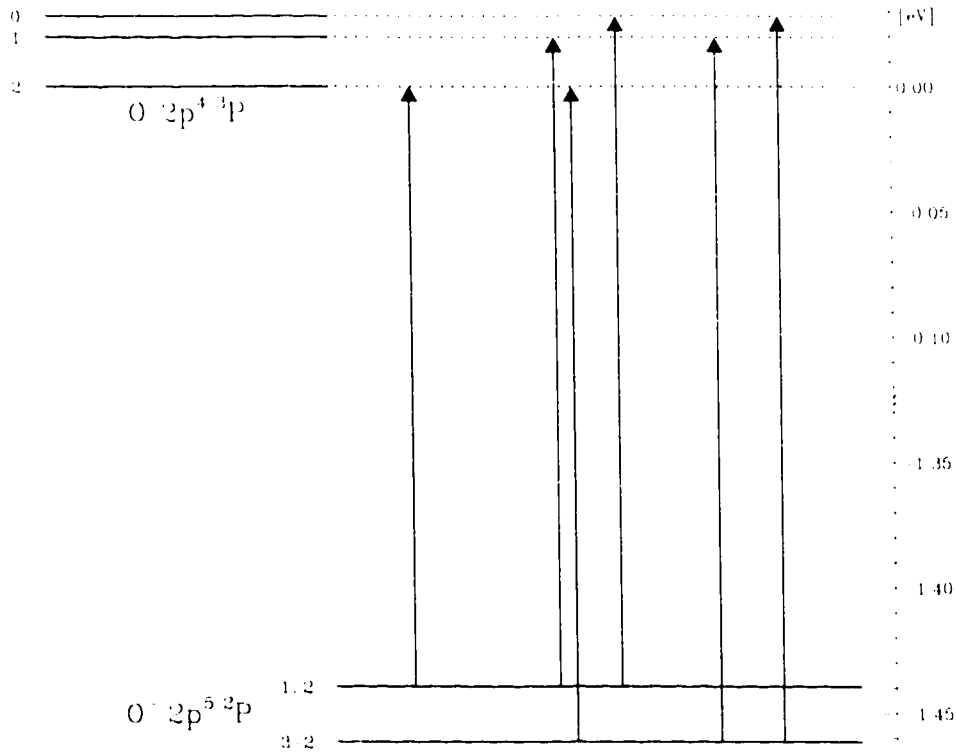

Figure 4.1: Schematic energy level diagram of O^- and O. Arrows indicate detachment thresholds, ordered by threshold energy. The horizontal spacing between arrows is proportional to the energy separation of the respective thresholds. For clarity of presentation, the diagram is shown with a broken energy axis.

The threshold region of the O^- detachment cross section was previously investigated by Neumark *et al.* [36] resulting in the most accurate binding energies

ever measured in a negative ion.[†] They report an electron affinity of 11781.648(6) cm^{-1} and a $O^-(^2P)$ fine structure splitting of 177.08(5) cm^{-1} (after subsequent corrections [37, 1]).

Due to its well established energy level structure and due to the fact that the detachment thresholds occur in the near-infrared regime, O^- is the ideal ion for a calibration of the present infrared LPT setup. As discussed in more detail in Sec. 3.4.2 a crossed laser-ion beam geometry is particularly susceptible to systematic errors due to Doppler shifts. For a light element such as oxygen and a typical ion beam energy of 15 keV a deviation from the 90° crossing angle by only 1° would result in a Doppler shift of 0.3 cm^{-1}.

Fig. 4.2 shows the photodetachment cross section of O^- over the region of the first four thresholds, as measured with the present setup. O^- is a very prolific negative ion from a Cs sputter source; the ≈1 μA obtained in the UHV section and the ≈20 mJ of pulse energy available around 850 nm provided for a high signal-to-noise ratio in the data. The observed threshold intensity ratios closely match the calculated values if the thermal population of the ionic levels is taken into account (Eq. 2.24).

For an accurate measurement of the ionic binding energies the two $^2P_J \rightarrow {}^3P_2$ thresholds (first and third threshold in Fig. 4.2) were also investigated separately, with high-resolution laser scans. The results are shown in Figs. 4.4 and 4.3. The observed photodetachment cross sections deviate from the ideal Wigner s-wave behavior (dashed line), primarily due to the finite laser bandwidth of ≈0.08 cm^{-1}. In addition, small modulations of the cross sections are apparent, which result from the presence of a weak electrostatic field. Although the current design of the UHV interaction

[†] These accuracies have been matched in a subsequent LPT study of S^- by the same group [1].

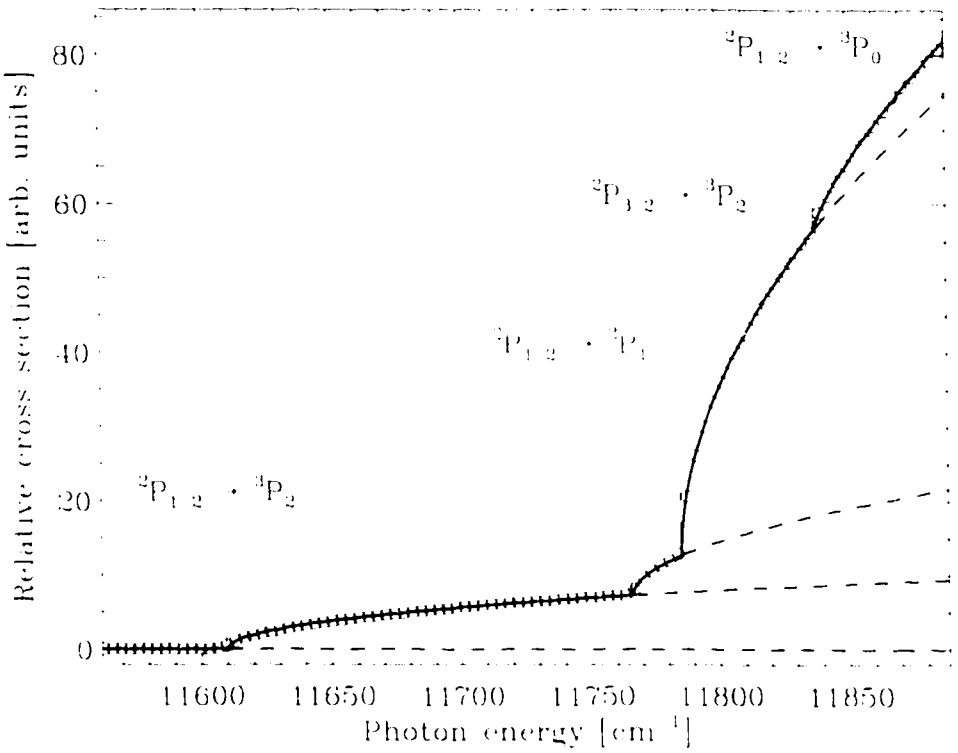

Figure 1.2: Measured photodetachment cross section of O^- in the region of the $^2P_{1/2} \rightarrow {}^3P_J$ thresholds. The result of sequential Wigner s-wave fits to the data is indicated by the solid line. Individual thresholds are extrapolated with dashed lines.

chamber provides for a shielding of the electrostatic deflection plates, stray fields of $\approx$10 V/cm seem to remain. Fortunately, the effect of static electric fields on s-wave thresholds has been thoroughly investigated in the past [23] and can be accurately modelled (as discussed in detail in Sec. 2.6). If the cross section obtained with this model is convoluted with a Lorentzian bandwidth function, the solid lines in Figs. 1.1 and 1.3 are obtained. The excellent agreement between fitted and measured cross sections allows for an accurate determination of the respective threshold energies: 11784.62(3) and 11607.65(5) cm^{-1} for $^2P_{3/2,1/2} \rightarrow {}^3P_2$ respectively. The uncertainties given here include the standard deviation obtained from the fitting routine and the laser calibration uncertainty. It is important to note that the same threshold values

are obtained if the effects of laser bandwidth and electric field are ignored in the fit (dashed lines in Figs. 1.1 and 1.3). Hence, the Wigner s-wave fit (Eq. 1.1) remains valid. The agreement between our value for the $^2P_{3/2}$ binding energy and the substantially more accurate literature value indicates that no significant Doppler shifts were present in our experiment.

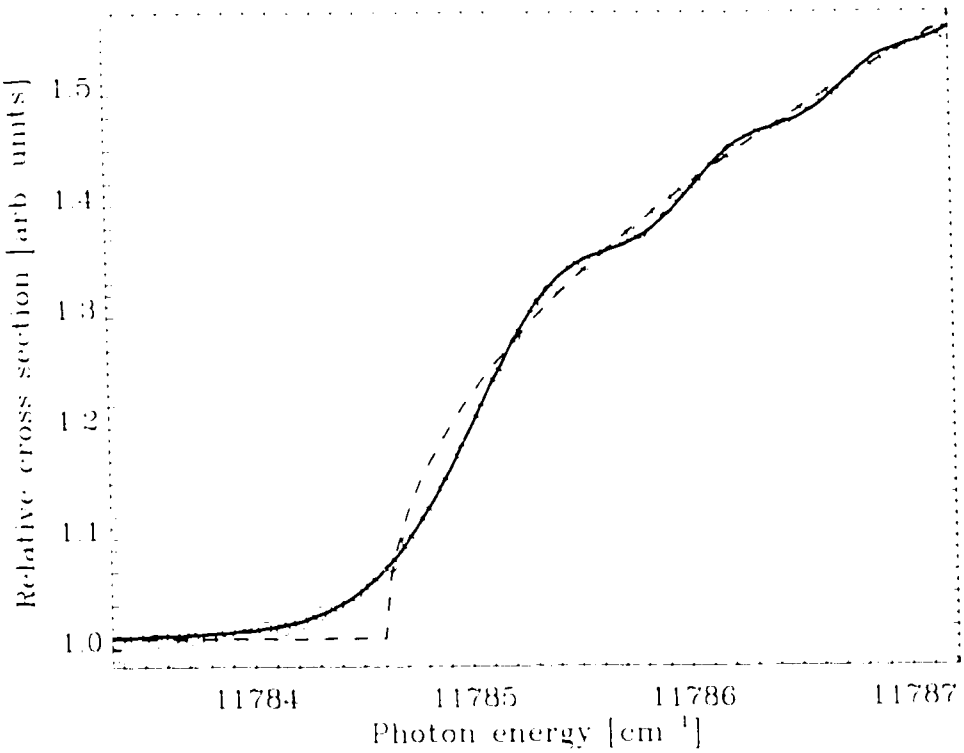

Figure 1.3: High-resolution scan of the O^- detachment cross section in the vicinity of the $^2P_{3/2} \rightarrow {}^3P_2$ threshold. An ideal Wigner s-wave is indicated by the dashed line, while the result of an s-wave fit that includes bandwidth and field effects is represented by the solid line.

The extremely high resolution in the collinear-beam LPT experiment of Neumark *et al.* was achieved with a cw infrared dye laser, operated in a single-mode ring-cavity configuration. Unfortunately, they used this configuration only for the $^2P_{3/2} \rightarrow {}^3P_2$ threshold scan, whereas a multi-mode standing-wave configuration was

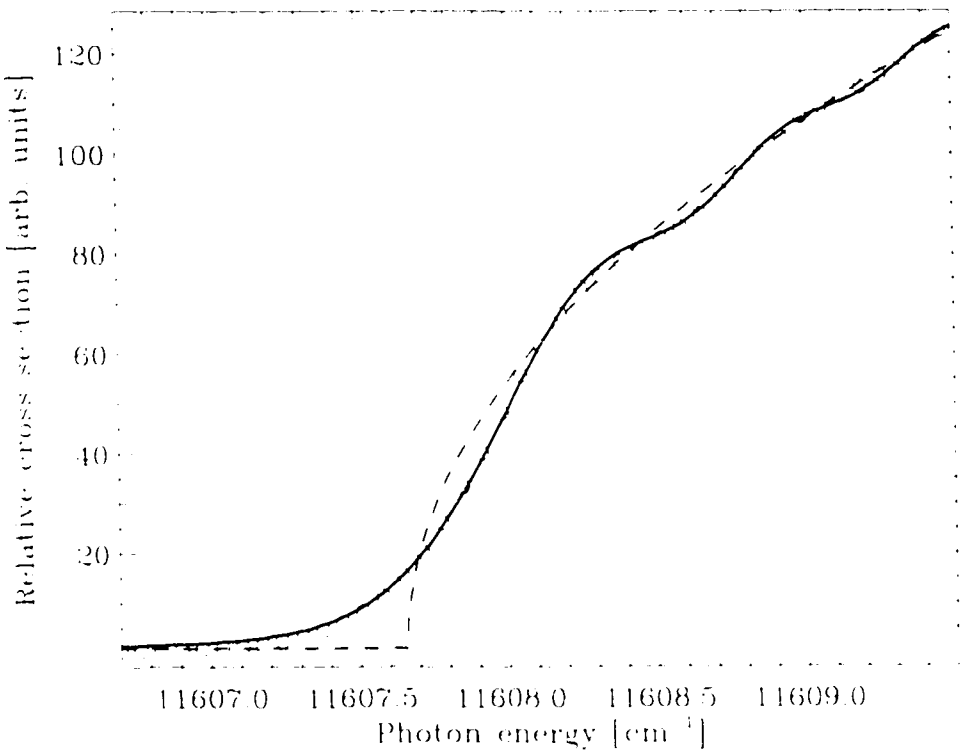

Figure 4.4: High-resolution scan of the O^- detachment cross section in the vicinity of the $^2P_{1/2} \rightarrow {}^3P_2$ threshold. An ideal Wigner s-wave is indicated by the dashed line, while the result of an s-wave fit that includes bandwidth and field effects is represented by the solid line.

utilized for the $^2P_{1/2} \rightarrow {}^3P_2$ threshold scan. This fact seems primarily responsible for the larger uncertainty of their value for the fine structure splitting, 177.08(5) cm^{-1}. In comparison, the difference of our two threshold values yields a value for the splitting of similar accuracy, 176.97(6) cm^{-1}. The two results just agree within one standard deviation.

4.3 Boron-group anions

Previous experimental investigations of the boron-group negative ions have found small binding energies (<0.5 eV) for all five ions. These studies employed LPES (for B^- and Al^-) and threshold spectroscopy with conventional light sources (for

Ga^-, In^-, and Tl^-) resulting in experimental uncertainties of 10 and ≈150 meV respectively. In all cases, the fine structure of the ionic ^3P term remains unresolved.

Thus far, we have conducted successful infrared LPT studies of B^- and Al^-, discussed in some detail below. These ions, particularly B^-, are prolific from a Cs sputter source. Beam currents of ≈100 nA for B^- and ≈10 nA for Al^- provided a good basis for photodetachment experiments. In contrast, In^- and particularly Ga^- and Tl^- are notoriously difficult to produce with sputter sources [39]. We have experimented with various indium metal cathodes but were never able to obtain more than ≈100 pA. This was sufficient to observe detachment for photon energies well above threshold but the threshold for detachment could not be located. To some extent, these difficulties may be associated with the very low melting point of indium. Further experiments are therefore planned with cathodes made of compounds such as InP and GaAs.

4.3.1 B^-

Our LPT study of B^- was motivated by the fact that this ion plays a special role among the anions of the light elements, most of which have been studied extensively in the past. The electron affinities of H, C, O, and F were measured via tunable laser threshold photodetachment leaving the neutral atom in its ground state [10, 9, 36, 40], whereas the binding energies of Li^- [6, 11] and the metastable He^- [42] and Be^- [43] ions have been determined through laser photodetachment involving an excited state of the atom and state-selective detection schemes. Accuracies of experimental EA's for these seven elements range from 0.3 meV (C^-) to 0.001 meV (O^-). In strong contrast, the EA of boron still relies on an early laser photodetached electron spectrum recorded by Feigerle *et al.* [44] which resulted in a value of 277(10) meV (after a subsequent recalibration [36]). Furthermore, no experimental data is available on the

fine structure of the ionic $2p^2\ ^3P$ ground state. The $2p^2\ ^1D$ and $2p^2\ ^1S$ terms of the ion, on the other hand, are likely unbound: a recent communication on resonance structures in collisionally detached electron spectra of B^- tentatively identified the ^1D term with a resonance located 104(8) meV above the ground state of boron [45]. Hence, the three ^3P_J levels are the only stable states of B^-.

Various approaches to the *ab initio* calculation of electron affinities of the light elements have been attempted in recent years [46, 47], but even these small systems remain challenging as electron correlations play a dominant role. This is particularly true for boron which forms the most weakly bound stable ion among the light elements. Of the numerous theoretical studies of the EA of boron [46, 47, 48, 49, 50], three recent works were aimed at accuracies better than 10 meV. Noro *et al.* [47] obtained an EA of 278 meV as the result of a large-basis-set multireference singly and doubly excited configuration-interaction (CI) calculation. Large-scale finite element multiconfiguration Hartree-Fock (MCHF) calculations, which do not suffer from basis set limitations have been performed by two groups, Sundholm and Olsen [48], and Froese Fischer *et al.* [49]. They report EA's of 268.6(17) and 273.2(2) meV respectively as the result of an initial valence correlation MCHF calculation that neglects core polarization effects. Sundholm and Olsen estimate core-valence correlations to lower the EA to 267.8(20) meV whereas Froese Fischer *et al.* predict the EA to increase to 279.5(20) meV through the inclusion of core-valence and core-core correlations (the latter via core rearrangement). However, the experimental EA of 277(10) meV [44] agrees with all of the above values within uncertainties; hence the fundamental question as to the effect and strength of core-valence and core-core correlations in B^- remains open and controversial.

Threshold detachment of B^- to the atomic ground state is expected to be

rather challenging, as the small binding energies involved necessitate tunability of the laser source over the 3.8 to 4.5 μm region. However, threshold detachment to the first excited state[†] of boron is even less favourable, primarily due to the uncertainty of 15 cm^{-1} in the separation between the doublet and quartet systems of the atom [51].

Our infrared LPT spectrum of the $B^-(^1P_1) \rightarrow B(^2P_{1/2})$ threshold region[‡] revealed five closely-spaced cascaded thresholds, enabling a very accurate determination of the EA of boron as well as the ionic fine structure splittings ($\sigma = 0.3$ meV). The results are summarized in Table 4.1 below. The new EA value, 279.723(25) meV, is in excellent agreement with the very recent theoretical result of Froese Fischer *et al.* [49], but in definite disagreement with the value calculated by Sundholm and Olsen [48]. Hence, the present result confirms the importance of core-valence and core-core correlation for the accurate treatment of the six-electron system B^-.

Details of the experimental work as well as its implications for the competing theoretical models are discussed in Paper 3 in the appendix.

4.3.2 Al^-

The negative ion of aluminum has been the subject of several previous experimental and theoretical studies. Utilizing laser photodetachment electron spectrometry, Feigerle *et al.* [44] measured the electron affinity of Al to be 442(10) meV, and found the $Al^-(^1D_2)$ level to lie 332(10) meV above ground state Al^-, with a binding of 110(10) meV. The latter value for the $^1D_2$ level agreed with the result of electric field dissociation experiments by Oparin *et al.* [52], where a binding of ≈ 95 meV was obtained. As a result of subsequent refined calibrations [36], an improved value for the

[†]The binding energies of some weakly-bound alkali and alkaline earth negative ions have in fact been accurately measured via detachment to the first excited state of the atom [6, 7].

[‡]Note that the energy level structure here is conceptually identical to that of O^- and O shown in Fig. 4.1, except that atomic and ionic terms are interchanged, which has no bearing on the relative threshold intensities.

EA of Ref. [4] was suggested to be 441(10) meV [1]. Recently, Calabrese *et al.* [53] measured the electron affinity of Al to be 440.94(+0.66−0.48) meV by utilizing a tunable F-center laser and a coaxial ion-laser beam apparatus. Although they were unable to investigate the actual threshold region and the associated fine structure, they compensated for lack of data in this region via extrapolating from higher photon energy data. In the past few years, calculations have been reported by Arnau *et al.* [54], who used a configuration-interaction (CI) method with pseudopotentials, Woon and Dunning [55], who employed a CI method with correlation consistent basis sets, and Wijesundera [50], who utilized a multiconfiguration Dirac Fock method. They obtained values of 450 meV [54], 437 meV [55], and 433 meV [50] respectively.

As with B^-, our investigation of Al^- was aimed at the $^3P_J \rightarrow {}^2P_{\frac{3}{2}}$ threshold region. Again, the first five thresholds could be resolved in the LPT spectrum. Due to the approximately ten times larger fine structure splittings compared to B^-, the first three thresholds were also measured individually in high-resolution scans, yielding more accurate threshold values. The results are summarized in Table 4.1.

The theoretical results quoted above are in good agreement with our value for the EA of Al, 432.83(5) meV, considering that the uncertainties in EA calculations of second-row elements are still of the order of 10 meV. However, a substantial disagreement with the recent experimental result of Calabrese *et al.* [53] is found. After a careful comparison of the two experimental works we conclude that some systematic error has probably arisen in the work of Calabrese *et al.*, in addition to the statistical errors incurred by the low signal-to-noise ratio of their data and the necessary extrapolation to threshold. Details of this comparison and a complete account of our results are given in Paper 4.

4.4 Carbon-group anions

The anions of the carbon group elements have been considered famous examples of negative ions with excited terms of the ground state configuration that still lie below the first detachment threshold [37]. Nevertheless, the experimental knowledge of these excited terms is still rather limited, particularly for Ge^- and Sn^- where the relative experimental uncertainties are as large as 50%. In addition to the ^4S term of the p^3 configuration, which provides the ionic ground state, previous studies have confirmed a bound ^2D term for C^-, Si^-, Ge^-, and Sn^-, whereas a bound ^2P term was only found in the case of Si^-. For the negative ion of lead, which is less strongly bound than the other anions of this group, the ^2D and ^2P terms are expected to be unbound, on the basis of isoelectronic extrapolation. As an example of the energy level structure of these systems the level diagram of Sn^- is shown in Fig. 1.5, also indicating various photodetachment thresholds.

The electron affinities of Si, Ge, and Sn were the target of the first LPT studies conducted by the McMaster group. Accurate values ($\sigma \leq 0.06$ meV) were obtained in all three cases (Paper 10). Our recent efforts with the carbon group anions have resulted in slightly improved EA's for these three elements ($\sigma \leq 0.02$ meV), due to refined and more rigorous calibration procedures. The final values are given in Table 4.1. In addition, we obtained an accurate EA for carbon as well as the first fine-structure-resolved binding energies for the ^2D_J levels of Si^-, Ge^-, and Sn^-. These measurements are described below.

The accuracy in the EA of lead ($\sigma = 8$ meV) could not be improved in experiments with the McMaster setup. Pb^- beams are very difficult to produce with a cesium sputter source. In various attempts with lead metal as well as lead oxide cathodes we were not able to produce more than $\approx$10 pA of Pb^-, which was insufficient

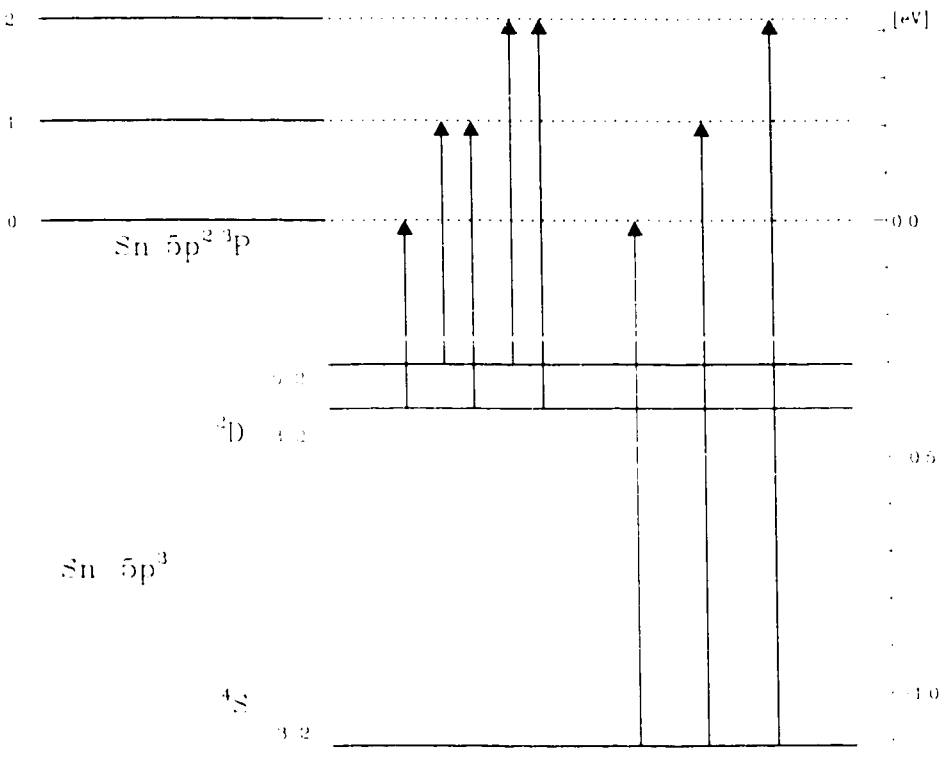

Figure 1.5: Schematic energy level diagram of Sn^- and the Sn ground state. Arrows indicate detachment thresholds, ordered by threshold energy. The horizontal spacing between arrows is proportional to the energy separation of the respective thresholds.

for a determination of the EA-defining $^4S_{3/2} \rightarrow {}^3P_0$ threshold. Similarly, various attempts towards an observation of the $C^-(^2D_J)$ and $Si^-(^2P_J)$ levels were unsuccessful. While the term-averaged binding energies of these levels were established in previous studies, the fine structure has never been resolved. Hence, the $C^-(^2D_J)$ and $Si^-(^2P_J)$ fine structure splittings remain the only undetermined structural features of the five carbon-group negative ions.

4.4.1 C^-

Despite the fact that carbon is a light (first row) element, there have been very few experimental investigations of its negative ion. The binding of the ionic $2p^3\ ^4S_{3/2}$ ground state was most accurately measured via infrared LPT by Feldmann [9] yielding

1.2629(3) eV. Feldmann used a laser pumped optical parametric oscillator for his pioneering infrared LPT work. In addition to the ground state detachment thresholds, his LPT spectrum also provided evidence for an ionic $2p^3\ ^2D$ term with a binding energy of 33(1) meV, which agreed with an earlier value of 37(3) meV, obtained via field ionization measurements [56].

Since the recent LPT studies of Li^- by Haeffler *et al.* [11] and our investigation of B^- (Sec. 1.3.1, Paper 3), carbon has become the first row element with the largest uncertainty in its electron affinity, 0.3 meV (versus 0.025 meV for B^-). Many calculations of the EA of carbon have been performed to date [57], but they typically exhibit errors of several meV. On the other hand, recent large-scale MCHF calculations of the EA of lithium [58] and boron [19] have indicated that calculation errors of less than one meV might be achievable in future *ab initio* calculations of other first-row elements. Hence, a more accurate determination of the EA of carbon seems appropriate.

A high-resolution scan of the EA-defining $^4S_{3/2} \rightarrow\ ^3P_0$ threshold and a subsequent s-wave fit to the data resulted in a threshold energy of 1.262119(20) eV. This value improves the accuracy of the EA of carbon by a factor of 15, but the value lies outside the error margin of Feldmann's result of 1.262903) eV [9]. This seems to indicate that a source of systematic error unaccounted for might have been present in the earlier work.

In an attempt to reproduce the weak $^2D_J \rightarrow\ ^1D_2$ threshold feature observed by Feldmann, we have carefully investigated the detachment cross section in the 945–965 nm range, which corresponds to ^2D binding energies between 21 and 18 meV. No evidence for a threshold structure was found. An insufficient population of the ^2D_J levels from our ion source is the most likely explanation for the absence of

the corresponding threshold features. (Please refer to Paper 5 for a more detailed discussion of our experiments with C^-.)

4.4.2 Si^-, Ge^-, and Sn^-

In addition to highly accurate ground state thresholds ($^4S_{3/2} \rightarrow {}^3P_0$), most of the $^2D_J \rightarrow {}^3P_{\bar{J}}$ thresholds could be measured for Si^-, Ge^-, and Sn^-. The major limitation for threshold detachment from excited ionic states in experiments with a sputter source is the small fractional population that is obtained in excited levels. Hence, large total beam currents are essential.

In the case of Si^-, a very large total current of $\approx 2\mu$A resulted in an excited level population of a few nA, which provided a good signal-to-noise ratio even in a single scan. All five allowed $^2D_J \rightarrow {}^3P_{\bar{J}}$ thresholds could be measured, yielding accurate ^2D_J binding energies ($\sigma \approx 0.03$ meV, Table 4.1).

In the cases of Ge^- and Sn^- excited level populations were very small due to the substantially smaller total beam currents of $\sim$100 nA. In addition, the previous experimental values for the term-averaged ^2D binding energies have uncertainties of 200 meV, necessitating search scans over very large photon-energy ranges. Nevertheless, two and four of the possible five $^2D_J \rightarrow {}^3P_{\bar{J}}$ thresholds were found for Ge^- and Sn^- respectively. Signal-to-noise ratios remained poor even after repetitive scans of these threshold features. The characteristically steep onset of s-wave thresholds still enabled accurate fits to the data ($\sigma \leq 0.1$ meV). As an example for s-wave thresholds involving excited ionic states, the weakest of the $Sn^-(^2D_J)$ thresholds, $^2D_{5/2} \rightarrow {}^3P_1$, is shown in Fig. 4.6. The poorer signal-to-noise compared to ground state thresholds (e.g. Figs. 4.3 and 4.4) is evident. ^2D_J binding energies that resulted from the threshold fits are summarized in Table 4.1. A detailed description of the experiments is given in Paper 5.

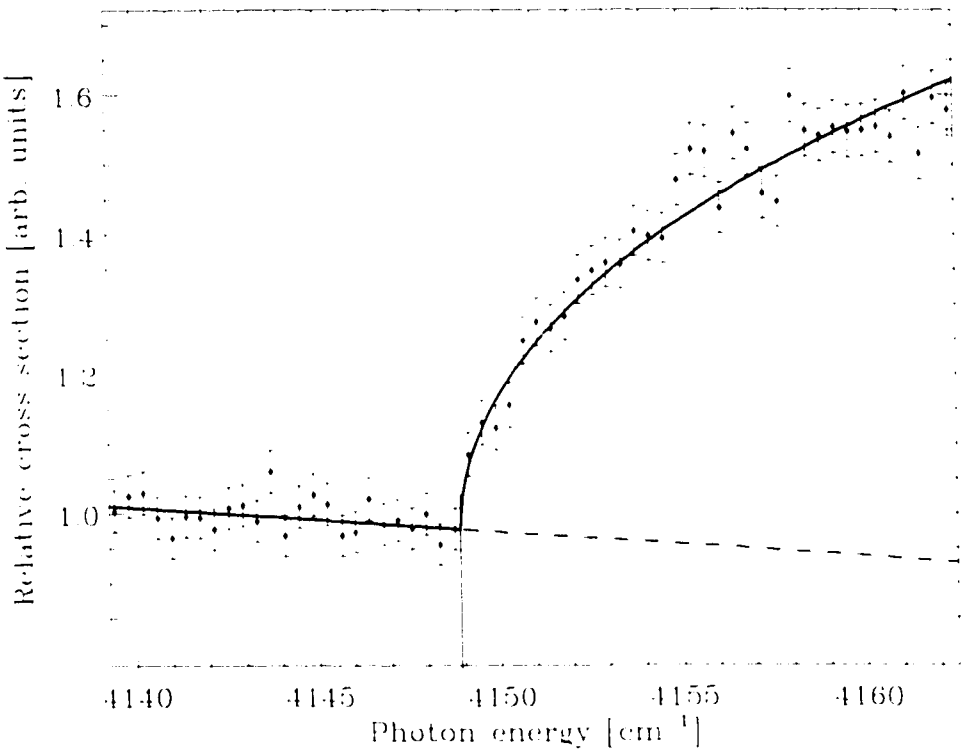

Figure 4.6: Measured Sn^- photodetachment cross section in the vicinity of the $^2D_{3/2} \rightarrow {}^3P_1$ threshold. The result of a Wigner s-wave fit is indicated by the solid line.

The ^2P term of Si^- and the ^2D term of Sn^- were also investigated via resonant multiphoton detachment schemes. Those experiments are discussed in Chapter 6 and are presented in detail in Paper 5.

4.5 Nitrogen-group anions

The atomic ground state of the nitrogen-group elements is the $p^3\ ^4S_{3/2}$ level. Attachment of a fourth electron to three spin-parallel p-electrons is energetically less favourable than p-electron attachment to the p^2 or p^1 configurations of the carbon- or oxygen-group atoms, respectively. It is therefore not surprising that the EA's of nitrogen-group elements are lower than the EA's of the elements in the neighboring groups. Paticularly noteworthy is nitrogen itself which does not form a stable nega-

tive ion [1]. The remaining four elements of the group, P, As, Sb, and Bi form stable negative ions in the p^4 configuration with electron affinities ranging from 0.75 to 1.05 eV. Of the three terms associated with p^4 configurations, ^3P, ^1D, and ^1S, the term with the highest multiplicity, ^3P, lies lowest in energy and exhibits an inverted order of the fine structure levels.

4.5.1 P^- and As^-

P^- is one of the three ions (the others being Li^- and C^-) that Feldmann investigated in his pioneering infrared LPT work [8]. He obtained accurate values for the EA as well as for the ^3P fine structure splittings (σ=0.3 meV). The EA of As, on the other hand, still relies on an early photodetachment experiment with a conventional light source which yielded a value of 0.814(3) eV [61]. However, the As^- ^3P_J fine structure splittings were recently measured in an LPES study with an accuracy of $\pm$ 5 meV [62]. Furthermore, the singlet terms for both P^- and As^- are expected to be unbound on the basis of isoelectronic extrapolation. Hence, the stable states of these two systems are reasonably well established, although an investigation with the McMaster setup would likely provide more accurate values, particularly for the EA of As.

4.5.2 Sb^-

In contrast to P^- and As^-, the energy level structure of Sb^- has not yet been established experimentally. To our knowledge, only two photodetachment experiments with this system have been reported previously. Feldmann *et al.* [61] used a conventional light source and obtained a $^3P_2$ binding energy of 8630(400) cm^{-1} and a $^3P_2 - {}^3P_{1,0}$ fine structure splitting of 2740(600) cm^{-1}. The J = 1,0 levels remained unresolved. The $J = 2-1$ and $J = 2-0$ fine structure and $^3P_2 - {}^1D_2$ term splittings have been predicted to be 2700(500), 3000(500) and $\sim$7600 cm^{-1} on the basis

of isoelectronic extrapolation [63, 64]. Polak *et al.* [65] derived an electron affinity of 8436(40) cm^{-1} from a laser photodetached electron spectrum and reported that no evidence of hot bands (i.e. of the $^3P_{1,0}$ and $^1D_2$ levels) was observed.

Our infrared LPT study of this system revealed three s-wave thresholds, the strong $Sb^-(^3P_2) \rightarrow Sb(^4S_{3/2})$ ground state threshold at 8447.86(15) cm^{-1}, and two significantly weaker thresholds at photon energies of 5763.30(3) and 5647.05(5) cm^{-1}. The latter two detachment thresholds originate from the two upper levels of the ^3P term and enable the first determination of the ^3P fine structure splittings, 2684.56(4) and 2800.8(6) cm^{-1} for $J = 2-1$ and $J = 2-0$ respectively (if a J=2 1 0 level order is assumed). The most likely order of the ^3P_J levels is certainly 2 1 0 but the large uncertainties of isoelectronic extrapolations leave a small probability for a 2 0 1 order which is found throughout the isoelectronic sequence (Te, I^+, etc.). The ultimate confirmation for a 2-1-0 level order is finally obtained from a 1+1 two-color photodetachment experiment which is described in Sec. 6.2.3. The previously unobserved $Sb^-(^1D_2)$ level is too weakly bound for a direct observation of the threshold for detachment into $Sb(^4S_{3/2})$. However, this level could be probed via multiphoton schemes (Chapter 6). A complete account of our single- and multiphoton detachment experiments with Sb^- may be found in Paper I.

4.5.3 Bi^-

The negative ion of bismuth, the heaviest non-radioactive element, has a measured electron affinity of 946(10) meV, determined by LPES [14]. Hence, Bi^- is about three times more strongly bound than Tl^- and Pb^-, the two other s-wave-detaching heavy ions, and is therefore the only hopeful candidate for an anion with a $6p^6$ configuration that possesses more than one stable state. In fact, a very recent RCI calculation indicates that the $^3P_0$ level is located 647 meV above the $^3P_2$ ground state.

i.e. that it is bound by 299 meV [66]. This binding energy corresponds to an infrared wavelength of 4.15 μm and would be within the tuning range of the current infrared laser setup. A LPT study of the $^3P_0$ level should thus be possible, provided that a sufficient population of this level can be obtained from the sputter source. The $^3P_1$ level, on the other hand, is expected to lie several hundred meV above the $^3P_0$ level and is likely unbound.

Our initial LPT experiments with Bi^- were aimed at a more accurate determination of the $^3P_2$ (ground state) binding energy. Despite a surprisingly low beam current of $\approx$5 nA good signal-to-noise was achieved in the $Bi^-(^3P_2) \rightarrow Bi\,(^4S_{3/2})$ threshold scans, resulting in a threshold value of 942.370(20) meV. A small detachment signal below threshold provides some evidence for the existence of a bound $^3P_0$ state. Unfortunately, the population of this state was insufficient for an observation of the actual detachment threshold.

The experiments were performed with a sputter cathode made of bismuth metal which has a low melting point of 273°C. It is conceivable for a Cs-sputter ion source that the use of metal cathodes with relatively low melting points could result in increased sputter rates for neutral particles and therefore in reduced ion beam currents. This might be particularly critical if high effective sputter temperatures are utilized, which in turn are essential for an efficient excited level population. In the LPT experiments with Sn^- (Sec. 4.4.2), for example, detachment signals from excited ionic levels were improved by two orders of magnitude by switching from a metal to an oxide cathode. Hence, it is hoped that the use of a bismuth oxide cathode in future experiments will finally enable a measurement of the $Bi^-(^3P_0) \rightarrow Bi\,(^4S_{3/2})$ threshold.

4.6 Oxygen-group anions

The negative ions of the oxygen-group elements are more strongly bound than the ions of the three groups dicussed thus far. Binding energies range from approximately 1.5 to 2.0 eV. Hence, LPT studies of these systems can be performed with tunable dye lasers without the need for infrared conversion. Consequently, the energy level structure of O^-, S^-, Se^-, and Te^- has been extensively studied in the past and is now extremely accurately known.

Prior to our infrared LPT studies of less accurately known ions we have measured the LPT spectrum of O^- with the aim to test the experimental setup for possible systematic errors. These experiments are described as a benchmark case in Sec. 4.2.

We have also investigated the photodetachment threshold of the upper fine structure level in Te^- on two different occasions. The $Te^-(^2P)$ and $Se^-(^2P)$ fine structures were the first target of resonant multiphoton detachment of atomic negative ions (Sec. 6.1 and Paper 9). In addition, the observation of the magnetic-dipole fine-structure transition in Te^- provided ultimate evidence for forbidden transitions in negative ions (Sec. 6.2.2 and Paper 7). In these contexts, the threshold measurements served as an independent confirmation of the ^2P fine structure splitting.

4.7 Fluorine-group anions

The atoms of the fluorine group are one electron short of shell closure. Hence, attachment of an extra electron results in an energetically very favourable noble gas configuration. It is therefore not surprising that these elements form the most strongly bound atomic negative ions, with binding energies ranging from 3.0 to 3.6 eV. The thresholds for single-photon detachment of these ions lie in the ultraviolet and have been accurately measured in the past with the aid of frequency-doubled dye lasers [37].

In terms of infrared LPT studies the fluorine-group anions constitute interesting targets for multiphoton threshold detachment. Various aspects of multiphoton detachment from negative ions have been investigated in the past [37], but there are only two previous studies of multiphoton detachment thresholds, namely the two-photon thresholds of H^- [68] and Cl^- [67]. However, the resolution that was achieved in these studies did not allow for a quantitative analysis of the cross section at threshold.

With the infrared capabilities of the current setup, an observation of the three-photon detachment threshold of Cl^- might be possible and would in fact provide the first example of a three-photon threshold. This experiment and two-photon detachment of the Au^- ion are the subject of a current study by the McMaster negative ion group.

4.8 Summary and outlook

Negative ion binding energies that were derived from s-wave fits to infrared LPT data are summarized in Table 4.1 together with previous experimental results for comparison. In most cases, improvements in accuracy over previous values of one to four orders of magnitude were achieved. Several bound excited states were in fact observed for the first time. Hence, the application of infrared LPT to the anions of group IIIA to VIA elements was overall very successful.

Only relatively few tasks remain regarding the experimental knowledge of these ions: The EA's of Ga, In, and Tl are only very poorly determined ($\sigma \geq 150$ meV) and may in principle be accurately measured via infrared LPT; also, the EA's of Pb and As could still be improved; finally, a more accurate determination of the

Table 4.1: Summary of ionic binding energies derived from s-wave thresholds.

		Binding energy [eV]		
Ion	Level	This work	Previous works	Ref.
B^-	$^3P_0$	0.279723(25)	0.277(10)	[44, 36]
	$^3P_1$	0.279323(20)		
	$^3P_2$	0.278681(20)		
Al^-	$^3P_0$	0.43283(5)	$0.44094(^{+42}_{-42})$	[53]
	$^3P_1$	0.43001(3)		
	$^3P_2$	0.42435(3)		
C^-	$^4S_{3/2}$	1.262119(20)	1.2629(3)	[9]
Si^-	$^4S_{3/2}$	1.389521(20)	1.385(5)	[59]
	$^2D_{3/2}$	0.527234(25)	0.523(5)*	[59]
	$^2D_{5/2}$	0.525489(20)	0.523(5)*	[59]
Ge^-	$^4S_{3/2}$	1.232712(15)	1.233(3)	[60]
	$^2D_{3/2}$	0.40144(10)	0.4(2)*	[1]
	$^2D_{5/2}$	0.37757(6)	0.4(2)*	[1]
Sn^-	$^4S_{3/2}$	1.112067(15)	1.112(4)	[60]
	$^2D_{3/2}$	0.397617(15)	0.4(2)*	[1]
	$^2D_{5/2}$	0.304635(15)	0.4(2)*	[1]
Sb^-	$^3P_2$	1.047402(20)	1.046(5)	[65]
	$^3P_1$	0.71456(4)	0.73(5)*	[61]
	$^3P_0$	0.70014(6)	0.73(5)*	[61]
Bi^-	$^3P_2$	0.942370(20)	0.946(10)	[44]
O^-	$^2P_{3/2}$	1.461107(5)	1.4611107(8)	[36, 37]
	$^2P_{1/2}$	1.439166(6)	1.439156(6)	[36, 1]
Te^-	$^2P_{1/2}$	1.350288(20)	1.3499(6)	[1]

^3P fine structure would be possible for P^- and As^-.

Further improved or alternative tunable infrared laser sources such as optical parametric oscillators may provide wider tuning ranges, higher repetition rates, and/or more energetic pulses. An extension of the lower limit of the tuning range from the currently 5 μm to, say, 8 μm may already be sufficient for LPT studies of the more 'exotic' s-wave-detaching ions discussed at the beginning of this chapter.

*Term-averaged value.

namely Sc^-, Y^-, La^-, and the anions of the lanthanides. These ions have attracted considerable attention by theorists over the past few years, as some of these ions, particularly La^- and Ce^-, may constitute the only examples of atomic negative ions that possess stable states of opposite parity (compare the discussion of Cs^- in Sec. 5.2.1 and Paper 2). The ionic states of these systems have odd parity if the extra electron is bound in a p orbital, whereas the parity is even whenever the extra electron occupies a d orbital [†]. Hence, detachment from odd parity states will exhibit an s wave threshold behavior, while p-wave thresholds will be observed if the initial ionic states has even parity. Infrared LPI studies could thus provide convincing evidence for the parity and the electronic configuration of the ionic levels in addition to accurate binding energies.

[†]Note that the s shell of these systems is full and that an occupation of an f orbital is predicted to be energetically unfavourable.

Chapter 5

Threshold Photodetachment into p-wave Continua

Whenever the photodetached electron carries one unit of angular momentum relative to the atomic core a p-wave cross section is observed. The free p-wave electron experiences a centrifugal barrier close to the atom. The fact that this barrier has to be penetrated in the detachment process is responsible for the shape of the p-wave cross section close to threshold, as outlined in Sec. 2.4. The Wigner threshold law (Eq. 2.22) predicts a vanishing cross section for photon energies, ε, below the threshold energy, ε_0, whereas a cross section proportional to $(\varepsilon - \varepsilon_0)^{1/2}$ is predicted for $\varepsilon > \varepsilon_0$. Due to the odd parity of the electric dipole moment operator, detachment into a p-wave continuum via a one-electron process can occur only if the bound electron to be detached has even parity, i.e. if it is an s- or d-electron.

H^- is certainly the most prominent ion possessing valence s-electrons. In fact, the $H^-(1s^2\ ^1S_0) \rightarrow H(1s\ ^2S_{1/2})$ detachment transition provides the most accurately measured p-wave threshold to date, 0.754195(20) eV [10]. The alkali metals, the other elements of group IA, also form stable negative ions in the ns^2 configuration with similar binding energies, $\sim$0.5 eV. These binding energies have been accurately

measured in previous LPT studies, but in contrast to H^-, detachment into the *s*-wave continuum associated with the first excited state of the atom, $np\ ^2P_{1/2}$, was employed here, rather than *p*-wave detachment into the atomic ground state, $ns\ ^2S_{1/2}$ [1].

The vast majority of *p*-wave detaching atomic negative ions is provided by the transition metal elements. However, of the 25 transition metals that are expected or known to form stable negative ions, only the strongly bound Ir^- [69], Pt^- [70, 71], and Au^- [1] ions have been previously investigated via LPT.

In photodetachment studies both the energy levels of the ion and the low lying levels of the atom are relevant. In the case of transition metals, the atomic energy level structure can be rather complex due to the near degeneracy of $(n-1)d^k$, $(n-1)d^{k-1}ns$, and $(n-1)d^{k-2}ns^2$ configurations that is often found in these systems. Hence, in several cases, stable anions may be formed by binding the extra electron in either an *s*- or a *d*-orbital.† Furthermore, the large number of valence electrons in both atom and ion may give rise to several terms for each electron configuration, sometimes with large multiplicities, i.e. many fine structure levels. In general, the photodetachment cross section of a transition metal anion will therefore exhibit a series of cascaded thresholds rather than just a single threshold. Cascaded thresholds were already discussed in the previous chapter for the case of main group anions with p^k configurations. However, an accurate determination of the higher-lying fine structure thresholds was possible in those cases primarily due to the sudden and conspicuous onset of *s*-wave thresholds. In the present case of *p*-wave thresholds the onset of detachment is smooth and slow, and a determination of the actual threshold depends sensitively on a *p*-wave fit to the data above threshold (see below). Series of cascaded *p*-wave thresholds are thus expected to be challenging and, to our knowledge,

†Notable exceptions are Sc^- and Y^- where the extra electron is bound in a *p* orbital (see Chapter 4).

have not been studied previously.

5.1 Threshold fit

For the *p*-wave fit to any particular photodetachment threshold located at an energy ε_0 other open detachment channels have to be taken into account. As long as the thresholds of these other channels are not too close to ε_0 their contributions to the total cross section in the vicinity of ε_0 are generally smooth and can be represented by a linear term. Therefore, the function that is fitted to the measured cross section is given by:

$$\sigma = \begin{cases} a_0 + a_1(\varepsilon - \varepsilon_0) + a_2(\varepsilon - \varepsilon_0)^{3/2}, & \text{for } \varepsilon > \varepsilon_0 \\ a_0 + a_1(\varepsilon - \varepsilon_0), & \text{for } \varepsilon \leq \varepsilon_0 \end{cases} . \qquad (5.1)$$

Two different methods of fitting this equation to the data are utilized. The first method employs a multi-parameter gradient expansion algorithm to perform a non-linear least-squares fit. The fitting parameters a_0, a_1, a_2, and ε_0 are optimized simultaneously. In the second method a linear least-squares fit to the data below threshold is carried out first, in order to determine the photodetachment background. The fitted background is then subtracted from the data which are subsequently linearized by exponentiating with 2/3. A linear least-squares fit finally provides the threshold value ε_0.

In previous studies of *p*-wave thresholds either one or the other fitting method was used. For example, of the two previous LPT studies of the EA of platinum the more recent work [71] employed the first method while the earlier study [70] utilized the second method. The results of these studies differ by more than the respective error margins would suggest.

In comparison, the first fitting method constitutes a more rigorous approach and also provides well defined standard deviations for the fitted parameters. We

found, however, that this method would also overcompensate for small systematic deviations from a p-wave curvature above threshold through a small shift of the background line. This effect is due to the very slow increase of the p-wave cross section at threshold and results in a small systematic shift of the fitted threshold value. The second method, on the other hand, tends to undercompensate for systematic deviations in the above threshold data. Hence, the average of the two fitted threshold values is adopted as the final result. Its uncertainty is evaluated from the difference between the two fitted values and from the standard deviation obtained with the first method.

Although Eq. (5.1) is an exact description of the photodetachment cross section close to threshold, systematic deviations may occur at the high-energy end of a threshold scan. In this case, correction terms to the Wigner law would have to be taken into account, as discussed in Chapter 2. However, previous studies of p-wave thresholds [70, 72] have shown that the range of validity of the Wigner law is clearly larger for p-wave than for s-wave detachment. Hence, an inclusion of higher-order terms to the fitting function (Eq. 5.1) is not deemed neccessary here. Of more concern are possible systematic deviations from the Wigner threshold behavior due to a saturation of the detachment process, i.e. a depletion of the ionic levels by the intense laser pulse. The linearity of detachment signal versus pulse energy is therefore checked on a case to case basis. In some cases it is possible to optimise the signal-to-background ratio by adjusting the (average) pulse intensity such that the background channels are saturated while the threshold channel is still linear.

5.2 Hydrogen-group anions

H^- is one of the most extensively studied negative ions. Most experimental studies have focused on the rich spectrum of autoionizing, doubly-excited states embedded in the continuum [73]. H^- constitutes a quantum-mechanical three-body system and, as such, has attracted much attention by theorists. Although the Schrödinger equation for a three body system cannot be solved analytically, numerical solutions are possible to very high precision, as approximations are not necessary. In comparison with the helium atom, electron correlations are particularly important in the case of H^-, since the two electrons have to share the attraction of a single proton. Two accurate *ab initio* calculations of the electron affinity of hydrogen have yielded values of 6083.01 and 6083.09 cm^{-1} respectively [74], with a reported accuracy of $\pm$ 0.01 cm^{-1}, whereas the most accurate experimental value is 6082.99(15) cm^{-1}, determined in an infrared LPT measurement [10]. The uncertainty of the experimental value is too large for a conclusive distinction between the two calculated values; hence a more accurate experimental value would be highly desirable. Unfortunately, the accuracy of a measurement of the $H^-(1s^2\,{}^1S_0) \rightarrow H(1s\,{}^2S_{1/2}, F=0)$ threshold is limited by the presence of the upper hyperfine level ($F=1$) in hydrogen and the notoriously slow rise of p-wave thresholds. Hence, the McMaster setup would not allow a more accurate determination of the EA of H, even if the laser bandwidth would be further reduced.

The alkali negative ions are peculiar in the respect that their second detachment threshold is associated with the atomic np state and hence an s-wave continuum. As mentioned above, this fact has enabled very accurate EA measurements for all alkali atoms. Infrared LPT studies of the p-wave-detaching first thresholds for the sole purpose of EA determinations are therefore obsolete.

Alkali negative ions also exhibit interesting H^--like properties. This is due

to the fact that these systems are well approximated with two correlated electrons that are bound by a positively-charged polarizable core. Within this approximation, a theoretical treatment of alkali negative ions is comparatively simple, and precise calculations are possible even for the heavier systems, Rb^- and Cs^-, where relativistic effects play an important role. As in the case of hydrogen, the ionic and atomic ground states are the $ns^2\,{}^1S_0^e$ and $ns\,{}^2S^e_{1/2}$ levels respectively. In addition, ionic $nsnp\,{}^1P_J$ states are quantum-mechanically possible for alkali anions.

5.2.1 Cs^-

The McMaster efforts with alkali negative ions were focused on the anion of cesium. Cs^- has been much discussed in numerous theoretical studies as potentially the only known candidate for a stable atomic negative ion that possesses an *excited bound configuration of opposite parity to the ground state*. Initially, several calculations on $Cs^-(6s6p\,{}^3P_J)$ indicated that the ${}^3P_J$ state might be slightly bound, by a maximum of a few tens of meV [75, 76, 77, 78], although Fabrikant [76], and Krause and Berry [77] expressed that this might not hold true if their calculations were refined. More recently, a relativistic scattering calculation based on the Dirac R-matrix method by Thumm and Norcross predicted the $J = 0, 1, 2$ levels to be narrow shape resonances just above the Cs(6s) threshold [79]. This result contradicted earlier scattering calculations [80] which employed a semi-relativistic Breit-Pauli R-matrix formalism, and which did not show any low energy resonance structure. This discrepancy was partially resolved in a subsequent theoretical study by Bartschat [81], in favour of the conclusions by Thumm and Norcross. This study compared the two different methods directly, but the earlier Breit-Pauli formalism was modified, in particular through the inclusion of a dielectronic core polarization term.

Initially, we performed a series of careful experiments with tunable infrared

laser light in a 1+1 (two-photon) detachment scheme, in search of a possibly bound $6s6p\ ^3P_1^o$ level.[†] If the level were bound, a strong resonant enhancement of the two-photon detachment yield due to the (spin-forbidden) $^1S_0^- \rightarrow {}^3P_1^o$ electric dipole transition would be expected. No indication of such a resonance feature was observed.

Subsequently we conducted one-photon infrared laser detachment spectroscopy above the $Cs(6s)$ threshold. We obtained good signals for the Wigner p wave threshold and also explored the relative single photon detachment cross section to an energy of 75 meV above the photodetachment threshold. The results are shown in Fig. 5.1. A feature which represents an enhancement of $\approx 25\%$ over the direct, p wave photodetachment yield is seen centered at a photon energy of 179.663) meV, 8.063) meV above threshold, with a width of 5.015) meV (full-width-half-maximum) according to a Lorentzian fit. A blowup of the resonant feature, with the photodetachment "background" subtracted, is shown in the inset of Fig. 5.1. We attribute this relatively weak resonant feature to the $Cs^-(6s6p\ ^3P_1^o)$ level embedded in the continuum. Although we cannot probe the $J = 0, 2$ levels of the $^3P^o$ term in the laser-based experiments, the theoretical predictions on fine structure splittings [79, 81] would suggest that $J = 0$ is also unbound, based on our position for $J = 1$. Hence, we conclude that Cs^- possesses no stable states other than the $6s^2\ ^1S_0$ ground state. A detailed description of our experiments with Cs^- is given in Paper 2, including a discussion of supporting storage ring experiments performed at the University of Aarhus, Denmark.

5.3 Transition metal anions without fine structure

As outlined above, the large number of valence electrons found in transition metal atoms and ions generally results in complex energy level structures. Simple structures

[†] Due to the selection rules for radiative transitions (Table 2.1) the laser-based experiment is only sensitive to the $J = 1$ level of $6s6p\ ^3P_J$.

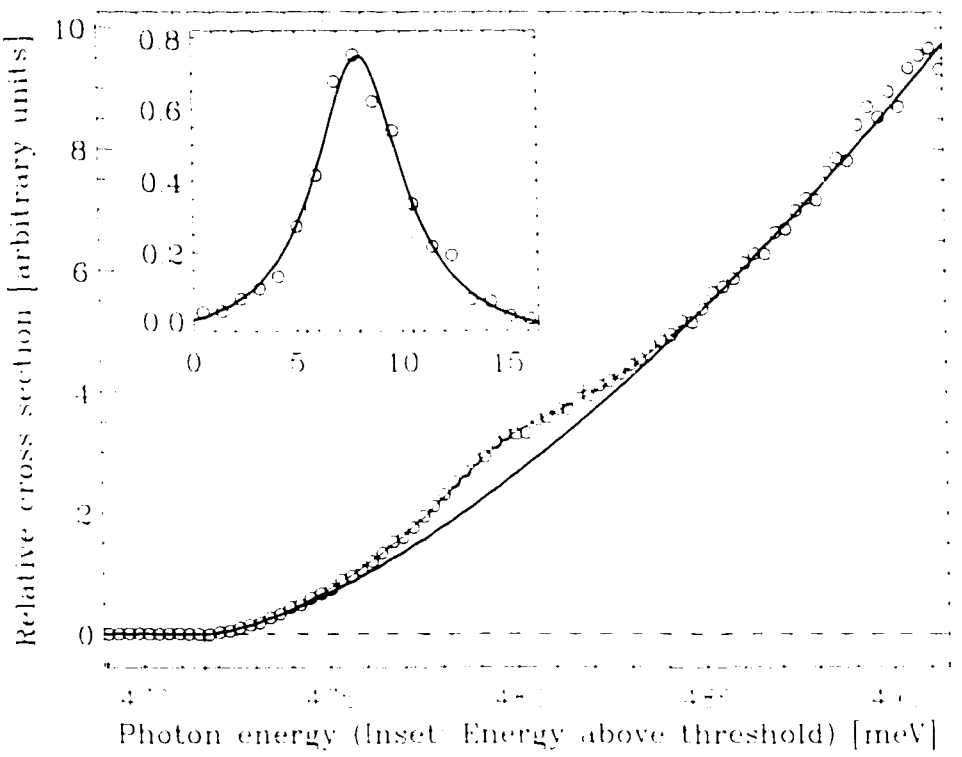

Figure 5.1: Cs^- photodetachment yield versus laser wavelength. The solid line represents a fitted Wigner p-wave threshold. Inset: Blowup of the one-photon detachment scan showing the resonant feature with the p-wave "background" subtracted. The result of a Lorentzian fit is indicated by the solid line.

would only be expected if the valence d-shell is half filled or full. The latter is the case for Cu, Ag, and Au. These elements form stable negative ions by attaching an s-electron to the $(n-1)d^{10}ns\ ^2S_{1/2}$ atomic ground state, resulting in a single ionic $^1S_0$ state. As for the alkali negative ions, photodetachment into the atomic ground state will therefore exhibit only one threshold. For Au^- this EA-defining threshold has been accurately measured in the past, as it can be probed with visible light. The $^1S_0 \rightarrow ^2S_{1/2}$ thresholds of Cu^- and Ag^-, on the other hand, require near-infrared light and have not been previously investigated. Both ions are very prolific from a cesium sputter source; currents of several hundred nA are routinely obtained. As a result, we achieved exellent signal-to-noise ratios in our Cu^- and Ag^- threshold scans.

enabling very accurate *p*-wave fits. The fitted threshold values are 1.23581(4) eV and 1.30447(2) eV respectively, which constitute significant improvements in accuracy over the previous experimental values of 1.235(5) eV [86] and 1.302(7) eV [87] respectively, obtained from LPES spectra. In fact, the accuracies realised here are comparable to the accuracy of the H^- LPT measurement by Lineberger's group [10] discussed above.

There are four transition metals with a half filled valence *d* shell in the atomic ground state, Cr, Mn, Mo, and Re. Mn and Re possess two valence *s* electrons in their ground states. Hence, the extra electron of the respective negative ion would have to occupy a *d*-orbital for possibly a *p*-orbital. The resulting ionic terms would then exhibit fine structure and are furthermore predicted to be either unstable or only very weakly bound (~300 meV) [1], which precludes infrared LPT with the current setup. Cr and Mn, on the other hand, form stable negative ions in the $(n-1)d^5ns^2$ configuration. This was established in LPES studies of these systems, which yielded EA's of 0.666(12) eV [82] and 0.748(2) eV [83] for Cr and Mn respectively. Again, the absence of fine structure should in principle enable a very accurate determination of the EA-defining $^6S_{5/2} \rightarrow ^7S_3$ threshold. Unfortunately, Cr^- and Mo^- are not very prolific from a Cs sputter source. Beam currents of only a few nA resulted in poorer signal-to-noise ratios of the threshold scans. In addition, the signal-to-background ratio was worse than in the experiments with Cu^- and Ag^-. In the absence of excited states of the atomic ion under investigation photodetachment background signals may still arise from small amounts of mass-coincident or nearly mass-coincident impurity molecules, such as hydrides. The fraction of such molecular impurities in the ion beam may have been higher in the case of Cr^- and Mo^-. The increased background can be compensated to some extent by increasing the scan range, but a larger uncertainty in the fit to the data is inevitable. Our final values for the EA's of Cr and Mo

are 0.67584(12) eV and 0.74726(2) eV respectively, which agree well with, and are substantial improvements over, the previous experimental values quoted above. A more detailed presentation of our experiments with Cr^-, Mo^-, Cu^-, and Ag^- may be found in Paper 11.

5.4 Transition metal anions with fine structure

Among the atomic negative ions that possess bound fine structure levels, Ir^- and Pt^- exhibit the largest fine structure splittings. Due to this fact these systems were chosen in our first attempts at multiphoton detachment via forbidden transitions, which are described in the next chapter. In the context of these experiments, the single photon detachment thresholds of the ionic ground states were also investigated. While the LPT work on Pt^- has been published in Paper 10 the Ir^- work is unpublished to date, as some initial difficulties with the LPT spectra could only be solved recently.

5.4.1 Ir^-: A sample case

An energy level diagram of Ir^- and the Ir ground state is shown in Fig. 5.2. In addition to the $5d^76s^2\ ^3F_4$ ionic ground state, for which a previous LPT study reports a binding energy of 1.5638(5) eV [69], the J=3 level of the ^3F term and a J=2 level which is of ^1D character are also predicted to be bound on the basis of multiconfiguration Dirac-Fock calculations (Paper 8).[†] The same calculations indicate that the J=2 level of the ^3F term might be slightly unbound. As the two excited levels are predicted to lie 5920 and 6671 cm^{-1} above the ionic ground state, they cannot be expected to be sufficiently populated by the sputter source for a direct observation of the respective p-wave thresholds. These levels may, however, give rise to a noticable photodetachment background in an LPT measurement of the ionic ground state.

[†]Note that the L and S quantum numbers have only a limited meaning in such heavy systems.

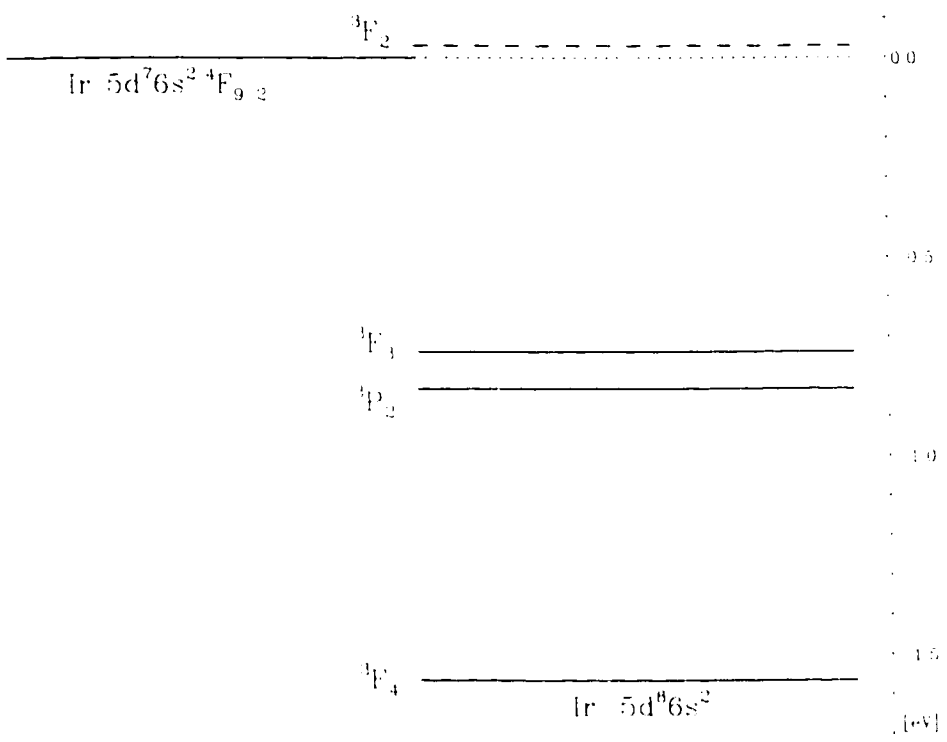

Figure 5.2: Energy level diagram of Ir^- and the Ir ground state. The calculated energy values are used for the excited ionic levels.

In our initial experiments with Ir^- a 3 mm diameter iridium metal pellet was used as the sputter target, mounted in a copper cathode. Beam currents of $\approx$100 nA were obtained at the average mass of Ir. However, the photodetachment scan of the $^3F_4 \rightarrow {}^4F_{9/2}$ threshold region did not reveal a *p*-wave threshold feature, but a very strong and almost constant detachment signal throughout the entire scan range, shown in Fig. 5.3 (upper curve). As this strong signal cannot result from Ir^- detachment (ground or excited states) it is likely due to an unusually stong molecular impurity. Since the Ir target is mounted in a Cu cathode some amount of Cu trimer anions might be present in the ion beam, and would be mass-coincident with Ir. We therefore attribute the observed signal to detachment of Cu_3^-.

A subsequent reinvestigation of the $^3F_4 \rightarrow {}^4F_{9/2}$ threshold region employed a

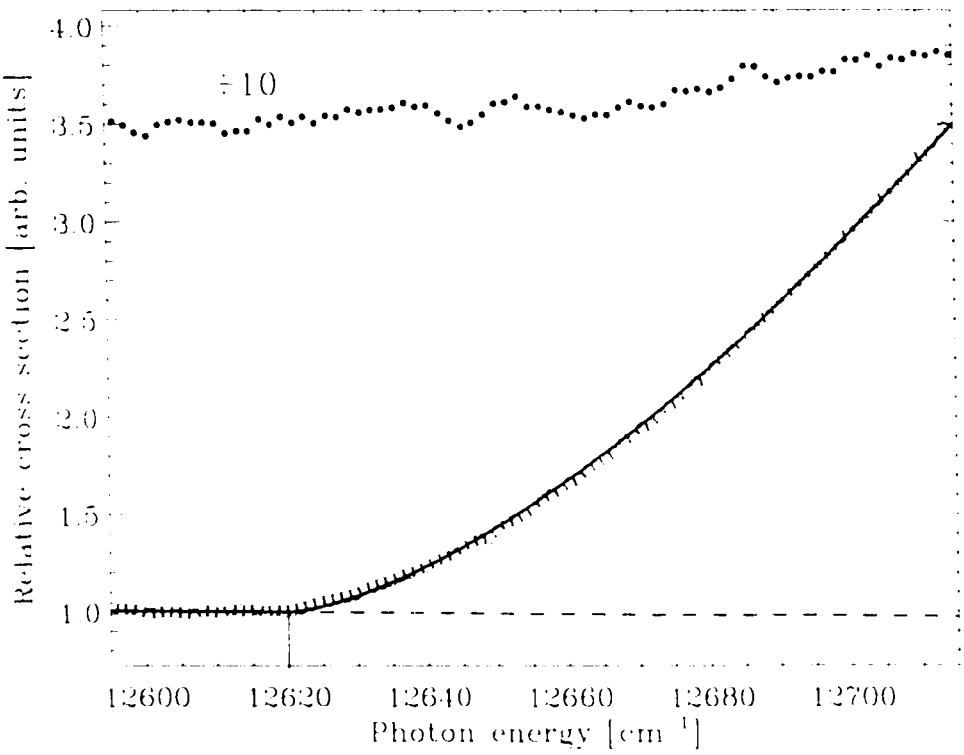

Figure 5.3: Ir^- photodetachment yield versus laser wavelength. Upper curve: signal obtained with a Ir/Cu cathode. Lower curve: signal obtained with a Ir/Al cathode. The solid line represents a fitted Wigner p-wave threshold. Over the large energy range shown here there appears to be a small systematic deviation between the data and the fitted curve. Hence, for the EA determination only the data close to threshold were used.

iridium pellet mounted in an aluminum cathode. The current obtained at the mass of Ir was again ≈100 nA, but this time, a clear p-wave threshold feature was observed in the detachment scan (lower curve in Fig. 5.3). A p-wave fit to the data yields a threshold value of 12618.0(15) cm^{-1} [1.56443(20) eV], in agreement with the previous experimental value. Only a small photodetachment background remains in the scan and might be due to detachment from the the excited levels of Ir^-. Despite the large beam current, the p-wave detachment signal is relatively weak. This is not unexpected, since a bound d-electron is removed from the ion in the detachment process. As discussed in detail in Paper 6, the cross section for d-electron detach-

ment is approximately an order of magnitude smaller than for s-electron detachment. Unfortunately, in the case of Ir^- the first s-electron detachment threshold is located $\approx$3000 cm^{-1} above the ground state threshold investigated here. Hence, the respective threshold would be superimposed on a very large detachment background. A small $^3F_4 \rightarrow {}^4F_{9/2}$ detachment cross section also explains why the threshold signal could be completely obscured by the signal from Cu_2 detachment.

5.4.2 Co^- and Rh

Cobalt and rhodium appear in the same column of the periodic table as iridium. They form stable negative ions also in the $(n-1)d^9ns^2$ configuration. For both Co^- and Rh^- all three fine structure levels of the ^3F term have been previously observed in LPES spectra and are reported to be the only ionic levels bound with respect to the atomic ground state. Fine structure splittings are smaller than in the case of Ir^-, such that a sufficient population of the upper levels may be expected from the Cs sputter source.

Our infrared LPT studies of Co^- and Rh^- are described in detail in Paper 6 and the results are summarized in Table 5.1. Accurate ground state binding energies were obtained for both ions. Fine structure measurements, on the other hand, were complicated by unfavourable cross sections for the relevant thresholds in the case of Co^-, and by surprisingly low ion beam currents in the case of Rh^-. These measurements remain incomplete.

5.4.3 Ni^-, Pd^-, and Pt^-

Nickel, palladium, and platinum form one column of the periodic table, yet their atomic and ionic energy level structures display some interesting irregularities. Ni^- and Pt^- possess two stable states, namely the fine structure levels of the $(n-1)d^9s^2\ ^2D$

term. In contrast, the ionic ground state of Pd^- is given by the $4d^{10}5s\ ^2S_{1/2}$ level and the first excited state is the $J=5/2$ level of the $4d^95s^2\ ^2D$ term; the $J=3/2$ level is likely unbound.

Our infrared photodetachment experiments with these three ions have resulted in accurate binding energies for all of the aforementioned bound levels. The values and their uncertainties are listed in Table 5.1. As an example of cascaded p wave thresholds, a portion of the photodetachment cross section of Ni^- is shown in Fig. 5.4. The LPT work on Ni^- and Pd^- is presented in detail in Paper 6. The $Pt^-(^2D_{3/2})$ detachment threshold is discussed in Paper 10 whereas the observation of the $Pt^-(^2D_{5/2})$ level via resonant multiphoton detachment is described in Paper 8.

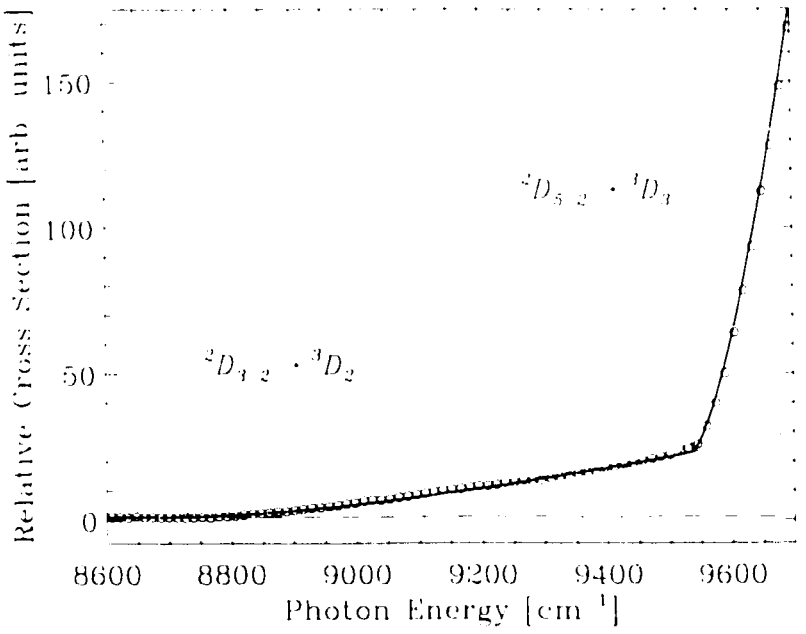

Figure 5.4: Photodetachment cross section of Ni^- over the region of the $^2D_{3/2} \rightarrow {}^3D_2$ and $^2D_{5/2} \rightarrow {}^3D_3$ thresholds.

5.5 Summary and Outlook

Table 5.1 summarizes negative ion binding energies that were derived from p-wave fits to our LPT data, and also gives previous experimental values for comparison. As can be seen, improvements in accuracy of up to two orders of magnitude were realised for both ground state and excited state binding energies. Infrared LPT spectroscopy has thus proven to be a valuable tool for the study of negative ions that exhibit p-wave thresholds. However, the experiments have also indicated some of the limitations of the technique. The limitations mostly result from the fact that the present experimental setup utilised neutral particle detection to monitor the photodetachment process. Neutral atoms produced via different photodetachment channels cannot be separated, i.e. only the total cross section for photodetachment is measured. Consecutive channels thus appear as a 'cascade' of thresholds in the neutral particle signal of an LPT study, as opposed to the series of individual peaks observed in the electron spectrum of a LPES measurement. This is not necessarily a limitation in the case of s-wave detachment (Chapter 4), but for p-wave channels, the detachment signal at threshold is notoriously small. The experiments presented in this chapter have shown that only the two or three strongest thresholds within a sequence of cascaded p-wave thresholds can be measured with an accuracy that is clearly superior to accuracies achieved with LPES. In cases such as Co^-, where a large number of thresholds is present, most thresholds cannot be resolved, as their strength relative to the photodetachment background is too small. In such cases an unambiguous interpretation of the LPT spectrum has to rely on previous LPES results in addition to calculated threshold strengths. Fortunately, the EA's of most of the remaining transition metal negative ions that could be studied in LPT experiments have been previously measured via LPES, so the average term energies are known.

Table 5.1: Summary of ionic binding energies derived from p-wave thresholds.

		Binding energy [eV]		
Ion	Level	This work	Previous works	[Ref.]
Cs^-	$^1S_0$	0.471641(6)	0.471630(25)	[1]
Cr^-	$^6S_{5/2}$	0.675841(12)	0.666(12)	[82]
Mo^-	$^6S_{5/2}$	0.7472(2)	0.748(2)	[83]
Co^-	$^3F_4$	0.663306	0.662(3)	[84]
	$^3F_3$	0.55480(20)	0.549(10)	[85]
Rh^-	$^3F_4$	1.114289(20)	1.138(8)	[82]
Ir^-	$^3F_4$	1.561430(20)	1.563805	[69]
Ni^-	$^2D_{5/2}$	1.157160(12)	1.157(10)	[85]
	$^2D_{3/2}$	0.97300(4)	0.975(12)	[85]
Pd^-	$^2S_{1/2}$	0.562140(12)	0.558(8)	[82]
	$^2D_{5/2}$	0.42240(5)	0.422(8)	[82]
Pt^-	$^2D_{5/2}$	2.12520(8)	2.12320(11)	[71]
			2.128(2)	[70]
Cu^-	$^1S_0$	1.235810(4)	1.235(5)	[86]
Ag^-	$^1S_0$	1.301470(2)	1.302(7)	[87]

The limitations described above could be removed by implementing techniques for a channel-selective detection of the photodetachment products. An approach which seems particularly promising was used in the LPT study of alkali negative ions with visible light [6]. There, the photodetached electrons were monitored through an electron spectometer as the laser was tuned. Electrons resulting from different detachment channels then appear as separated peaks in the spectrum, and the dependency of a particular peak on the photon energy is directly proportional to the partial cross section of the respective detachment channel. Hence, a combination of this detection scheme with the infrared LPT techniques demonstrated here should in principle allow a resolution of dense threshold manifolds as found in Co^-. In practice, ion beam energies higher than those used here would probably be required in order to provide threshold electrons with sufficient energy for detection. If necessary, the signal-to-

noise ratio could always be improved by using an interaction region with collinear rather than crossed laser and ion beams. Resonant ionisation spectroscopy (RIS) constitutes an alternative approach for state-selective detection. In recent years, this technique has been very successfully applied to the study of alkaline earth negative ions [7]. The excellent signal-to-noise ratio achievable with RIS enables the detection of even the weakest detachment channels. On the other hand, the atomic energy level structure of the element under investigation must provide for a practical resonant ionisation scheme, which might not be the case for some transition metals.

A very different approach to the study of the fine structure of transition metal negative ions could involve two-photon rather than single photon threshold spectroscopy. The observation of two-photon detachment thresholds has been reported for three main group negative ions, namely H^- [68], Cl^- [67], and Si^- (Sec. 6.3.2, Paper 5). This detachment scheme is particularly interesting for transition metal negative ions, as their two-photon thresholds follow the Wigner s-wave law with its characteristic sharp onset. Cascades of even closely spaced s-wave thresholds as in the case of B^- (Sec. 4.3.1) have proven to be an accurate measure of ionic fine structure. The threshold shifts that are inevitable with the high laser intensities necessary for the two-photon process would be the same for all fine structure thresholds and thus the splitting would remain unchanged.

Both LPT and LPES studies depend on an initial population of the ionic levels to be investigated. Hence, for a 'thermal' ion source, bound states that lie more than ~0.5 eV above the ionic ground state typically remain undetected. A study of such high-lying bound ionic states would have to employ a 'non-thermal' ion source (e.g. a charge exchange chamber) or resonant multiphoton schemes in the detachment process. Various possibilities for resonant multiphoton detachment from

atomic negative ions have been successfully demonstrated thus far. These experiments are discussed in the following chapter.

Chapter 6

Resonant Multiphoton Detachment

Laser photodetachment threshold studies, as discussed in the two previous chapters, have to rely on an initial population of the ionic states to be investigated. This is generally not a constraint in measurements of the ionic ground state and its fine structure, as the corresponding level splittings are typically small. However, higher lying excited terms or possibly electronically excited configurations would be only very weakly populated from a 'thermal' ion source. In such cases, resonant multiphoton detachment may provide an alternative approach.

The interest in multiphoton phenomena involving negative ions began with the early demonstration of non-resonant two-photon detachment of I^- by Hall [88], and with the resonant two-photon detachment of C_2^- by Lineberger and Patterson [11]. Over the past few years, several other multiphoton phenomena have been observed in negative ions.

Most studies investigated non-linear optical processes such as excess-photon detachment [89], two-photon threshold detachment [67, 68], and ponderomotive threshold shifts [35]. Negative ions represent qualitatively different targets for such strong-laser-field studies. In comparison, multiphoton ionization spectra of atoms often

exhibit complex structures, as they are strongly influenced by the presence of an infinite series of Rydberg states converging to the ionization limit. These states act as 'intermediate' states in a multiphoton transition (compare Eq. 2.20), and even if the transition is not in resonance with the unperturbed levels of the atom, the strong fields needed to drive a multiphoton transition will often shift some Rydberg levels into resonance. Multiphoton detachment spectra of atomic negative ions, on the other hand, are conceptually simple due to the absence of such a Rydberg series of states. As discussed in more detail in Chapter 2, the lack of Rydberg states is a result of the short range potential that binds the extra electron of a negative ion. Hence, atomic negative ions are ideal targets whenever the non-resonant character of multiphoton phenomena is of interest.

While the various non-resonant multiphoton detachment phenomena mentioned above were investigated by several different groups over the past 10 years, resonant multiphoton detachment of atomic negative ions was only recenty demonstrated for the first time, in a collaborative effort between the Aarhus and McMaster groups (Ref. [90], Paper 9). This may seem surprising considering that the structural knowledge of atomic species is primarily derived from observations of bound-bound transitions. In particular, resonant multiphoton ionisation (REMPI) of atoms, to which resonant multiphoton detachment is the negative ion analogy, has been a very successful spectroscopic technique. The fundamental difference between anionic and atomic systems is that excited of negative schemes, bound excited negative ion states almost always refer to the terms and fine structure of the same (ground state) electronic configuration. Hence, single photon electric dipole (E1) transitions between such levels are strictly forbidden as a result of the parity selection rule. A simultaneous absorption of two photons, on the other hand, would be allowed in an electric

dipole interaction and would give rise to a resonant enhancement in a multiphoton detachment spectrum.† The "cross sections" for such second-order processes are very small but the transition probabilities scale with the square of the laser intensity (compare Eq. 2.20). Hence, a tightly focused laser pulse may very well compensate for a small two-photon cross section. detachment spectra in a

In addition to two-photon E1 transitions between states of the same parity, small probabilities often exist for single photon transitions of magnetic dipole (M1) or electric quadrupole (E2) character. Such "forbidden" transitions have very small probabilities (Einstein A coefficients of $\sim 1\ s^{-1}$) and, in absorption, depend only linearly on the laser intensity. Nevertheless, forbidden transitions are a well known phenomenon in atomic spectroscopy and are readily observed if large sample volumes can be made available, as for example in multipass absorption cells or interstellar gas clouds. In contrast, sample volumes available in negative ion studies are very limited due to the fragile nature of this species. Both ion traps and ion beam machines provide at most a few cm^3 of sample volume with low ion densities ($\sim 10^4\ cm^{-3}$). Due to these limitations, resonant multiphoton detachment via forbidden transitions was initially considered less likely than via two-photon transitions. The first observations of such forbidden transitions in negative ions were made only recently and so far only by the McMaster group, as described in detail below.

6.1 2+1 photon detachment in a Raman coupling scheme

As binding energies of atomic negative ions are often small (<1 eV) and the splittings between bound levels are even smaller, single photon transitions between such levels

†Selection rules for one- and two-photon transitions are listed in Table 2.1.

would typically require tunable infrared sources. Single color two-photon transitions would be even more demanding in terms of infrared tunability and pulse energy. Of course, two-photon transitions are also possible for photons of unequal frequency, i.e. if two light fields of different colors are present, and even if the second light field causes a stimulated emission rather than an absorption of a photon. The difference between a straight two-photon transition (two absorptions) and a two-photon Raman transition (absorption and stimulated emission) is simply given by a sign change in the quantum mechanical expression for a two-photon transition (Eq. 2.20). A two-photon Raman transition is therefore a very attractive scheme for fine structure studies via resonant multiphoton detachment (particularly if the fine structure cannot be resolved in LPT measurements).

Se^- and Te^- are good candidates for a first application of this detachment scheme. Both ions are stable only in the p^5 configuration which gives rise to a single ^2P term. The energy level diagram of Te^- is shown in Fig. 6.1 as an example. The J=3/2–1/2 fine structure splitting is reasonably well known from previous LPT studies which yielded values of 2279(2) and 5008(5) cm^{-1} for Se^- and Te^- respectively [1]. Hence, no ambiguity would remain if the corresponding resonances could be observed in the 2(Raman)+1 photon detachment spectra. Furthermore, due to the large ground state binding energies of these ions ($\approx$2 eV) the multiphoton experiments can be carried out without the need for tunable infrared light.

The Te^- experiment was first conducted by the Aarhus group [90] utilizing tunable light around 694 nm and the fundamental radiation of a Nd:YAG laser ($\approx$1064 nm). A clear resonance structure was observed in that study corresponding to a fine structure splitting of 5004.7(2) cm^{-1}. The resonance feature and its position were confirmed in a subsequent study by the McMaster group which yielded a splitting

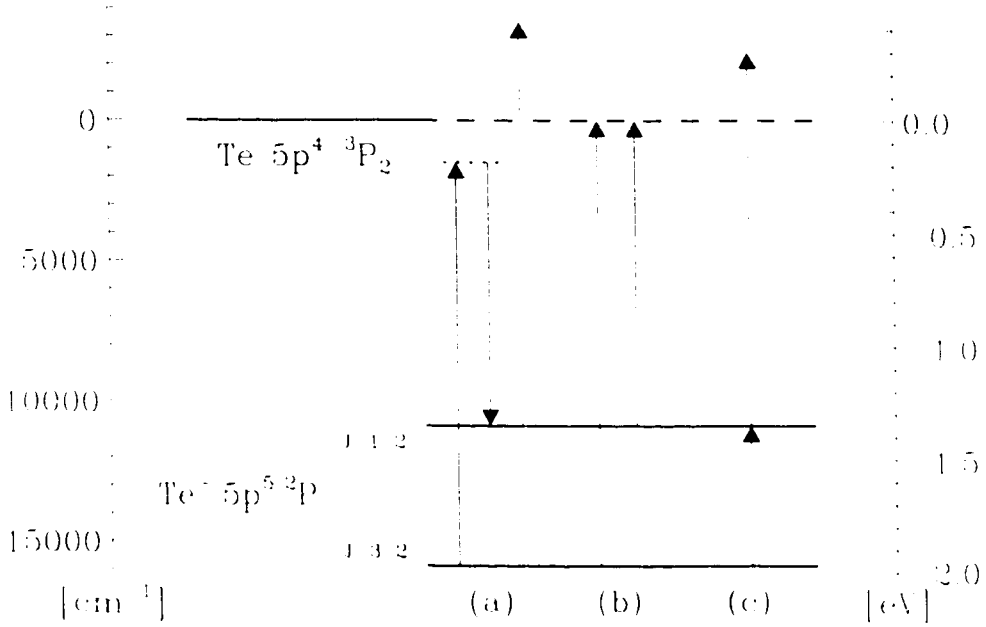

Figure 6.1: Schematic energy level diagram of Te^- and Te. Different photodetachment schemes aimed at a determination of the fine structure splitting are indicated by arrows: (a) three-photon detachment via two-photon Raman E1 resonance; (b) one-photon detachment thresholds; (c) two-photon detachment via one-photon M1 resonance.

of 5004.6(5) cm^{-1}. This experiment and the analogous study of Se^- conducted at Aarhus are described in detail in Paper 9 in the appendix.

While the 2(Raman)+1 scheme is very effective in circumventing the need for tunable infrared light, it still remains a challenging multiphoton experiment. Special care must be taken to assure good spatial and temporal overlap of the two different laser pulses, which also have to be focused tightly in order to drive the two-photon transition efficiently. Furthermore, an accurate fine structure measurement depends on a reliable and accurate calibration of both laser sources. The small differences that are found between the 2(Raman)+1 measurements and the 1+1 measurement (see below) of the Te^- fine structure splitting are in fact believed to be due to small systematic errors in the laser calibration of the 2(Raman)+1 experiments.

6.2 1+1 photon detachment via magnetic dipole transitions

The 2(Raman)+1 scheme discussed above is well suited in cases where ionic fine structure splittings are only a few thousand cm^{-1} or less, in particular if the ion is strongly bound. However, for the anions of the heavy elements (6th period) fine structure splittings may become rather large (e.g. $\approx 10000\ cm^{-1}$ for Pt^-) which makes an implementation of the 2(Raman)+1 scheme increasingly difficult. Furthermore, this scheme is not useful for resonant multiphoton detachment via weakly bound excited states. In such cases 1+1 photon detachment via forbidden transitions may provide an alternative scheme. This approach is particularly attractive if the excited state under investigation is bound by less than half of the ground state binding energy, as the 1+1 photon detachment process can then be realised with only a single color. Nevertheless, the 1+1 photon detachment process remains challenging even in these favourable cases, as virtually all bound-bound transitions in atomic negative ions are single-photon E1 forbidden, and therefore have only small transition probabilities of M1 and/or E2 character.

The feasibility of the 1+1 photon approach for a particular excited state is therefore evaluated in a computer simulation of the laser-ion beam interaction prior to the actual experiment. The simulation assumes a Lorentzian laser bandwidth, and Gaussian profiles for the the temporal and spatial shapes of the laser beam as well as for the spatial shape of the ion beam. The number of detachment events per laser pulse is calculated as a function of the various ion and laser source parameters and as a function of estimated bound-bound and bound-free transition probabilities. Competing detachment channels such as single photon detachment of the initial excited level population and non-resonant two-photon detachment of the ionic ground state

are also included. It was found in the simulation as well as in the experiment that the success in driving a "forbidden" 1+1 photon detachment process often depends on effective suppression of these competing channels. While a collimated laser beam gives rise to a large one-photon (excited state) and only a very small two-photon (ground state) detachment background, the situation is reversed for a tightly focused beam. Depending on the cross sections of the various processes, the best resonant-signal to background signal ratio may be obtained with one or the other beam geometry, or an intermediate geometry such as a cylindrical focus.

6.2.1 Ir^- and Pt^-

Our first investigation of multiphoton detachment via forbidden transitions was carried out on the negative ions of iridium and platinum. The ground states of these ions, $5d^96s^2\ ^3F_4$ and $5d^76s^2\ ^4D_{7/2}$ respectively, are strongly bound (12618.0(15) and 17141(6) cm^{-1}, Table 5.1). Yet, isoelectronically extrapolated values of 7600(1500) cm^{-1} for the $^3F_4 - {}^3F_3$ fine structure splitting in Pt^- and 10000(1000) cm^{-1} for the $^4D_{7/2}-{}^4D_{5/2}$ splitting in Ir^- indicated that 1+1 photon detachment might be achieved with a single, near infrared color. We therefore scanned the single-color two-photon detachment spectrum of both ions over wide photon energy ranges. For both, Ir^- and Pt^- a single, sharp resonance feature was eventually found at a photon energy of 7087.3(1) and 9740.9(5) cm^{-1} respectively. The interpretation of these resonances as being due to magnetic dipole fine structure transitions was supported by multiconfiguration Dirac-Fock calculations (performed by W. P. Wijesundera) which provided transition energies of 6671 and 9535 cm^{-1} and probabilities (Einstein A coefficients) of 7 and 14 s^{-1} respectively. Using these transition probabilities the above-mentioned photon-ion interaction simulation predicted resonant signals of the order of several counts per laser pulse, in agreement with observed signal levels. Unfortunately, some

uncertainty in the interpretation remained due to the fact that signals could neither be obtained for the corresponding 2(Raman)+1 processes, nor for single photon detachment from the excited levels. The failure of the 2(Raman)+1 experiments might well be explained by small cross sections for such processes in these species. The strength of a two-photon transition depends sensitively on intermediate states which, in the case of atomic negative ions, are primarily continuum states. Hence, it may be relevant that Ir^- and Pt^- detach into p wave continua whereas Se^- and Te^-, for which 2(Raman)+1 resonances were observed, detach into s wave continua. The lack of single photon detachment from the excited levels, on the other hand, is readily explained by the fact that the highly excited levels are essentially unpopulated in species derived from the sputter ion source. A detailed description and analysis of our experiments with Ir^- and Pt^- is given in Paper X.

6.2.2 Te^-

Due to the small uncertainty regarding the interpretation of the resonances observed in Ir^- and Pt^- an attempt was made at driving the magnetic dipole $^2P_{3/2} - {}^2P_{1/2}$ fine structure transition in Te^-. In contrast to the two previous cases, the Te^- fine structure is very well known from the 2(Raman)+1 experiment described above as well as from earlier LPT studies [1].

Laser wavelength scans of the region expected to yield the 1+1 (M1) photodetachment resonance were carried out by eliminating from the Raman cell output all components except the residual dye laser and second Stokes beams and then focussing the light on the ion beam utilizing a 60 cm focal-length lens. While the second Stokes light provides for the fine structure transition the residual laser light is needed for the subsequent detachment process, as depicted in Fig. 6.1. An example of the resonant signal is shown in Fig. 6.2. The sharp resonant feature is seen to be 0.16(2) cm^{-1} wide

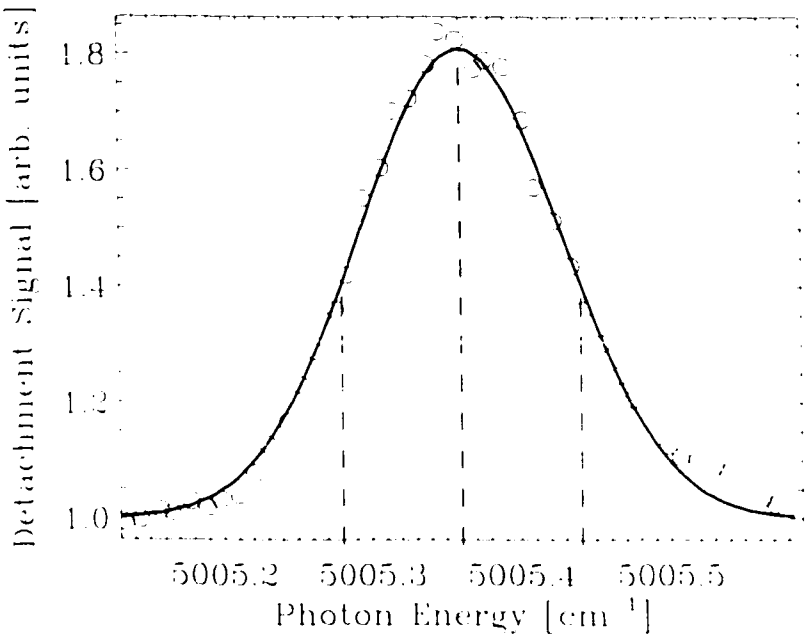

Figure 6.2: Two colour two-photon detachment signal of Te^- versus infrared laser photon energy in the vicinity of the magnetic-dipole fine-structure resonance. The solid line represents a Gaussian fit.

and the signal-to-background ratio is about 1:1. The resonance is clearly resolved and exhibits high signal-to-noise. The background level is primarily due to one-photon detachment of the excited $Te^-(5p^5\ ^2P_{1/2})$ ions since the thermal population from the sputter ion source leads to an initial population of this level of $\sim 1\%$. The resonance position is found to be 5005.36(10) cm^{-1}.

The new value for the fine structure splitting can be compared with the values obtained from the 2(Raman)+1 experiments, 5004.7(2) cm^{-1} [90] and 5004.6(5) cm^{-1} (Paper 9). Although the values are close and misinterpretation of the resonance in Fig. 6.2 can be ruled out, it was of some concern that the present value differs from that of Ref. [90] by about three standard deviations, given the fact that we assume that an accuracy of ≈ 0.2 cm^{-1} can be routinely obtained in our respective pulsed laser measurements. Hence, numerous checks were conducted on the laser calibration

and other experimental parameters in the present work. In order to obtain an independent measure of the fine structure splitting, we conducted a careful measurement of the single photon detachment threshold from the upper Fe^- level as described in Chapter 1. This experiment yielded a value of 5005.38(16) cm^{-1} for the fine structure splitting, in excellent agreement with the result from the 1+1 experiment. A more detailed discussion of the present and previous Fe^- experiments may be found in Paper 7.

The clear demonstration of a two-photon detachment via a 1+1 magnetic dipole resonance in a case where the interpretation is perfectly clear, verifies the perspectives which were outlined at the beginning of this chapter. The M1 transition in Fe^- is expected to be of only moderate strength, having an Einstein A coefficient of $\approx 2\ s^{-1}$, estimated on the basis of isoelectronic extrapolation. The fact that many other atomic negative ions are expected to possess fine structure transitions of similar strength suggests that the 1+1 photon detachment scheme may indeed be generally applicable.

6.2.3 Sb^-

Sb^- is a rather interesting negative ion, as it is expected to have four bound states, namely the fine structure levels of the ^3P and ^1D terms of the $5p^4$ configuration. Nevertheless, the previous knowledge of these states is very limited (as outlined in Sec. 1.5.2). Our LPT studies of this system, which are discussed in Sec. 1.5.2, provided accurate binding energies for all three ^3P_J levels, but did not conclusively confirm a J=2-1-0 order of the levels. The thresholds from the two upper levels had similar strengths and were separated by only 116.3 cm^{-1}. Considering the large uncertainties of isoelectronic extrapolations, this left a small probability for a 2-0-1 order which is found throughout the isoelectronic sequence (Te, I^+, etc.). Hence, a 1+1 two-color

photodetachment experiment was conducted which employed second Stokes radiation around 3.6 μm for the resonant transition and first Stokes radiation for the subsequent detachment. Only one resonance was found at 2684.37(15) cm^{-1} and must be assigned to a transition between $^3P_2$ and $^3P_1$ based on estimated transition probabilities, confirming a 2-1-0 level order.

With the aim to locate the previously unobserved but possibly bound $^1D_2$ term, the single color two-photon detachment spectrum of Sb$^-$ ($^3P_2$) was recorded. The 2(Raman)+1 photon detachment scheme would not be suitable here as the $^1D_2$ level is only weakly bound. The 1+1 magnetic dipole resonance which has an isoelectronically extrapolated transition probability of 1.1 s^{-1} was found at a photon energy of 7392.55(15) cm^{-1} giving a $^1D_2$ binding energy of 1055.3(2) cm^{-1}.

The M1 resonances observed in Sb$^-$ exhibit a line broadening that could not be explained until the effects of ionic hyperfine structure were considered. While the hyperfine structure of numerous neutral and positively charged systems has been studied in the optical regime, studies of this kind do not exist for negative ions. The measured 1+1 M1 resonance peak profiles were therefore modelled on the basis of calculated hyperfine structure A and B constants. These relativistic configuration interaction calculations (performed by D. R. Beck) and the hyperfine structure model are described in detail in Paper I.

6.2.4 Si$^-$, Ge$^-$, and Sn$^-$

Our infrared LPT studies of the excited ^2D_J states in the anions of silicon, germanium and tin (Sec. 4.1.2) provided accurate binding energies in all three cases. Nevertheless, an attempt was made to confirm and possibly improve these values (listed in Table 4.1) via 1+1 photon detachment. Unfortunately, M1 as well as E2 probabilities for the $^4S_{3/2} \rightarrow {}^2D_J$ transitions are very small, as the (approximate) selection rules $\Delta L = 0$

and $\Delta S = 0$ are violated. Transition probabilities of $\sim 1\ s^{-1}$ are only expected in the case of Sn^-, a system that is not well described by the LS-coupling approximation. Consequently, no resonance features were found in the two-photon detachment spectra of Si^- and Ge^-, whereas both $^1S_{1/2} \rightarrow {}^2D_J$ resonances could be accurately located in the case of Sn^- at photon energies of 5762.50(10) and 6512.37(10) cm^{-1}, respectively.

Of the five carbon-group anions only Si^- is expected to possess a bound ^2P term. As the very small binding energy of this term precludes a determination of the detachment threshold to the atomic ground state, we have attempted to probe the ^2P_J levels via resonant multiphoton detachment. Various possibilities for resonant multiphoton detachment exist in this case involving either the $^1S_{1/2}$ or the ^2D_J states as the initial level. However, no resonant features were apparent in any of the two-photon detachment scans. This (negative) result is discussed in detail in Paper 5 and is primarily attributed the substantial $Si^-(^2D)$ photodetachment and $Si^-(^1S)$ collisional detachment background levels.

Ge^-, and

6.3 Single-color 2+1 photon detachment

As outlined at the beginning of this chapter, an alternative to driving a transition between states of the same parity via an E1-forbidden one-photon absorption is the possibility of E1-allowed two-photon absorption. However, in the case of weakly bound excited states the 2(Raman)+1 approach discussed above is not suitable. Instead, the bound-bound transition must be realised here in a straight two-photon absorption, requiring very intense infrared pulses, of Sb^-.

6.3.1 Sb^-

In order to confirm position and parity of the weakly bound $^1D_2$ level found in Sb^- via 1+1 photon detachment, the $^3P_2 \rightarrow {}^1D_2$ transition was also driven via an electric dipole allowed two-photon absorption. As the $^1D_2$ binding energy is less than half the $^3P_2 - {}^1D_2$ splitting energy, the transition could be observed as a 2+1 resonance in the single color three photon detachment spectrum of $Sb^-(^3P_2)$. This resonance, which is the first example of a single color 2+1 photon detachment, is shown in Fig. 6.3. The signal-to-background ratio of the resonance was significantly improved by retaining a fraction of the first Stokes radiation in the infrared pulse. In doing so, the probability for absorption of the third and detaching photon was substantially increased and only a small single photon detachment background from the upper ^3P_J levels was introduced. A photon energy of 3696.35(15) cm^{-1} gives a splitting energy of 7392.70(30) cm^{-1} which agrees well with the value obtained from the 1+1 MI resonance.

6.3.2 Si^-

The $Si^-(^2P_J)$ levels, which could not be located in the 1+1 photon experiments are only very weakly bound. Hence, the $^4S_{3/2} \xrightarrow{2h\nu} {}^2P_J$ two-photon resonances are expected to lie just below the threshold for two-photon detachment, $^4S_{3/2} \xrightarrow{2h\nu} {}^3P_0$. This threshold was investigated first, in order to optimize the focussing geometry for higher-order processes. The result is shown in Fig. 6.4. The threshold for two-photon detachment at 11370(15) cm^{-1} and the expected p-wave threshold behavior are apparent. (A two-photon p-wave threshold has been previously observed in Cl^- detachment [67].) The observed threshold value compares well with 11357 cm^{-1}, the average threshold value for an unresolved $Si(^3P)$ fine structure (although a pon-

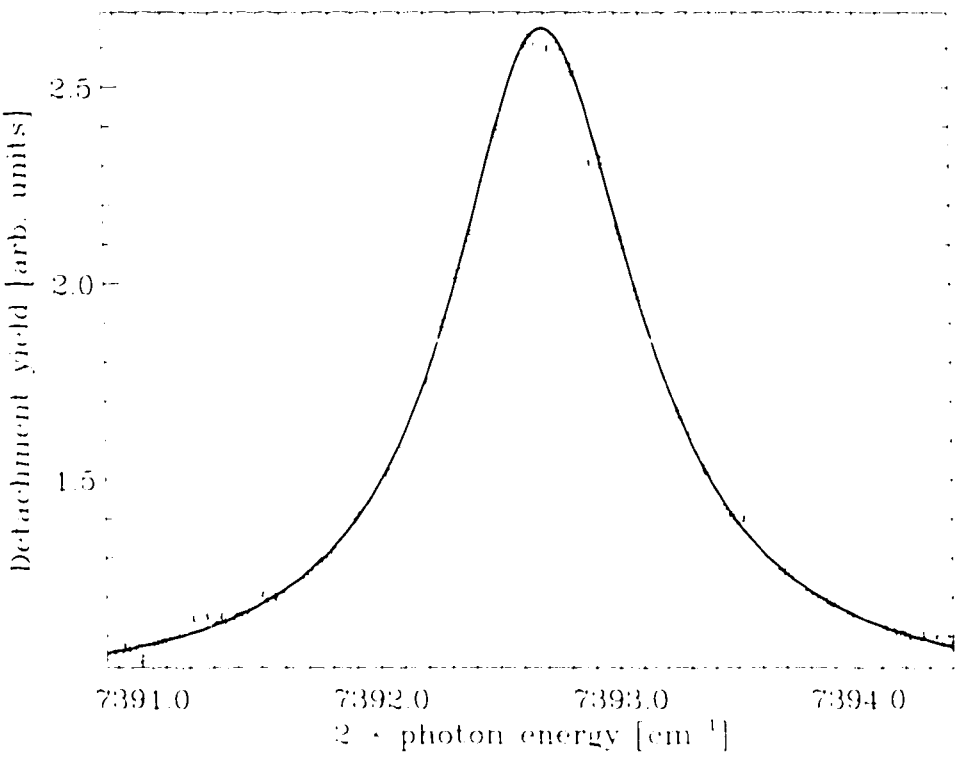

Figure 6.3: $Sb^- \, {}^3P_2 \xrightarrow{2h\nu} {}^1D_2$ E1 resonance in the three-photon detachment yield. The solid line represents a Lorentzian fit.

deromotive threshold shift of a few cm^{-1} may be present). At energies below the two-photon threshold a small photodetachment signal is observed. This signal results from one-photon detachment of $Si^-(^2D)$ and from three-photon detachment of $Si^-(^4S)$. However, no resonant features were found. The absence of any resonance structure is likely due to a very small transition probability. The transitions would be 'spin-forbidden', and although this is also the case for the $^3P_2 \xrightarrow{2h\nu} {}^1D_2$ transition observed in Sb^-, a spin change is a much more serious constraint for a transition in a light system which is well described by LS-coupling, such as Si^-.

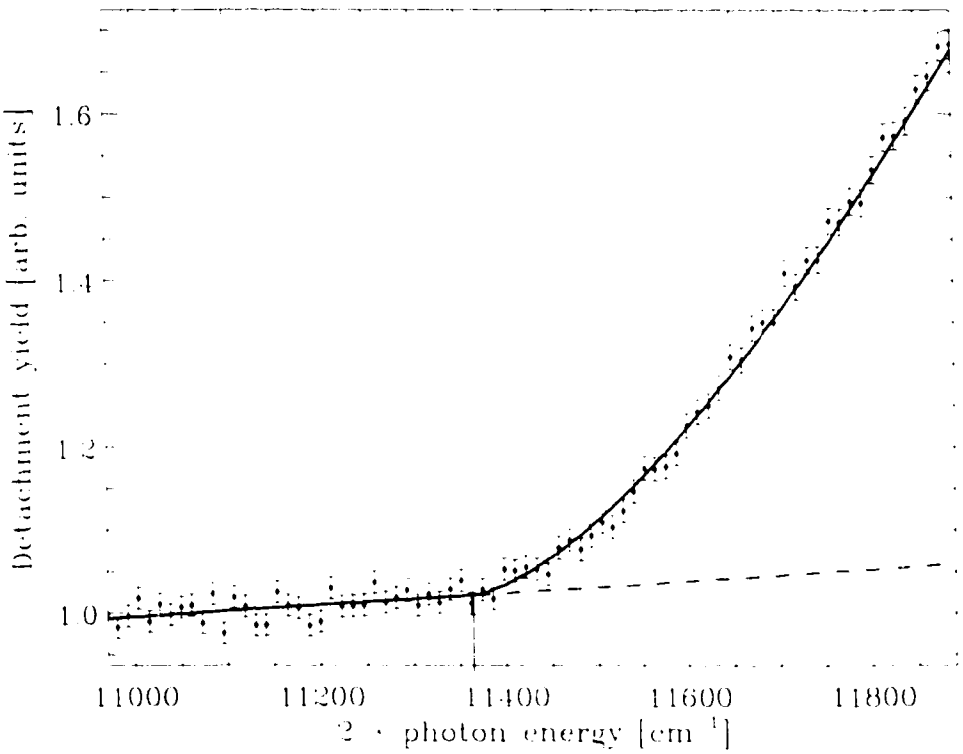

Figure 6.4: Measured two-photon $Si^-(^4S_{3/2}) \xrightarrow{2h\nu}$ $Si(^3P)$ detachment threshold. The solid line shows the result of a Wigner p-wave fit to the data.

6.4 Summary and outlook

Three different resonant multiphoton detachment schemes were successfully applied in our studies of bound excited negative ion states. 1+1 photon detachment via forbidden transitions was proven to be applicable in cases where large fine structure splittings (Te^-, Ir^-, Pt^-) or excited terms (Sn^-, Sb^-) are present. 2+1 photon detachment via two-photon Raman transitions was found to work well for smaller fine structure splittings (Se^-, Te^-) and finally, straight (single color) 2+1 photon detachment was demonstrated for the case of weakly bound excited states (Sb^-). The results of these experiments are summarized in Table 6.1.

In terms of future studies, the observation of the $^4S_{3/2} \rightarrow {}^2D_{5/2}$ resonance in Sn^- has demonstrated that laser-driven transitions into metastable ionic levels with

Table 6.1: Summary of energy level splittings derived from multiphoton detachment experiments.

Ion	Levels	Scheme	Splitting [cm^{-1}]
Sn^-	$^1S_{3/2} - ^3D_{3/2}$	1+1	5762.5004(10)
	$^1S_{3/2} - ^3D_{5/2}$	1+1	6512.3704(10)
Sb^-	$^3P_2 - ^3P_1$	1+1	2684.3704(5)
	$^3P_2 - ^1D_2$	1+1	7392.5504(5)
		2+1	7392.7003(0)
Te^-	$^2P_{3/2} - ^2P_{1/2}$	1+1	5005.3604(10)
		2(Raman)+1	5004.665(5)
Ir^-	$^4F_4 - ^4F_3$	1+1	7087.304(4)
Pt^-	$^2D_{5/2} - ^2D_{3/2}$	1+1	9740.905(5)

radiative lifetimes as long as ~100 s are currently possible. Novel storage rings (e.g. ELISA in Aarhus, Denmark) may in fact enable accurate liftime measurements of such long-lived ionic states. Further improved or alternative tunable infrared laser sources such as optical parametric oscillators may provide wider tuning ranges, higher repetition rates, and/or more energetic pulses. Somewhat shorter pulses, say 100 ps, could provide higher intensities and thus increase the probabilities of nonlinear processes, with only moderate spectral broadening.

Although our attempts to observe 2(Raman)+1 fine structure resonances in Ir^- and Pt^- were not successful, it is still believed that this detachment scheme may prove very valuable in future fine structure measurements of transition metal anions. Most of these systems have ionic ground states of large multiplicity, often with only small and yet undetermined fine structure splittings. These systems furthermore exhibit p-wave detachment thresholds, which makes a fine structure determination based on LPT spectra of cascaded thresholds very challenging (compare Chapter 5).

The only single-color two-photon E1 transition observed thus far, $^3P_2 \rightarrow ^1D_2$ in Sb^-, was also driven as a one-photon M1 transition. However, cases exist where

both one-photon E1 and M1 transitions are strictly forbidden by the selection rules (Table 2.1), e.g. the yet unobserved $^3F_4 \rightarrow {}^3F_2$ transition in Ir^-. A one-photon transition would then be of electric quadrupole character and therefore extremely weak, but a two-photon transition might be sufficiently strong in some cases. In particular, the near degeneracy of the $(n-1)d^n$, $(n-1)d^{n-1}ns$, and $(n-1)d^{n-2}ns^2$ configurations found in most transition metal atoms suggests that the respective ions may exist in more than one stable electron configuration. However, Pd^- is the only experimentally proven case thus far (Sec. 5.4.3). Such excited even parity configurations of transition metal anions are likely weakly bound. Hence, single-color 2+1 photon detachment might be the only feasible detachment scheme here.

In some of the cases investigated here, resonant enhancements in multiphoton detachment spectra were expected on the basis of computer simulations, but not observed due to a substantial one-photon detachment background from excited ionic levels. In such cases, a strong laser pulse could be employed to deplete the excited level population of the ion beam via saturation detachment, before the ion beam is electrostatically deflected into the interaction region where the actual multiphoton detachment takes place.

So far, multiphoton experiments that were aimed at excited states of atomic negative ions all employed photons in the optical regime. However, many possibilities seem to exist for resonant detachment schemes that involve photons of very different fequencies, e.g. in the optical and microwave regime. Combinations of laser and microwave sources have been successfully used in the past to study the hyperfine structure of $^{33}S^-$ [91] and the threshold detachment of S^- and Cl^- [25].

Finally, as already mentioned in Chapter 5, a very different approach to the study of the fine structure of transition metal negative ions could involve two-photon

rather than single photon threshold spectroscopy. The observation of the two-photon detachment threshold of Si^- (Fig. 6.4), a negative ion of average binding energy, indicates that this scheme might be generally applicable. This detachment scheme is particularly interesting for transition metal negative ions, as their two-photon thresholds follow the Wigner s-wave law with its characteristic sharp onset. Cascades of even closely spaced s-wave thresholds as in the case of B^- (Sec. 4.3.4) have proven to be an accurate measure of ionic fine structure. The threshold shifts that are inevitable with the high laser intensities necessary for the two-photon process would likely be the same for all fine structure thresholds and thus the splitting would remain unchanged.

Chapter 7

Conclusion

This Thesis has described the design and initial testing of a pulsed, tunable infrared laser source and its application in photodetachment studies of atomic negative ions. In all, 21 elements and three distinct aspects of negative ion spectroscopy have been investigated systematically.

A large subset of the elements of the periodic table (namely the main group IIIA-VIIA elements) form stable negative ions which detach into *s*-wave continua. Several of these systems have been studied here by means of infrared laser photodetachment threshold spectroscopy, resulting in highly accurate values for ionic binding energies and new information on excited ionic states. The studies have lead to a substantial proliferation of the experimental knowledge of these systems, to an extent that only very few questions remain regarding their bound energy level structure.

Another major group of stable atomic anions is characterized by photodetachment into *p*-wave continua. These ions are primarily given by transition metal elements which had not been studied previously via photodetachment threshold spectroscopy (with the exception of Ir^-, Pt^-, and Au^-). Ten systems were investigated in the present study, and accurate binding energies for the respective ionic ground states

and their fine structure levels were obtained in most cases. Here, a primary goal was to investigate the structure of 'cascaded' p-wave thresholds, which had not been done previously. Although negative ion fine structure splittings could be determined from such cascaded thresholds, some limitations of the technique became apparent. Fortunately, these limitations could be removed in future experiments if state-selective detections schemes were employed. Infrared photodetachment threshold spectroscopy would then provide a promising tool for the investigation of the 11 remaining stable transition metal anions, which are largely unexplored to date.

Finally, the possibility for resonant multiphoton detachment of negative ions was investigated. Resonant multiphoton schemes are new to the study of atomic negative ions. Three detachment schemes could be established: 1+1 photon detachment via magnetic dipole resonances, and 2+1 photon detachment via two-photon electric dipole resonances in either a straight (single-color) or a two-color Raman coupling regime. Each scheme was found to be best suited for a different energy level structure, hence their combination may provide a complete set of multiphoton probes of ionic structure. The studies were conducted with several different anions providing highly accurate ionic energy level splittings and clearly demonstrating that multiphoton probes are generally applicable to negative ions.

Many possibilities exist for further and novel laser-based negative ion studies. Except for the case of Cs^-, ionic structure embedded in the detachment continuum has not been addressed in the present work. However, the continuum structure of negative ions has been an area of active and extensive research over the past few decades. The infrared techniques demonstrated in this Thesis could, in fact, be applied to a region of the continuum of many ionic species that has not yet been explored. In particular, the negative ions of heavy transition metals may be expected

to possess interesting continuum structures (somewhat similar to Cs^-). Some of these systems could also provide the first example of an atomic anion with opposite parity bound states. Resonant multiphoton schemes could be utilized in this context to probe narrow (i.e. metastable) continuum states, as has been done in the case of alkaline earth anions [7]. As yet unexplored seems to be the possibility of using short (picosecond) optical pulses which, in multiphoton transitions to higher lying continuum structures, could prevent the ion from 'premature' detachment. The high intensities associated with such short pulses would also provide a powerful tool for studies of negative ions in strong fields. Multiphoton detachment thresholds and interferences between different multiphoton detachment channels are very interesting phenomena that have not yet been studied quantitatively. Multiphoton threshold spectroscopy could also provide an alternative probe of ionic structure, a prospect that is currently being investigated by the McMaster group.

Bibliography

[1] H. Hotop and W.C. Lineberger, J. Phys. Chem. Ref. Data **14**, 731 (1985).

[2] A.R.P. Rau, Comments At. Mol. Phys. **14**, 285 (1984).

[3] S.J. Buckmann, C.W. Clark, Rev. Mod. Phys. **66**, 539 (1994).

[4] R. Wildt, Astrophys. J. **89**, 295 (1939).

[5] L.M. Branscomb, in *Atomic and Molecular Processes* (Edited by D.R. Bates), p. 100, Academic Press, New York (1962).

[6] J. Dellwo, Y. Liu, D.J. Pegg, G.D. Alton, Phys. Rev. A **45**, 1544 (1992).

[7] T. Andersen, H.H. Andersen, P. Balling, P. Kristensen, and V.V. Petrunin, J. Phys. B **30**, 3317 (1997).

[8] D. Feldmann, Z. Phys. A **277**, 19 (1976).

[9] D. Feldmann, Chem. Phys. Lett. **47**, 338 (1977).

[10] K.R. Lykke, K.K. Murray, and W.C. Lineberger, Phys. Rev. A **43**, 6104 (1991).

[11] W.C. Lineberger and T.A. Patterson, Chem. Phys. Lett. **13**, 40 (1972).

[12] H. Friedrich, *Theoretical Atomic Physics*, Springer-Verlag, Berlin (1991).

[13] I.I. Sobelman, *Atomic Spectra and Radiative Transitions*, Springer-Verlag, Berlin (1979).

[14] A. Corney, *Atomic and Laser Spectroscopy*, Clarendon Press, Oxford (1977).

[15] R. Eisberg and R. Resnick, *Quantum Physics of Atoms, Molecules, Solids, Nuclei, and Particles*, Wiley, New York (1985).

[16] M. Roberts *et al.*, Phys. Rev. Lett. **78**, 1876 (1997); P. Beiersdorser Phys. Rev. Lett. **67**, 2272 (1991).

[17] N. Melikechi and L. Allen, J. Opt. Soc. Am. B **3** 11 (1986); K.D. Bonin and T.J. McIlrath, J. Opt. Soc. Am. B **1** 52 (1984).

[18] E.P. Wigner, Phys. Rev. **73**, 1002 (1948).

[19] J.W. Farley, Phys. Rev. A **40**, 6286 (1989).

[20] T.F. O'Malley, Phys. Rev. **137**, A1668 (1964).

[21] P.A. Cox, in *Structure and Bonding*, edited by J.D. Dunitz *et al.* (Springer Verlag, Berlin, 1975), Vol. 24, pp. 59-81.

[22] P.C. Engelking and W.C. Lineberger, Phys Rev. A **19**, 149 (1979).

[23] N.D. Gibson, B.J. Davies, and D.J. Larson, Phys. Rev. A **47**, 1946 (1993); C.H. Greene and N. Rouze, Z. Phys. D **9**, 219 (1988); P. Frey, F. Breyer, and H. Hotop, J. Phys. B **11**, L589 (1978).

[24] N.D. Gibson, B.J. Davies, and D.J. Larson, Phys. Rev. A **48**, 310 (1993).

[25] M.C. Baruch, W.G. Sturrus, N.D. Gibson, and D.J. Larson, Phys. Rev. A **45**, 2825 (1992).

[26] R. Middleton, Nuc. Instr. and Meth. **214**, 139 (1983).

[27] D.R. Bates, Adv. At. Mol. Opt. Phys. **27**, 1 (1991); T. Andersen, Phys. Scr. **T34**, 23 (1991).

[28] E.R. Cohen and B.N. Taylor, Rev. Mod. Phys. **59**, 1121 (1987).

[29] W.K. Bischel and M.J. Dyer, Phys. Rev. A **33** 3113 (1986); E.C. Looi, J.C. Stryland, and H.L. Welsh, Can. J. Phys. **56**, 1102 (1978); and references therein.

[30] P. Rabinowitz, B.N. Perry, and N. Levinos, IEEE J. Quant. Elect. **22**, 797 (1986).

[31] W. Heuer and H. Zacharias, IEEE J. Quant. Elect. **24**, 2087 (1988).

[32] H. Bryant, K. Sentrayan, and V. Kushawaha, Spectrosc. Lett. **25**, 1387 (1992).

[33] L. Minnhagen, J. Opt. Soc. Am. **63**, 1185 (1973).

[34] J.R. Nestor, Appl. Opt. **21**, 1151 (1982).

[35] R. Trainham, G.D. Fletcher, N.B. Mansour, and D.J. Larson, Phys. Rev. Lett. **59**, 2291 (1987); M.D. Davidson, J. Wals, H.G. Muller, and H.B. van Linden van den Heuvell, Phys. Rev. Lett. **71**, 2192 (1993).

[36] D.M. Neumark, K.R. Lykke, T. Andersen, and W.C. Lineberger, Phys. Rev. A **32**, 1890 (1985).

[37] C. Blondel, Phys. Scr. **T58**, 31 (1995);

[38] S.H. Vosko, J.B. Lagowski, I.L. Mayer, and J.A. Chevary, Phys. Rev. A **43**, 6389 (1991); D. Datta and D.R. Beck, Phys. Rev. A **50** 1107 (1994); K. Dinov, D.R. Beck, and D. Datta, Phys. Rev. A **50** 1144 (1994).

[39] R. Middleton, *A Negative Ion Cookbook* (unpublished).

[40] C. Blondel, P. Cacciani, C. Delsart, and R. Trainham, Phys. Rev. A **40**, 3698 (1989).

[41] G. Haeffler, D. Hanstorp, I. Kiyan, A.E. Klingmuller, and U. Ljungblad, Phys. Rev. A **53**, 4127 (1996).

[42] P. Kristensen, U.V. Pedersen, V.V. Petrunin, T. Andersen, and K.T. Chung, Phys. Rev. A **55**, 978 (1997).

[43] P. Kristensen, V.V. Petrunin, H.H Andersen, and T. Andersen, Phys. Rev. A, **52**, R2508 (1995).

[44] C.S. Feigerle, R.R. Corderman, and W.C. Lineberger, J. Chem. Phys. **74**, 1513 (1981).

[45] D.H. Lee, W.D. Brandon, D. Hanstorp, and D.J. Pegg, Phys. Rev. A **53**, R633 (1996).

[46] K. Raghavachari, J. Chem. Phys. **82**, 1142 (1985); J.J. Novoa, F. Mota, and F. Arnau, J. Phys. Chem. **95**, 3096 (1991); R.A. Kendall, T.H. Dunning, Jr., and R.J. Harrison, J. Chem. Phys. **96**, 6796 (1992).

[47] T. Noro, M. Yoshimine, M. Sekiya, and F. Sasaki, Phys. Rev. Lett. **66**, 1157 (1991).

[48] D. Sundholm and J. Olsen, Chem. Phys. Lett. **171**, 53 (1990).

[49] C. Froese Fischer, A. Ynnerman, and G. Gaigalas, Phys. Rev. A **51**, 4611 (1995).

[50] W.P. Wijesundera, Phys. Rev. A **55**, 1785 (1997); E. Eliav, Y. Ishikawa, P. Pyykkö, and U. Kaldor, Phys. Rev. A **56**, 4532 (1997).

[51] B. Edlén, H.P. Palenius, K. Bockasten, R. Hallin, and J. Bromander, Solar Phys. **9**, 432 (1969).

[52] V.A. Oparin, R.N. Il'in, I.I. Serenkov, and E.S. Solov'ev, Sov. Phys. JETP **39**, 989 (1974) [Zh. Eksp. Teor. Fiz. **66**, 2008 (1974)].

[53] D. Calabrese, A.M. Covington, J.S. Thompson, R.W. Marawar, and J.W. Farley, Phys. Rev. A **54**, 2797 (1996).

[54] F. Arnau, F. Mota, and J.J. Novoa, Chem. Phys. **166**, 77 (1992).

[55] D.E. Woon and T.H. Dunning Jr., J. Chem. Phys. **99**, 3730 (1993).

[56] V.A. Oparin, R.N. Il'in, I.I. Serenkov, and E.S. Solov'ev, Zh. Eksp. Teor. Fiz. **66**, 2008 (1974) [Sov. Phys.-JETP **39**, 989 (1974)].

[57] T. Noro, M. Yoshimine, M. Sekiya, and F. Sasaki, Phys. Rev. Lett. **66**, 1157 (1991); K. Raghavachari, J. Chem. Phys. **82**, 4142 (1985); R.A. Kendall, T.H. Dunning, Jr., and R.J. Harrison, J. Chem. Phys. **96**, 6796 (1992).

[58] C. Froese Fischer, J. Phys. B **26**, 855 (1993).

[59] A. Kasdan, E. Herbst, and W.C. Lineberger, J. Chem. Phys. **62**, 541 (1975).

[60] T.M. Miller, A.E. Stevens Miller, W.C. Lineberger, Phys. Rev. A **33**, 3558 (1986).

[61] D. Feldmann, R. Rackwitz, E. Heinicke, and H.J. Kaiser, Z. Phys. A **282**, 143 (1977).

[62] U. Ljungblad, *Photodetachment Studies of Continuum Structure in Negative Ions*, Chalmers Repro Service, Göteborg, (1996).

[63] H. Hotop and W.C. Lineberger, J. Phys. Chem. Ref. Data **4**, 539 (1975).

[64] R.J. Zollweg, J. Chem. Phys. **50**, 4251 (1969).

[65] M.L. Polak, G. Gerber, J. Ho, and W.C. Lineberger, J. Chem. Phys. **97**, 8990 (1992).

[66] D.R. Beck, private communication.

[67] R. Frainham, G.D. Fletcher, and D.J. Larson, J. Phys. B **20**, L777 (1987).

[68] C.Y. Tang *et al.*, in *Multiphoton Processes*, edited by G. Mainfray and P. Agostini (SPA, C E Saclay, France, 1990), p. 69.

[69] B.J. Davies, C.W. Ingram, D.J. Larson, and U. Ljungblad, J. Chem. Phys. **106**, 5783 (1997).

[70] H. Hotop and W.C. Lineberger, J. Chem. Phys. **58**, 2379 (1973).

[71] N.D. Gibson, B.J. Davies, and D.J. Larson, J. Chem. Phys. **98**, 5104 (1992).

[72] D. Feldmann, Z. Phys. A **277**, 19 (1976).

[73] T. Andersen, Phys. Scr. **T34**, 23 (1991).

[74] C.L. Pekeris, Phys. Rev. **126**, 1470 (1962); K. Aashamar, Nucl. Instrum. Methods **90**, 263 (1970).

[75] C.H. Greene, Phys. Rev. A **42**, 1405 (1990).

[76] I.I. Fabrikant, Opt. Spectrosc. (U.S.S.R.) **53**, 131(1982) [Opt. Spektrosk. **53**, 223 (1982)].

[77] J.L. Krause and R.S. Berry, Comments At. Mol. Phys. **18**, 91 (1986).

[78] C. Froese Fischer and D. Chen, J. Mol. Struct. **199**, 61 (1989).

[79] C. Thumm and D.W. Norcross, Phys. Rev. Lett. **67**, 3495 (1991); Phys. Rev. A **45**, 6349 (1992); **47**, 305 (1993).

[80] N.S. Scott, K. Bartschat, P.G. Burke, O. Nagy, and W.B. Eissner, J. Phys. B **17**, 3755 (1984); P.G. Burke and J.F.B. Mitchell, J. Phys. B **6** L161 (1973).

[81] K. Bartschat, J. Phys. B **26**, 3595 (1993).

[82] C.S. Feigerle, R.R. Corderman, S.V. Bobashev, and W.C. Lineberger, J. Chem. Phys. **74**, 1580 (1981).

[83] R.F. Gunion,S.J. Dixon-Warren, and W.C. Linberger, J. Chem. Phys. **104**, 1765 (1996).

[84] D.G. Leopold and W.C. Lineberger, J. Chem. Phys. **85**, 51 (1986).

[85] R.R. Corderman, P.C. Engelking, and W.C. Lineberger, J. Chem. Phys. **70**, 1474 (1979).

[86] D.G. Leopold,J. Ho, and W.C. Lineberger, J Chem. Phys. **86**, 1715 (1987).

[87] H. Hotop,R.A. Bennett, and W.C. Lineberger, J. Chem. Phys. **58**, 2373 (1973).

[88] J.L. Hall, E.J. Robinson, and L.M. Branscomb, Phys. Rev. Lett. **14**, 1013 (1965).

[89] M.D. Davidson, H.G. Muller, and H.B. van Linden van den Heuvell, Phys. Rev. Lett. **67**, 1712 (1991); H. Stapelfeldt, P. Balling, C. Brink, and H.K. Haugen, Phys. Rev. Lett. **67**, 1731 (1991); C. Blondel, M. Crance, C. Delsart, and A. Giraud, J. Phys. B **24**, 3575 (1991).

[90] P. Kristensen *et al.*, Phys. Rev. Lett. **71**, 3435 (1993).

[91] R. Trainham, R.M. Jopson, and D.J. Larson, Phys. Rev. A **39**, 3223 (1989).

Paper 1

Single- and Multiphoton Infrared Laser Spectroscopy of Sb^-: A Case Study.

Michael Scheer, Harold K. Haugen, and Donald R. Beck.

Physical Review Letters **79**, 1101-7 (1997).

Single- and Multiphoton Infrared Laser Spectroscopy of Sb^-: A Case Study

Michael Scheer and Harold K. Haugen*
Department of Physics and Astronomy, McMaster University, Hamilton, Ontario, L8S 4M1, Canada

Donald R. Beck
Physics Department, Michigan Technological University, Houghton, Michigan 49931
(Received 11 June 1997)

A combination of single- and multiphoton tunable infrared laser experiments is utilized to accurately and conclusively determine the bound terms and fine structure of $Sb^-(5p^4)$. The $^3P_2$ binding energy is determined to be 8447.86(15) cm^{-1} (electron affinity of antimony) and the previously unobserved $^3P_1$, $^3P_0$, and $^1D_2$ levels are found at 2684.37(15), 2800.8(6), and 7392.55(15) cm^{-1} above the $^3P_2$ ground level, respectively. Relativistic configuration interaction calculations predict these splittings to be 2516, 2831, and 7628 cm^{-1}. Widths and shapes of resonances observed in two-photon detachment yields are modeled on the basis of calculated hyperfine structure constants. [S0031-9007(97)04614-0]

PACS numbers: 32.80.Gc, 31.25.Jf, 31.30.Jv, 32.80.Wr

The spectroscopy of negative ions has been an area of considerable interest for the past two decades (for recent reviews, see Ref. [1]). Recently, multiphoton techniques have been successfully established in this field. Studies either addressed fundamental optical phenomena since negative ions, due to their short range potentials, represent qualitatively different targets for strong-laser-fields studies [2], or they were aimed at the elucidation of negative ion structure. Both resonant structures in the continuum of negative ion species [3] as well as bound excited states [4,5] have been probed via multiphoton schemes. The energy levels of a negative ion below its first detachment limit almost always refer to the terms and fine structure of the same (ground state) electronic configuration and are still only poorly determined in many negative ion systems. Optical transitions between such levels are forbidden in a conventional single photon electric dipole scheme as a result of the parity selection rule. However, a simultaneous absorption of two photons would be allowed in an electric dipole interaction and has been demonstrated in negative ions for the case where the two photons have different energies and are absorbed via a Raman coupling scheme [4]. In addition, small probabilities exist for single-photon transitions of magnetic dipole (M1) or electric quadrupole (E2) character between most bound negative ion levels. Such "forbidden" transitions have very recently been reported between fine structure levels of Ir^- and Pt^-, although the lack of a confirmation via a two-photon Raman transition left the M1 interpretation somewhat open [5]. In this paper we present a case study where a combination of one-, two-, and three-photon detachment experiments is utilized to completely and accurately determine all bound terms and fine structure levels of the antimony negative ion. The results fully confirm the potential of forbidden transitions in optical studies of negative ions [5]. Also, a single-color 2 + 1 photon detachment scheme is demonstrated for the first time, suggesting prospects for the study of some weakly bound excited states in other systems. In addition, we present RCI calculations of fine structure and term splittings and of hyperfine structure constants. Finally, these constants are used to simulate the observed thresholds and M1 resonance peak profiles.

The experimental setup is described in detail elsewhere [4–6]. Nanosecond pulses in the 0.7–1.0 μm range are generated using a dye laser which is pumped by the second harmonic of a 10 Hz Q-switched Nd:YAG laser. Stimulated Raman scattering in a single pass high pressure hydrogen cell is employed to convert the dye laser output into tunable infrared radiation via first and second Stokes generation, with a measured Raman shift of 4155.20(2) cm^{-1}. Infrared pulse energies range from 10 mJ at 1 μm to 0.1 mJ at 5 μm. A 15 keV Sb^- beam is extracted from a Cs sputter ion source, magnetic field analyzed, and further charge state analyzed in an ultrahigh vacuum chamber and then crossed perpendicularly with a collimated or focused infrared laser beam (for single photon or multiphoton detachment, respectively). The photodetached neutral atoms impinge on a discrete dynode electron multiplier for analog data collection.

A schematic energy level diagram of the negative ion of antimony is shown in Fig. 1. To our knowledge, only two photodetachment experiments with this system have been reported previously. Feldmann *et al.* [7] used a conventional light source and obtained a $^3P_2$ binding energy of 8630(400) cm^{-1} and a $^3P_2 - {}^3P_{1,0}$ fine structure splitting of 2740(600) cm^{-1}. The $J = 1,0$ levels remained unresolved. The $J = 2 - 1$ and $J = 2 - 0$ fine structure and $^3P_2 - {}^1D_2$ term splittings have been predicted to be 2700(500), 3000(500), and ~7600 cm^{-1} on the basis of isoelectronic extrapolation [8,9]. Polak *et al.* [10] derived an electron affinity of 8436(40) cm^{-1} from a laser photodetached electron spectrum and reported that no evidence of hot bands was observed.

The photodetachment spectrum of Sb^- in the vicinity of the $Sb^-(^3P_2) \rightarrow Sb(^4S_{3/2})$ threshold is shown in Fig. 2. Wigner's threshold law which applies to the

 0031-9007/97/79(21)/4104(4)$10.00

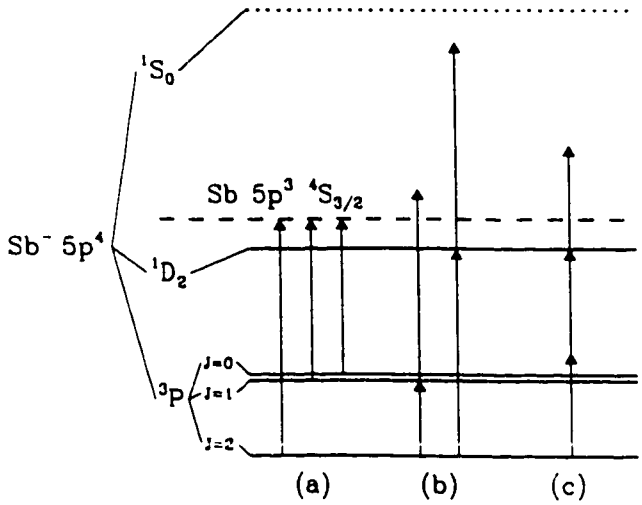

FIG. 1. Schematic energy level diagram of Sb . Arrows indicate different photodetachment schemes: (a) single photon detachment thresholds; (b) two-photon detachment via single photon M1 resonances; (c) three-photon detachment via two-photon E1 resonance.

photodetachment of negative ions predicts the cross section to be proportional to $\varepsilon^{\ell+1/2}$ where ε is the energy of the detached electron and ℓ its angular momentum. Detachment of a bound p electron therefore exhibits an s-wave threshold which has been fitted to the experimental data (dashed line in Fig. 2). From this fit, a $Sb^-(^3P_2)$ binding energy of 8447.83(15) cm^{-1} is obtained. (Uncertainties will always include possible systematic errors due to laser calibration and Doppler shifts.) This result is in good agreement with the previous measurements, but exhibits a nearly 300-fold increase in accuracy. The foot right at the onset of the threshold in Fig. 2 indicates line broadening effects due to hyperfine structure (see below) in addition to the effects of laser bandwidth and Doppler broadening, the latter two of which, if combined, are typically less than 0.2 cm^{-1}. Two more, although significantly weaker, thresholds are found at photon energies of 5763.3(3) and 5647.0(5) cm^{-1} which results in fine structure splittings of 2684.5(4) and 2800.8(6) cm^{-1} between the $^3P_2$ ground level and the two upper levels of the ^3P term. The most likely order of the ^3P_J levels is certainly 2-1-0 but the large uncertainties of isoelectronic extrapolations leave a small probability for a 2-0-1 order as it is found throughout the isoelectronic sequence. To be sure, a 1 + 1 two-color photodetachment experiment is conducted which employs second Stokes radiation around 3.6 μm for the resonant transition and first Stokes radiation for the subsequent detachment. Only one resonance is found at 2684.37(15) cm^{-1} as shown in Fig. 3 and must be assigned to a transition between $^3P_2$ and $^3P_1$, confirming a 2-1-0 level order. This assignment is based on estimated transition probabilities of 0.4 s^{-1}(M1) and 0.9×10^{-3} s^{-1} (E2) for $J = 1 \rightarrow 2$ and 2×10^{-3} s^{-1} (E2) for $J = 0 \rightarrow 2$ which are derived from probabilities for forbidden transitions in the $5p^4$ configurations, calculated by Biémont *et al.* [11]. According to that, a $J = 2 \rightarrow 0$ electric quadrupole transition would be about 200 times weaker than the dominantly magnetic dipole $J = 2 \rightarrow 1$ resonance, too weak to be observed under the given experimental conditions.

In order to locate the previously unobserved but possibly bound $^1D_2$ term, the single-color two-photon detachment spectrum of $Sb^-(^3P_2)$ was recorded. Isoelectronic $^1D_2 \rightarrow {}^3P_2$ transition probabilities of 1.1 s^{-1} (M1) and 3×10^{-2} s^{-1} (E2) (based on Ref. [11]) suggest that a 1 + 1 resonance should be of M1 character and observable under the given experimental conditions. Figure 4 shows this resonance which was found at a photon energy of 7392.55(15) cm^{-1} giving a $^1D_2$ binding energy

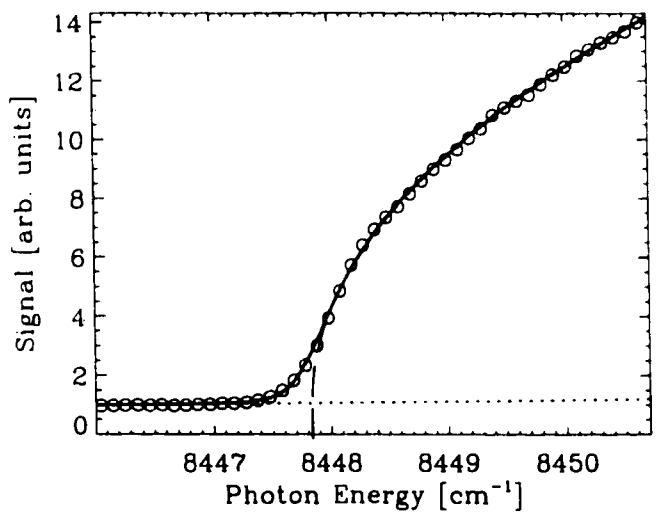

FIG. 2. Measured $Sb^-(^3P_2) \rightarrow Sb(^4S_{3/2})$ photodetachment threshold. Wigner s-wave fits with and without the inclusion of line broadening effects are indicated by the solid and dashed line, respectively.

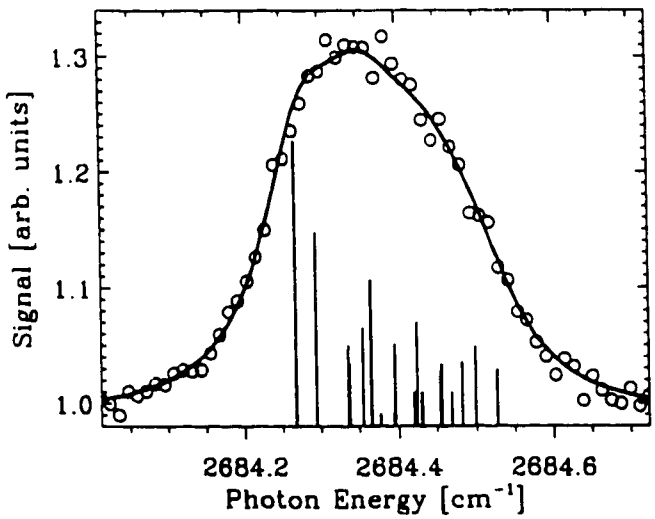

FIG. 3. $^3P_2 \rightarrow {}^3P_1$ M1 resonance in the two-photon detachment yield. The solid line represents the simulated resonance profile (see text), and the vertical lines indicate positions and relative strengths of individual hyperfine components.

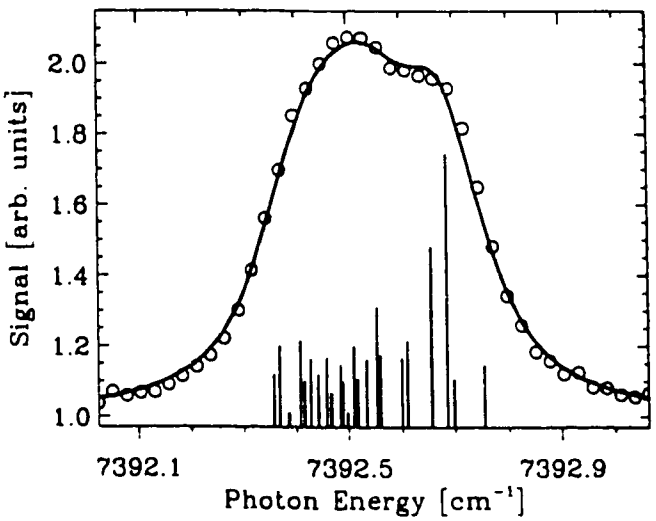

FIG. 4. $^3P_2 \rightarrow {}^1D_2$ M1 resonance in the two-photon detachment yield. The solid line represents the simulated resonance profile (see text), and the vertical lines indicate positions and relative strengths of individual hyperfine components.

of 1055.3(2) cm^{-1}. In order to check the level parity, the $^3P_2 \rightarrow {}^1D_2$ transition was also driven via an electric dipole allowed two-photon absorption. As the $^1D_2$ binding energy is less than half the $^3P_2 - {}^1D_2$ splitting energy, the transition could be observed as a 2 + 1 resonance in the single-color three-photon detachment spectrum of $Sb^-(^3P_2)$. The signal-to-background ratio of this resonance was significantly improved by retaining a fraction of the first Stokes radiation in the infrared pulse. In doing so, the probability for absorption of the third and detaching photon was substantially increased and only a small single photon detachment background from the upper ^3P_J levels was introduced. A photon energy of 3696.35(15) cm^{-1} gives a splitting energy of 7392.7(3) cm^{-1} which agrees well with the value obtained from the 1 + 1 M1 resonance.

All three resonances observed in Sb^- exhibit a line broadening that cannot be explained on the basis of laser bandwidth and Doppler effects alone. A comparison with the equivalent transitions in isoelectronic Te and I^+ [12] and transitions between levels of the $5p^3$ configuration in Sb [13] indicates that Sb^- hyperfine structure could give rise to a broadening of a few tenths of wave numbers. The hyperfine structure of numerous neutral and positively charged systems has been studied in the optical regime, but studies of this kind do not exist for negative ions. Therefore, the measured 1 + 1 M1 resonance peak profiles have been modeled on the basis of calculated hyperfine structure A and B constants (see below). The energy E_F of a hyperfine sublevel F belonging to a fine structure level J with average energy E_J is given by

$$E_F = E_J + A\frac{C}{2} + B\frac{3C(C+1) - 4IJ(I+1)(J+1)}{8IJ(2I-1)(2J-1)},$$

where $C = F(F+1) - J(J+1) - I(I+1)$. The relative intensity of a hyperfine component ($F \rightarrow F'$) of a fine structure transition ($\alpha J \rightarrow \alpha' J'$) can be expressed as

$$S_{FF'} \propto (2F+1)(2F'+1)\begin{Bmatrix} I & J & F \\ j & F' & J' \end{Bmatrix}^2,$$

where $j = 1$ for dipole transitions (or $j = 1/2, 3/2$ for s-wave thresholds; see below). In the case of Sb^- the spectral profile of a single component could not be measured directly but it is inferred to be mainly Lorentzian with a width of 0.16(2) cm^{-1} (FWHM) based on previously measured M1 resonances [5]. The best overlap of measured and calculated profiles is found by performing a least square fit using $\Delta E = E_{J'} - E_J$ and the peak height as fitting parameters. Unfortunately, the measured profiles do not exhibit enough structure for hyperfine A and B constants to be included as parameters in the fit which would result in experimental values for these constants. Instead, the calculated values are used. Figures 3 and 4 show the fitted data including line spectra which indicate the individual hyperfine components. The transition energies ΔE obtained from the fit are those given in the preceding paragraphs. The situation was complicated due to the fact that the antimony used in the sputter cathode contained both isotopes ^{121}Sb and ^{123}Sb in their natural abundances of 57% and 43%. As a result, the two M1 resonances were composed of 18 and 26 hyperfine components, respectively. Nevertheless, the good agreement between measured and calculated line profiles is a convincing indication of hyperfine structure in the bound levels of Sb^-. The interpretation is consistent with the fact that the previously observed bound-bound transitions in Ir^- and Pt^- [5] and high resolution threshold spectra of other negative ions [1] did not exhibit additional line broadening as the corresponding nuclei have zero spin or only small magnetic dipole and electric quadrupole moments or the electronic angular momentum J is zero.

As mentioned above, the $Sb^-(^3P_2) \rightarrow Sb(^4S_{3/2})$ threshold appears broadened as well. It is composed of several closely spaced thresholds due to the hyperfine structure in both the neutral atom [13] and negative ion states. The threshold was modeled using the above equations, convoluted with the line shape function, and then fitted to the data (solid line in Fig. 2). This resulted in an average $Sb^-(^3P_2)$ binding energy of 8447.79(15) cm^{-1}, $^{121}Sb^-(^3P_2, F = 1/2)$ and $^{123}Sb^-(^3P_2, F = 3/2)$ binding energies of 8447.87(15) and 8447.85(15) cm^{-1} (relative to the lowest hyperfine level of the respective atom), and finally an isotopically averaged electron affinity of antimony of 8447.86(15) cm^{-1}.

Since the experimental conditions did not allow for a discrimination between the two isotopes of Sb, the possibility of isotope shifts should be considered. Calculated values for the normal mass shifts of the observed M1 transitions are 6 MHz for $^3P_2 \rightarrow {}^3P_1$ and 15 MHz for $^3P_2 \rightarrow {}^1D_2$ [14]. Buchholz *et al.* [15] measured isotope shifts in transitions between the $5s^25p^3$ and $5s^25p^26s$

configurations of neutral antimony. The residual isotope shifts in these transitions are smaller than 300 MHz and indicate that residual shifts in transitions between the ^2P and ^2D terms of the $5p^3$ configuration would only be of the order of 30 MHz. We therefore conclude that isotope shifts in the $^3P_2 \rightarrow {}^3P_1$ and $^3P_2 \rightarrow {}^1D_2$ transitions of Sb^- should be no larger than 100 MHz (or 0.003 cm^{-1}), i.e., 2 orders of magnitude smaller than the calculated hyperfine splittings.

Relativistic configuration interaction (RCI) calculations were carried out by first obtaining a Dirac-Fock wave function for $5p^4$ using the program of Desclaux [16]. The Dirac-Coulomb Hamiltonian was used during the variation, and Breit effects added perturbatively. The Dirac-Fock solution was then correlated, using our RCI program [17], by including single and double excitations from the $5s$ and $5p$ subshells, and single excitations from the $4d$ subshell. To substantially reduce the amount of excitation needed, all energies were referenced to the negative ion ground state. For energy differences the most important excitations were $5p \rightarrow vf$, $5s \rightarrow vd$, and $4d \rightarrow vg$, where the virtual (unoccupied) subshells are represented by relativistic screened hydrogenic functions. Further details of the methodology may be found elsewhere [18,19]. The calculations predict the $^3P_1$, $^3P_0$, and $^1D_2$ levels to lie 2516, 2831, and 7628 cm^{-1} above the $^3P_2$ ground level, respectively. These values are in good agreement with the experimentally determined energy splittings given above. In addition, RCI results indicate the $^1S_0$ level to lie $\approx$16 700 cm^{-1} above $^3P_2$, i.e., to be unbound by $\approx$8350 cm^{-1}. Using the RCI wave functions, hyperfine structure constants were calculated. The magnetic dipole A constants are -292, 489, and 1264 MHz for the $^3P_1$, $^3P_2$, and $^1D_2$ levels of $^{121}Sb^-$, respectively, and -158, 265, and 684 MHz for the corresponding levels of $^{123}Sb^-$. For these three levels calculated B/Q values are -321, 647, and -1423 MHz/b from which the electric quadrupole B constants are obtained using $Q_{121} = -0.36$ b and $Q_{123} = -0.49$ b [15]. Results for matrix elements of hyperfine structure operators can be found in Ref. [20].

In summary, infrared laser experiments have provided accurate binding energies for all four bound levels of Sb^-. The $^3P_1$, $^3P_0$, and $^1D_2$ levels were observed for the first time. Level splittings obtained from RCI calculations support the experimental results. The studies have clearly confirmed that magnetic dipole transitions in negative ions can be observed under typical experimental conditions with pulsed laser sources and keV ion beams. Resonance peak profiles have been successfully modeled on the basis of calculated hyperfine structure constants, indicating the potential of multiphoton spectroscopy in the experimental determination of negative ion hyperfine structure. In addition, a single color two-photon (bound-bound) transition was demonstrated for the first time in negative ions. In the study of other negative ion systems this transition scheme may provide a probe for weakly bound excited states which often cannot be addressed otherwise. To conclude, the combination of single and multiphoton techniques illustrated in this work provides a complete approach to the study of bound levels of atomic negative ions.

We thank the Natural Science and Engineering Research Council of Canada (NSERC) for support of the experimental work and the National Science Foundation, Grant No. 93-17828 for partial support of the theoretical work. The input of T. Andersen during various stages of the work is also greatly appreciated. We wish to thank J. D. Garrett for manufacturing the Sb-Pb alloy sputter cathode used in the experiments.

*Also with the Department of Engineering Physics, the Brockhouse Institute for Materials Research, and the Center for Electrophotonic Materials and Devices.

[1] D. R. Bates, Adv. At. Mol. Opt. Phys. **27**, 1 (1991); T. Andersen, Phys. Scr. **T34**, 23 (1991); S. J. Buckmann and C. W. Clark, Rev. Mod. Phys. **66**, 539 (1994); C. Blondel, Phys. Scr. **T58**, 31 (1995).

[2] M. D. Davidson, H. G. Muller, and H. B. van Linden van den Heuvell, Comments At. Mol. Phys. **29**, 65 (1993).

[3] H. Stapelfeldt *et al.*, Phys. Rev. A **50**, 1618 (1994).

[4] P. Kristensen *et al.*, Phys. Rev. Lett. **71**, 3435 (1993); J. Thøgersen, L. D. Steele, M. Scheer, H. K. Haugen, P. Kristensen, P. Balling, H. Stapelfeldt, and T. Andersen, Phys. Rev. A **53**, 3023 (1996).

[5] J. Thøgersen, M. Scheer, L. D. Steele, H. K. Haugen, and W. P. Wijesundera, Phys. Rev. Lett. **76**, 2870 (1996).

[6] M. Scheer, C. A. Brodie, R. C. Bilodeau, and H. K. Haugen, Phys. Rev. A (to be published).

[7] D. Feldmann, R. Rackwitz, E. Heinicke, and H. J. Kaiser, Z. Phys. A **282**, 143 (1977).

[8] H. Hotop and W. C. Lineberger, J. Phys. Chem. Ref. Data **4**, 539 (1975).

[9] R. J. Zollweg, J. Chem. Phys. **50**, 4251 (1969).

[10] M. L. Polak, G. Gerber, J. Ho, and W. C. Lineberger, J. Chem. Phys. **97**, 8990 (1992).

[11] E. Biémont, J. E. Hansen, P. Quinet, and C. J. Zeippen, Astron. Astrophys. Suppl. Ser. **111**, 333 (1995).

[12] C. Morillon and J. Vergès, Phys. Scr. **12**, 145 (1975).

[13] F. Hassini, Z. Ben Ahmed, O. Robaux, J. Vergès, and J.-F. Wyart, J. Opt. Soc. Am. B **5**, 2060 (1988).

[14] W. H. King, *Isotope Shifts in Atomic Spectra* (Plenum Press, New York, 1984).

[15] B. Buchholz, H.-D. Kronfeldt, G. Müller, M. Voss, and R. Winkler, Z. Phys. A **288**, 247 (1978).

[16] J. P. Desclaux, Comput. Phys. Commun. **9**, 31 (1975).

[17] D. R. Beck, program RCI.

[18] S. M. O'Malley and D. R. Beck, Phys. Rev. A **54**, 3894 (1996).

[19] K. D. Dinov and D. R. Beck, Phys. Rev. A **52**, 2632 (1995).

[20] D. R. Beck and D. Datta, Phys. Rev. A **48**, 182 (1993).

Paper 2

Experimental Evidence that the $6s6p\ ^3P_J$ States of Cs^- are Shape Resonances.

M. Scheer, J. Thogersen, R.C. Bilodeau, C.A. Brodie, H.K. Haugen, H.H. Andersen, P. Kristensen, and T. Andersen.

Physical Review Letters **80**, 684-7 (1998).

Experimental Evidence that the $6s6p\ ^3P_J$ States of Cs^- Are Shape Resonances

M. Scheer, J. Thøgersen,* R. C. Bilodeau, C. A. Brodie, and H. K. Haugen†
Department of Physics and Astronomy, McMaster University, Hamilton, Ontario, L8S 4M1, Canada

H. H. Andersen, P. Kristensen, and T. Andersen
Institute of Physics and Astronomy, University of Aarhus, DK-8000 Aarhus C, Denmark
(Received 23 June 1997)

An experimental study of the previously unobserved and controversial Cs⁻ ($6s6p\ ^3P_J^o$) states has been conducted using a combination of infrared laser and storage ring experiments. This first application of photodetachment spectroscopy to the study of low-lying resonances in atomic negative ions has resulted in the observation of a narrow resonance structure, lying only 8.0(3) meV above the first detachment threshold of Cs⁻. The storage ring experiments suggest that all fine structure levels of the $6s6p$ configuration are unbound, thereby eliminating possibly the only serious candidate for a stable atomic negative ion with opposite parity bound states. [S0031-9007(97)05108-9]

PACS numbers: 32.80.Gc, 32.80.Dz

Atomic negative ions are a topic of considerable current interest [1], in part motivated by a number of practical implications. Negative ions play an important role in a variety of atomic and plasma phenomena, and in a more specialized context, they provide the basis of ultrasensitive atom and isotope detection through accelerator mass spectrometry (AMS) [2]. In a general context, the interest in negative ions stems from the fact that they are qualitatively different in their structure from neutral atoms and positive ions. To a large extent these differences are a result of the short range interactions between the extra electron and the atomic core; in a mean field treatment the electron is bound in the dipole potential that it induces in the atom. Negative ions therefore offer the unique opportunity to study short range potentials on an atomic scale, which are of fundamental importance to other fields such as nuclear physics. In contrast to a Coulomb potential, a short range potential cannot support an infinite number of bound states; in fact, most negative ions have only one. On the other hand, all negative ions possess many unstable excited states which are embedded as resonances in the energy continuum associated with an atom and a free electron. The extensive theoretical and experimental work on atomic negative ion resonances was recently reviewed by Buckman and Clark [3]. Resonances involving the atom in its ground state occur when the extra electron is trapped in a potential well resulting from the overlap of the attractive short range potential of the polarized atom and the repulsive centrifugal potential. Traditionally, these low-lying shape resonances have been investigated via electron-atom scattering or ion-atom collisions, but the study of very low-lying resonances has proven to be rather challenging with these techniques. Despite considerable efforts on various atomic ions the recently observed $Li^-(2s2p\ ^3P)$ resonance at 50(6) meV [4] is the lowest-lying feature previously reported. The present work therefore employs photodetachment spectroscopy which is new to the study of low-lying atomic shape resonances.

The cesium negative ion, which is the important example of a H^--like two-electron system with a polarizable core and strong relativistic effects, has been the subject of considerable investigation in the past, both experimental and theoretical. A diagram of the energy level structure of Cs⁻ and Cs, up to Cs($6p$), is given in Fig. 1. Two decades ago, laser-based experiments [5] of the Cs⁻ continuum just below the Cs($6p$) threshold

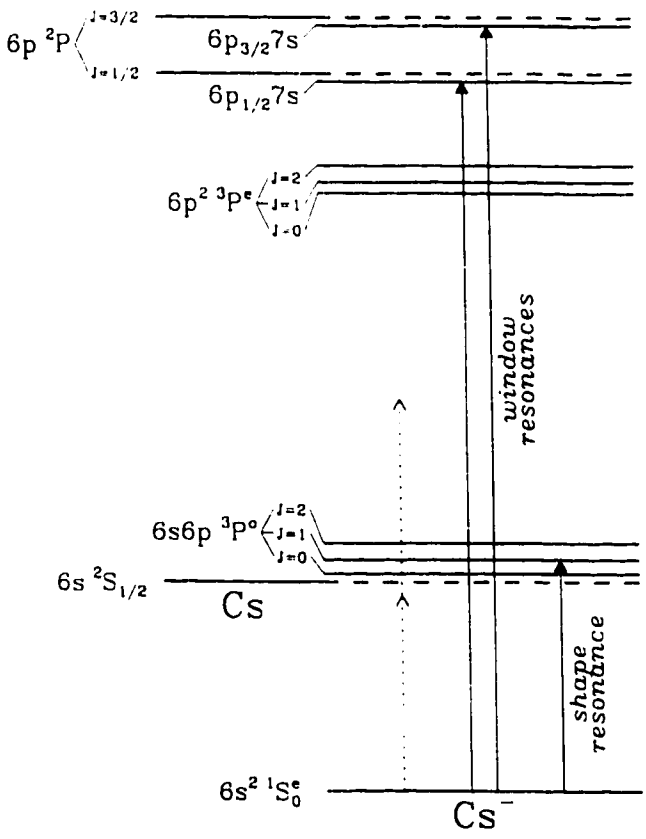

FIG. 1. Schematic energy level diagram of Cs⁻ and Cs. For clarity of presentation level splittings are not to scale.

 0031-9007/98/80(4)/684(4)$15.00

revealed a narrow window resonance. Recently, Greene [6] conducted an extensive theoretical study of Cs^-, in part reproducing the window feature. Also, multiphoton studies have incorporated the narrow window resonances in Cs^- and Rb^- [7]. The cesium negative ion has been much discussed in numerous theoretical studies as potentially the only known candidate for a stable atomic negative ion that possesses an *excited bound configuration of opposite parity to the ground state*. Initially, several calculations on $Cs^-(6s6p\ ^3P_J^o)$ indicated that the $^3P_J^o$ state might be slightly bound, by a maximum of a few tens of meV [6,8–10], although Fabrikant [8], and Krause and Berry [9] expressed that this might not hold true if their calculations were refined. More recently, a relativistic scattering calculation based on the Dirac R-matrix method by Thumm and Norcross predicted the $J = 0, 1, 2$ levels to be narrow shape resonances just above the Cs(6s) threshold [11]. This result contradicted earlier scattering calculations [12] which employed a semirelativistic Breit-Pauli R-matrix formalism, and which did not show any low energy resonance structure. This discrepancy was partially resolved in a subsequent theoretical study by Bartschat [13], in favor of the conclusions by Thumm and Norcross. This study compared the two different methods directly, but the earlier Breit-Pauli formalism was modified, in particular through the inclusion of a dielectronic core polarization term. The work reported in the present Letter is the first experimental investigation aimed at resolving this long-standing issue.

The experimental approach involved tunable infrared laser spectroscopy at McMaster University, and heavy ion storage ring experiments at Aarhus University using the ASTRID [14] storage ring. The experimental setup at McMaster is described in detail elsewhere [15,16]. A tunable laser source consisting of a Nd:YAG pumped dye laser and nonlinear optical conversion equipment provided nanosecond infrared pulses with energies of $\approx$0.5 mJ at 3 μm. In an ultrahigh vacuum chamber the infrared laser beam was crossed at 90° with a 10 keV Cs^- beam, which was extracted from a Cs sputter ion source. Photodetached neutral atoms were detected by a discrete dynode electron multiplier.

A series of careful experiments was conducted with tunable infrared laser light, either in a 1 + 1 (two-photon) detachment scheme, in search of a possibly bound $6s6p\ ^3P_1^o$ level, or aimed at observation of a resonant feature above threshold in the one-photon detachment spectrum. A resonant enhancement of the two-photon detachment yield due to a spin-forbidden $^1S_0^e \rightarrow {}^3P_1^o$ electric dipole transition would be expected in the 1 + 1 photon detachment regime. The laser-based experiment is only sensitive to the $J = 1$ level of $6s6p\ ^3P_J^o$. Greene [6] predicted binding energies of 32, 25 and 11 meV for the $J = 0, 1, 2$ levels, respectively, while Fabrikant [8], Krause and Berry [9], and Froese Fischer and Chen [10] determined the average binding energy for the $^3P_J^o$ term to be 27, 12, and 1 to 11 meV, respectively. In addition, Greene predicted an Einstein A coefficient for the $6s6p\ ^3P_1^o$ level of 77 s^{-1}, but other theoretical estimates indicate that the A coefficient would be substantially larger [17]. Since we have previously demonstrated [18] that we can readily observe signals for resonantly enhanced 1 + 1 transitions via magnetic dipole transitions with A coefficients of $\sim$1 s^{-1}, then a large signal, in the case of a bound excited level, would be expected in the present case.

We have performed a series of experiments in the near-threshold region of Cs^- without observing any indication of a bound $6s6p\ ^3P_1$ level. The experiments were carried out under a wide range of experimental conditions, utilizing a tightly focused laser beam or an unfocused beam in order to allow for a range of oscillator strengths and detachment cross sections. The expected experimental signals were modeled on a computer program. Both analog and digital data collection methods were utilized. In all, the first 100 meV below threshold were probed.

Subsequently, we conducted one-photon infrared laser detachment spectroscopy above the Cs(6s) threshold. We obtained good signals for the Wigner p-wave threshold and also explored the relative single photon detachment cross section to an energy of 75 meV above the photodetachment threshold. The results are shown in Fig. 2. A feature which represents an enhancement of $\approx$25% over the direct, p-wave photodetachment yield is seen centered at a photon energy of 479.6(3) meV, 8.0(3) meV above threshold, with a width of 5.0(5) meV (full width at half maximum) according to a Lorentzian fit. We attribute this relatively weak resonant feature to the $Cs^-(6s6p\ ^3P_1^o)$ level embedded in the continuum. A blowup of the resonant feature, with the photodetachment "background" subtracted, is shown in Fig. 3. Numerous checks were done in an attempt to verify the validity of this feature. In order to remove the effects of atmospheric absorption of the

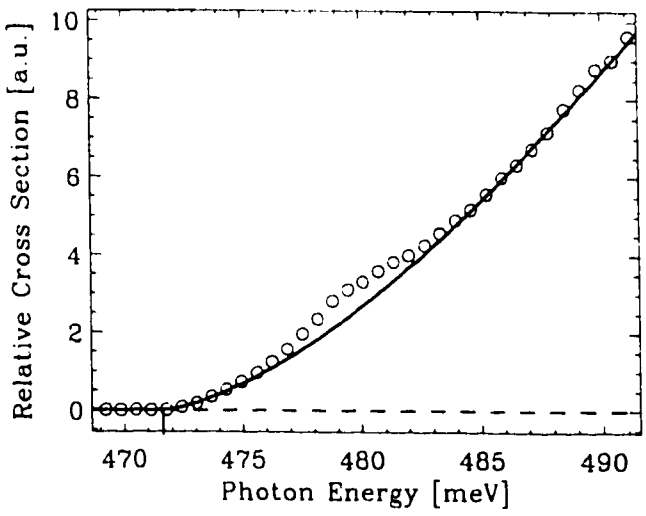

FIG. 2. Photodetachment yield versus laser wavelength. The solid line represents a fitted Wigner p-wave threshold.

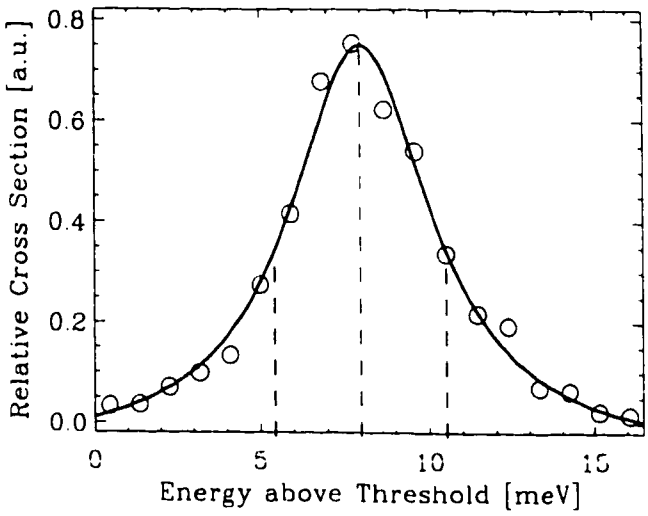

FIG. 3. Blowup of the one-photon detachment scan showing the resonant feature with the p-wave "background" subtracted. The result of a Lorentzian fit is indicated by the solid line.

infrared light the laser path was purged with dry nitrogen and the data normalized to the laser power in the interaction region. We do not believe that this results in any artifact in the final data for the following reasons: the absorption features are small and much narrower than the observed feature, they do not coincide with the proposed resonance, and variations in purge quality in different experiments have led to the same result. It is also possible that a molecular impurity ion, with a mass close to that of Cs^-, could lead to a false resonance, but the relative size of the feature was constant in measurements separated by a few months. Moreover, this is the only feature which we observe in the entire spectral region, including a 100 meV region below threshold where a (unstructured) very weak background was obtained. We consider it very unlikely that a single impurity-ion-based feature would manifest itself solely at this photon energy.

In addition, our infrared photodetachment data enable an accurate determination of the electron affinity (EA) of Cs. We obtain a final value of 471.64(6) meV. A somewhat more accurate value, 471.630(25) meV, which was determined by Lineberger and co-workers via photodetachment to Cs($6p$) using visible cw laser light, was only tabulated in the Hotop and Lineberger review [19] from 1985. Our tunable infrared laser work provides a second and entirely complementary measure of the EA of Cs with high accuracy.

The absence of a 1 + 1 resonant signal in our laser based studies, combined with the observation of a resonant feature in the single-photon detachment yield, which we attribute to the $6s6p\ ^3P_1^o$ level, is in excellent agreement with the theoretical work of Thumm and Norcross [11] and Bartschat [13]. These advanced theoretical works predict the resonant structure in the case of electron scattering on Cs, and seem to have achieved a high level of accuracy. Thumm and Norcross calculated the $J = 0, 1, 2$ levels to lie 1.78, 5.56, and 12.76 meV above threshold with widths of 0.42, 2.42, and 9.32 meV, respectively (Bartschat obtained very similar results), compared to our values for the $J = 1$ photodetachment resonance, 8 and 5 meV for position and width, respectively. Our increased width would appear to be qualitatively consistent with the increased energy above the Cs($6s$) threshold. The excellent agreement of theory [11,13] and the present experiment on the $J = 1$ resonance energy is even more convincing when presented with respect to the energy of the Cs^- ground state: 477.2 meV versus 479.6 meV, respectively. We do not yet have theoretical input on the expected magnitude of the feature due to an unbound $^3P_1^o$ level in the optical case, since the existing theoretical results apply to electron scattering. Crude extrapolations from the isoelectronic neutral Ba atom might suggest an order of magnitude of a few percent enhancement in the photodetachment yield.

Although we cannot probe $J = 0, 2$ in the laser-based experiments, the theoretical predictions on fine structure splittings would suggest that $J = 0$ is also unbound, based on our position for $J = 1$. Greene [6], Thumm and Norcross [11], and Bartschat [13] predict the $J = 0 - 1$ splitting to be 7, 3.78, and 3.33 meV (Breit-Pauli approach), respectively. In order to make an entirely separate check on the possibility of bound excited levels in Cs (especially $J = 0$), we conducted a series of storage ring experiments at the ASTRID facility in Aarhus. The Cs^- ions were produced in either of two different ways, which enhanced the probability of effectively populating a weakly bound Cs^- level. In one run, the ions were extracted directly from a cesium sputter (negative) ion source. Subsequently, in a separate run, Cs^+ ions were extracted from a positive ion source at a kinetic energy of 100 keV, and were charge exchanged in a K metal vapor cell to produce Cs^- ions, which were then injected into the storage ring. The Cs^- beam currents were a few nA. Neutral atoms stemming from either collisional or blackbody-radiation-induced detachment were detected at one corner of the storage ring. The measured 1.1 s lifetime of the Cs^- ground state was consistent with the expected collisional detachment rate. Blackbody-radiation-induced photodetachment on a short ms time scale would provide a sensitive measure of a weakly bound level, up to a binding $\approx$150 meV. A description of the blackbody-radiation effects on weakly bound negative ions can be found in Ref. [20]. We observed no signal associated with a weakly bound level, despite a sensitivity of $\approx 5{:}10^4$ or better [20]. The storage ring experiment has limitations, but offers a very useful double check. The most notable limitation in the present context is that the experiment is insensitive for binding energies less than $\approx$3 meV. Our calculations, based on Ref. [21] indicate that the Lorentz force generated during passage of the 90° bending magnets would destroy more weakly bound ions before they could be observed [14,20]. Hence our final conclusion that $J = 0$ is likely unbound

depends on the validity of the earlier fine structure calculations [11,13]. In contrast to the magnetic field stripping effect, our simulations predict no serious limitation due to an excessive blackbody detachment rate for very weak bindings since the Planck radiation flux drops off rapidly at long photon wavelengths—corresponding to an ionic binding of a few meV.

In summary, we have reported the first experimental evidence that the $J = 1$ level of the $Cs^-(6s6p\ ^3P_J^o)$ state is a shape resonance, rather than a bound state of opposite parity to the $Cs^-(6s^2\ ^1S_0^e)$ ground state. We have further obtained substantial evidence that the $J = 0$ and $J = 2$ levels are also unbound, although the conclusion for $J = 0$ hinges on earlier calculations of the $^3P_J^o$ fine structure. To this extent, Cs^- can be eliminated as possibly the only known good candidate for a stable atomic negative ion with a second bound state of opposite parity to the ground state [22], thereby resolving a long-standing controversy. With regards to future experimental work, the successful application of photodetachment spectroscopy to the study of low-lying shape resonances in the present work strongly suggests similar investigations in other atomic negative ion systems. For Cs^-, Thumm and Norcross [11] and Bartschat [13,23] have also predicted the existence of a $6p^2\ ^3P_J^e$ state embedded in the continuum, below $Cs(6p)$. A multiphoton experiment aimed at the first optical observation of these levels might proceed using Raman coupling via the window resonance, ideally using picosecond-duration optical pulses. We finally note that the cesium negative ion is forming the basis of a relatively new tracer in AMS [24], and that knowledge of its excited states is of practical importance.

We gratefully acknowledge the Natural Science and Engineering Research Council of Canada (NSERC) for support of the experimental work at McMaster University, and the National Research Council (SNF) and the Aarhus Center for Advanced Physics (ACAP) for support of the work in Aarhus. We especially wish to thank C. H. Greene, L. R. Kilius, A. E. Litherland, S. H. Vosko, and W. P. Wijesundera, who have been part of an (NSERC-based) initiative aimed at the study of Ba^- and Cs^-, for numerous helpful discussions. The contributions of Linas Kilius and Sy Vosko were greatly appreciated and they will be sorely missed. U. Thumm has also provided very helpful theoretical input during the course of this project.

*Present address: Department of Chemistry, University of Aarhus, DK-8000 Aarhus C, Denmark

†Also with the Department of Engineering, the Brockhouse Institute for Materials Research, and the Center for Electrophotonic Materials and Devices.

[1] D. R. Bates, Adv. At. Mol. Opt. Phys. **27**, 1 (1991); T. Andersen, Phys. Scr. **T34**, 23 (1991); S. J. Buckmann and C. W. Clark, Rev. Mod. Phys. **66**, 539 (1994); C. Blondel, Phys. Scr. **T58**, 31 (1995).

[2] A. E. Litherland, Annu. Rev. Nucl. Part. Sci. **30**, 437 (1980); W. Kutschera and M. Paul, Annu. Rev. Nucl. Part. Sci. **40**, 411 (1990).

[3] S. J. Buckman and C. W. Clark, Rev. Mod. Phys. **66**, 539 (1994).

[4] D. H. Lee, W. D. Brandon, D. Hanstorp, and D. J. Pegg, Phys. Rev. A **53**, R633 (1996).

[5] T. A. Patterson, H. Hotop, A. Kasdan, D. W. Norcross, and W. C. Lineberger, Phy. Rev. Lett. **32**, 189 (1974); J. Slater, F. H. Read, S. E. Novick, and W. C. Lineberger, Phys. Rev. A **17**, 201 (1978).

[6] C. H. Greene, Phys. Rev. A **42**, 1405 (1990).

[7] H. Stapelfeldt and H. K. Haugen, Phys. Rev. Lett. **69**, 2638 (1992); H. Stapelfeldt, P. Kristensen, U. Ljungblad, T. Andersen, and H. K. Haugen, Phys. Rev. A **50**,1618 (1994).

[8] I. I. Fabrikant, Opt. Spectrosc. **53**, 131 (1982) [Opt. Spektrosk. **53**, 223 (1982)].

[9] J. L. Krause and R. S. Berry, Comments At. Mol. Phys. **18**, 91 (1986).

[10] C. Froese Fischer and D. Chen, J. Mol. Struct. **199**, 61 (1989).

[11] U. Thumm and D. W. Norcross, Phys. Rev. Lett. **67**, 3495 (1991); Phys. Rev. A **45**, 6349 (1992); **47**, 305 (1993).

[12] N. S. Scott, K. Bartschat, P. G. Burke, O. Nagy, and W. B. Eissner, J. Phys. B **17**, 3755 (1984); P. G. Burke and J. F. B. Mitchell, J. Phys. B **6**, L161 (1973).

[13] K. Bartschat, J. Phys. B **26**, 3595 (1993).

[14] L. H. Andersen *et al.*, Phys. Lett. A **162**, 336 (1992).

[15] J. Thogersen, L. D. Steele, M. Scheer, C. A. Brodie, and H. K. Haugen, J. Phys. B **29**, 1323 (1996).

[16] M. Scheer, C. A. Brodie, R. C. Bilodeau, and H. K. Haugen (to be published).

[17] W. P. Wijesundera and A. E. Litherland (private communication).

[18] J. Thogersen, M. Scheer, L. D. Steele, H. K. Haugen, and W. P. Wijesundera, Phys. Rev. Lett. **76**, 2870 (1996).

[19] H. Hotop and W. C. Lineberger, J. Phys. Chem. Ref. Data **14**, 731 (1985).

[20] H. K. Haugen *et al.*, Phys. Rev. A **46**, R1 (1992).

[21] M.-J. Nadeau and A. E. Litherland, Nucl. Instrum. Methods Phys. Res., Sect. B **52**, 387 (1990); V. A. Oparin, R. N. Il'in, I. T. Serenkov, and E. S. Solov'ev, Sov. Phys. JETP **39**, 989 (1974) [Zh. Eksp. Teor. Fiz. **66**, 2008 (1974)].

[22] Theoretical studies of the negative ions of some lanthanides and actinides seem to indicate the possibility of opposite parity bound states in these complex systems; S. H. Vosko, J. B. Lagowski, I. L. Mayer, and J. A. Chevary, Phys. Rev. A **43**, 6389 (1991); D. Datta and D. R. Beck, Phys. Rev. A **50**, 1107 (1994); K. Dinov, D. R. Beck, and D. Datta, Phys. Rev. A **50**, 1144 (1994).

[23] K. Bartschat, A. R. Johnston, and P. D. Burrow, J. Phys. B **27**, L231 (1994).

[24] T. Lee, T.-L. Ku, H. L. Lu, and J.-C. Chen, Geochim. Cosmochim Acta **57**, 3493 (1993).

Paper 3

Negative Ion of Boron: An Experimental Study of the ^3P Ground State.

Michael Scheer, René C. Bilodeau, and Harold K. Haugen.

Physical Review Letters **80**, 2562-5 (1998).

Negative Ion of Boron: An Experimental Study of the ^3P Ground State

Michael Scheer, René C. Bilodeau, and Harold K. Haugen*

Department of Physics and Astronomy, McMaster University, Hamilton, Ontario L8S 4M1, Canada

(Received 15 October 1997)

An investigation of the B $(2p^2\,^3P_J) \rightarrow$ B$(2p\,^2P_J)$ photodetachment thresholds using a tunable infrared laser source has yielded a substantially improved value for the electron affinity of boron and the first experimental data on the fine structure of the ionic ground state. The $J = 0-1$ and $J = 1-2$ splittings are found to be 3.23(15) cm^{-1} and 5.18(15) cm^{-1}, respectively, and the electron affinity is determined to be 2256.12(20) cm^{-1} [(279.723(25) meV]. The present result for the electron affinity is the first to challenge the extensive and controversial theoretical studies of this system. [S0031-9007(98)05630-0]

PACS numbers: 32.80.Gc, 32.10.Fn, 32.10.Hq

Present day high-performance computers enable sophisticated *ab initio* calculations of increasingly complex systems with unprecedented precision. Within the realm of atomic physics, negative ions are currently a subject of intensive studies (for recent reviews see Ref. [1]). In general, the fundamental interest in negative ions is motivated by a number of features which are qualitatively different from neutral or positively charged systems; short range interactions lead to a finite number of bound states, and strong electron correlations give rise to correlation energies which are often larger than or comparable to the binding energies in these systems. New experimental techniques now allow the determination of binding energies, fine structure, and excited states in a number of negative ion systems with very high accuracy [2]. The interplay of high-resolution experiments on negative ions and state-of-the-art theoretical calculations provides an important platform for advances in atomic physics. Finally, in terms of applications, negative ions play a role in a variety of atomic and plasma phenomena, as well as in some advanced experimental techniques (e.g., accelerator mass spectrometry).

The negative ions of the light elements, hydrogen through fluorine, have been studied extensively. The electron affinities (EA) of H, C, O, and F were measured via tunable laser threshold photodetachment leaving the neutral atom in its ground state [3–6], whereas the binding energies of Li^- [7,8] and the metastable He^- [9] and Be^- [10] ions have been determined through laser photodetachment involving an excited state of the atom and state-selective detection schemes. Accuracies of experimental EA's for these seven elements range from 0.3 meV (C^-) to 0.001 meV (O^-). In strong contrast, the EA of boron still relies on an early laser photodetached electron spectrum recorded by Feigerle *et al.* [11] which resulted in a value of 277(10) meV (after a subsequent recalibration [5]). Various approaches to the *ab initio* calculation of electron affinities of the light elements have been attempted in recent years [12,13], but even these small systems remain challenging as electron correlations play a dominant role. This is particularly true for boron which forms the most weakly bound stable ion among the light elements. Of the numerous theoretical studies of the EA of boron [12–16], three recent works were aiming at accuracies better than 10 meV. Noro *et al.* [13] obtained an EA of 278 meV as the result of a large-basis-set multireference singly and doubly excited configuration-interaction calculation. Large-scale finite element multiconfiguration Hartree-Fock (MCHF) calculations, which do not suffer from basis set limitations, have been performed by two groups, Sundholm and Olsen [14], and Froese Fischer *et al.* [15]. They report EA's of 268.6(17) and 273.2(2) meV, respectively, as the result of an initial valence correlation MCHF calculation that neglects core polarization effects. Sundholm and Olsen estimate core-valence correlations to lower the EA to 267.8(20) meV, whereas Froese Fischer *et al.* predict the EA to increase to 279.5(20) meV through the inclusion of core-valence and core-core correlations (the latter via core rearrangement). However, the experimental EA of 277(10) meV [11] agrees with all of the above values within uncertainties; hence the fundamental question as to the effect and strength of core-valence and core-core correlations in B^- remains open and controversial. The work reported in this Letter is the first experimental investigation aimed at resolving this important issue, and furthermore provides the first experimental values for the fine structure splittings of the $B^-(2p^2\,^3P_J)$ ground state.

An energy level diagram of B^- in the vicinity of the ground and first excited states of boron is shown in Fig. 1. The $B^-(2p^2\,^3P_J)$ ground state is expected to have fine structure levels with splittings estimated from isoelectronic extrapolations of 4(1) cm^{-1} for $J = 0-1$ and 9(1) cm^{-1} for $J = 0-2$ [17]. The ^1D and ^1S terms of $B^-(2p^2)$ are likely unbound; a recent communication on resonance structures in collisionally detached electron spectra of B^- tentatively identified the ^1D term with a resonance located 104(8) meV above the ground state of boron [18]. The latter is a $2p^2P_J$ state with a fine structure $J = 1/2-3/2$ splitting of 15.254 cm^{-1}

 0031-9007/98/80(12)/2562(4)$15.00

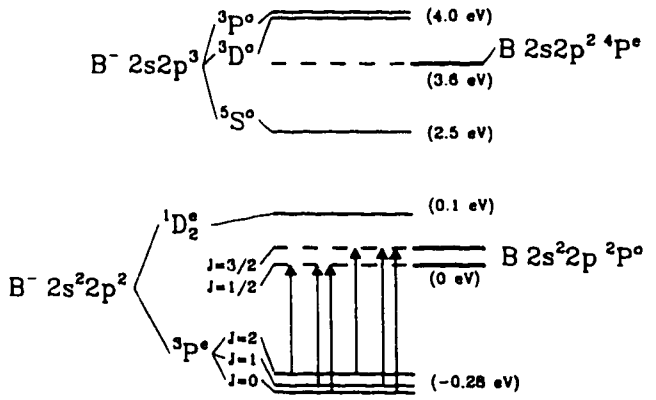

FIG. 1. Schematic energy level diagram of B^- and B. Arrows indicate photodetachment thresholds in order of increasing photon energy. For clarity of presentation, level spacings are not shown to scale. Parity labels on term symbols as shown here are omitted in the text.

[19]. The core excited $2s2p^2$ configuration gives rise to the first excited state of boron, a ^4P_J term which is located 3579(2) meV above the ^2P_J atomic ground state as derived on the basis of isoelectronic extrapolation [20]; as yet no intercombination lines between the doublet and quartet systems have been observed. The EA of the first excited state, i.e., the binding energy of the metastable $2s2p^3\,^5S_2$ negative ion level, was the subject of a recent theoretical study and predicted to be 1072(2) meV [21]. One experimental [22] and two theoretical [23,24] studies of the B^- photodetachment cross section in the vicinity of the ^4P threshold find the ^3P and ^3D terms of the $2s2p^3$ configuration quasibound and responsible for a resonance structure in that energy region. An accurate determination of the ^4P threshold would still be possible if state-selective detection (as in Li^- [7]) and tunable light around 320 nm were employed, and would, in fact, seem to be more convenient than the experimentally challenging infrared photodetachment around the ^2P threshold. Unfortunately, the uncertainty in the ^4P energy would prevent a determination of the EA of boron to a high accuracy. Therefore, our experimental approach involves tunable infrared laser spectroscopy in the 3.8 to 4.5 μm region.

The experimental setup is described in detail elsewhere [25]. Nanosecond laser pulses in the 920–950 nm range were produced with a dye laser, pumped by the second harmonic of a 10 Hz Q-switched Nd:YAG laser. Raman scattering in a high pressure hydrogen cell was employed to convert the dye laser output into tunable infrared radiation via second Stokes generation, with a measured Raman shift of 4155.20(2) cm^{-1}. The infrared pulse energies were $\approx$120 μJ, and the bandwidth was $\approx$0.1 cm^{-1}. Calibrations of the dye laser setup were routinely performed using an optogalvanic cell filled with argon. Second Stokes photon energies were also calibrated directly against well known transitions in N_2O using an absorption cell. A Cs sputter ion source with a cathode prepared from ^{10}B powder provided a 17 keV B^- beam. The ion beam and infrared laser beam were crossed at 90° within an ultrahigh vacuum chamber. At this stage the $^{10}B^-$ current was $\approx$60 nA. Neutral atoms resulting from photodetachment were detected with a discrete dynode electron multiplier.

Numerous infrared laser scans of the ^2P threshold region have been conducted. Figure 2 shows the sum of several scans over the region of 2240–2280 cm^{-1}. Approximately 5000 laser shots were utilized per wave number. Five nested thresholds are evident in Fig. 2, corresponding to the following transitions (from low to high energy): $^3P_2 \rightarrow {}^2P_{1/2}$, $^3P_1 \rightarrow {}^2P_{1/2}$, $^3P_0 \rightarrow {}^2P_{1/2}$, $^3P_2 \rightarrow {}^2P_{3/2}$, and $^3P_1 \rightarrow {}^2P_{3/2}$. It was possible to fit Wigner s-wave thresholds very accurately to the data, and the resulting threshold energies are summarized in Table I. The quoted uncertainties on the values are largely associated with the fits to the nested thresholds but also allow for systematic errors in the calibration and potential Doppler shifts. The sixth and last threshold ($^3P_0 \rightarrow {}^2P_{3/2}$) could not be resolved due to a weak transition strength and the noise in the other detachment signals. Thus, the fit was extrapolated beyond the sixth threshold using its calculated transition strength [26]. The $^3P_0 \rightarrow {}^2P_{1/2}$ threshold provides the EA of B and yields 2256.12(20) cm^{-1} or 279.723(25) meV (with 8.065 541 cm^{-1}/meV [27]). The well-known fine structure splitting of the atomic ground state can be obtained from the difference of the threshold values for the $^3P_2 \rightarrow {}^2P_{1/2,3/2}$ as well as $^3P_1 \rightarrow {}^2P_{1/2,3/2}$ transitions. This leads to values of 15.19(15) and 15.24(20) cm^{-1}, respectively, which are in excellent agreement with the accepted value of 15.254 cm^{-1} [19]. The fine structure splittings of the ion are obtained from the first three thresholds ($^3P_J \rightarrow {}^2P_{1/2}$): 3.23(15) cm^{-1} and 5.18(15) cm^{-1}, respectively, for $J = 0$–1 and $J = 1$–2 [and 8.41(20) cm^{-1} for $J = 0$–2]. A second determination of the $J = 1$–2 splitting of 5.23(20) cm^{-1} is provided by the next two thresholds ($^3P_{2,1} \rightarrow {}^2P_{3/2}$). The respective magnitudes of our threshold signals are in good agreement with theory [26], assuming a statistical population of the ionic levels. The calculated values for the relative strengths of the transitions are shown in Table I, together with the experimental values. The relative photodetachment cross section further above threshold was investigated by scanning the laser over the full tuning range of the dye used (LDS 925). The result of this scan, after correction for variations in the infrared pulse energy, is shown in the inset of Fig. 2. A single Wigner s wave has been fitted to the data (dashed line) as well as an s wave including the leading correction term to the Wigner law (solid line), as derived by Farley [28] on the basis of the zero-core-contribution (ZCC) model of photodetachment [29]. The latter curve fits the data well; hence, the ZCC model seems to be applicable here. In contrast, a limitation of the ZCC model was found in the case of Al^- photodetachment [30,31].

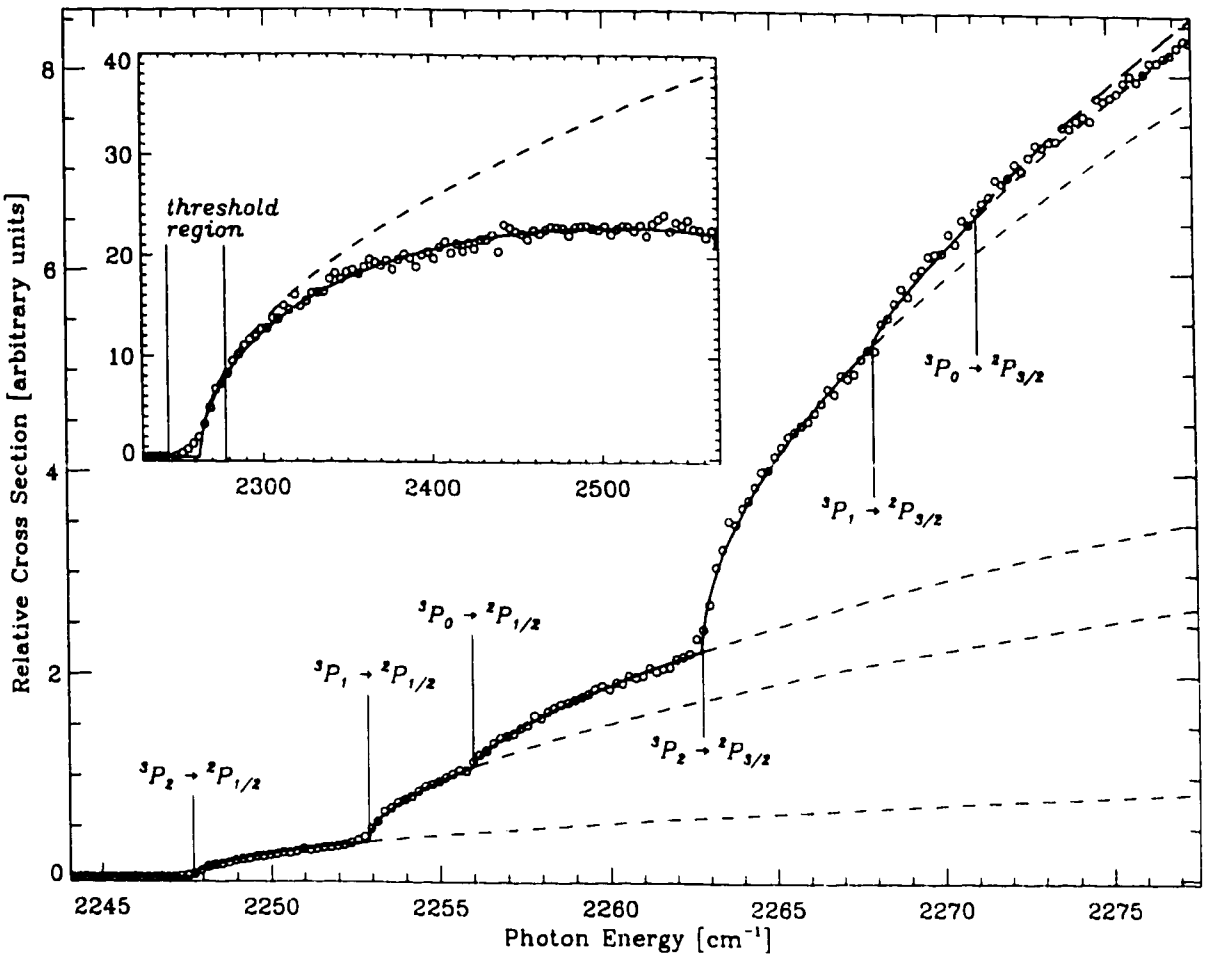

FIG. 2. Photodetachment yield versus laser wavelength. The overall result of a Wigner s-wave fit is indicated by the solid line (and extrapolated with long dashes). Individual thresholds are extrapolated with dashed lines. Inset: Relative photodetachment cross section up to 320 cm^{-1}(15%) above threshold. The dashed line represents a fitted Wigner s wave and the solid line an s wave with leading correction. These two lines define the upper and lower limits of s-wave thresholds within the ZCC model.

The present result for the electron affinity of boron [279.723(25) meV] is in agreement with the earlier measurement of Feigerle *et al.* [11,17] of 277(10) meV, in excellent agreement with the very recent theoretical result of Froese Fischer *et al.* [15] who obtained 279.5(20) meV, but in definite disagreement with the theoretical result of 267.8(20) meV obtained by Sundholm and Olsen [14]. Both theoretical works employ iterations of systematic MCHF calculations with orbital sets of increasing size. Thus, for a given model they are able to obtain the EA as the series limit with an uncertainty due to the necessary extrapolation. But even with an inactive $1s^2$ shell (i.e., valence correlation only) a complete active space calculation cannot be sustained to the limit, and some restrictions to the number of active orbitals need to be applied. This problem was handled differently by Sundholm and Olsen, and Froese Fischer *et al.* which seems to be responsible for their different results at this level, 268.6(17) and 273.2(2) meV, respectively. The choice of model restrictions becomes even more important if core polarizations are included through excitations of one of the $1s$ electrons. This was demonstrated by Froese Fischer *et al.* who treated core polarizations with two slightly different models, resulting in EA's of 273.1 and 279.5 meV, respectively (after a relativistic correction of -1.1 meV). Froese Fischer *et al.* consider the second core polarization model which increased the EA by 6.3 meV the more accurate one as it included core-valence correlation to a higher degree and even some core-core correlation via core rearrangement. Nevertheless, they estimated the uncertainty on their final EA value to be 2 meV, mainly due to the

TABLE I. Results of the s-wave fits to the data.

Transition	Threshold Energy [cm^{-1}]	Relative strength Measured	Calculated
$^3P_2 \rightarrow {}^2P_{1/2}$	2247.71(15)	4.0(4)	5
$^3P_1 \rightarrow {}^2P_{1/2}$	2252.89(15)	8.6(6)	9
$^3P_0 \rightarrow {}^2P_{1/2}$	2256.12(20)	4.2(4)	4
$^3P_2 \rightarrow {}^2P_{3/2}$	2262.90(15)	27(3)	25
$^3P_1 \rightarrow {}^2P_{3/2}$	2268.13(25)	8(2)	9
$^3P_0 \rightarrow {}^2P_{3/2}$	...	...	2

uncertainty associated with the choice of a particular model. Sundholm and Olsen used yet another core polarization model which lowered the EA by 0.8 meV. It should be noted that the calculated EA's above represent weighted averages over the levels of each term and have to be reduced by 0.56 meV to give the EA of $^3P_0$ relative to $^2P_{1/2}$ (which would be the conventional defi-nition for the EA of B). The final EA of Froese Fischer *et al.* would then be 279(2) meV, a value that is only 0.7 meV lower than our experimental result. Earlier values for the fine structure splittings of B^-, 4(1) and 9(1) cm^{-1} for $J = 0-1$ and $J = 0-2$, respectively, which were based on isoelectronic extrapolations [17], are valid within quoted uncertainties if compared with our experimental values [3.23(15) and 8.41(20) cm^{-1}, respectively]. Unfortunately, Froese Fischer *et al.* perform a full Breit-Pauli calculation of the fine structure only in the context of their valence calculation. This calculation was later refined [32] yielding $B^-(^3P_J)$ splittings of 2.92 and 7.79 cm^{-1} for $J = 0-1$ and $J = 0-2$, respectively. These values are too small in comparison with experiment, but they are expected to increase in a Breit-Pauli calculation that includes core-valence correlations [32]. It is hoped that the present results will stimulate renewed theoretical interest in B^-.

In summary, we have obtained the first experimental values for the fine structure of the $B^-(^3P)$ ground state and have determined the electron affinity of boron with a 400-fold increase in accuracy over the previous experimental value. The new EA is in very good agreement with the most recent calculation [15] and thereby confirms the importance of core-valence and core-core correlation for the accurate treatment of this six-electron system.

We gratefully acknowledge the Natural Science and Engineering Research Council of Canada (NSERC) for support of this work.

*Also with the Department of Engineering Physics, the Brockhouse Institute for Materials Research, and the Center for Electrophotonic Materials and Devices.

[1] D.R. Bates, Adv. At. Mol. Opt. Phys. **27**, 1 (1991); T. Andersen, Phys. Scr. **T34**, 23 (1991); S.J. Buckmann and C.W. Clark, Rev. Mod. Phys. **66**, 539 (1994); C. Blondel, Phys. Scr. **T58**, 31 (1995).

[2] P. Kristensen, C.A. Brodie, U.V. Pedersen, V.V. Petrunin, and T. Andersen, Phys. Rev. Lett. **78**, 2329 (1997); J. Thøgersen, M. Scheer, L.D. Steele, H.K. Haugen, and W.P. Wijesundera, Phys. Rev. Lett. **76**, 2870 (1996); V.V. Petrunin, J.D. Voldstad, P. Balling, P. Kristensen, T. Andersen, and H.K. Haugen, Phys. Rev. Lett. **75**, 1911 (1995); P. Kristensen, H. Stapelfeldt, P. Balling, T. Andersen, and H.K. Haugen, Phys. Rev. Lett. **71**, 3435 (1993).

[3] K.R. Lykke, K.K. Murray, and W.C. Lineberger, Phys. Rev. A **43**, 6104 (1991).

[4] D. Feldmann, Chem. Phys. Lett. **47**, 338 (1977).

[5] D.M. Neumark, K.R. Lykke, T. Andersen, and W.C. Lineberger, Phys. Rev. A **32**, 1890 (1985).

[6] C. Blondel, P. Cacciani, C. Delsart, and R. Trainham, Phys. Rev. A **40**, 3698 (1989).

[7] J. Dellwo, Y. Liu, D.J. Pegg, and G.D. Alton, Phys. Rev. A **45**, 1544 (1992).

[8] G. Haeffler, D. Hanstorp, I. Kiyan, A.E. Klingmuller, and U. Ljungblad, Phys. Rev. A **53**, 4127 (1996).

[9] P. Kristensen, U.V. Pedersen, V.V. Petrunin, T. Andersen, and K.T. Chung, Phys. Rev. A **55**, 978 (1997).

[10] P. Kristensen, V.V. Petrunin, H.H. Andersen, and T. Andersen, Phys. Rev. A **52**, R2508 (1995).

[11] C.S. Feigerle, R.R. Corderman, and W.C. Lineberger, J. Chem. Phys. **74**, 1513 (1981).

[12] K. Raghavachari, J. Chem. Phys. **82**, 4142 (1985); J.J. Novoa, F. Mota, and F. Arnau, J. Phys. Chem. **95**, 3096 (1991); R.A. Kendall, T.H. Dunning, Jr., and R.J. Harrison, J. Chem. Phys. **96**, 6796 (1992).

[13] T. Noro, M. Yoshimine, M. Sekiya, and F. Sasaki, Phys. Rev. Lett. **66**, 1157 (1991).

[14] D. Sundholm and J. Olsen, Chem. Phys. Lett. **171**, 53 (1990).

[15] C. Froese Fischer, A. Ynnerman, and G. Gaigalas, Phys. Rev. A **51**, 4611 (1995).

[16] W.P. Wijesundera, Phys. Rev. A **55**, 1785 (1997); E. Eliav, Y. Ishikawa, P. Pyykkö, and U. Kaldor, Phys. Rev. A **56**, 4532 (1997).

[17] H. Hotop and W.C. Lineberger, J. Phys. Chem. Ref. Data **14**, 731 (1985).

[18] D.H. Lee, W.D. Brandon, D. Hanstorp, and D.J. Pegg, Phys. Rev. A **53**, R633 (1996).

[19] G.A. Odintzova and A.R. Striganov, J. Phys. Chem. Ref. Data **8**, 63 (1979).

[20] B. Edlén, H.P. Palenius, K. Bockasten, R. Hallin, and J. Bromander, Sol. Phys. **9**, 432 (1969).

[21] C. Froese Fischer and G. Gaigalas, J. Phys. B **29**, 1169 (1996).

[22] P. Kristensen, H.H. Andersen, P. Balling, L.D. Steele, and T. Andersen, Phys. Rev. A **52**, 2847 (1995).

[23] C.A. Ramsbottom and K.L. Bell, J. Phys. B **28**, 4501 (1995).

[24] G.Y. Kaskenock and V.K. Ivanov, J. Phys. B (to be published).

[25] J. Thøgersen, L.D. Steele, M. Scheer, C.A. Brodie, and H.K. Haugen, J. Phys. B **29**, 1323 (1996); M. Scheer, C.A. Brodie, R.C. Bilodeau, and H.K. Haugen (to be published).

[26] P.C. Engelking and W.C. Lineberger, Phys. Rev. A **19**, 149 (1979).

[27] E.R. Cohen and B.N. Taylor, Rev. Mod. Phys. **59**, 1121 (1987).

[28] J.W. Farley, Phys. Rev. A **40**, 6286 (1989).

[29] R.M. Stehman and S.B. Woo, Phys. Rev. A **20**, 281 (1979).

[30] D. Calabrese, A.M. Covington, J.S. Thompson, R.W. Marawar, and J.W. Farley, Phys. Rev. A **54**, 2797 (1996).

[31] M. Scheer, R.C. Bilodeau, J. Thøgersen, and H.K. Haugen, Phys. Rev. A **57**, R1493 (1998).

[32] C. Froese Fischer (private communication).

Paper 4

Threshold photodetachment of Al^-: Electron affinity and fine structure.

Michael Scheer, René C. Bilodeau, Jan Thøgersen, and Harold K. Haugen.

Physical Review A **57**, R1193-6 (1998).

Threshold photodetachment of Al^-: Electron affinity and fine structure

Michael Scheer, René C. Bilodeau, Jan Thøgersen,* and Harold K. Haugen†
Department of Physics and Astronomy, McMaster University, Hamilton, Ontario, Canada L8S 4M1
(Received 14 July 1997)

Tunable infrared laser spectroscopy of $Al^-(3p^2\ ^3P_J)$ has yielded an improved value for the electron affinity of aluminum and experimental data on the previously unobserved fine structure of the ionic ground state. The electron affinity is determined to be 3491.0(4) cm^{-1} [432.83(5) meV], and the $J=0$-1 and $J=1$-2 splittings are found to be 22.7(3) and 45.7(2) cm^{-1}, respectively. The result for the electron affinity is in substantial disagreement with a very recent experimental investigation. Our work also indicates that isoelectronic extrapolations for the ionic fine structure were accurate within uncertainties, and is in good agreement with recent calculations of the electron affinity. [S1050-2947(97)50512-9]

PACS number(s): 32.10.Hq, 32.80.Gc, 32.10.Fn

The study of atomic negative ions continues to be an active area of investigation [1] and many improvements in the knowledge of electron affinities and ionic fine structure have been obtained since the 1985 review of Hotop and Lineberger [2]. In part, the interest in atomic negative ions stems from the qualitatively different features resulting from the short range potential, and is due to the theoretical challenges posed by the relativistic and strong electron correlation effects. Nevertheless, negative ions are of practical interest as well, including in the ultrasensitive detection of atoms and isotopes through accelerator mass spectrometry [3]. The negative ion of aluminum has been the subject of substantial experimental and theoretical work. Utilizing laser photodetachment electron spectrometry, Feigerle *et al.* [4] measured the electron affinity (EA) of Al to be 442(10) meV, and found the $Al^-(^1D_2)$ level to lie 332(10) meV above ground-state Al^-, with a binding energy of 110(10) meV. The latter value for the $^1D_2$ level agreed with the result of electric-field dissociation by Oparin *et al.* [5], where a binding energy of $\approx$95 meV was obtained. As a result of subsequent refined calibrations [6], an improved value for the EA of Ref. [4] was suggested to be 441(10) meV [2]. Recently, Calabrese *et al.* [7] measured the electron affinity of Al to be 440.94(+0.66/−0.48) meV by utilizing a tunable F-center laser and a coaxial ion-laser beam apparatus. Although they were unable to investigate the actual threshold region and the associated fine structure, they compensated for lack of data in this region via extrapolating from higher photon energy data. In the past few years, calculations have been reported by Arnau *et al.* [8], who used a configuration-interaction (CI) method with pseudopotentials, Woon and Dunning [9], who employed a CI method with correlation-consistent basis sets, and Wijesundera [10], who utilized a multiconfiguration Dirac-Fock method. They obtained values of 450 meV [8], 437 meV [9], and 433 meV [10], respectively. The present Rapid Communication reports an accurate experimental determination of the electron affinity of aluminum. In addition, the fine-structure splittings of the $Al^-(3p^2\ ^3P_J)$ term have been measured, to our knowledge, for the first time.

An energy-level diagram of Al^- and the ground state of Al is shown in Fig. 1. The $Al^-(3p^2\ ^3P_J)$ ground state is expected to have fine-structure levels with splittings estimated from isoelectronic extrapolations, of 26(3) cm^{-1} for $J=0$-1 and 76(7) cm^{-1} for $J=0$-2 [2]. The ground state of Al is a $3p\ ^2P_J$ state with a fine-structure $J=1/2$-3/2 splitting of 112.061 cm^{-1} [11]. Our experimental approach to the determination of the EA of aluminum involves tunable infrared laser spectroscopy and keV-energy ion-beam technology. Details of the apparatus are described elsewhere [12,13]. Nanosecond-duration laser pulses in the 820–880-nm range were generated using a dye laser, pumped by the second harmonic of a 10-Hz Q-switched Nd:YAG (neodymium-doped yttrium aluminum garnet) laser. The dye laser output was converted into tunable infrared radiation via second Stokes generation using stimulated Raman scattering in a high-pressure hydrogen cell, with a measured Raman shift of 4155.20(2)cm^{-1}. The infrared light had a bandwidth of

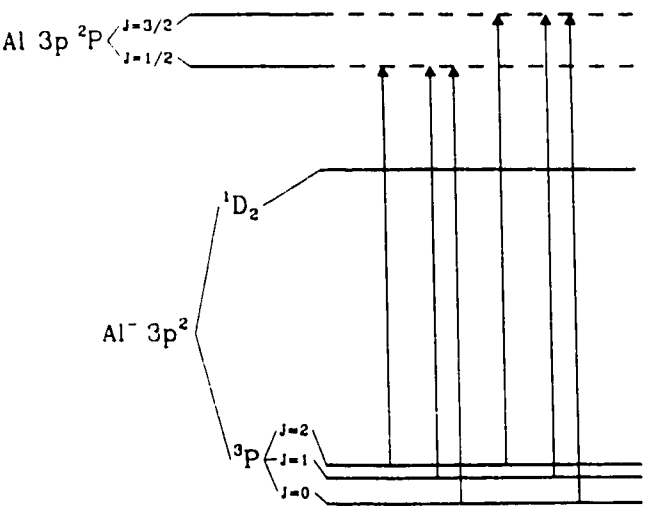

FIG. 1. Schematic energy-level diagram of Al^- and Al. Arrows indicate photodetachment thresholds in order of increasing photon energy. For clarity of presentation, fine-structure splittings are not shown to scale.

*Present address: Department of Chemistry, University of Aarhus, DK-8000 Aarhus C, Denmark.

†Also with the Department of Engineering Physics, the Brockhouse Institute for Materials Research, and the Center for Electrophotonic Materials and Devices.

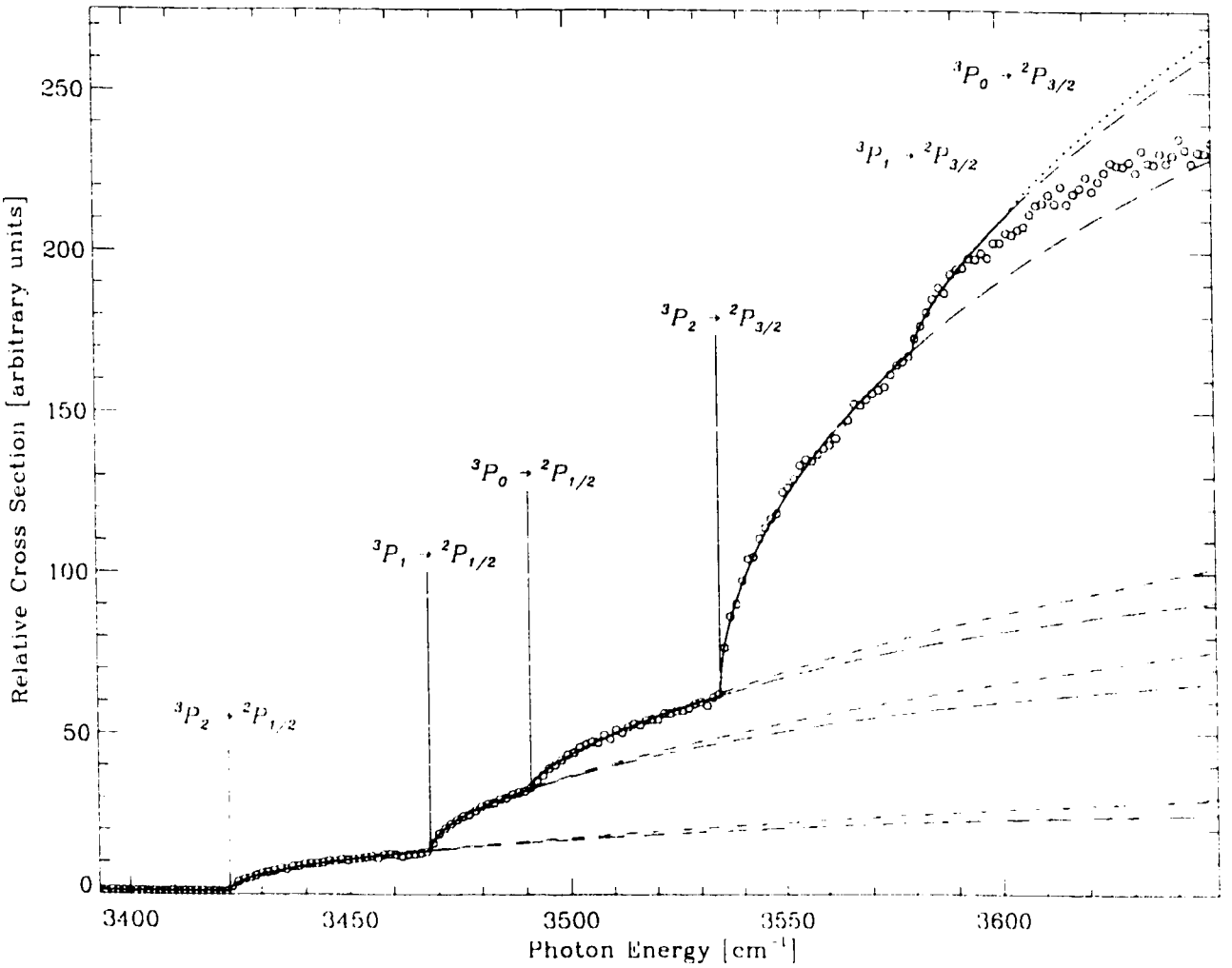

FIG. 2. Photodetachment yield versus laser wavelength. The overall result of a Wigner s-wave fit including the leading correction term is indicated by the solid line (and extrapolated with a dotted line). Individual thresholds are extrapolated with dashed lines: short dashes for a Wigner s wave (first three thresholds only), and long dashes for a Wigner s wave with leading correction. These two lines define the upper and lower limits of s wave thresholds within the ZCC model.

$\approx 0.1\ \text{cm}^{-1}$ and pulse energies were ≈ 0.5 mJ at 3 μm. A 16-keV Al^- beam was extracted from a Cs sputter ion source. Ultrapure aluminum cathodes were utilized in order to greatly minimize the potential contamination from prolific Si^- impurity beams, although our mass resolution discriminates quite effectively against mass 28 at mass 27. The beam was then magnetically analyzed and deflected 30° into an ultrahigh-vacuum chamber. There it was further charge-state analyzed in an electric field before being crossed at 90° with a collimated infrared laser beam. The Al^- current at this stage was typically several nA. The charge states created in the interaction region were analyzed by a second set of electric-field deflection plates. The photodetached neutral atoms impinged on a discrete dynode electron multiplier for analog data acquisition via a gated integrator and boxcar averager. Calibrations of the dye laser setup were routinely performed using an optogalvanic cell, but rigorous comparisons of the wavelength of the second Stokes generated light with known ionic energy intervals have also been performed, including in the cases of Te^- [14] and Cs^- [2]. Various tests indicate that the second Stokes wavelength calibration is reliable to at least $0.2\ \text{cm}^{-1}$.

We have conducted numerous infrared laser scans of the threshold region for Al^- photodetachment. The sum of several scans over the region of 3400–3650 cm^{-1} is shown in Fig. 2. The data correspond to approximately 1200 laser shots per wave number. Five nested thresholds are seen in the figure, corresponding to the following transitions (from low to high energy): $^3P_2 \rightarrow {}^2P_{1/2}$, $^3P_1 \rightarrow {}^2P_{1/2}$, $^3P_0 \rightarrow {}^2P_{1/2}$, $^3P_2 \rightarrow {}^2P_{3/2}$, and $^3P_1 \rightarrow {}^2P_{3/2}$. Wigner s-wave thresholds could be fitted very accurately to the data and the resulting threshold energies are summarized in Table I. The same threshold energies but a slightly closer fit to the data above

TABLE I. Results of the s-wave fits to the data.

Transition	Threshold Energy (cm^{-1})	Relative strength Measured	Calculated
$^3P_2 \rightarrow {}^2P_{1/2}$	3422.6(2)	5.0(3)	5
$^3P_1 \rightarrow {}^2P_{1/2}$	3468.3(2)	8.5(7)	9
$^3P_0 \rightarrow {}^2P_{1/2}$	3491.0(4)	4.8(9)	4
$^3P_2 \rightarrow {}^2P_{3/2}$	3534.8(2)	29(6)	25
$^3P_1 \rightarrow {}^2P_{3/2}$	3579.8(8)	8(2)	9
$^3P_0 \rightarrow {}^2P_{3/2}$			2

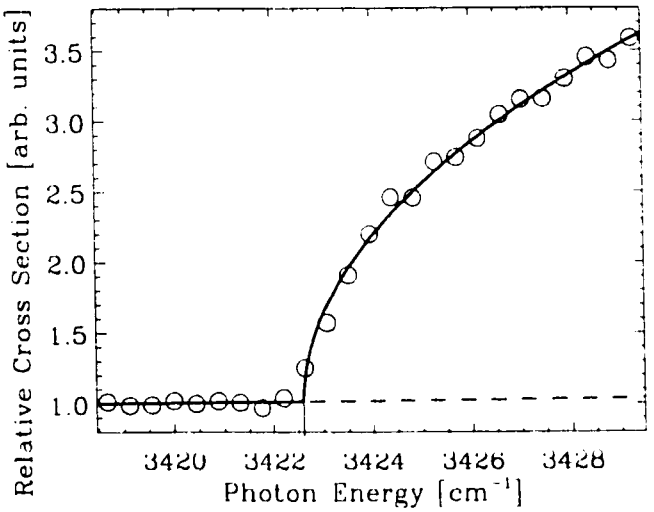

FIG. 3. High-resolution scan of the $^3P_2 \rightarrow {}^2P_{1/2}$ threshold region. The solid line represents a fitted s wave.

threshold were obtained by including in the fitting routine the leading correction term to the Wigner law, as derived by Farley [15] on the basis of the zero-core-contribution (ZCC) model of photodetachment [16]. The result of this fit is indicated by the solid line in Fig. 2. The sixth and last threshold ($^3P_0 \rightarrow {}^2P_{3/2}$) could not be resolved due to a weak transition strength combined with the fact that it appears on top of the other detachment signals. The fit to the data was therefore extrapolated beyond the sixth threshold (dotted line in Fig. 2) using its calculated transition strength [17] (see below). The increasing deviation between the fit and the data in this region seems to indicate a limitation of the ZCC model, which was also observed and discussed by Calabrese *et al.* [7] (it should be noted, however, that some equations in Ref. [7] contain typographical errors). The first three thresholds were also scanned at a very slow rate of 8000 laser shots per wave number in order to improve the accuracy of the fitted threshold values. As an example, the region of the first threshold is shown in Fig. 3, which also demonstrates the small but measureable signal resulting from photodetachment of the weakly populated $Al^-(^1D_2)$ level. The EA of Al is found from the $^3P_0 \rightarrow {}^2P_{1/2}$ threshold, and is determined to be 3491.0(4)cm^{-1} or 432.83(5) meV (using 8.065 541 0 cm^{-1}/meV [11]). The well-known fine-structure splitting of the Al ground state can be extracted from the difference of the thresholds for the $^3P_2 \rightarrow {}^2P_{1/2,3/2}$ transitions as well as $^3P_1 \rightarrow {}^2P_{1/2,3/2}$. This yields experimental values of 112.2(3) and 111.5(8) cm^{-1}, respectively, which are in excellent agreement with the tabulated value of 112.061 cm^{-1} [11]. The first three thresholds ($^3P_J \rightarrow {}^2P_{1/2}$) provide values of the fine-structure splittings of the ion: 22.7(3) cm^{-1} and 45.7(2) cm^{-1}, respectively, for $J=0$-1 and $J=1$-2 [and 68.4(3) cm^{-1} for $J=0$-2]. The next two thresholds ($^3P_{2,1} \rightarrow {}^2P_{3/2}$) enable a second determination of the $J=1$-2 splitting of 45.0(8) cm^{-1}. The quoted uncertainties of the values are largely associated with the fits to the nested thresholds. The respective magnitudes of our threshold signals are in good agreement with theory [17], assuming a statistical population of the ionic levels. The calculated values for the relative strengths of the transitions are shown in Table I, together with the experimental values. The errors in the experimental values account for the fact that the two different s-wave fits give slightly different values for the relative strengths of the thresholds.

Our experimental result [432.83(5) meV] for the electron affinity of Al is in agreement with the earlier measurement of Feigerle *et al.* [4,2] of 441(10) meV, but in definite disagreement with the very recent result of Calabrese *et al.* [7], who obtained 440.94(+0.66/−0.48) meV. The photodetachment data of Ref. [7] have a signal-to-noise ratio of ≈10 while ours is ≈100. This difference in statistics should be reflected in the respective uncertainties of the final EA values, but the two results still differ by about 16 standard deviations, based on the lower error margin quoted in Ref. [7]. There are major differences between the experiments, which we will therefore outline briefly. Calabrese *et al.* conducted their photodetachment study with a cw F-center laser, with a stated resolution of ≈0.13 cm^{-1}, in a coaxial (3-keV) ion-laser beam configuration. Our laser resolution is very similar to theirs, and our average laser power very comparable. Our typical ion currents are two orders of magnitude higher than those of Ref. [7], but our interaction region is also two orders of magnitude shorter. More importantly, the setup of Ref. [7] was very prone to intracavity and extracavity water absorption lines, such that their laser power was reduced to near zero in several wavelength regions. We are much less susceptible to this problem since our infrared light is generated just before the interaction region, and the remaining infrared beam path is effectively purged with dry nitrogen gas. As Calabrese *et al.*, we still normalize the data to the laser power transmitted through the ultrahigh-vacuum region. The most striking difference, however, between the experiments is that Calabrese *et al.* were not able to make measurements at or below the threshold region due to an upper limit of 2820 nm on the wavelength scan for the KCl:Li color center laser crystal. Thus they were unable to truly exploit the narrow linewidth of the cw laser, and in contrast to our measurements, could not explore the multiple thresholds due to fine-structure splittings (the lower end of their scan range is 3585 cm^{-1}). Fitting a single s wave to their data Calabrese *et al.* obtain an approximate electron affinity of 3580.5(2.0) cm^{-1}, which coincides with our value for the $^3P_1 \rightarrow {}^2P_{3/2}$ threshold. Due to its small relative strength of 17%, it seems unlikely, however, that this threshold was observed alone, without substantial contributions from the first four thresholds (compare Fig. 2). Therefore, Calabrese *et al.* extrapolate their data to threshold via higher-order fits and weighted averages over the transitions between all possible levels of the ion and atom, using the appropriate theoretical frameworks [15–17]. We have tested their procedures by applying them to our data in the region above 3585 cm^{-1}. This yielded an electron affinity of 3480(15) cm^{-1}, which agrees with the value for the $^3P_0 \rightarrow {}^2P_{1/2}$ threshold within error margins. Hence, the extrapolation procedures seem valid. All in all, it appears that the low-energy data (first six points) of Ref. [7] for some reason rise too steeply with increasing photon energy if compared with our data for this energy region. The respective slopes differ by approximately a factor of 3. We conclude that some systematic error has probably arisen in the work of Calabrese *et al.*, in addition to the statistical errors incurred by the low signal-to-noise ratio and the necessary extrapolation to threshold.

Although much theoretical effort has been directed to calculations on even lighter species, aluminum is sufficiently light that advanced calculations are being attempted. There have been three recent theoretical works on the electron affinity of aluminum. Arnau *et al.* obtained 450 meV [8], Woon and Dunning [9] a value of 437 meV, and Wijesundera 433 meV [10]. All three numbers, which have uncertainties of the order of 10 meV, are in good agreement with experiment. Our experimental determination of the fine-structure splittings of Al^- indicates that the earlier values based on isoelectronic extrapolations [2], 26(3) cm^{-1} and 76(7) cm^{-1} for $J=0$-1 and $J=0$-2, respectively, were essentially valid within quoted uncertainties. The negative ion of aluminum has also been the subject of recent experimental and theoretical studies [18] in terms of the continuum far above the detachment threshold. As regards future studies of Al^-, a highly accurate value of the binding energy of the $^1D_2$ term might, in principle, be obtained via a multiphoton detachment scheme. However, the expected low transition probability of the $^3P \rightarrow {}^1D$ transition ($\sim 10^{-4}$ s^{-1}) [19] would seem to make a 1 + 1 photon detachment scheme via an electric-dipole-forbidden bound-bound resonance rather unlikely [20]. Alternatively, one could use charge-exchange production techniques to maximize the population in the excited level, and employ resonant ionization spectroscopy [21] with detachment to an excited state of the aluminum atom. In contrast, single-photon detachment from $Al^-(^1D_2)$ would be technically very demanding from a nonlinear optical standpoint, requiring tunable midinfrared radiation.

In summary, we have measured the electron affinity of aluminum with an accuracy of 0.05 meV, and have resolved the fine structure of the ion. The measurement is in good agreement with recent calculations [8–10] but calls seriously into question the very recent experimental result of Calabrese *et al.* [7]. Several considerations would suggest that the present EA value be adopted. Perspectives for future work have also been briefly discussed.

We gratefully acknowledge the Natural Science and Engineering Research Council of Canada (NSERC) for support of this work. We also thank T. Andersen for his helpful comments on the manuscript.

[1] D. R. Bates, Adv. At., Mol., Opt. Phys. **27**, 1 (1991); T. Andersen, Phys. Scr. **T34**, 23 (1991); S. J. Buckmann, C. W. Clark, Rev. Mod. Phys. **66**, 539 (1994); C. Blondel, Phys. Scr. **T58**, 31 (1995).

[2] H. Hotop and W. C. Lineberger, J. Phys. Chem. Ref. Data **14**, 731 (1985).

[3] A. E. Litherland, Annu. Rev. Nucl. Part. Sci. **30**, 437 (1980); W. Kutschera and M. Paul, *ibid.* **40**, 411 (1990).

[4] C. S. Feigerle, R. R. Corderman, and W. C. Lineberger, J. Chem. Phys. **74**, 1513 (1981).

[5] V. A. Oparin, R. N. Il'in, I. T. Serenkov, and E. S. Solov'ev, Zh. Eksp. Teor. Fiz. **66**, 2008 (1974) [Sov. Phys. JETP **39**, 989 (1974)].

[6] D. M. Neumark, K. R. Lykke, T. Andersen, and W. C. Lineberger, Phys. Rev. A **32**, 1890 (1985).

[7] D. Calabrese, A. M. Covington, J. S. Thompson, R. W. Marawar, and J. W. Farley, Phys. Rev. A **54**, 2797 (1996).

[8] F. Arnau, F. Mota, and J. J. Novoa, Chem. Phys. **166**, 77 (1992).

[9] D. E. Woon and T. H. Dunning, Jr., J. Chem. Phys. **99**, 3730 (1993).

[10] W. P. Wijesundera, Phys. Rev. A **55**, 1785 (1997).

[11] J. R. Fuhr, W. C. Martin, A. Musgrove, J. Sugar, and W. L. Wiese, NIST Atomic Spectroscopic Data Base, http://physics.nist.gov.

[12] J. Thøgersen, L. D. Steele, M. Scheer, C. A. Brodie, and H. K. Haugen, J. Phys. B **29**, 1323 (1996).

[13] M. Scheer, C. A. Brodie, R. C. Bilodeau, and H. K. Haugen (unpublished).

[14] J. Thøgersen *et al.*, Phys. Rev. A **53**, 3023 (1996).

[15] J. W. Farley, Phys. Rev. A **40**, 6286 (1989).

[16] R. M. Stehman and S. B. Woo, Phys. Rev. A **20**, 281 (1979).

[17] P. C. Engelking and W. C. Lineberger, Phys. Rev. A **19**, 149 (1979).

[18] B. J. Davies, C. W. Ingram, D. J. Larson, C.-N. Liu, and A. F. Starace, Phys. Rev. A **56**, 378 (1997).

[19] C. Mendoza and C. J. Zeippen, Mon. Not. R. Astron. Soc. **199**, 1025 (1982).

[20] J. Thøgersen, M. Scheer, L. D. Steele, H. K. Haugen, and W. P. Wijesundera, Phys. Rev. Lett. **76**, 2870 (1996).

[21] V. V. Petrunin *et al.*, Phys. Rev. Lett. **75**, 1911 (1995).

Paper 5

Systematic study of the stable states of C^-, Si^-, Ge^-, and Sn^- via infrared laser spectroscopy.

Michael Scheer, René C. Bilodeau, Cicely A. Brodie, and Harold K. Haugen.

Physical Review A **58**, issue 1 (October 1998).

Systematic study of the stable states of C^-, Si^-, Ge^-, and Sn^- via infrared laser spectroscopy

Michael Scheer, René C. Bilodeau, Cicely A. Brodie, and Harold K. Haugen*
Department of Physics and Astronomy, McMaster University, Hamilton, Ontario, Canada L8S 4M1
(Received 24 April 1998)

The bound excited $np^3\ ^2D$ terms of Si^-, Ge^-, and Sn^- have been investigated with a combination of single- and multiphoton tunable infrared laser experiments. The binding energies of the two $J=3/2$ and $J=5/2$ fine-structure levels were found to be 0.527 234(25) and 0.525 489(20) eV, respectively for Si^-, 0.401 44(10) and 0.377 27(6) eV for Ge^-, and 0.397 617(15) and 0.304 635(15) eV for Sn^-. These results constitute improvements in accuracy over previous experimental values of up to four orders of magnitude and further provide the experimental values for the ^2D fine-structure splittings: 14.08(20), 192.6(9), and 749.95(15) cm^{-1} for Si^-, Ge^-, and Sn^- respectively. In addition, the photodetachment thresholds of the ionic $^4S_{3/2}$ ground states have been reinvestigated. This resulted in improved electron affinities of 1.262 119(20), 1.389 521(20), 1.232 712(15), and 1.112 067(15) eV for C^-, Si^-, Ge^-, and Sn^-, respectively. Various attempts towards an observation of the very weakly bound $C^-(^2D)$ and $Si^-(^2P)$ terms remain unsuccessful. [S1050-2947(98)01910-6]

PACS number(s): 32.80.Gc, 32.80.Wr, 32.10.Fn

I. INTRODUCTION

Excited states of atomic negative ions that are bound with respect to the atomic ground state have long been considered as rare occurrences. For many ions, the experimental knowledge of such states is still poor, despite considerable effort over the past decades (see Refs. [1, 2] for recent reviews). Excited negative-ion states that are embedded as resonances in the energy continuum above the atomic ground state have been extensively studied with a variety of experimental techniques [3]. Most early investigations of bound excited states, on the other hand, were based on two techniques: laser photodetached electron spectrometry (LPES) and threshold photodetachment with conventional light sources. Both techniques are applicable to most stable negative ions, but the energy resolution is often insufficient for a determination of fine-structure splittings. The energy resolution achieved in laser photodetachment threshold (LPT) experiments is significantly higher and LPT studies of the more strongly bound O^-, S^-, Se^-, and Te^- ions have provided accurate values for the respective ^2P fine-structure splittings [4]. LPT studies of weakly bound (<1 eV) ions are more challenging as they require tunable infrared laser sources. Nevertheless, accurate ionic fine-structure splittings have been obtained for Li^- [5] and recently also for B^- [6] and Al^- [7]. Both LPES and LPT studies have to rely on an initial population of the excited states to be investigated. This is generally not a constraint in measurements of the fine structure of the ionic ground state, as the corresponding level splittings are typically small. However, higher-lying excited terms or possibly electronically excited configurations would be only very weakly populated from a thermal ion source. In such cases, resonant multiphoton detachment may provide an alternative approach.

The interest in multiphoton phenomena involving negative ions began with the early demonstration of nonresonant two-photon detachment of I^- by Hall [8] and with the resonant two-photon detachment of C_2^- by Lineberger and Patterson [9]. Over the past few years, several other multiphoton phenomena have been observed in negative ions. Most studies investigated nonlinear optical processes such as excess-photon detachment [10], two-photon threshold detachment [11,12], and ponderomotive threshold shifts [13]. Negative ions represent qualitatively different targets for such strong-laser-field studies due to the absence of a Rydberg series of states, which is a result of the short-range potential that binds the extra electron of a negative ion. However, some multiphoton studies were aimed at the elucidation of negative-ion structure. Both bound excited states [14–16] and resonant structures in the continuum of negative-ion species [17,18] have been probed via multiphoton schemes. Bound excited negative-ion states almost always refer to the terms and fine structure of the same (ground-state) electronic configuration. Hence single-photon electric dipole ($E1$) transitions between such levels are strictly forbidden as a result of the parity selection rule. A simultaneous absorption of two photons, on the other hand, would be allowed in an electric dipole interaction and would give rise to a resonant enhancement in a multiphoton detachment spectrum. Recently, such a resonance has been observed in the single-color three-photon detachment spectrum of Sb^- [16] and previously in two-color detachment spectra of Se^- and Te^- where the two-photon bound-bound transition was realized in a Raman coupling scheme [14]. In addition to two-photon $E1$ transitions, small probabilities often exist for single-photon transitions of magnetic dipole ($M1$) or electric quadrupole ($E2$) character. Such "forbidden" transitions have recently been reported between fine-structure levels of Ir^- and Pt^- [15] and also between the fine-structure levels and terms of Sb^- [16]. In the latter case study of the antimony negative ion we have been able to demonstrate that a combination of resonant multiphoton techniques with traditional LPT spectroscopy can provide a complete knowledge of the stable states of an

*Also at Department of Engineering Physics, the Brockhouse Institute for Materials Research, and the Center for Electrophotonic Materials and Devices.

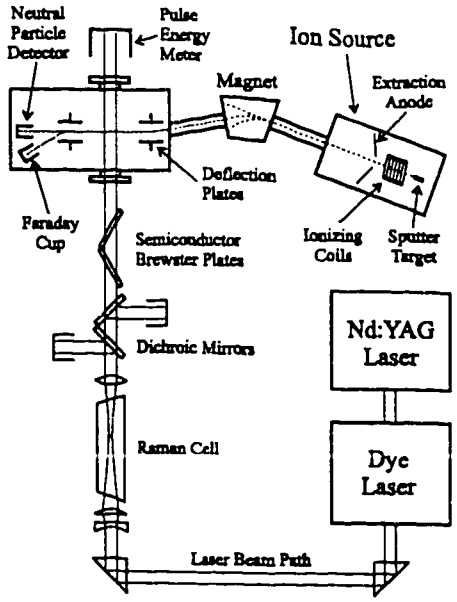

FIG. 1. Schematic diagram of the experimental setup (see the text for details).

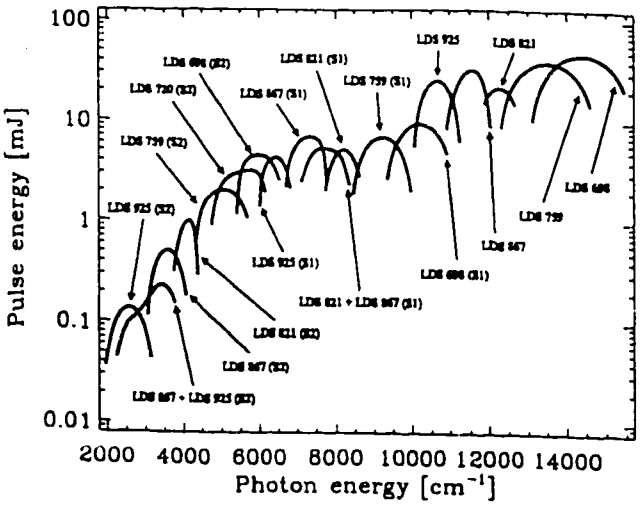

FIG. 2. Pulse energy curves for selected laser dyes and for the associated first and second Stokes conversions [indicated with the labels ($S1$) and ($S2$), respectively].

atomic negative ion. It was the aim of the work described in the present article to systematically apply these techniques to the negative ions of the carbon group: C^-, Si^-, Ge^-, and Sn^-.

The anions of the carbon group elements have been considered particularly notable examples of negative ions with excited terms of the ground-state configuration that still lie below the first detachment threshold [1]. Nevertheless, the experimental knowledge of these excited terms is still rather limited, particularly for Ge^- and Sn^- where the relative experimental uncertainties are as large as 50%. In recent years, C^-, Si^-, and Ge^- have attracted considerable attention by theorists as well as experimentalists for their photodetachment cross section close to the $nsnp^3\ ^5S_2$ threshold, several eV above the first detachment threshold ($ns^2np^2\ ^3P_0$). Theoretical works [19] have predicted pronounced window resonances for these three ions, but experimental studies have found a resonance feature only in Si^- [20] and not in C^- [21] (to our knowledge, Ge^- has not yet been investigated in that respect).

II. METHODOLOGY

A. Experimental setup

The experimental apparatus that was utilized in the photodetachment studies described herein is comprised of a negative-ion source, an infrared laser source, and an ultrahigh vacuum (UHV) interaction chamber. The setup is schematically depicted in Fig. 1 and is described in detail in Ref. [22].

A Lumonics HD-300 dye laser is pumped by the second harmonic of a 10-Hz Q-switched Nd:YAG laser (where YAG denotes yttrium aluminum garnet), a Lumonics YM-800. Tunability over the (680–980)-nm region is achieved by utilizing a 1800-lines/mm grating and near-infrared dyes. Over this tuning range the $\approx$8-ns laser pulses have a spectral bandwidth of 0.1–0.06 cm^{-1}. For wavelength conversion further into the infrared, the dye-laser beam is focused into a 120-cm-long high-pressure hydrogen cell, where stimulated Raman scattering of the dye-laser light causes the generation of a first Stokes laser beam. In addition, coherent second Stokes and anti-Stokes radiation is emitted from the Raman cell as the result of parametric four-wave-mixing processes. Optogalvanic resonances of argon were utilized in a direct measurement of the first Stokes Raman shift. A value of 4155.197(20) cm^{-1} was obtained, which agrees well with the literature value of 4155.187(5) cm^{-1} [23] for a cell pressure of 22(1) bars. After the Raman cell, the beam is recollimated and then passed through dichroic mirrors to attenuate the undesired wavelength components by $\sim$90% (anti-Stokes, residual pump, and also first Stokes radiation if second Stokes light is to be used). The final optical filtering is achieved with Brewster-angle pairs of silicon or germanium plates. This laser system allows for the production of tunable infrared laser light over the region of 1–5 μm (see Fig. 2). Finally, the laser light passes through a CaF_2 viewport into the ultrahigh vacuum interaction chamber where it crosses the ion beam at 90°. The laser light is monitored with a pulse-energy meter located after the exit port of the chamber. In order to effectively eliminate absorption of the infrared light in air, the entire optics table and the pulse-energy meter can be sealed and purged with nitrogen gas.

Negative-ion beams are generated with a Middleton-type high-intensity cesium sputter source [24] and are accelerated to energies of 13–15 keV. For ions possessing more than one stable state, the relative population of these states depends on the effective temperature of the sputter surface. Depending on various ion source parameters, this temperature can be varied between approximately 500 and 1500 K. A 30° bending magnet with magnetic fields of up to 0.52 T serves to separate the atomic ion beam of interest from other atomic and molecular species. In order to minimize collisional detachment, the ion beam is passed through a differential pressure tube into an UHV chamber with background pressures of $\sim 10^{-8}$ mbar. There the beam is charge-state analyzed with a pair of electrostatic deflection plates, producing a deflection of $\sim$10°. The ions then enter a field-free region where they interact with the collimated or focused laser

beam. A second pair of electrostatic deflection plates is employed to deflect the residual negative ions into a Faraday cup, while the photodetached neutral atoms are detected with a discrete-dynode electron multiplier. The detector is operated in the analog regime, as the total number of detachment events per laser pulse is typically larger than one. After preamplification, the output signal of the detector is fed into a gated integrator and boxcar averager. A gate width of ~50 ns is usually sufficient to ensure that all the neutral particles produced during the laser pulse are collected. Such narrow gating very effectively reduces the number of collisional background events to ~1 count per pulse, per μA of beam current. Finally, the integrated signal for each pulse (or the average of a number of pulses) is recorded by a personal computer.

B. Data acquisition and analysis

A region of interest in the photodetachment cross section of a negative ion is typically investigated with a slow [(20–30)-min] dye-laser scan. Depending on the signal-to-noise ratio, the scan procedure is repeated up to ten times and individual scans are summed. A poor signal-to-noise ratio can be due to a large photodetachment background, small ion-beam currents, and/or low infrared pulse energies. Beam current and pulse energy are always recorded parallel to the neutral particle signal and are utilized to normalize the photodetachment data.

1. Threshold fit

A theoretical description of the relative cross section for photodetachment close to threshold is given by Wigner's threshold law [25]. It predicts a zero cross section for photon energies (ε) below the threshold energy (ε_0) and a cross section proportional to $(\varepsilon-\varepsilon_0)^{l'+1/2}$ for $\varepsilon>\varepsilon_0$, where l' denotes the angular momentum of the detached (i.e., free) electron. Hence detachment into an s-wave continuum exhibits a threshold with a sharp onset ($\sigma\propto\sqrt{\Delta\varepsilon}$), whereas the onset of a p-wave threshold is smooth ($\sigma\propto\Delta\varepsilon^{3/2}$). However, in most of the cases investigated here, the cross section displays a series of cascaded thresholds rather than just a single threshold. Hence, for an accurate fit to any particular threshold it is necessary to account for the effect of the other photodetachment channels. The contribution of these other channels to the total cross section in the vicinity of ε_0 will be smooth and can be represented by a linear term, as long as the respective thresholds are not too close to ε_0. In this case, the function that is fitted to an individual s-wave threshold is given by

$$\sigma_0=\begin{cases}a+b(\varepsilon-\varepsilon_0)+c_0\sqrt{\varepsilon-\varepsilon_0} & \text{for } \varepsilon>\varepsilon_0\\ a+b(\varepsilon-\varepsilon_0) & \text{for } \varepsilon\leq\varepsilon_0.\end{cases} \quad (1)$$

The fitting routine that is utilized here performs a nonlinear least-squares fit via a multi-parameter gradient-expansion algorithm. The fitting parameters a, b, c_0, and ε_0 are optimized simultaneously.

For a series of closely spaced thresholds the linear background approximation is not valid. In this case, all thresholds are fitted simultaneously. The fitted function is then defined recursively:

$$\sigma_n=\sigma_{n-1}+\begin{cases}c_n\sqrt{\varepsilon-\varepsilon_n} & \text{for } \varepsilon>\varepsilon_n\\ 0 & \text{for } \varepsilon\leq\varepsilon_n.\end{cases} \quad (2)$$

Here $n=0,1,2,\ldots$ labels the individual thresholds in the series. Such a simultaneous fit is found to work well if only two or three thresholds are present and if their relative intensities are not too different. However, if several thresholds or thresholds with largely differing intensities have to be fitted, this fitting routine may fail to converge properly. In such a case, a sequential threshold fit is performed by fitting Eq. (1) to the lowest-energy threshold first, subtracting the fit from the data, then fitting the second threshold, again subtracting the fit from the data, and so on. This method is less rigorous than the simultaneous fit as the coupling between the fitting parameters is reduced. This may result in overoptimistic standard deviations in the fitted parameters, which are therefore verified on a case to case basis.

The range of validity of the Wigner law (1) is limited to the photodetachment cross section close to threshold. For a theoretical description of the cross section higher above threshold, correction terms have to be taken into account [26]. However, in cases where a deviation from the Wigner law is observed, an inclusion of higher-order terms to the fitting function (1) is avoided by restricting the final scan range to a region over which the Wigner law is valid. Generally, this does not result in an increased uncertainty of the fitted threshold value as the onset of an s-wave threshold is steep and well pronounced. In contrast, for p-wave detachment the cross section higher above threshold is often essential for a determination of the threshold value from a fit to the data [22,27].

Systematic deviations from the Wigner threshold behavior may also result from a (partial) saturation of the detachment process by the intense laser pulse. Partial saturation should not affect the near threshold data, i.e., the fitted threshold value, but it may have an effect on the measured relative threshold intensities, particularly if different thresholds are observed that originate from the same ionic level. In measurements of threshold strengths the linearity of detachment signal versus pulse energy is checked at the high-energy end of the scan range.

2. Threshold strength

The various photodetachment channels are associated with different electronic configurations, terms, or fine-structure levels in either the ion or the atom. The ions investigated here are stable only in the p^3 configuration. The resulting terms ^4S, ^2D, and ^2P are well separated in energy, as are the ^3P, ^1D, and ^1S terms of the p^2 configuration of the respective atoms. However, fine-structure splittings in both the atom and ion are small and will therefore give rise to closely spaced cascaded thresholds. Engelking and Lineberger [28] have presented a theory that quantifies the relative intensities of the various fine-structure transitions that constitute the photodetachment channels going from an ionic ^{2S+1}L term to an atomic $^{2S'+1}L'$ term. In this framework, the relative intensity of a fine-structure transition $J\rightarrow J'$ is given by

$$I(J,J') \propto \sum_{j=|l-1/2|}^{l+1/2} (2j+1)(2J+1)(2J'+1) \times \begin{Bmatrix} S & L & J \\ \frac{1}{2} & l & j \\ S' & L' & J' \end{Bmatrix}^2, \quad (3)$$

as long as the spin-orbit coupling of the electrons can be approximated by LS coupling and the ionic levels are statistically populated. Here l and j denote the orbital and total angular momentum of the bound electron that is to be detached. (It should be noted that the angular momentum l' of the detached electron is not relevant here, although it determines the shape of the threshold.) The selection rules for photodetachment are determined by the properties of the $9J$ symbol in Eq. (3):

$$|\Delta S| \leq \tfrac{1}{2}, \quad |\Delta L| \leq l, \quad |\Delta J| \leq l + \tfrac{1}{2}. \quad (4)$$

The ionic fine-structure levels are populated according to their statistical weights only if the level splittings are much smaller than kT, where T is the effective ion source temperature. If this is not the case, a Boltzmann factor $\exp[-E(J)/kT]$ must be included in Eq. (3) to account for a thermal population of the different energy levels. As Eq. (3) is derived on the basis of the LS-coupling approximation, a deviation between measured and calculated threshold intensities indicates the breakdown of this coupling scheme for the particular ion.

3. Resonances

As outlined in the Introduction, resonant multiphoton detachment constitutes an alternative to threshold detachment in the study of bound excited states. If a resonant enhancement in a multiphoton detachment spectrum is observed, an accurate determination of the corresponding excited level is rather straightforward. However, virtually all bound-bound transitions in atomic negative ions are single-photon $E1$ forbidden and therefore have only small transition probabilities of $M1$ and/or $E2$ character. The feasibility of the multiphoton approach for a particular excited state is therefore evaluated in a computer simulation of the laser–ion-beam interaction prior to the actual experiment. The simulation assumes a Lorentzian laser bandwidth and Gaussian profiles for the temporal and spatial shape of the laser beam as well as for the spatial shape of the ion beam. The number of detachment events per laser pulse is calculated as a function of the various ion and laser source parameters and as a function of estimated bound-bound and bound-free transition probabilities. Competing detachment channels such as single-photon detachment of the initial excited level population and nonresonant two-photon detachment of the ionic ground state are also included. It was found in the simulation as well as in the experiment that the success in driving a "forbidden" (1 + 1)-photon detachment process often depends on the effective suppression of these competing channels. While a collimated laser beam gives rise to a large one-photon (excited-state) and only a very small two-photon (ground-state) detachment background, the situation is reversed for a tightly focused beam. Depending on the cross sections of the various processes, the best resonant-signal-to-background-signal ratio may be obtained with one or the other beam geometry or an intermediate geometry such as a cylindrical focus.

4. Energy resolution

The resolution that can be achieved in photodetachment experiments with the present setup is limited by several factors. Most importantly, the finite bandwidth of the infrared laser source ($\approx 0.08\ \mathrm{cm}^{-1}$) gives rise to a predominantly Lorentzian broadening of all spectroscopic features. Doppler effects may cause an additional Gaussian broadening. For the crossed-beam setup used here the angular divergence of the ion beam is the major source of Doppler broadening. Geometric considerations of the interaction chamber suggest that the beam divergence angle should not be more than 0.5°. In the case of photodetachment with visible light this angle may very well cause a Doppler broadening larger than the laser bandwidth, but for a typical infrared photodetachment experiment (2-μm light, 15-keV beam energy, atomic mass of 60) a broadening of only $0.03\ \mathrm{cm}^{-1}$ results. Doppler broadening due to a (thermal) tangential velocity spread in the ion beam is even smaller and can therefore be neglected.

In principle, the finite interaction time between the fast ion beam and the pulsed laser beam constitutes an additional source of broadening. In practice, for a collimated laser beam this time is given by the duration of the laser pulse (~ 8 ns) and the resulting broadening is negligible. It is only for a tightly focused laser beam, as may be used in multiphoton detachment studies, that ion transfer times reach the subnanosecond regime and then cause broadenings of $\sim 0.1\ \mathrm{cm}^{-1}$.

5. Systematic errors

In an attempt to minimize potential sources of systematic errors we have performed various tests with the infrared laser setup prior to the actual photodetachment experiments. Very well known transitions in argon [29] were used as a calibration standard for the tuning control unit of the dye laser. The calibrations were conducted with the aid of an argon-filled hollow cathode discharge lamp (Hamamatsu). Discharge lamps yield an optogalvanic effect, i.e., a measurable change in the discharge impedance whenever the laser wavelength is in resonance with certain atomic transitions of the filler gas [30]. Discharge lamps constitute a very convenient and quick means of wavelength calibration, but provide only relatively few calibration lines. There are 25 optogalvanically active transitions available within the (680–980)-nm dye-laser tuning range, with gaps between consecutive lines of up to 45 nm. Hence the wavelength calibration of most photodetachment experiments would have to rely on an extrapolation from the nearest argon lines, i.e., the calibration accuracy would strongly depend on the degree of nonlinearity in the tuning mechanism. Figure 3 shows differences between tabulated [29] and measured argon line positions in wave-number units. The lines span a wavelength range of 60 nm and were measured after the tuning control unit had been calibrated using only two lines. The data in Fig. 3 appear to fluctuate randomly about the zero line by small amounts of less than $0.05\ \mathrm{cm}^{-1}$. However, the deviation of any particular line is reproducible ($\pm 0.01\ \mathrm{cm}^{-1}$) in different measurements. The

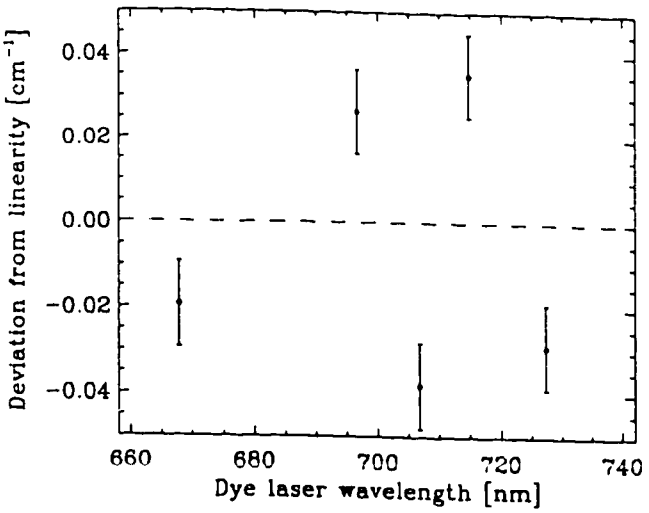

FIG. 3. Differences between measured and tabulated optogalvanic transitions in argon as a function of transition wavelength.

fluctuations are therefore believed to be the result of small "local" nonlinearities in the tuning mechanism. In order to determine an upper limit for this effect an étalon was employed to monitor the laser tuning over small regions (≈2 nm) at different wavelengths within the full tuning range. Deviations from linearity were very small, similar to those found for the argon lines. Therefore, a dye laser calibration uncertainty of 0.05 cm^{-1} is assumed for all experiments.

In addition to nonlinearities, possible temperature drifts are of some concern as certain threshold or resonance scans can take several hours. The dye laser was found to require a 2-h warmup period before a drift of less than 0.01 cm^{-1} per hour is established. In addition to the water cooling of the laser dye, temperature gradients are minimized by continuously flushing the laser housing with cool nitrogen gas. A calibration performed on the temperature-stabilized laser would therefore remain valid throughout the experiment. The laser is recalibrated for each experiment to eliminate the possibility of small day-to-day fluctuations. In very long experiments that require the highest accuracy, laser calibrations are carried out before as well as after the detachment scans. This enables a correction of the data for possible wavelength drifts.

As a pulsed laser source is utilized, with peak intensities of $\sim 10^7$ and $\sim 10^{10}$ W/cm^2 for a collimated or focused beam, respectively, the possibility of intensity shifts has to be considered. The threshold for photodetachment in strong laser fields is shifted to higher energies due to the ponderomotive energy of a free electron in an electromagnetic field [13]. We have therefore investigated the $^4S_{3/2} \rightarrow {}^3P_0$ thresholds of C^- and Ge^- with a collimated laser beam (≈3 mm diameter), a cylindrically focused beam (25 cm focal length), and a spherically focused beam (20 cm focal length). While identical threshold values were obtained in the first two cases, a threshold shift of ~1 cm^{-1} resulted in the third case. To surely avoid possible intensity shifts, all photodetachment threshold experiments are conducted with collimated laser light. The bound-bound transition of a multiphoton detachment scheme, on the other hand, may be shifted in the presence of a strong laser field as a result of an ac Stark shift of the negative-ion levels involved. However, for the transitions investigated here the ion levels belong to the same electronic configuration and should therefore exhibit very similar Stark shifts. Hence the transition energy should remain unshifted within experimental uncertainties. To be certain of this, we have measured the $Sn^-(^4S_{3/2} \rightarrow {}^2D_{3/2})$ resonance (see Sec. III D) with the three aforementioned focusing geometries. No shifts in the resonance position were apparent.

A particular problem with the crossed-beam geometry of the present experimental setup is its susceptibility to linear Doppler shifts. In the rest frame of the fast ion beam the laser frequency will appear shifted whenever the crossing angle deviates from 90°. An alignment of this angle based on the geometry of the interaction chamber alone has an uncertainty of ~2°, necessitating further alignment checks. For a typical ion beam energy of 15 keV and a light element such as oxygen with an electron affinity of 11 784.648(6) cm^{-1} [1,31] a misalignment of 2° would result in a Doppler shift of 0.6 cm^{-1}. In addition to its extremely well known binding energy, O^- is also a very prolific ion from a Cs sputter source for almost any oxide cathode and furthermore detaches with a sharp s-wave threshold. Hence a detachment experiment with O^- provides a sensitive test for Doppler effects. A careful measurement of the $O^-(^2P_{3/2} \rightarrow {}^3P_2)$ detachment threshold and a subsequent s-wave fit to the data resulted in a threshold value of 11 784.62(3) cm^{-1}. The uncertainty given here represents the standard deviation obtained from the fitting routine and the calibration uncertainty for this particular wavelength range. Our value agrees with the more accurate literature value within one standard deviation. We therefore deduce an upper limit of 0.03 cm^{-1} for possible Doppler shifts due to laser beam misalignment. While the laser beam alignment is easily maintained between experiments, some uncertainty remains regarding small deviations in the beam path for different ions. Again, geometric considerations of the interaction chamber suggest that this uncertainty should not be more than 0.5°. Hence residual Doppler uncertainties are calculated on the basis of this value and the 0.03-cm^{-1} uncertainty from the O^- experiment. Final values range from 0.05 to 0.13 cm^{-1} depending on atomic mass and photon energy.

Finally, the uncertainty in the Raman shift has to be accounted for whenever first or second Stokes radiation is employed. Values of 0.02 and 0.04 cm^{-1} are used, respectively, based on the uncertainty of our experimentally determined Raman shift (see Sec. II A). The uncertainties of the final experimental results given in this paper always include these various systematic errors in addition to the standard deviations obtained from the numerical fits to the data.

III. RESULTS AND DISCUSSION

A. Carbon

Despite the fact that carbon is a light (first-row) element, there have been very few experimental investigations of its negative ion. The binding energy of the ionic $2p^3\ {}^4S_{3/2}$ ground state was measured via LPES by Bennett and Hall [32] and via infrared LPT by Feldmann [33]. They obtained values of 1.268(5) eV and 1.2629(3) eV, respectively. Feldmann used a laser-pumped optical parametric oscillator for his pioneering infrared LPT work. In addition to the ground-

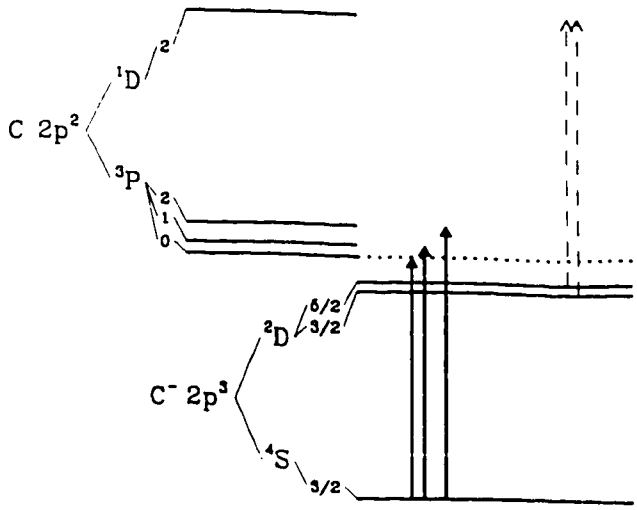

FIG. 4. Schematic energy level diagram of C^- and C. Arrows indicate detachment thresholds, ordered by threshold energy. The horizontal spacing between arrows is proportional to the energy separation of the respective thresholds. Only the $^4S_{3/2} \rightarrow {}^3P_J$ thresholds (solid arrows) could be measured in the present study. For clarity of presentation, fine-structure splittings are not shown to scale.

state detachment thresholds, his LPT spectrum also provided evidence for an ionic $2p^3\ ^2D$ term with a binding energy of 33(1) meV, which agreed with earlier values of 37(3) meV and 50(20) meV, obtained via field ionization measurements [34] and LPES [32], respectively. Based on these previous investigations, the energy level structure of C^- and the order of photodetachment thresholds are depicted in Fig. 4.

Since the recent LPT studies of Li^- [35] and B^- [6], carbon has become the first-row element with the largest uncertainty in its electron affinity, 0.3 meV (versus 0.025 meV for B^-). Many calculations of the electron affinity (EA) of carbon have been performed to date [36], but they typically exhibit errors of several meV. On the other hand, recent large-scale multiconfiguration Hartree-Fock calculations of the EA of lithium [37] and boron [38] have indicated that calculation errors of less than 1 meV might be achievable in future *ab initio* calculations of other first-row elements. Hence a more accurate determination of the EA of carbon seems appropriate.

We have investigated the photodetachment cross section of C^- over the photon energy range of 10 160–10 580 cm^{-1} or 1.260–1.312 eV [1 eV=8065.5410(24) cm^{-1} [39]]. The region that exhibits the three $^4S_{3/2} \rightarrow {}^3P_J$ thresholds is shown in Fig. 5. As can be seen, the thresholds follow the Wigner s-wave behavior very closely (solid line). The ratio of measured transition strengths, 0.9:3.1:5.0, agrees well with the ratio of statistical weights for the fine-structure levels of the atomic ground state, 1:3:5. The intervals between the three thresholds are 16.3(2) and 26.8(2) cm^{-1}, also in good agreement with tabulated values for the fine-structure splittings of the atom, 16.40 and 27.00 cm^{-1}, respectively [40]. A high-resolution scan of the EA-defining $^4S_{3/2} \rightarrow {}^3P_0$ threshold is shown in Fig. 6. The scan range of 2.4 cm^{-1} corresponds to one standard deviation of the earlier result by Feldmann [33]. The observed photodetachment cross section deviates from the ideal Wigner s-wave behavior (dashed line), primarily due to the finite laser bandwidth of

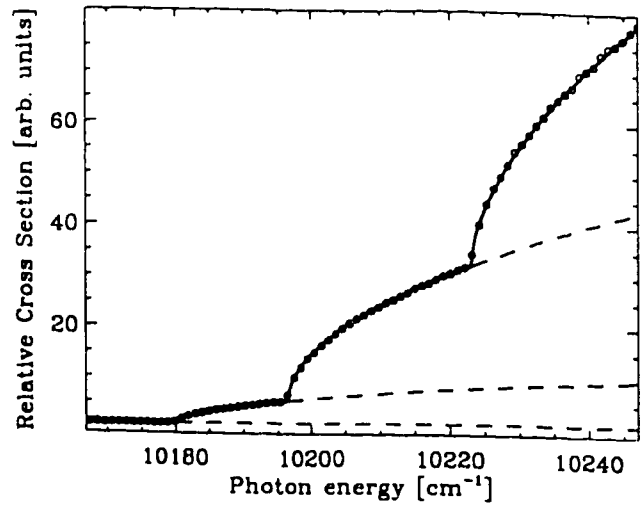

FIG. 5. Measured photodetachment cross section of C^- in the region of the $^4S_{3/2} \rightarrow {}^3P_J$ thresholds. The result of a Wigner s-wave fit to the data is indicated by the solid line. Individual thresholds are extrapolated with dashed lines.

~0.1 cm^{-1}. In addition, a small modulation of the cross section is apparent, which results from the presence of a weak electrostatic field. Although the current design of the UHV interaction chamber provides for a shielding of the electrostatic deflection plates, stray fields of ~10 V/cm seem to remain. Fortunately, the effect of static electric fields on s-wave thresholds has been thoroughly investigated in the past [41] and can be accurately modeled with a theory presented by Baruch *et al.* [42]. If the cross section obtained with this model is convoluted with a Lorentzian bandwidth function, the solid line in Fig. 6 is obtained. The excellent agreement between fitted and measured cross sections allows for an accurate determination of the threshold energy: 10 179.67(15) cm^{-1} [1.262 119(20) eV]. The uncertainty given here includes possible systematic errors in the calibration or due to Doppler shifts (see Sec. II B 5). It is important

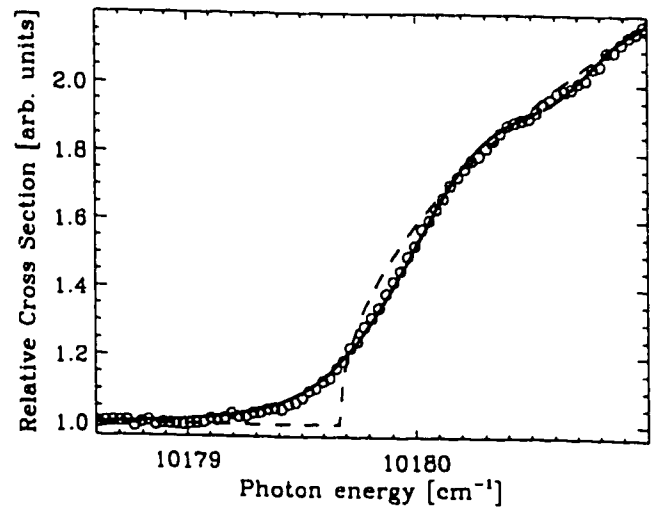

FIG. 6. High-resolution scan of the C^- detachment cross section in the vicinity of the $^4S_{3/2} \rightarrow {}^3P_0$ threshold. An ideal Wigner s-wave fit is indicated by the dashed line, while the result of an s-wave fit that includes bandwidth and field effects is represented by the solid line.

to note that the same threshold value is obtained if the effects of laser bandwidth and electric field are ignored in the fit (dashed line in Fig. 6). Hence the Wigner s-wave fit (1) remains valid.

Our value improves the accuracy of the EA of carbon by a factor of 15, but the value lies outside the error margin of Feldmann's result of 1.2629(3) eV [33]. This seems to indicate that a source of systematic error unaccounted for might have been present in the earlier work.

In an attempt to reproduce the weak $^2D_J \rightarrow {}^1D_2$ threshold feature observed by Feldmann, we have carefully investigated the detachment cross section in the (945–965)-nm range, which corresponds to ^2D binding energies between 21 and 48 meV. No evidence for a threshold structure was found. There can be no doubt about the existence of the $^2D_J \rightarrow {}^1D_2$ thresholds, as the positive ^2D binding energy was confirmed in five independent studies [33,34,32,43,44]. Hence an insufficient population of the ^2D_J levels from our ion source is the most likely explanation for the absence of the corresponding threshold features. Nonthermal population mechanisms cannot be ruled out for a sputter ion source, but if we assume a mainly thermal population, less than 0.1% of the ions would be produced in the excited ^2D_J states. Thus a signal-to-noise ratio of better than 1000 would be required for an unambiguous observation of the $^2D_J \rightarrow {}^1D_2$ thresholds, due to the substantial photodetachment signal from the ionic ground state. In the study of Feldmann the ions were produced via a discharge, which likely resulted in a higher ^2D population. Recent LPES studies of the C^- detachment cross section at 2.076 eV have shown that a fractional ^2D population of 50% can be achieved if the C^- beam is produced by charge exchanging a C^+ beam [43,44]. Hence a combination of this beam generation technique and infrared LPT (and possibly state-selective detection) should enable an accurate determination of the two $C^-(^2D_J)$ levels.

B. Silicon

The energy level structure of Si^-, which is schematically shown in Fig. 7, is similar to that of C^-, with the interesting difference that for Si^- both the ^2D and the ^2P excited terms of the p^3 configuration are bound with respect to the atomic ground state. Early indications for this scenario were confirmed in an LPES study by Kasdan *et al.* [46], which determined ^2D and ^2P binding energies of 523(5) and 29(5) meV, respectively. For the ^2P term a binding energy of 35(4) meV was also obtained by Oparin *et al.* in a field ionization measurement [34]. To our knowledge, none of the previous studies of these bound ionic terms have been able to resolve the respective fine structure. The binding energy of the $^4S_{3/2}$ ionic ground state, i.e., the electron affinity of silicon, is well known from the LPES experiment of Kasdan *et al.* [1.385(5) eV [46]] and more accurately from our previous infrared LPT study of this system, which yielded 1.389 49(6) eV [47]. Since improved calibration procedures now allow us to measure EA's with uncertainties as small as 0.01 meV, we decided to reinvestigate the EA-defining $^4S_{3/2} \rightarrow {}^3P_0$ threshold. (A determination of excited-state binding energies via bound-bound resonances hinges on an accurately known EA; see below.) A high-resolution scan over the (11 205–11 211)-cm^{-1} photon energy range

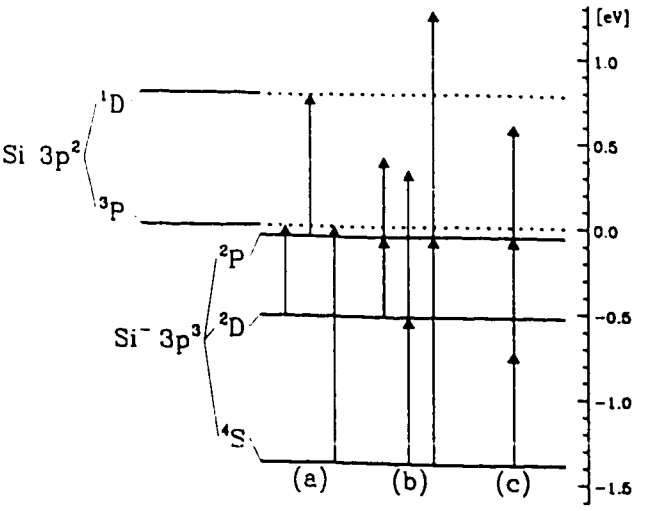

FIG. 7. Schematic energy-level diagram of Si^- and the Si ground state. Arrows indicate the various detachment schemes that were attempted in the present study: (a) one-photon threshold detachment, (b) resonant two-photon detachment via one-photon $M1$-$E2$ transitions, and (c) resonant three-photon detachment via two-photon E1 transitions. For simplicity, fine-structure splittings are not shown.

yielded a threshold energy of 11 207.24(15) cm^{-1} [1.389 521(20) eV], in good agreement with our earlier value. A strong photodetachment background indicated a useful population of the excited ion levels, approximately a few nA out of the 2 μA total Si^- current. Hence an observation of the actual $^2D_J \rightarrow {}^3P_{J'}$ thresholds seemed possible. A subsequent scan over a photon energy range of 4200–4500 cm^{-1}, shown in Fig. 8, revealed five nested thresholds. We attempted to fit the data over the full range shown using the Wigner s-wave law and its leading correction term [26] (solid line in Fig. 8). As can be seen, the data deviate from the predicted threshold behavior already after the third threshold ($^2D_{3/2} \rightarrow {}^3P_1$). Similar deviations were

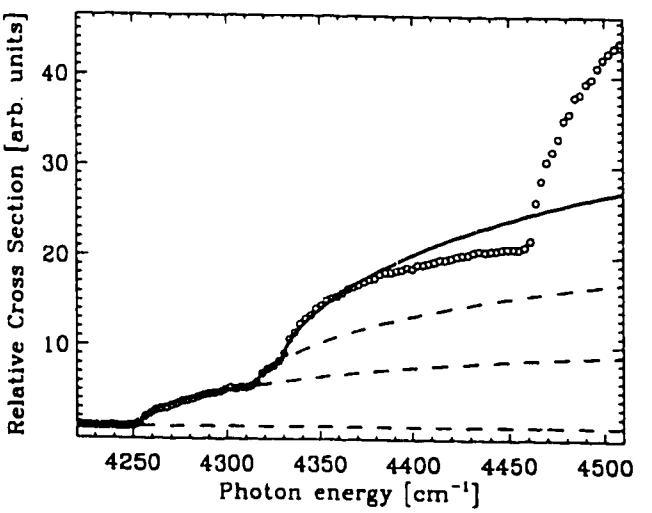

FIG. 8. Measured photodetachment cross section of Si^- in the region of the $^2D_J \rightarrow {}^3P_{J'}$ thresholds. For the first three thresholds the result of a Wigner s-wave fit including the leading correction term is indicated by the solid line. Individual thresholds are extrapolated with dashed lines.

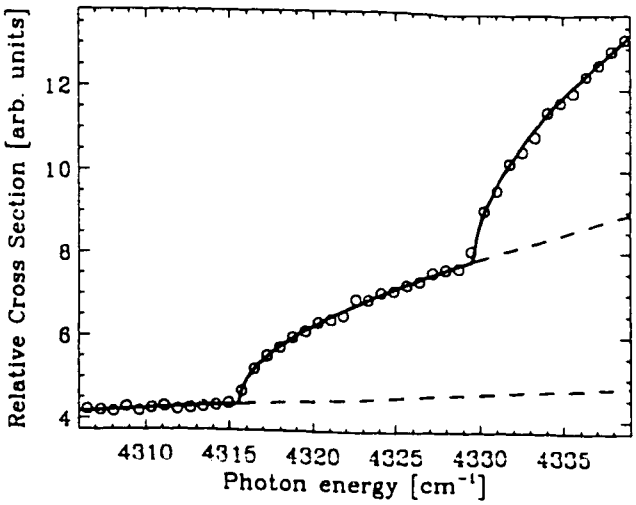

FIG. 9. Si^- photodetachment data in the vicinity of the $^2D_J \rightarrow {}^3P_1$ thresholds.

previously observed for Al^- photodetachment thresholds [48,7]. Hence an accurate determination of threshold energies and strengths had to rely on the near-threshold data alone. The regions of the $^2D_J \rightarrow {}^3P_1$ and $^2D_J \rightarrow {}^3P_2$ thresholds were therefore rescanned with higher resolution. The results are shown in Figs. 9 and 10, respectively. Threshold energies and strengths that were obtained from a Wigner s-wave fit to these data sets (where the background was approximated linearly) are summarized in Table I. Calculated threshold strengths (3) are given for comparison. Separations between thresholds of 77.11(25) cm^{-1} for $^2D_{3/2} \rightarrow {}^3P_{0,1}$ and 145.92(20) cm^{-1} for $^2D_{5/2} \rightarrow {}^3P_{1,2}$ were found, in good agreement with 77.115 and 146.042 cm^{-1}, respectively, the tabulated values for the fine-structure splittings of the $Si(3p^2\ {}^3P)$ term [40]. This proves that detachment to the atomic ground state is observed. The presence of a ^2D term as the initial ionic state is evident from the good agreement between measured and calculated threshold strengths, in particular from the absence of the ΔJ-forbidden $^2D_{5/2} \rightarrow {}^3P_0$ threshold. The $Si^-(^2D_J)$ binding energies that can be extracted from the threshold values are 4252.43(20) and

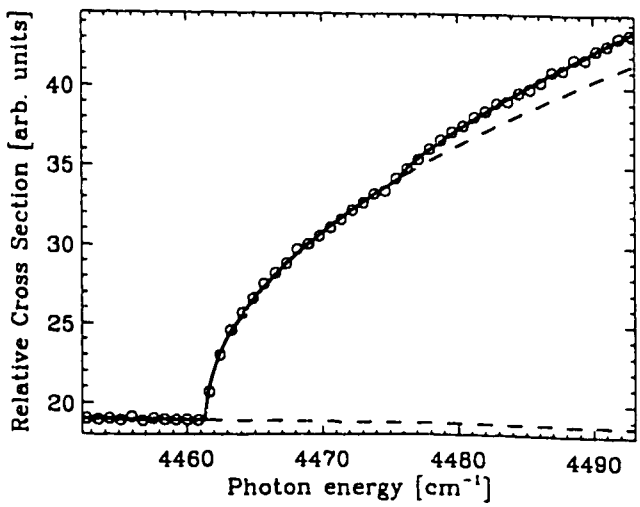

FIG. 10. Photodetachment cross section of Si^- in the $^2D_J \rightarrow {}^3P_2$ threshold region.

TABLE I. Results of the s-wave fits to the Si^- photodetachment data.

Transition	Threshold Energy (cm^{-1})	Relative strength Measured	Calculated
$^2D_{5/2} \rightarrow {}^3P_0$	a	a	0
$^2D_{3/2} \rightarrow {}^3P_0$	4252.43(25)	10(1)	10
$^2D_{5/2} \rightarrow {}^3P_1$	4315.53(20)	11(1)	9
$^2D_{3/2} \rightarrow {}^3P_1$	4329.54(20)	19(2)	21
$^2D_{5/2} \rightarrow {}^3P_2$	4461.45(15)	45(2)	45
$^2D_{3/2} \rightarrow {}^3P_2$	4475.7(5)	5(1)	5

[a]This transition is forbidden by the ΔJ selection rule.

4238.35(15) cm^{-1} [527.234(25) and 525.489(20) meV] for $J = 3/2$ and $J = 5/2$, respectively. These values compare well with the average binding energy of 523(5) meV measured by Kasdan *et al.* [46]. The difference between our two values gives a ^2D fine-structure splitting of 14.08(20) cm^{-1}, which is in disagreement with 7(2) cm^{-1}, a value that was obtained earlier from isoelectronic extrapolation [45].

The very small binding energy of the $Si^-(^2P)$ term precludes a determination of the detachment thresholds to the atomic ground state. The thresholds for detachment to $Si(3p^2\ {}^1D_J)$ would be within the tuning range of the present infrared laser source, but would suffer from a very unfavorable signal-to-background ratio, similar to the $^2D_J \rightarrow {}^1D_2$ thresholds in C^- (Sec. III A). We have therefore attempted to probe the ^2P_J levels via resonant multiphoton detachment. The various possibilities for resonant multiphoton detachment from Si^- are shown in Fig. 7. Probabilities for single-photon bound-bound transitions can be extrapolated from calculated Einstein A coefficients for the phosphorous isoelectronic sequence [49]. The number of detachment events per laser pulse is then evaluated with a computer simulation of the laser–ion-beam interaction (as described in Sec. II B 3). The results obtained for Si^- are summarized in Table II. Depending on scan speed and background counts, signal enhancements as small as 0.1 events per pulse can be detected with the present setup. We have therefore searched for the $^4S_{3/2} \rightarrow {}^2P_J$ resonances over a 30-meV-wide photon energy range (10 841–11 093 cm^{-1}), which covers a 3σ error

TABLE II. Estimated probabilities for single-photon bound-bound transitions in Si^-.

Transition Levels	Type[a]	Rate A (s^{-1})	Counts/pulse[b]
$^4S_{3/2}$-$^2P_{3/2}$	$M1$[c]	0.005	3
$^4S_{3/2}$-$^2P_{1/2}$	$M1$[c]	0.002	1
$^2D_{3/2}$-$^2P_{3/2}$	$E2$	0.008	0.06
$^2D_{3/2}$-$^2P_{1/2}$	$E2$	0.013	0.1
$^2D_{5/2}$-$^2P_{3/2}$	$E2$	0.016	0.2
$^2D_{5/2}$-$^2P_{1/2}$	$E2$	0.008	0.1

[a]Only the dominant character of the transition is indicated.
[b]Counts/pulse are calculated for a focal spot size of 0.1 mm and a bound-free cross section of 10^{-17} cm^2.
[c]These transitions violate the ΔS and ΔL selection rules. This reduces the accuracy of isoelectronic extrapolation.

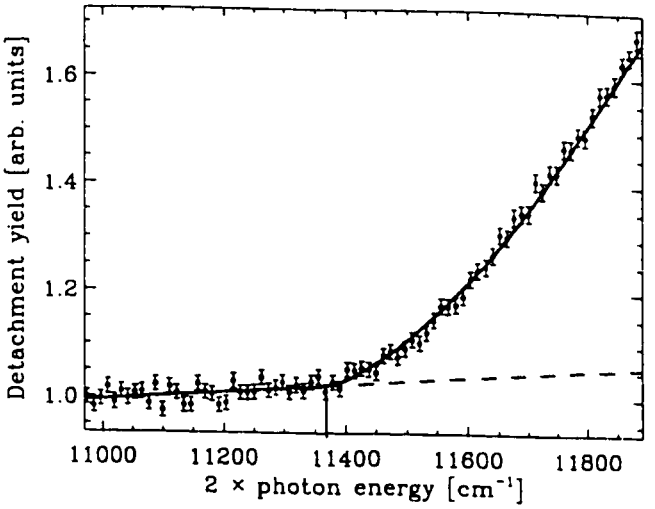

FIG. 11. Measured two-photon $Si^-(^4S_{3/2}) \rightarrow Si(^3P)$ detachment threshold. The solid line shows the result of a Wigner p-wave fit to the data.

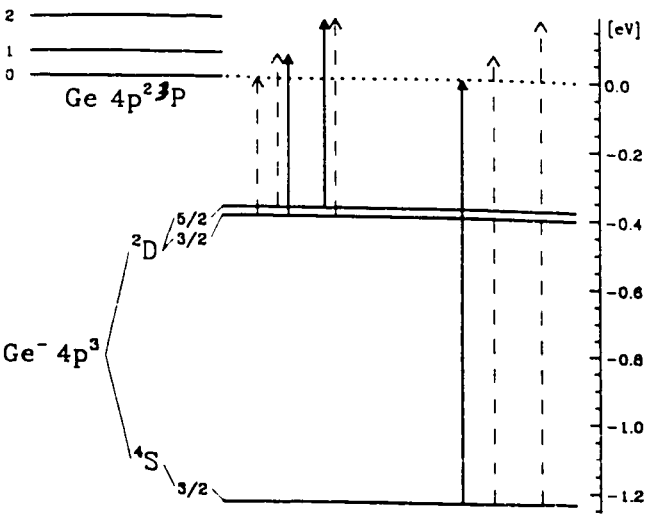

FIG. 12. Schematic energy-level diagram of Ge^- and the Ge ground state. Arrows indicate expected photodetachment thresholds in order of increasing photon energy. Thresholds that were observed are shown with solid arrows; others are dashed.

margin of the ^2P binding energy measured by Kasdan *et al.* [46]. No resonant features were apparent in this scan (which was conducted at a rate of 1000 laser pulses per cm^{-1}). The resonances could be somewhat weaker than the estimates suggest and would then likely be hidden in the substantial $Si^-(^2D)$ detachment background of ~50 counts per pulse. Similarly, a search for the $^2D_J \rightarrow {}^2P_{J'}$ resonances over the (3925–4090)-cm^{-1} range with the same scan rate remained unsuccessful. The photodetachment background was much smaller in this case, but so were the estimated resonance signals (Table II). Most importantly, the background signal due to collisions of the Si^- ions with rest gas molecules in the UHV chamber was very high (~1 event/pulse). This collisional background is due to the large (≈1 μA) Si^- beam current and is likely responsible for the absence of the expected resonance features. As for $C^-(^2D)$, these complications could be avoided in future experiments if different ion-beam techniques such as charge exchange, an improved UHV system, and/or state-selective detection schemes were employed.

An alternative to driving a particular transition via an $E1$-forbidden one-photon absorption is the possibility of $E1$-allowed two-photon absorption. Since the $Si^-(^2P_J)$ levels are only weakly bound, the $^4S_{3/2} \xrightarrow{2h\nu} {}^2P_J$ two-photon resonances are expected to lie just below the threshold for two-photon detachment, $^4S_{3/2} \xrightarrow{2h\nu} {}^3P_0$. This threshold was investigated first in order to optimize the focusing geometry for higher-order processes. The result is shown in Fig. 11. The threshold for two-photon detachment at 11 370(15) cm^{-1} and the expected p-wave threshold behavior are apparent. (A two-photon p-wave threshold has been previously observed in Cl^- detachment [11].) The observed threshold value compares well with 11 357 cm^{-1}, the average threshold value for an unresolved $Si(^3P)$ fine structure (although a ponderomotive threshold shift of a few cm^{-1} may be present). At energies below the two-photon threshold a small photodetachment signal is observed. This signal results from one-photon detachment of $Si^-(^2D)$ and from three-photon detachment of $Si^-(^4S)$. However, our final search for the $^4S_{3/2} \xrightarrow{2h\nu} {}^2P_J$ two-photon transitions over the (5590–5400)-cm^{-1} photon energy range (at a rate of 500 pulses/cm^{-1}) revealed no resonant enhancements over the detachment background. The absence of any resonance structure is likely due to a very small transition probability. The transitions would be "spin forbidden" and although we previously succeeded in driving a spin-forbidden two-photon transition in the case of Sb^- [16], a spin change is a much more serious constraint for a transition in a light system that is well described by LS coupling, such as Si^-.

C. Germanium

An energy level diagram for Ge^- and the Ge ground state is presented in Fig. 12. Accurate $Ge^-(^4S_{3/2})$ binding energies (EA of Ge) of 1.233(3) eV and 1.232 73(5) eV were previously obtained in LPES [50] and infrared LPT [47] studies, respectively. As with Si^-, we have reinvestigated the $^4S_{3/2} \rightarrow {}^3P_0$ photodetachment threshold of Ge^- in the present study. An improved value for the EA of Ge was obtained: 9942.49(12) cm^{-1} [1.232 712(15) eV], in good agreement with the previous values.

In contrast to the Ge^- ground state, there has been only one previous observation of the excited $Ge^-(^2D)$ term, which was reported by Feldmann *et al.* [51]. Their photodetachment threshold experiment employed a conventional light source and indicated a low-energy threshold at 0.4 eV, which was attributed to detachment from $Ge^-(^2D)$. No uncertainties are given in the original paper, but the result is referenced in the 1985 Hotop-Lineberger tables [4] with an uncertainty of 0.2 eV, which seems consistent with the typical errors of that experimental technique. Based on this average ^2D binding energy, the five $^2D_J \rightarrow {}^3P_{J'}$ thresholds would be expected in the (1800–6200)-cm^{-1} photon energy range, spread out over ~1400 cm^{-1}. Using the isoelectronically extrapolated value of 160(30) cm^{-1} for the ^2D fine-structure splitting [45], the thresholds would appear in the order shown in Fig. 12. A scan of the (3184–5975)-cm^{-1} range revealed only two weak s-wave threshold features at

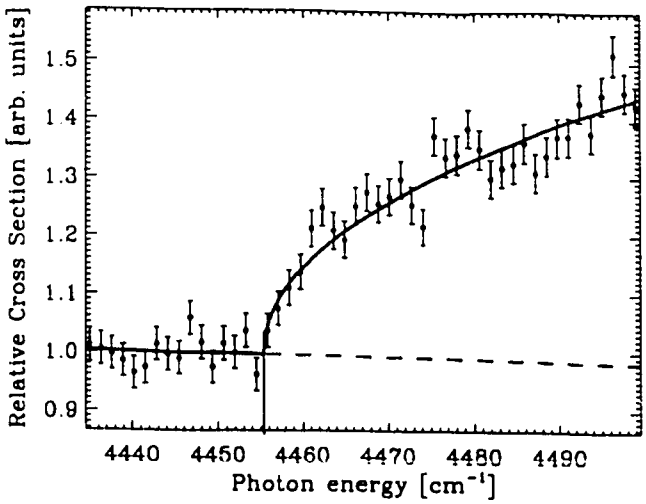

FIG. 13. Measured photodetachment cross section of Ge^- in the region of the $^2D_{5/2} \rightarrow {}^3P_2$ threshold. The result of a Wigner s-wave fit to the data is indicated by the solid line. Error bars are estimated on the basis of counting statistics.

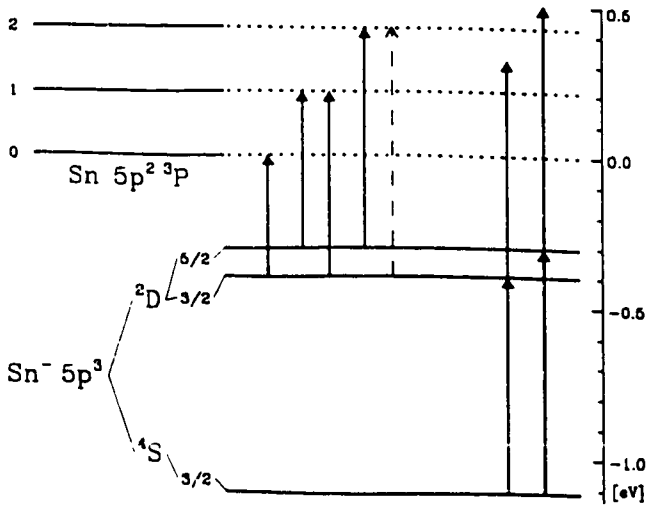

FIG. 14. Schematic energy-level diagram of Sn^- and the Sn ground state. Arrows indicate $^2D_J \rightarrow {}^3P_J$, photodetachment thresholds and resonant two-photon detachment schemes. For simplicity, $^4S_{3/2} \rightarrow {}^3P_J$, thresholds are not shown.

3795.0(8) and 4455.3(5) cm^{-1}, the latter of which is shown in Fig. 13. The substantially smaller signal compared to the equivalent experiment with Si^- must be attributed to the much lower total ion-beam current available here ($\approx$100 nA). The signal obtained for the threshold at 3795 cm^{-1} was in fact close to the detection limit of the apparatus. Since the two thresholds are separated by 660.3(9) cm^{-1}, which does not match with any separation between the Ge(^3P_J) levels (0, 557.1341, and 1409.9609 cm^{-1} for $J=0$, 1, and 2, respectively [40]), the thresholds must originate from different ionic levels. The only reasonable assignment for the two thresholds seems to be $^2D_{3/2} \rightarrow {}^3P_1$ and $^2D_{5/2} \rightarrow {}^3P_2$, respectively. With this assignment, an ionic fine-structure splitting of 192.6(9) cm^{-1} is obtained, which falls within a 2σ error margin of the isoelectronic value of 160(30) cm^{-1}. Any other assignment would result in a negative splitting or in an unreasonably large value of 660 cm^{-1} or more. The two assigned thresholds also happen to be the strongest thresholds in the series, which would suggest that the signal from the three remaining thresholds was simply too small for detection with the current setup. We therefore conclude that the $^2D_{3/2}$ and $^2D_{5/2}$ levels of Ge^- are bound by 3237.9(8) and 3045.3(5) cm^{-1} [401.44(10) and 377.57(6) meV], respectively. Unfortunately, a confirmation of these level energies via resonant multiphoton detachment is rather challenging, considering the very small $^2D_{3/2,5/2} \rightarrow {}^4S_{3/2}$ transition probabilities of 0.01 and 0.0005 s^{-1} (extrapolated from calculated isoelectronic values [52]). Attempts to drive the $^4S_{3/2} \rightarrow {}^2D_{3/2}$ $M1$ transition remain unsuccessful.

D. Tin

As for Ge^-, the $^4S_{3/2}$ ground state of Sn^- has been accurately measured in two previous studies. Miller *et al.* [50] obtained a binding energy of 1.112(4) eV from LPES data, while an infrared LPT study by Thøgersen *et al.* [47] yielded 1.112 09(6) eV. Our initial experiments with Sn^- were aimed at a confirmation of this EA value. A high-resolution scan provided a threshold value of 8969.42(12) cm^{-1} [1.112 067(15) eV] for the EA-defining $^4S_{3/2} \rightarrow {}^3P_0$ transition, in excellent agreement with the earlier works. The ~300-nA Sn^- beam employed here was derived from a solid metal sputter cathode. This cathode was found to perform very poorly at higher effective sputter temperatures, which are essential for efficient detachment from excited ionic levels. As a result, ^2D detachment signals were disappointingly small.

Unfortunately, the previous experimental knowledge of the $Sn^-(^2D)$ term is even less established than in the case of Ge^-. Again, the only previous investigation is the photodetachment study of Feldmann *et al.* [51]. Photodetachment well below 1 eV is evident from their spectrum and is assigned to the $^2D \rightarrow {}^3P$ transitions. However, the identification of actual thresholds is somewhat inconclusive; no final value for the ^2D binding energy is given. Nevertheless, the Hotop-Lineberger tables from 1985 quote a value of 0.4(2) eV, which is apparently an estimate based on the work of Feldmann *et al.* For the ^2D splitting an isoelectronically extrapolated value of 800(200) cm^{-1} is available [45]. The resulting energy level structure of Sn^- is shown in Fig. 14, including various photodetachment schemes aimed at the ^2D_J levels.

The ionic $^4S_{3/2} \leftarrow {}^2D_{3/2,5/2}$ $M1$ transition probabilities are promising in this case; A coefficients of 0.2 and 0.01 s^{-1}, respectively, are obtained by extrapolating from calculated values of the Sb isoelectronic sequence [53], which translates into estimated counts per pulse of 10 and 0.5, respectively. We have searched for the $^4S_{3/2} \rightarrow {}^2D_J$ $M1$ resonances by scanning the two-photon detachment spectrum of $Sn^-(^4S_{3/2})$ from high to low energies, starting at 7600 cm^{-1}. An enhancement in the signal of ~6 counts per pulse was found at 5762.50(10) cm^{-1}. This resonance feature is shown in Fig. 15 and must be assigned to the $^4S_{3/2} \rightarrow {}^2D_{3/2}$ transition on the basis of its strength. Apparently, the much weaker $^4S_{3/2} \rightarrow {}^2D_{5/2}$ transition had been missed. Therefore, an attempt was made at locating the $^2D_{5/2} \rightarrow {}^3P_J$ thresholds.

A tin oxide instead of a tin metal cathode was utilized and found to perform much better at high effective sputter tem-

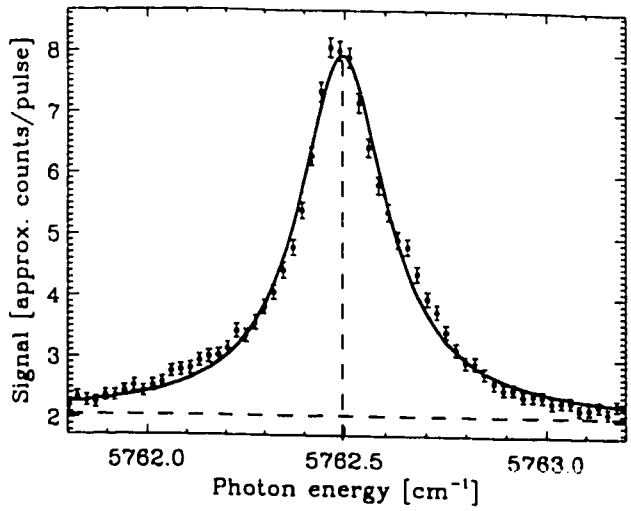

FIG. 15. Two-photon detachment yield in the vicinity of the $^4S_{3/2}\rightarrow{}^2D_{3/2}$ $M1$ resonance. The result of a Lorentzian fit to the data is indicated by the solid line.

peratures, albeit with a somewhat lower total Sn^- beam current of ~100 nA. The resulting increase in ^2D population of over an order of magnitude now enabled a determination of four out of the five $^2D_J\rightarrow{}^3P_{J'}$ thresholds with a reasonable signal-to-noise ratio. The $^2D_{5/2}\rightarrow{}^3P_2$ threshold is shown in Fig. 16 as an example. The threshold values that were obtained from Wigner s-wave fits to the four data sets are summarized in Table III. Binding energies of 3207.06(15) and 2457.04(10) cm^{-1} are obtained for $^2D_{3/2}$ and $^2D_{5/2}$, respectively, by subtracting from the threshold values the accurately known energies of the atomic $^3P_{J'}$ levels (0, 1691.806, and 3427.673 cm^{-1} [40]). It was now possible to zoom in on the thus far unobserved $^4S_{3/2}\rightarrow{}^2D_{5/2}$ $M1$ transition. The sum of several scans over a 1.5-cm^{-1} photon energy range is shown in Fig. 17. The weak but unambiguous resonance feature is centered at 6512.37(10) cm^{-1}. The resonant signal amounts to only 20% of the background signal, which is about a factor of 15 less than the signal-to-background ratio of the $^4S_{3/2}\rightarrow{}^2D_{3/2}$ resonance. This compares well with the ratio of ~20 for the extrapolated transition probabilities given above.

TABLE III. Results of the Wigner s-wave fits to the $Sn^-(^2D)$ photodetachment data.

Transition	Threshold Energy (cm^{-1})	Binding energy of ionic level (cm^{-1})
$^2D_{3/2}\rightarrow{}^3P_0$	3207.04(20)	3207.04(20)
$^2D_{5/2}\rightarrow{}^3P_1$	4148.88(15)	2457.08(15)
$^2D_{3/2}\rightarrow{}^3P_1$	4898.90(15)	3207.10(15)
$^2D_{5/2}\rightarrow{}^3P_2$	5884.67(10)	2457.00(10)
$^2D_{3/2}\rightarrow{}^3P_2$	a	a

[a]This threshold was not observed due to a small transition strength.

Finally, subtracting the measured resonance energies from the EA value yields a second set of $^2D_{3/2}$ and $^2D_{5/2}$ binding energies, 3206.93(15) and 2457.06(15) cm^{-1}, respectively, in excellent agreement with the values obtained from the threshold measurements. Based on the average of the two measurements we give final $^2D_{3/2}$ and $^2D_{5/2}$ binding energies of 3207.00(12) and 2457.05(12) cm^{-1} [397.617(15) and 304.635(15) meV], respectively, and a ^2D_J splitting of 749.95(15) cm^{-1}.

The experimental results obtained here may be compared with the very recent relativistic configuration-interaction (RCI) calculations by O'Malley and Beck [54]. They report $^4S_{3/2}$-$^2D_{3/2,5/2}$ splittings of 5903 and 6493 cm^{-1}, respectively, compared to our experimental values of 5762.48(10) and 6512.37(10) cm^{-1}. This is very satisfactory agreement, considering the complexity of the 51-electron system Sn^-. (Equally good agreement between measured and calculated level splittings was previously found in the case of Sb^- [16].)

The RCI calculation of O'Malley and Beck also provided $M1$ transition probabilities of 0.744 and 0.00420 s^{-1} for $^4S_{3/2}\leftarrow{}^2D_{3/2,5/2}$, respectively [54]. These $M1$ transition probabilities strongly depend on a small (~0.1%) admixture of $^2D_{3/2}$ into the $^4S_{3/2}$ state. With this in mind, they have

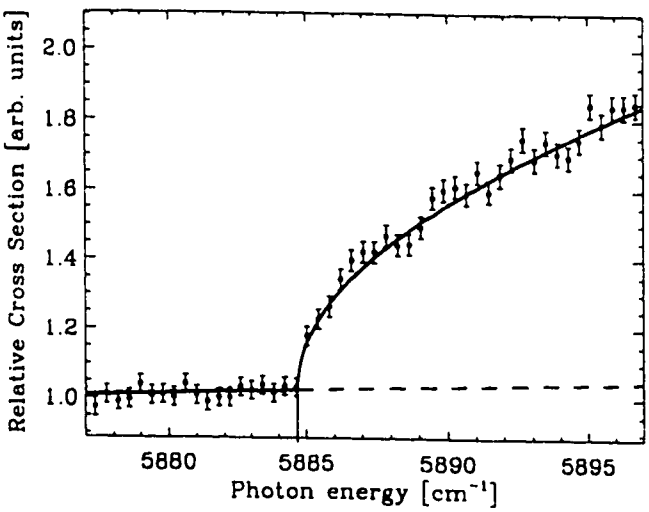

FIG. 16. Measured photodetachment cross section of Sn^- in the region of the $^2D_{5/2}\rightarrow{}^3P_2$ threshold. The result of a Wigner s-wave fit to the data is indicated by the solid line.

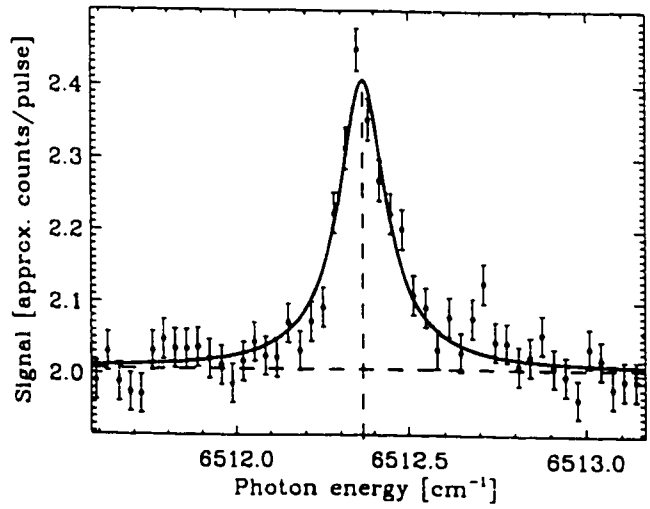

FIG. 17. Two-photon detachment yield in the vicinity of the $^4S_{3/2}\rightarrow{}^2D_{5/2}$ $M1$ resonance. The solid line represents a Lorentzian fit. Each data point corresponds to the signal from 3000 laser pulses.

TABLE IV. Summary of measured binding energies and fine structure splittings.

Ion	This work	Previous works	Ref.
	$^4S_{3/2}$ binding energy (eV)		
C^-	1.262119(20)	1.2629(3)	[5]
Si^-	1.389521(20)	1.38949(6)	[47]
Ge^-	1.232712(15)	1.23273(5)	[47]
Sn^-	1.112067(15)	1.11209(6)	[47]
Pb^-	a	0.364(8)	[56]

Ion	This work $J=3/2$	This work $J=5/2$	Previous works (term average)	Ref.
	^2D binding energies (eV)			
C^-	a	a	0.033(1)	[5]
Si^-	0.527234(25)	0.525489(20)	0.523(5)	[46]
Ge^-	0.40144(10)	0.37757(6)	0.4(2)	[4]
Sn^-	0.397617(15)	0.304635(15)	0.4(2)	[4]

Ion	Measured	Extrapolated	Ref.
	^2D fine-structure splitting (cm^{-1})		
C^-	a	3(1)	[45]
Si^-	14.08(20)	7(2)	[45]
Ge^-	192.6(9)	160(30)	[45]
Sn^-	749.95(15)	800(200)	[45]

[a]Could not be measured in the present study.

revised their transition rates by more carefully treating the correlation of the $^2D_{3/2}$ level in the calculation of the $^4S_{3/2}$ wave function. They report revised $M1$ rates of 0.0791 and 0.004 31 s^{-1} as well as $E2$ rates of 0.003 49 and 0.005 91 s^{-1} for $^4S_{3/2}\leftarrow{}^2D_{3/2,5/2}$, respectively [55]. Based on these numbers, which are somewhat smaller than the isoelectronically extrapolated values given above, the two transitions should differ in strength by a factor of 8, whereas an intensity ratio of 15 is observed.

E. Summary and outlook

The results of our infrared photodetachment studies of the carbon group negative ions C^-, Si^-, Ge^-, and Sn^- are summarized in Table IV. Values obtained in previous experimental investigations or isoelectronically extrapolated values are given for comparison. The negative ion of lead, the last element in the carbon group, was not investigated here. Pb^- beams are very difficult to produce with a cesium sputter source. In various attempts with lead metal as well as lead oxide cathodes we were not able to produce more than ~10 pA of Pb^-, which was insufficient for a determination of the EA-defining $^4S_{3/2}\rightarrow{}^3P_0$ threshold. However, the EA of lead has been measured previously [56] and the ^2D and ^2P terms of Pb^- are expected to be unstable, on the basis of isoelectronic extrapolation. Hence highly accurate binding energies are now available for almost all stable states of the carbon group negative ions. The remaining exceptions are the $C^-(^2D_J)$, $Si^-(^2P_J)$, and $Pb^-(^4S_{3/2})$ levels. As outlined earlier, these levels could be measured via infrared photodetachment threshold spectroscopy if alternative ion-beam production techniques such as charge exchange, and possibly state-selective detection schemes were utilized (discussed in detail in Ref. [22]).

In terms of multiphoton detachment, the observation of the $^4S_{3/2}\rightarrow{}^2D_{5/2}$ resonance in Sn^- has demonstrated that laser-driven transitions into metastable ionic levels with radiative lifetimes as long as ~100 s are currently possible. Different storage rings (e.g., ELISA in Aarhus, Denmark) may in fact enable accurate lifetime measurements of such long-lived ionic states. Further improved or alternative tunable infrared laser sources such as optical parametric oscillators may provide wider tuning ranges, higher repetition rates, and/or more energetic pulses. Somewhat shorter pulses, say, 100 ps, could provide higher intensities and thus increase the probabilities of nonlinear processes, without additional spectral broadening. In some of the cases investigated here, resonant enhancements in multiphoton detachment spectra were expected on the basis of computer simulations, but not observed due to a substantial photodetachment background from excited ionic levels. In such cases, a strong laser pulse could be employed to deplete the excited level population of the ion beam via saturation detachment, before the ion beam is electrostatically deflected into the interaction region where the actual multiphoton detachment takes place. So far, multiphoton experiments that were aimed at excited states of atomic negative ions all employed photons in the optical regime. However, many possibilities seem to exist for resonant detachment schemes that involve photons of very different frequencies, e.g., in the optical and microwave regime. Combinations of laser and microwave sources have been successfully used in the past to study the hyperfine structure of $^{33}S^-$ [57] and the threshold detachment of S^- and Cl^- [42].

IV. CONCLUSION

This article has presented the results of a spectroscopic study of the C^-, Si^-, Ge^-, and Sn^- ions. A tunable infrared laser source and a combination of single- and multiphoton detachment schemes were employed to very accurately determine most of the stable states of these ions (σ <0.1 meV). The $C^-(^2D_J)$ and $Si^-(^2P_J)$ fine-structure splittings now remain the only undetermined structural features of the five carbon group negative ions.

ACKNOWLEDGMENTS

We gratefully acknowledge the Natural Science and Engineering Research Council of Canada (NSERC) for their support of this work. We also wish to thank J. D. Garrett for manufacturing the various sputter cathodes.

[1]

[1] C. Blondel, Phys. Scr. **T58**, 31 (1995).
[2] D. R. Bates, Adv. At., Mol., Opt. Phys. **27**, 1 (1991); T. Andersen, Phys. Scr. **T34**, 23 (1991).
[3] S. J. Buckmann and C. W. Clark, Rev. Mod. Phys. **66**, 539 (1994); T. Andersen, H. H. Andersen, P. Balling, P. Kristensen, and V. V. Petrunin, J. Phys. B **30**, 3317 (1997).
[4] H. Hotop and W. C. Lineberger, J. Phys. Chem. Ref. Data **14**, 731 (1985).
[5] D. Feldmann, Z. Phys. A **277**, 19 (1976).
[6] M. Scheer, R. C. Bilodeau, and H. K. Haugen, Phys. Rev. Lett. **80**, 2562 (1998).
[7] M. Scheer, R. C. Bilodeau, J. Thógersen, and H. K. Haugen, Phys. Rev. A **57**, R1493 (1998).
[8] J. L. Hall, E. J. Robinson, and L. M. Branscomb, Phys. Rev. Lett. **14**, 1013 (1965).
[9] W. C. Lineberger and T. A. Patterson, Chem. Phys. Lett. **13**, 40 (1972).
[10] M. D. Davidson, H. G. Muller, and H. B. van Linden van den Heuvell, Phys. Rev. Lett. **67**, 1712 (1991); H. Stapelfeldt, P. Balling, C. Brink, and H. K. Haugen, *ibid.* **67**, 1731 (1991); C. Blondel, M. Crance, C. Delsart, and A. Giraud, J. Phys. B **24**, 3575 (1991).
[11] R. Trainham, G. D. Fletcher, and D. J. Larson, J. Phys. B **20**, L777 (1987).
[12] C. Y. Tang *et al.*, in *Multiphoton Processes*, edited by G. Mainfray and P. Agostini (SPA, Saclay, 1990), p. 69.
[13] R. Trainham, G. D. Fletcher, N. B. Mansour, and D. J. Larson, Phys. Rev. Lett. **59**, 2291 (1987); M. D. Davidson, J. Wals, H. G. Muller, and H. B. van Linden van den Heuvell, *ibid.* **71**, 2192 (1993).
[14] P. Kristensen *et al.*, Phys. Rev. Lett. **71**, 3435 (1993); J. Thógersen *et al.*, Phys. Rev. A **53**, 3023 (1996).
[15] J. Thógersen, M. Scheer, L. D. Steele, H. K. Haugen, and W. P. Wijesundera, Phys. Rev. Lett. **76**, 2870 (1996).
[16] M. Scheer, H. K. Haugen, and D. R. Beck, Phys. Rev. Lett. **79**, 4104 (1997).
[17] H. Stapelfeldt *et al.*, Phys. Rev. A **50**, 1618 (1994).
[18] A. Stintz *et al.*, Phys. Rev. Lett. **75**, 2924 (1995).
[19] V. K. Ivanov and L. P. Krukovskaya, J. Phys. B **27**, 4111 (1994); C. A. Ramsbottom, K. L. Bell, and K. A. Berrington, *ibid.* **26**, 4399 (1993); G. F. Gribakin, A. A. Gribakina, B. V. Gul'tsev, and V. K. Ivanov, *ibid.* **25**, 1757 (1992).
[20] P. Balling, P. Kristensen, H. Stapelfeldt, T. Andersen, and H. K. Haugen, J. Phys. B **26**, 3531 (1993).
[21] G. Haeffler, D. Hanstorp, I. Yu Kiyan, U. Ljungblad, H. H. Andersen, and T. Andersen, J. Phys. B **29**, 3017 (1996).
[22] M. Scheer, C. A. Brodie, R. C. Bilodeau, and H. K. Haugen, Phys. Rev. A (to be published).
[23] W. K. Bischel and M. J. Dyer, Phys. Rev. A **33**, 3113 (1986); E. C. Looi, J. C. Stryland, and H. L. Welsh, Can. J. Phys. **56**, 1102 (1978), and references therein.
[24] R. Middleton, Nucl. Instrum. Methods Phys. Res. **214**, 139 (1983).
[25] E. P. Wigner, Phys. Rev. **73**, 1002 (1948).
[26] J. W. Farley, Phys. Rev. A **40**, 6286 (1989); T. F. O'Malley, Phys. Rev. **137**, A1668 (1964).
[27] R. C. Bilodeau, M. Scheer, and H. K. Haugen, J. Phys. B (to be published).
[28] P. C. Engelking and W. C. Lineberger, Phys. Rev. A **19**, 149 (1979).
[29] L. Minnhagen, J. Opt. Soc. Am. **63**, 1185 (1973).
[30] J. R. Nestor, Appl. Opt. **21**, 4154 (1982).
[31] D. M. Neumark, K. R. Lykke, T. Andersen, and W. C. Lineberger, Phys. Rev. A **32**, 1890 (1985).
[32] R. A. Bennett and J. L. Hall (unpublished). The results are quoted in Ref. [33].
[33] D. Feldmann, Chem. Phys. Lett. **47**, 338 (1977).
[34] V. A. Oparin, R. N. Il'in, I. T. Serenkov, and E. S. Solov'ev, Zh. Éksp. Teor. Fiz. **66**, 2008 (1974) [Sov. Phys. JETP **39**, 989 (1974)].
[35] G. Haeffler, D. Hanstorp, I. Kiyan, A. E. Klingmuller, and U. Ljungblad, Phys. Rev. A **53**, 4127 (1996).
[36] T. Noro, M. Yoshimine, M. Sekiya, and F. Sasaki, Phys. Rev. Lett. **66**, 1157 (1991); K. Raghavachari, J. Chem. Phys. **82**, 4142 (1985); R. A. Kendall, T. H. Dunning, Jr., and R. J. Harrison, *ibid.* **96**, 6796 (1992).
[37] C. Froese Fischer, J. Phys. B **26**, 855 (1993).
[38] C. Froese Fischer, A. Ynnerman, and G. Gaigalas, Phys. Rev. A **51**, 4611 (1995).
[39] E. R. Cohen and B. N. Taylor, Rev. Mod. Phys. **59**, 1121 (1987).
[40] E. B. Saloman, Spectrochim. Acta B **45**, 37 (1990); **47**, 517 (1992).
[41] N. D. Gibson, B. J. Davies, and D. J. Larson, Phys. Rev. A **47**, 1946 (1993); C. H. Greene and N. Rouze, Z. Phys. D **9**, 219 (1988); P. Frey, F. Breyer, and H. Hotop, J. Phys. B **11**, L589 (1978).
[42] M. C. Baruch, W. G. Sturrus, N. D. Gibson, and D. J. Larson, Phys. Rev. A **45**, 2825 (1992).
[43] D. J. Pegg, C. Y. Tang, J. Dellwo, and G. D. Alton, J. Phys. B **26**, L789 (1993).
[44] D. H. Lee, W. D. Brandon, D. J. Pegg, and D. Hanstorp, Phys. Rev. A **56**, 1346 (1997).
[45] H. Hotop and W. C. Lineberger, J. Phys. Chem. Ref. Data **4**, 539 (1975).
[46] A. Kasdan, E. Herbst, and W. C. Lineberger, J. Chem. Phys. **62**, 541 (1975).
[47] J. Thógersen, L. D. Steele, M. Scheer, C. A. Brodie, and H. K. Haugen, J. Phys. B **29**, 1323 (1996).
[48] D. Calabrese, A. M. Covington, J. S. Thompson, R. W. Marawar, and J. W. Farley, Phys. Rev. A **54**, 2797 (1996).
[49] C. Mendoza and C. J. Zeippen, Mon. Not. R. Astron. Soc. **194**, 1 (1981).
[50] T. M. Miller, A. E. Stevens Miller, and W. C. Lineberger, Phys. Rev. A **33**, 3558 (1986).
[51] D. Feldmann, R. Rackwitz, E. Heinicke, and H. J. Kaiser, Z. Naturforsch. A **32A**, 302 (1977).
[52] E. Biémont and J. E. Hansen, Phys. Scr. **33**, 117 (1986).
[53] E. Biémont, J. E. Hansen, P. Quinet, and C. J. Zeippen, Astron. Astrophys., Suppl. Ser. **111**, 333 (1995).
[54] S. M. O'Malley and D. R. Beck, Phys. Rev. A **57**, 1743 (1998).
[55] S. M. O'Malley and D. R. Beck (private communication).
[56] C. S. Feigerle, R. R. Corderman, and W. C. Lineberger, J. Chem. Phys. **74**, 1513 (1981).
[57] R. Trainham, R. M. Jopson, and D. J. Larson, Phys. Rev. A **39**, 3223 (1989).

Paper 6

Laser Spectroscopic Measurements of Binding Energies and Fine Structure Splittings of Co^-, Ni^-, Rh^-, and Pd^-.

Michael Scheer, Cicely A. Brodie, René C. Bilodeau, and Harold K. Haugen.

Physical Review A **58**, issue 3 (September 1998).

Laser spectroscopic measurements of binding energies and fine-structure splittings of Co^-, Ni^-, Rh^-, and Pd^-

Michael Scheer, Cicely A. Brodie, René C. Bilodeau, and Harold K. Haugen*
Department of Physics and Astronomy, McMaster University, Hamilton, Ontario, Canada L8S 4M1
(Received 20 April 1998)

A tunable infrared laser source is utilized to study the photodetachment threshold spectra of the transition-metal negative ions Co^-, Ni^-, Rh^-, and Pd^-. The binding energies of the respective ionic ground states are found to be 663.3(6), 1157.16(12), 1142.89(20), and 562.14(12) meV. In addition, a $^3F_4 - {}^3F_3$ fine-structure splitting of 875(15) cm^{-1} is measured for Co^-, and the $^2D_{5/2} - {}^2D_{3/2}$ splitting of Ni^- is determined to be 1485(3) cm^{-1}. For Pd^-, the electronically excited $4d^9 5s^2\ {}^2D_{5/2}$ state is found to lie 1127(4) cm^{-1} above the $4d^{10}5s\ {}^2S_{1/2}$ ionic ground state, i.e., it is bound by 422.4(5) meV. The results agree with previous values obtained from laser photodetached electron spectra, but constitute improvements in accuracy of up to two orders of magnitude. [S1050-2947(98)05009-4]

PACS number(s): 32.80.Gc, 32.10.Hq, 32.10.Fn

I. INTRODUCTION

Over the past three decades negative ions have attracted considerable attention from theorists as well as experimentalists due to both their fundamental and practical implications. More recent efforts have investigated various species and phenomena such as molecular ions [1], continuum resonances [2], metastable states [3], ions in strong fields [4], and resonant multiphoton detachment [5–7]. Progress in the knowledge of binding energies in atomic negative ions has continued since the 1985 review article by Hotop and Lineberger [8]. Still, the stable negative ion states of many elements remain only poorly known, and in some cases even totally unknown.

Most experimental determinations of negative ion binding energies are based on either laser photodetachment threshold (LPT) studies or laser photodetached electron spectrometry (LPES). LPES is a powerful technique, as it can be applied to virtually any stable negative ion, irrespective of the binding energy to be measured. The accuracy of measured energy values is, however, limited to the resolution of the electron spectrometer, which is typically a few meV. Accuracies of LPT measurements, on the other hand, range from 0.1 to 0.001 meV, as they are often only limited by the laser bandwidth. The constraint on LPT studies involving detachment to the atomic ground state is that the tunable photon energies have to match the ionic binding energies. Most previous LPT studies have utilized visible laser light and have therefore been restricted to systems with electron affinities (EA's) larger than 1.4 eV. (A notable exception are the alkali-metal and alkaline-earth negative ions, where detachment to excited states of the respective atoms and state selective detection schemes were employed [3,9].) In particular, of the 25 transition metals that are expected or known to form stable negative ions, only the strongly bound Ir^-, Pt^-, and Au^- ions have been previously investigated via LPT methods. The applicability of *infrared* LPT to the study of weakly bound negative ions (the EA is less than 1 eV) was first demonstrated by Feldmann [10]. This investigation of P^-, and our recent studies of B^- [11] and Al^- [12], have shown that infrared LPT spectroscopy can provide accurate electron affinities as well as ionic fine-structure splittings.

The fine structure of the initial ionic and the final atomic state is manifested in the photodetachment spectrum as a series of cascaded thresholds. For each of these thresholds, Wigner's threshold law for photodetachment [13] predicts a partial cross section proportional to $\varepsilon^{\ell+1/2}$, where ε is the energy of the detached electron and ℓ is its angular momentum. In the above cases of ions with valence p electrons, the detached electron carries no angular momentum. This makes the onset of detachment sudden and conspicuous, and an accurate determination even of the higher-lying fine-structure thresholds becomes possible. The situation is significantly different for transition-metal negative ions, since they detach into a p-wave continuum. The onset of detachment is smooth and slow, and a determination of the actual threshold depends sensitively on a p-wave fit to the data above threshold. Series of cascaded p-wave thresholds are thus expected to be challenging and, to our knowledge, have not been studied previously.

It is the aim of the present paper to determine the feasibility of LPT spectroscopy for fine-structure measurements in transition-metal negative ions. Co^-, Ni^-, Rh^-, and Pd^- are chosen, as the fine structure of these systems has been previously investigated with LPES; a comparison of the two techniques is therefore possible. Early theoretical treatments of these four ions have employed semiempirical methods [14] such as horizontal analysis [15] or isoelectronic extrapolation [16] to obtain estimated EA values. *Ab initio* calculations of atomic EA's for systems with an open d shell are extremely challenging. Both electron correlations and relativistic effects play an important role [17]. To our knowledge, the errors associated with the EA calculations presented to date [18] are still significantly larger than the uncertainties of the respective experimental (LPES) values.

*Also with the Department of Engineering Physics, the Brockhouse Institute for Materials Research, and the Center for Electrophotonic Materials and Devices.

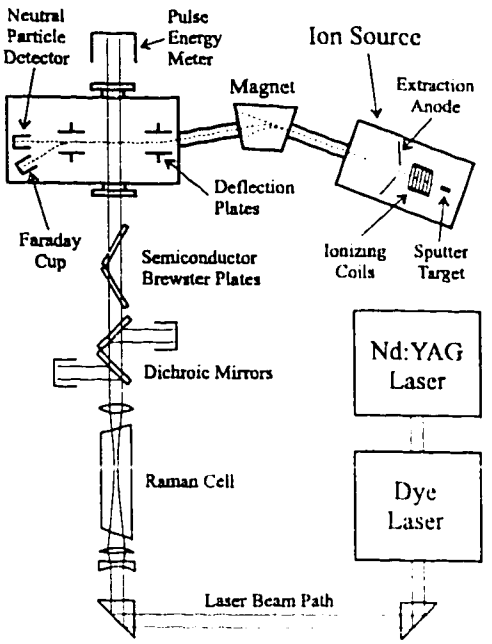

FIG. 1. Schematic diagram of the experimental setup. See text for details.

II. EXPERIMENTAL PROCEDURES

Figure 1 gives a schematic overview of the experimental apparatus that was used in the photodetachment studies described herein. The setup consists of a negative ion beam apparatus and an infrared laser source, arranged in a crossed-beam geometry. The beam apparatus is comprised of a cesium sputter source, a bending magnet, an interaction chamber, and detection electronics. The infrared laser source includes a Nd:YAG (neodymium:yttrium-aluminum-garnet) laser, a dye laser, and various optical components for wavelength conversion and filtering.

A. Ion-beam apparatus

The ion source is a home-built version of the high-intensity cesium sputter source developed by Middleton. The principle of operation of this type of negative ion source is described in detail elsewhere [19]. In brief, a continuous flow of cesium vapor is admitted into the evacuated (pressure $\lesssim 10^{-6}$ mbar) source chamber, where some of the cesium atoms condense on the cooled surface of the sputter target, while others are ionized by a heated tantalum coil. The target is negatively biased with respect to the ionizer such that the Cs^+ ions are accelerated and electrostatically focused onto the target. The cesium layer on the target reduces the effective work function of the sputter surface, and thereby greatly enhances the probability that an atom (or molecule) of the target material picks up an extra electron as it is sputtered off the surface. Once formed, the negative ions are accelerated through the ionizer and a subsequent extraction anode. Typical voltage settings in the experiments described here were 4 kV for the target bias and 10 kV for the extraction anode. The extracted ion beam is collimated with the aid of an electrostatic Einzel lens (not shown in Fig. 1), and then magnetically deflected through 30°. The magnet is operated at fields of $\lesssim 5.2$ kG, which enables a reasonable mass separation of the various ion-beam components ($\Delta M/M \approx 5\%$). Since cesium sputter sources operate with solid targets, the beam composition can indeed be manifold. In addition to atomic negative ions, the ions of dimers and trimers are often present, as well as the ions of oxides and various compounds which result from target impurities or from reactions of the target with the background gas of the source. In cases where the masses of atomic and molecular ions cannot be separated, the problem is often alleviated by the fact that most prolific molecular ions are too strongly bound to be photodetached by infrared light [1].

While the various source parameters are generally optimized to yield maximum beam currents of the ion species of interest, the present study also had to be concerned with the fractional population of different negative ion levels. The temperature of the sputter area gives rise to a Boltzmann population of the ionic energy levels, based on the assumption that the negative ions are able to thermalize before leaving the sputter surface. This temperature should depend on the energy and current of the sputter beam [19], but also on the size of the sputter area. The latter can be easily varied by moving the target back or forth. It was found that this has only a small effect on the total beam current but a significant effect on the population of excited ion levels. As expected, large excited level populations are obtained with the sputter target on focus, whereas the excited ion-beam currents are up to two orders of magnitude smaller with the target off focus. These tests and estimates based on previous photodetachment studies of Se^- and Te^- [20] indicate a range of 500–1500 K for the effective temperature of the sputter source.

Negative ions from a keV ion beam are easily detached in collisions with rest gas molecules, hence the background signal in a measurement of photodetachment events strongly depends on the collisional detachment rate. As this rate is proportional to the rest gas pressure, the photon-ion interaction is carried out in an ultrahigh vacuum (UHV) chamber at pressures of less than 10^{-8} mbar. The ion beam is fed into the interaction chamber through a differential pressure tube. Although the transmitted beam current is typically reduced by a factor of 2–5 the reduction in rest gas pressure of over two orders of magnitude still warrants a significant net improvement in the signal-to-background ratio. In the UHV chamber the ion beam is deflected through 10° by a pair of electrostatic deflection plates which removes any neutral particles from the beam, and brings the beam on axis with the detector. The ion beam then passes through the interaction region where it is crossed at 90° by a pulsed laser beam. A second pair of electrostatic deflection plates, located behind the interaction region, deflects the residual ion beam into a Faraday cup, while neutral particles that were produced in the photon-ion interaction remain unaffected and finally impinge on the open cathode of a discrete-dynode electron multiplier. The signal from the electron multiplier is passed through a fast preamplifier to minimize electronic noise, and is then fed into a gated integrator and boxcar averager. The gate is typically set to 50 ns, which provides a sufficiently large window for the detection of all photodetachment events resulting from a ≈ 8-ns laser pulse, and at the same time facilitates a substantial suppression of the collisional background count, down to ~ 0.1 events for a typical beam current of 100 nA. The data acquisition window is delayed by 1–2 μs relative to the laser pulse in order to accommodate the flight time of the photodetached neutral particles from the

interaction region to the detector. The time-of-flight difference between species of slightly different mass in fact enables a factor of 2 improvement in mass separation ($\approx 2\%$) if narrow gates and a tightly collimated (or focused) laser beam are used. In the experiments described here, the number of photodetachment events per pulse was usually larger than one, which is the reason the data acquisition was conducted via analog signal integration rather than digital pulse counting. Consequently, special care had to be taken that the electron multiplier would operate in a linear regime. The data are finally read from the boxcar averager by a personal computer for further processing.

B. Infrared laser source

The generation of tunable infrared light is based on a Nd:YAG laser, a Lumonics YM-800. The laser is operated with a Q-switched cavity, i.e., in a pulsed mode with a 10-Hz repetition rate. It is optimized to provide maximum output at 532 nm, the second harmonic of the fundamental YAG wavelength, with up to 400 mJ of energy in a ≈ 8 ns pulse. The pulse energy is stabilized against temperature drifts by purging the laser housing with cool nitrogen gas. The 532-nm laser pulse is used to pump a Lumonics HD-300 dye laser. This laser is operated with a 1800 lines/mm grating rather than the more common 2400 lines/mm grating in order to enable tunability over the 680–980 nm range. For this tuning range the spectral bandwidth of the laser ranges from 0.1 to 0.06 cm^{-1}. Accurate dye laser wavelength calibrations are routinely performed with a hollow cathode discharge lamp (made by Hamamatsu). Discharge lamps yield an optogalvanic effect, i.e., a measurable change in the discharge impedance whenever the laser wavelength is in resonance with certain atomic transitions of the filler gas [21]. In light of the near-infrared tuning range of our dye laser setup, argon is chosen as the filler gas as it offers many accurately known and optogalvanically active transitions ranging from 670 to 1150 nm [22].

The dye laser is optimized to achieve maximum pulse energies which results in a somewhat reduced quality of the spatial pulse profile. Typical pulse energies are 50 mJ at 700 nm, and 25 mJ at 950 nm. The associated peak powers of $\approx 10^7$ W are sufficient to achieve frequency conversion through the nonlinear optical properties of various media. In the present case, conversion of the dye laser pulses further into the infrared was tested with two different methods, difference frequency mixing in nonlinear optical crystals, and stimulated Raman scattering in a single-pass high-pressure hydrogen cell. The latter approach was finally chosen, as it provides a broader infrared tuning range with a simpler and less delicate optical setup. A 120-cm-long, 8-mm-diameter cell is used, filled with H_2 at a pressure of ≈ 22 bar. Good conversion of the dye laser pulse into first Stokes radiation (with quantum efficiencies of up to 40%) is achieved by focusing the ≈ 3-mm-diameter beam into the center of the cell. A Galilean telescope ($f_1 = -5$ cm, $f_2 = 10$ cm) with an effective focal length of ≈ 90 cm was utilized for this purpose. As stimulated Raman scattering is a coherent (although nonlinear) optical process, spatial, spectral, and temporal properties of the dye laser pulse are generally adopted by the first Stokes pulse. For a measured cell pressure of 22(1) bar

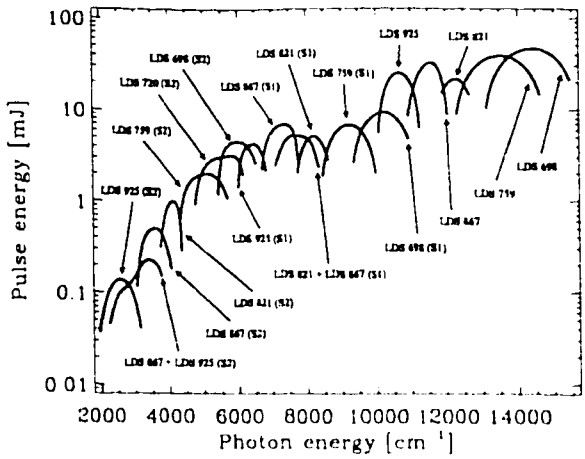

FIG. 2. Pulse energy curves for selected laser dyes and for the associated first and second Stokes conversions [indicated with the labels ($S1$) and ($S2$), respectively].

a Raman shift of 4155.187(5) cm^{-1} is expected, based on accurate studies of the pressure dependence of the fundamental Raman band in H_2 [23]. In addition, for first Stokes wavelengths shorter than 1150 nm the optogalvanic lamp could be used for a direct calibration of the Raman-shifted light. This yielded a shift of 4155.197(20) cm^{-1}, in excellent agreement with the literature value. The dye laser tuning range of 680–980 nm translates into a 950–1650-nm tuning range for the first Stokes light, although the use of different dyes is required for different regions of the tuning range. This is illustrated in Fig. 2, which shows pulse energy curves for the different dyes and their first and second Stokes conversions.

Conversion to second Stokes radiation becomes necessary whenever tunability beyond 1650 nm is required. Raman scattering of the first Stokes radiation, i.e., *sequential* stimulated Raman scattering would appear to be the most likely process for the generation of second Stokes radiation. However, the sequential scattering process has to compete against another nonlinear process, namely, parametric four-wave mixing, where the nonlinear susceptibility $\chi^{(3)}$ of the medium acts as the mixing parameter. Parametric four-wave mixing exhibits a somewhat different intensity and wavelength dependence than stimulated Raman scattering. As a result, it has been shown that Raman cells of sophisticated design are capable of suppressing the parametric process or at least some of its undesired properties. Such cells are Herriott-type multipass cells with refocusing geometry [24], or single-pass cells with capillary confinement of the focused laser beam [25]. Both these designs rely on a significant extension of the focused path length, which cannot be achieved with a simple single-pass cell. Hence, with the present setup second Stokes generation has to proceed via parametric four-wave mixing. The disadvantages of this process are an inevitable generation of various anti-Stokes orders, a lower theoretically achievable conversion efficiency, and the requirement of phase matching between the mixed waves. Despite the small dispersion of H_2 gas, the phase-matching requirement noticeably affects the spatial beam profiles; in contrast to the essentially Gaussian profiles of the dye laser and first Stokes beams, the second Stokes and anti-Stokes beam profiles are donut shaped, with an almost zero intensity at the center. Commensurate with its high order of

nonlinearity, the four-wave mixing process is found to be strongly dependent on the laser-pulse energy, the beam quality, and the focusing geometry, but only moderately dependent on the cell pressure, in agreement with other studies [26]. For the 3-mm-diameter dye laser beam used here, best results are obtained with a focal length around 120 cm and a focal position close to the exit window of the cell. The increased path length before the focus is believed to enhance the generation of first Stokes photons before the focus is reached, which then results in a more effective seeding of the four-wave mixing process [26]. For a dye laser tuning range of 680–980 nm, a second Stokes wavelength range of 1.6–5.2 μm is obtained, as shown in Fig. 2. Quantum conversion efficiencies of up to 25% are realized at shorter wavelengths, which is only a factor of 2 less than the efficiency achieved with multipass cells [24]. Although the conversion efficiency drops for longer wavelengths (down to 2% at 5 μm), it was still found to be sufficient in most of the photodetachment studies.

Further Raman conversion, i.e., the generation of third Stokes radiation is expected to be rather inefficient in a single-pass cell. In fact, we found no evidence of the presence of a third Stokes component in the Raman cell output, even for the most energetic pulses at 680 nm. Hence, the use of laser dyes that operate in the near infrared rather than the visible regime is of great advantage whenever a single-pass cell is utilized.

Various combinations of optical filters are employed to eliminate the unwanted wavelength components from the Raman cell output. In experiments that require the use of first Stokes radiation long-pass filters made from Schott glass are often sufficient to remove the dye laser and anti-Stokes wavelengths. Two rectangular filters are used, tilted in opposite directions to Brewster's angle. This minimizes reflection losses without introducing a lateral beam displacement. In cases where the second Stokes wavelength falls within the transmission range of the glass filter, no further filtering is deemed necessary as the presence of second Stokes radiation should not affect an experiment that uses the first Stokes beam. Whenever dye laser wavelengths beyond 800 nm or first Stokes radiation have to be suppressed, pairs of 45° dichroic mirrors are utilized to attenuate the unwanted beam components by $\approx$90%. The final filtering is then achieved with a Brewster-angle pair of semiconductor plates, made from either silicon or germanium. In all cases, a CaF_2 lens with an appropriate focal length is used to recollimate the Raman cell output such that the desired wavelength component would have a beam diameter of 3–5 mm. The infrared laser beam is finally transmitted via CaF_2 viewports through the interaction chamber, where it crosses the ion beam perpendicularly. The alignment of the crossing angle is crucial but had to be carried out only once (as described in Ref. [33]). This is a major advantage of using filters rather than dispersing prisms as wavelength-selective components; the laser-beam alignment becomes wavelength independent. A pyroelectric energy meter located behind the exit window is utilized to monitor the energy of the laser pulses. The energy meter as well as the entire infrared optics table are sealed off and purged with dry nitrogen gas, as infrared absorption-bands of atmospheric molecules such as CO_2 or H_2O would otherwise lead to a substantial laser-beam attenuation.

C. Data acquisition and analysis

The photodetachment cross section in the vicinity of a given threshold is recorded by performing a slow dye laser scan (20–30 min) over an appropriate wavelength range. The wavelength range is usually adjusted to provide sufficient information for both the region below and the region above threshold, which is particularly important in the case of p-wave detachment (see below). Depending on the ion-beam currents and infrared pulse energies available for a particular experiment, the signal-to-noise ratio of a single scan is often insufficient. The scan procedure is then repeated up to ten times, and individual scans are added together. The photodetachment data are finally normalized against ion-beam current and infrared pulse energy, which are recorded in all scans parallel to the neutral particle signal.

1. Threshold fit

After conversion of the scan range from dye laser wavelength to infrared photon energy, Wigner's p-wave threshold law [13] is fitted to the data. For any p-wave photodetachment channel the threshold law predicts a vanishing cross section for photon energies, ε, below the threshold energy, ε_0, whereas a cross section proportional to $(\varepsilon-\varepsilon_0)^{3/2}$ is predicted for $\varepsilon>\varepsilon_0$. However, in most of the cases investigated here other open photodetachment channels have to be taken into account. As long as the thresholds of these other channels are not too close to ε_0, their contributions to the total cross section in the vicinity of ε_0 are generally smooth and can be represented by a linear term. Therefore, the function that is fitted to the measured cross section is given by

$$\sigma=\begin{cases} a_0+a_1(\varepsilon-\varepsilon_0)+a_2(\varepsilon-\varepsilon_0)^{3/2} & \text{for } \varepsilon>\varepsilon_0 \\ a_0+a_1(\varepsilon-\varepsilon_0) & \text{for } \varepsilon<\varepsilon_0 . \end{cases} \quad (1)$$

Two different methods of fitting this equation to the data are utilized. The first method employs a multiparameter gradient-expansion algorithm to perform a nonlinear least-squares fit. The fitting parameters a_0, a_1, a_2, and ε_0 are optimized simultaneously. In the second method a linear least-squares fit to the data below threshold is carried out first, in order to determine the photodetachment background. The fitted background is then subtracted from the data, which are subsequently linearized by exponentiating with 2/3. A linear least-squares fit finally provides the threshold value ε_0.

In previous studies of p-wave thresholds either one or the other method was used. For example, of the three independent LPT studies of the EA of platinum, the two more recent works [27,28] employed the first method while the earlier study [30] utilized the second method. The results of these studies differ by more than the respective error margins would suggest.

In comparison, the first fitting method constitutes a more rigorous approach, and also provides well-defined standard deviations for the fitted parameters. We found, however, that this method would also overcompensate for small systematic deviations from a p-wave curvature above threshold, through a small shift of the background line. This effect is due to the very slow increase of the p-wave cross section at threshold, and results in a small systematic shift of the fitted threshold

value. The second method, on the other hand, tends to undercompensate for systematic deviations in the above-threshold data. Hence the average of the two fitted threshold values is adopted as the final result. Its uncertainty is evaluated from the difference between the two fitted values and from the standard deviation obtained with the first method.

Although Eq. (1) is an exact description of the photodetachment cross section close to threshold, systematic deviations may occur at the high-energy end of a threshold scan. In this case, correction terms to the Wigner law would have to be taken into account [29]. However, previous studies of p-wave thresholds [30,10] have shown that the range of validity of the Wigner law is clearly larger for p-wave detachment than for s-wave detachment. Hence an inclusion of higher-order terms to the fitting function [Eq. (1)] is not deemed necessary here. Of more concern are possible systematic deviations from the Wigner threshold behavior due to a saturation of the detachment process, i.e., a depletion of the ionic levels by the intense laser pulse. The linearity of detachment signal versus pulse energy is therefore checked on a case to case basis. In some cases it is possible to optimize the signal-to-background ratio by adjusting the (average) pulse intensity such that the background channels are saturated while the threshold channel is still linear.

2. Threshold strength

The presence of more than one photodetachment channel is due to the existence of different electronic configurations, terms, or fine-structure levels in either the ion or the atom. For an ionic electron configuration with only one open shell (which is the d shell for most transition metal ions) the intensity for photodetachment from an ionic ^{2S+1}L term to an atomic $^{2S'+1}L'$ term is given by

$$I(LS,L'S') \propto n_l |\langle SL\{|S'L'\}l\rangle|^2 \times \sum_{l'=|l-1|}^{l+1} |\langle l\|\mu\|l'\rangle|^2. \quad (2)$$

Here n_l is the number of electrons in the open shell of the ion, $\langle SL\{|S'L'\}l\rangle$ is the fractional parentage coefficient for the decomposition of the ionic ^{2S+1}L term into an atomic $^{2S'+1}L'$ term and an l electron, and $\langle l\|\mu\|l'\rangle$ is the reduced matrix element of the electric dipole moment operator for the photodetachment of a bound l electron into the $\varepsilon l'$ continuum [31,32]. This $^{2S+1}L \rightarrow {}^{2S'+1}L'$ photodetachment transition is further composed of up to $(2S+1)(2S'+1)$ fine-structure transitions. In the case that the spin-orbit coupling of the electrons can be approximated by LS coupling, the relative intensity of a fine-structure transition $J \rightarrow J'$ is given by

$$I(J,J') \propto \sum_{j=|l-1/2|}^{l+1/2} (2j+1)(2J+1)(2J'+1) \times \begin{Bmatrix} S & L & J \\ \frac{1}{2} & l & j \\ S' & L' & J' \end{Bmatrix}^2 \exp\left(\frac{-E(J)}{kT}\right), \quad (3)$$

where l and j denote orbital and total angular momenta of the bound electron that is to be detached. (Note that the angular momentum l' of the detached electron, which determines the shape of the threshold, is not relevant here.) The properties of the $9J$ symbol in Eq. (3) determine the selection rules for photodetachment:

$$|\Delta S| \leq \tfrac{1}{2}, \quad |\Delta L| \leq l, \quad |\Delta J| \leq l + \tfrac{1}{2}. \quad (4)$$

For transition metals with both s and d valence electrons, l can be either 0 or 2. Typically, a large number of thresholds is allowed in the detachment of a d electron, but for s-electron detachment the number is clearly limited by the selection rules. The Boltzmann factor $\exp(-E(J)/kT)$ in Eq. (3) accounts for a thermal population of the different ionic energy levels, and must be included unless the level splittings are much smaller than kT, where T is the effective ion source temperature (see Sec. II A). T can be evaluated from Eq. (3) if it is possible to determine experimentally two fine-structure thresholds for a given ionic term, as the relative intensities are then given by the fitting parameter a_2 in Eq. (1). If the relative intensities of more than two thresholds are measured, a comparison with the theoretical predictions of Eq. (3) will indicate the validity of the LS coupling approximation for the particular ion.

3. Experimental uncertainties

The accuracy of a crossed-beam photodetachment experiment is ultimately limited by a number of factors such as the calibration uncertainty, the laser bandwidth, Doppler broadening, and possible Doppler shifts or thermal wavelength drifts. However, these various sources of error, which are described in detail in Ref. [33], typically give rise to an uncertainty of only ≈ 0.1 cm^{-1} or less. In the present study of cascaded p-wave thresholds, this contribution to the total experimental uncertainty is clearly dwarfed by the statistical uncertainty associated with the p-wave fit to the data, which is 1 cm^{-1} or more (see below).

III. RESULTS AND DISCUSSION

A. Nickel

Previous experimental studies of Ni^- in Refs. [34] and [35] have found the $J=\frac{5}{2}$ level of the $3d^9 4s^2\,{}^2D$ term to be the ionic ground state with binding energies of 1.157(10) and 1.15(15) eV, respectively. The authors of Ref. [34] also measured a value of 1470(100) cm^{-1} for the fine-structure splitting of the ^2D term. (Note that 1 eV = 8065.5410(24) cm^{-1} [36].) No indication was found for the existence of other bound ionic states. Due to this simple and well-established energy-level structure, Ni^- seemed to be a suitable candidate for a first attempt at photodetachment threshold spectroscopy with cascaded p waves. Unfortunately, the situation is complicated by the many low-lying energy levels of the atom, which arise from a near degeneracy between the $3d^9 4s$ and $3d^8 4s^2$ configurations. This can be seen in Fig. 3, which shows a schematic energy-level diagram for Ni^- and Ni. In addition to the ^3F term of the $3d^8 4s^2$ configuration, of which the $J=4$ level constitutes the atomic ground state, four other levels are present which belong to the ^3D and ^1D terms of the $3d^9 4s$ configuration. According to the selection

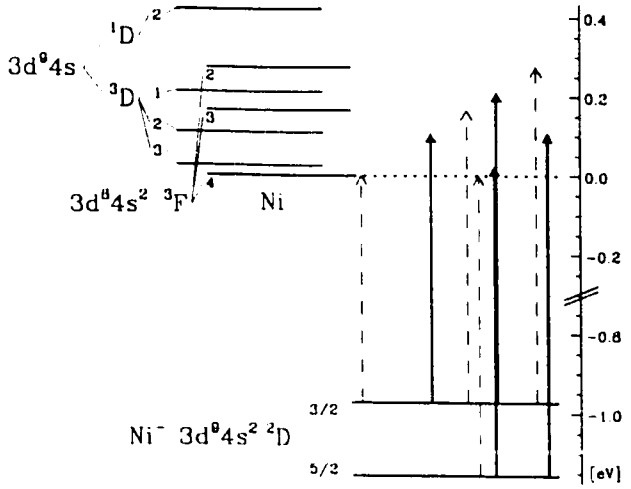

FIG. 3. Schematic energy-level diagram of Ni^- and Ni. Arrows indicate photodetachment thresholds expected to lie within the investigated photon energy range. Dashed or solid lines are used depending on whether a threshold is predicted to be weak or strong, respectively (see text). The horizontal spacing between arrows is proportional to the energy separation of the respective thresholds.

rules for photodetachment [Eq. (4)], the cross section of Ni should thus exhibit 12 thresholds within the near-infrared regime; the first eight are indicated by arrows in Fig. 3.

We have measured the photodetachment cross section of Ni^- over a photon energy range of 7500–10 400 cm^{-1}. Pulse energies ranged from 5 to 9 mJ (compare Fig. 2), and an ion-beam current of $\approx$250 nA was obtained from a sputter target made of high-purity nickel. Although the scan range covered eight of the 12 infrared thresholds, only two were observed. The part of the scan that displayed these two p-wave features is shown in Fig. 4. The result might seem surprising, but four of the possible eight thresholds were expected to be very weak, namely, those where a d electron is removed from the ionic configuration. Various LPES studies of transition-metal negative ions, including the investigation of Ni in Ref. [34], have indicated that photodetachment processes which involve the removal of a d electron are typically about an order of magnitude weaker than processes where an s electron is detached [32,34,37]. Hence, all of the

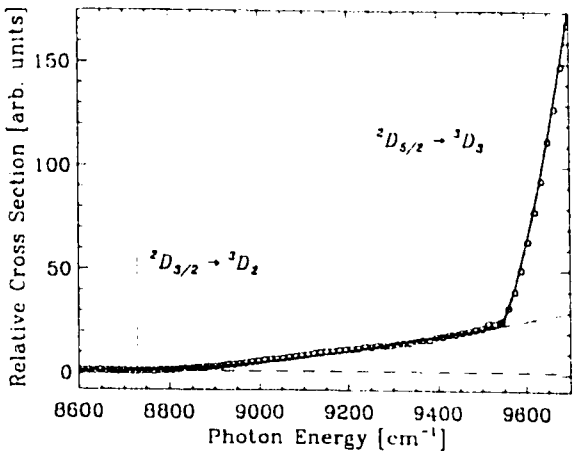

FIG. 4. Photodetachment cross section of Ni^-. Only the portion of the investigated photon energy range that exhibited threshold structures is shown.

TABLE I. Calculated intensities of Ni thresholds.

Threshold[a]	Relative intensity[b]		
	$T=\infty$	$T=650$ K	$T=1300$ K
$^2D_{3/2}\rightarrow{}^3D_2$	20.0	1.2	5.7
$^2D_{5/2}\rightarrow{}^3D_3$	46.7	75.9	68.8
$^2D_{3/2}\rightarrow{}^3D_1$	20.0	1.2	5.7
$^2D_{5/2}\rightarrow{}^3D_2$	13.3	21.7	19.7
$^2D_{3/2}\rightarrow{}^3F_4$	4.3	0.3	1.2
$^2D_{3/2}\rightarrow{}^3F_3$	16.7	1.0	4.8
$^2D_{5/2}\rightarrow{}^3F_4$	38.6	62.7	56.9
$^2D_{3/2}\rightarrow{}^3F_2$	19.0	1.2	5.5
$^2D_{5/2}\rightarrow{}^3F_3$	16.7	27.1	24.6
$^2D_{5/2}\rightarrow{}^3F_2$	4.8	7.7	7.0

[a]The thresholds within each group are ordered from low to high energies.

[b]The relative intensities within each group are given in percent of the total transition strength.

$^2D_J\rightarrow{}^3F_{J'}$ thresholds (except $J=\frac{3}{2}\rightarrow J'=4$, the threshold with the lowest energy, see below) are likely to be hidden in the detachment cross section resulting from the other thresholds. This suggests in particular that the $^2D_{5/2}\rightarrow{}^3D_3$ threshold (fifth arrow in Fig. 3) rather than the EA-defining $^2D_{5/2}\rightarrow{}^3F_4$ threshold (fourth arrow in Fig. 3) should be the first noticable threshold that originates from the ionic ground state. This $^2D_{5/2}\rightarrow{}^3D_3$ threshold can only be the second threshold seen in Fig. 4, as the first one occurs at a photon energy clearly smaller than the EA and must therefore result from the $^2D_{3/2}\rightarrow{}^3D_2$ transition. However, due to the near coincidence between the $^2D_{5/2}\rightarrow{}^3D_3$ and $^2D_{3/2}\rightarrow{}^3D_1$ thresholds, their relative intensities must be considered before an unambiguous assignment can be made. Table I comprises the relative intensities of the first ten infrared thresholds for a pure statistical population of the ionic levels ($T=\infty$), and for populations resulting from a "cool" ($T=650$ K) as well as a "hot" ($T=1300$ K) sputter source. According to these numbers, the contribution of the $^2D_{3/2}\rightarrow{}^3D_1$ transition to the second threshold feature in the detachment cross section is at a negligible level of $\approx$1–2% for a cool source while it is at a critical level of $\approx$10% for a hot source. Hence special care was taken that the source would operate at a relatively low temperature (as described in Sec. II A).

Both thresholds were finally scanned at a higher resolution to enable an accurate determination of the threshold energies. Values of 8728(3) and 9537.9(10) cm^{-1}, respectively, were obtained from a p-wave fit to the data. The scan over the region of the $^2D_{5/2}\rightarrow{}^3D_3$ threshold is shown in Fig. 5. A single p wave [Eq. (1)] fits the data well, indicating that the contribution of the $^2D_{3/2}\rightarrow{}^3D_1$ threshold is indeed negligible. The accuracy of the fit is mainly limited by the strong and sloped photodetachment background that originates from the $^2D_{3/2}\rightarrow{}^3D_2$ transition, and would have been worse for a higher ion source temperature. By subtracting the accurately known energies of the atomic levels involved [38] from the threshold values, the electron affinity of nickel is determined to be 9333.1(10) cm^{-1} [1.15716(12) eV], and a

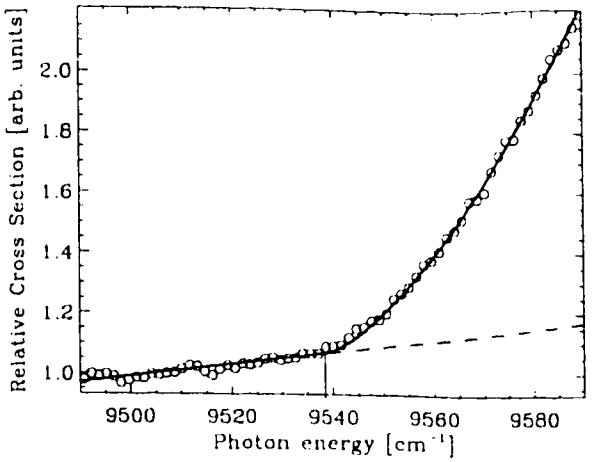

FIG. 5. Photodetachment cross section of Ni$^-$ in the vicinity of the $^2D_{5/2} \rightarrow {}^3D_3$ threshold. The solid line indicates the result of a p-wave fit to the data.

fine-structure splitting of 1485(3) cm^{-1} is obtained for the Ni$^-$ (^2D) term. These values are in excellent agreement with the results of Ref. [34], but constitute an improvement in accuracy of almost two orders of magnitude.

Since two thresholds were measured here, their relative intensities may be compared with the calculated values given in Table I in order to obtain the effective source temperature. A measured intensity ratio of 0.016(2) gives a temperature of 650(30) K, commensurate with the above considerations. More interestingly, the relative strengths of s-electron versus d-electron detachment can be evaluated from a comparison between the signal and the background of the (s-electron detaching) $^2D_{3/2} \rightarrow {}^3D_2$ threshold. The background must be due to the d-electron detaching $^2D_{3/2} \rightarrow {}^1F_3$ transition, ≈ 900 cm^{-1} above its threshold. (The threshold itself is too weak for a direct observation.) Under the assumption that the p-wave law is applicable 10% above threshold (as seems to be the case for the $^2D_{3/2} \rightarrow {}^3D_2$ threshold in Fig. 4) the actual threshold coefficient can be calculated, and an intensity ratio of 0.029(5) is obtained for the two thresholds. Normalizing this ratio with the relative threshold intensities (Table I) and with the appropriate coefficients from Eq. (2) finally yields a value of 22(6) for s-electron versus d-electron detachment of Ni$^-$. This number agrees with the range of 5–20 quoted in LPES studies [32,34,37], but the present value has the advantage of being a direct measure for the ratio of the reduced matrix elements $\langle s \| \mu \| p \rangle$ and $\langle d \| \mu \| p \rangle$ at *threshold* (where $\langle d \| \mu \| f \rangle$ is negligible), without the need to take energy dependencies (other than Wigner's law) into account [34].

It should be noted that the above derivations could be subject to a small systematic error as a result of the weak perturbation of the atomic $^3D_2$ level by the $^1D_2$ level. Corderman, Engelking, and Lineberger discussed this perturbation in detail, and showed that it may explain the increased strength of the $^2D_{5/2} \rightarrow {}^3D_2$ LPES peak that was observed in their study. If that is the case, the $^2D_{3/2} \rightarrow {}^3D_2$ transition should be proportionally weakened. However, a quantitative evaluation of this effect would have to rely on a comparison of $^2D_J \rightarrow {}^3D_J$, and $^2D_J \rightarrow {}^1D_J$, intensities, the latter of which cannot be derived from the present measurements of total cross sections.

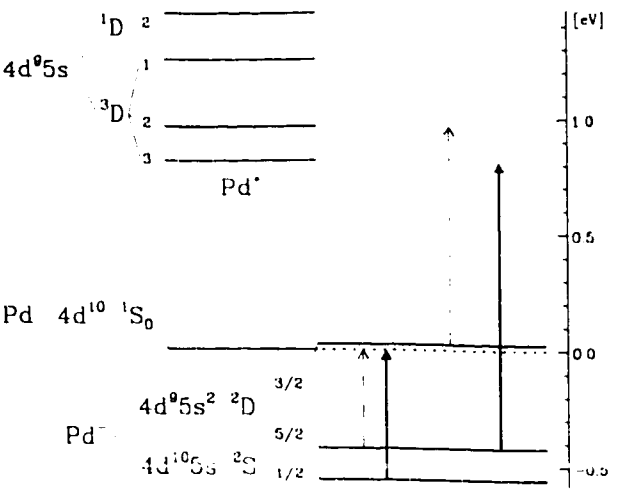

FIG. 6. Schematic energy-level diagram of Pd$^-$ and Pd. The unobserved ionic $^2D_{3/2}$ level is probably unbound, as shown here. Solid arrows indicate observed photodetachment thresholds; dashed arrows represent thresholds too weak for observation with the present setup.

B. Palladium

Despite the fact that palladium appears in the same column of the Periodic Table as nickel, the energy-level structure of both the atom and the negative ion is significantly different. The situation is illustrated in Fig. 6. In contrast to Ni, the order of the d^8s^2, d^9s, and d^{10} configurations is reversed for Pd: the ground state is given by $4d^{10}\,{}^1S_0$, and the ^3D and ^1D terms of the $4d^9 5s$ configuration give rise to the first four excited levels. The level structure of the ion was established by Feigerle *et al.* [37] in the only previous experimental study of this system. The analysis of their spectrum of LPES peaks revealed two final-state sequences, which indicated the existence of two bound energy levels in the ion. Based primarily on the detachment selection rules [Eq. (4)], these levels were identified as $4d^9 5s^2\,{}^2D_{5/2}$ and $4d^{10}5s\,{}^2S_{1/2}$, the latter being the ionic ground state. This is a striking contrast to the level structure of Ni$^-$, and constitutes the rather special case of a negative ion with two stable electronic configurations (albeit of the same parity). Feigerle *et al.* did not observe any LPES peaks that could have been assigned to the $J = \frac{3}{2}$ level of the ionic ^2D term. Based on an isoelectronic extrapolation, they estimated a binding energy of 6 ± 43 meV for this level, hence it is not established whether this level is weakly bound or slightly unbound with respect to the atomic ground state.

From the point of view of photodetachment threshold spectroscopy, the case of Pd$^-$ is relatively straightforward. The first allowed threshold that can originate from the ionic ground state is $^2S_{1/2} \rightarrow {}^1S_0$, which also defines the EA of palladium. This threshold involves the detachment of an s electron, and is thus expected to be strong. Figure 7 shows the result of a photodetachment scan in the vicinity of this threshold. (A Pd$^-$ current of 30 nA and pulse energies of ≈ 1.5 mJ were available in this experiment.) The p-wave fit to the data yields a threshold value of 4534.0(10) cm^{-1} [562.14(12) meV]. This value for the EA of Pd agrees with Feigerle *et al.*'s value of 558(8) meV, and marks a near 70-fold improvement in accuracy. The background signal seen in Fig. 7 is approximately three times larger than the purely

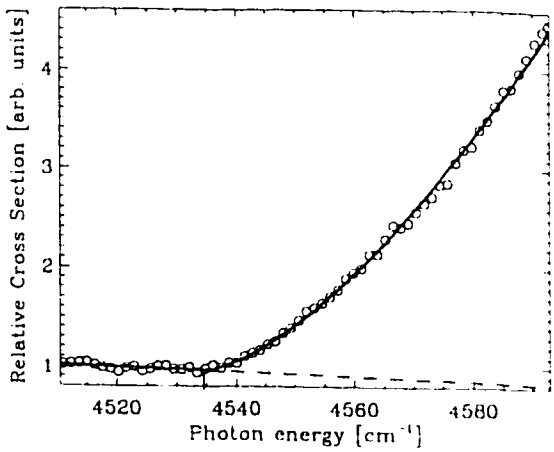

FIG. 7. Photodetachment cross section of Pd$^-$ around the $^2S_{1/2}\rightarrow{}^1S_0$ threshold which defines the EA of Pd.

collisional background that is observed when the laser is blocked. It is attributed to the "forbidden" $4d^9 5s^2\,{}^2D_{5/2} \rightarrow 4d^{10}\,{}^1S_0$ photodetachment transition. This transition involves a two-electron process, and most likely draws its strength from a configuration interaction between the $^2D_{5/2}$ level and higher-lying resonance states of Pd$^-$ [37]. It was also observed as a small peak in the LPES spectrum of Feigerle *et al.* The energy dependence of the cross section for such a forbidden detachment process is not known. It may very well display a slightly negative slope, as the background signal in Fig. 7 suggests.

The first allowed photodetachment transition involving the $^2D_{5/2}$ level of the ion is the *s*-electron detaching transition to the atomic $^3D_3$ level. Its threshold occurs at significantly higher photon energies than the $^2S_{1/2}\rightarrow{}^1S_0$ threshold discussed above. Therefore, the cross section in the vicinity of the $^2D_{5/2}\rightarrow{}^3D_3$ threshold will likely exhibit a substantial background due to the $^2S_{1/2}\rightarrow{}^1S_0$ transition. This is clearly seen in the photodetachment scan over that region, shown in Fig. 8. Although a threshold is undoubtedly present, its contribution to the total cross section amounts to only 20% for photon energies 200 cm^{-1} above threshold. An accurate determination of the threshold energy is nevertheless possible, primarily because the background is extremely flat. This circumstance might be due to a relatively flat cross section for the $^2S_{1/2}\rightarrow{}^1S_0$ transition over this particular photon energy range, and/or due to a saturation of that transition by the intense laser pulse. A threshold energy of 9971(4) cm^{-1} is obtained from the *p*-wave fit to the data. Subtracting the energy of the atomic $^3D_3$ level [39] finally results in a binding energy of 3407(4) cm^{-1} [422.4(5) meV] for the ionic $^2D_{5/2}$ level. This value compares favorably with the result of Feigerle *et al.*, 422(8) meV.

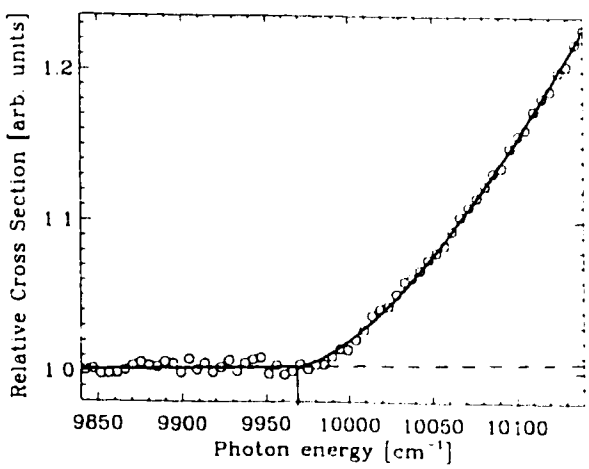

FIG. 8. Photodetachment cross section of Pd$^-$ in the region of the $^2D_{5/2}\rightarrow{}^3D_3$ threshold, far above the EA-defining $^2S_{1/2}\rightarrow{}^1S_0$ threshold.

The relative detachment cross sections found in our threshold measurements unambiguously confirm the assignment of Pd$^-$ energy levels made by Feigerle *et al.* The $4d^{10}5s\,{}^2S_{1/2}$ level must be the ionic ground state, with the $4d^9 5s^2\,{}^2D_{5/2}$ level lying 1127(4) cm^{-1} above it.

The single remaining question regarding the stable states of the ion is whether the $J=\frac{3}{2}$ level of the $4d^9 5s^2\,{}^2D$ term is also bound. If that were the case, the total cross section should in principle exhibit a threshold due to the detachment of thermal $^2D_{3/2}$ population into the $^3D_3$ level of the atom (which is the first allowed detachment channel). In practice, the thermal population would be rather small (even for a hot ion source), and its detachment into $^3D_3$ would be competing against the forbidden detachment into the atomic ground state and would also be subject to a strong background resulting from the $^2S_{1/2}\rightarrow{}^1S_0$ transition. Hence the lack of observation of the $^2D_{3/2}\rightarrow{}^3D_3$ threshold is not conclusive.

We therefore attempted to locate the $^2D_{3/2}$ level via the $^2D_{5/2}\rightarrow{}^2D_{3/2}$ magnetic dipole ($M1$) transition. It should occur at photon energies between 3100 and 3800 cm^{-1}, based on the isoelectronic extrapolation by Feigerle *et al.* [37]. The applicability of laser-driven $M1$ transitions to the study of negative ion fine structure has been demonstrated previously: first in an investigation of Ir$^-$ and Pt$^-$ [6], and recently in experiments on Te$^-$ [40] and Sb$^-$ [7]. The $4d^9 5s^2\,{}^2D$ term under investigation here is most similar to the $5d^9 6s^2\,{}^2D$ term that was studied in Pt$^-$, where the observed fine-structure $M1$ transition was in fact fairly strong. However, allowance has to be made for the fact that the fine-structure splitting in Pt$^-$ is about three times larger than in Pd$^-$; hence pulse energies were about 20 times larger than the $\sim$0.5 mJ available in the present case. Furthermore, the Einstein B coefficient for the transition in Pd$^-$ should be about a factor of 3 smaller than in Pt$^-$, as $M1$ rates roughly scale with the square of the nuclear charge. Also taking the difference in beam currents into account, resonance signals of less than one count per laser pulse were estimated for a tight focus of $\sim$50 μm. A tight focus was considered necessary, as for a bound (stable) $^2D_{3/2}$ level the detachment after the resonant transition had to proceed via a forbidden transition into the atomic ground state. An unbound $^2D_{3/2}$ level, on the other hand, would be metastable with respect to autodetachment, and is therefore expected to show up as a narrow resonance feature as well. We have searched for the Pd$^-$ $M1$ transition in the photon energy range of 3050–3980 cm^{-1} with a scan rate of 200 laser pulses per cm^{-1} (15 pulses per laser bandwidth). No evidence of a resonance structure was found. Unfortunately, this result remains inconclusive as well. It is conceivable that the actual M1 transition strength is somewhat smaller than the above estimates suggest, perhaps too small for the sensitivity of the current setup. Further improvements of the experimental apparatus (or an entirely dif-

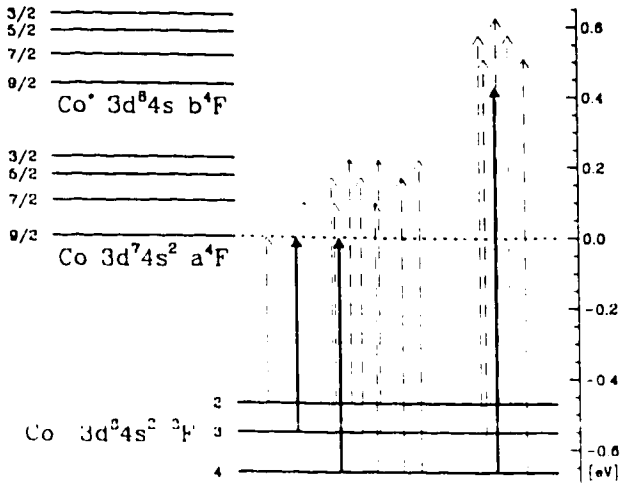

FIG. 9. Schematic energy-level diagram of Co^- and Co. The many infrared photodetachment thresholds of this system are indicated with arrows whose horizontal separation is proportional to the energy separation of the thresholds. The three thresholds that were measured here are shown with solid arrows.

ferent approach) seem therefore necessary for a determination of the $^2D_{3/2}$ binding energy.

C. Cobalt

An energy-level diagram for the negative ion of cobalt including the eight lowest-energy levels of the atom is shown in Fig. 9. The atomic levels are grouped into two ^4F terms (denoted as a and b) which belong to two different electron configurations, $3d^74s^2$ and $3d^84s$, respectively. Unlike the situation found in nickel, the average term energies are well separated here. The negative ion structure was first investigated in Ref. [34]. They identified the three fine-structure levels of the $3d^84s^2\,^3F$ term, and found no evidence for the existence of any other stable ionic states.

The major complication for a photodetachment threshold study of this system results from the fact that detachment to the first four atomic levels involves the removal of a d electron, and is thus expected to be weak. Strong channels of s-electron detachment, on the other hand, do not open up until photon energies are reached well above the threshold for ground-state detachment. Hence we expect that the corresponding (s-electron) threshold signals will have to compete against a substantial photodetachment background from the 12 open d-electron detachment channels.

The most promising thresholds for a LPT study were chosen on the basis of their calculated relative intensities. These intensities are listed in Table II, ordered by threshold energies. Again, values for a pure statistical level population ($T=\infty$), and for populations resulting from a "cool" ($T=650$ K) as well as "hot" ($T=1300$ K) sputter source were calculated. The EA of cobalt is defined by the $^3F_4 \rightarrow a^4F_{9/2}$ threshold, the sixth threshold in the sequence. Fortunately, the intensities of the first five thresholds are relatively small, particularly for $T=650$ K. Figure 10 shows the photodetachment signal that was recorded in the region of the sixth threshold, with the source operated at a low effective temperature, providing 350 nA of Co^-. In contrast to the thresholds studied in Ni^- and Pd^-, the photodetachment

TABLE II. Calculated intensities of Co^- thresholds.

Threshold[a]	Relative intensity[b]		
	$T=\infty$	$T=650$ K	$T=1300$ K
$^3F_2 \rightarrow a^4F_{9/2}$	1.0	0.0	0.2
$^3F_3 \rightarrow a^4F_{9/2}$	21.2	2.8	7.8
$^3F_2 \rightarrow a^4F_{7/2}$	15.9	0.5	2.8
$^3F_2 \rightarrow a^4F_{5/2}$	31.1	1.0	5.5
$^3F_3 \rightarrow a^4F_{7/2}$	45.5	6.1	16.6
$^3F_4 \rightarrow a^4F_{9/2}$	100.0	100.0	100.0
$^3F_2 \rightarrow a^4F_{3/2}$	33.5	1.1	6.0
$^3F_3 \rightarrow a^4F_{5/2}$	32.7	4.4	12.0
$^3F_4 \rightarrow a^4F_{7/2}$	36.4	36.4	36.4
$^3F_3 \rightarrow a^4F_{3/2}$	14.7	2.0	5.4
$^3F_4 \rightarrow a^4F_{5/2}$	9.6	9.6	9.6
$^3F_4 \rightarrow a^4F_{3/2}$	0.7	0.7	0.7
$^3F_2 \rightarrow b^4F_{5/2}$	26.7	0.8	4.8
$^3F_3 \rightarrow b^4F_{5/2}$	60.0	8.0	21.9
$^3F_4 \rightarrow b^4F_{9/2}$	100.0	100.0	100.0
$^3F_2 \rightarrow b^4F_{3/2}$	40.0	1.3	7.1
$^3F_3 \rightarrow b^4F_{5/2}$	33.3	4.5	12.2
$^3F_4 \rightarrow b^4F_{7/2}$	20.0	20.0	20.0

[a]Thresholds are ordered from low to high energies.
[b]Relative intensities are given in percent of the strongest transition within each group.

background here is strongly sloped, which is the limiting factor for the accuracy of the p-wave fit. A value of 5350(5) cm^{-1} [663.3(6) meV] was obtained, which compares very well with the EA value of 662(3) meV that was measured by Leopold and Lineberger via LPES [41]. The other three $^3F_4 \rightarrow a^4F_J$ thresholds have smaller relative intensities than $^3F_4 \rightarrow a^4F_{9/2}$ and can therefore not be expected to allow a more accurate EA measurement. The $^3F_4 \rightarrow b^4F_{9/2}$ threshold, on the other hand, which is the first and also the strongest s-electron detaching threshold involving the ionic ground state, might be strong enough to allow at least a confirmation of the above EA value. A photon energy region of 8750–8950 cm^{-1} was scanned, and the threshold was

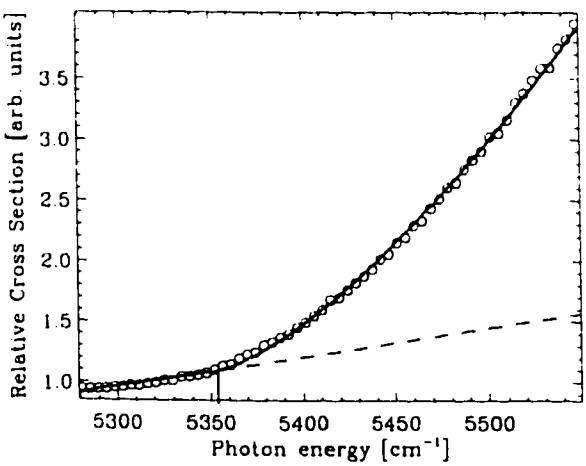

FIG. 10. Measured photodetachment cross section for the $^3F_4 \rightarrow a^4F_{9/2}$ threshold of Co^-, which defines the EA of cobalt.

found at 8845(15) cm^{-1}. As expected, the threshold was superimposed on a very large photodetachment background, which is the reason for the large uncertainty in the fitted value. Upon subtracting the $b^4F_{9/2}$ energy [38], an electron affinity of 5362(15) cm^{-1} [664.8(20) meV] is obtained, in agreement with the other values.

A determination of the negative ion fine structure seemed straightforward, as the two thresholds that are lowest in energy involve the two upper fine-structure levels. Unfortunately, the relative intensity of the first threshold, $^3F_2 \rightarrow a^4F_{9/2}$ is extremely small, only about 1% of the $^3F_4 \rightarrow a^4F_{9/2}$ intensity at $T=\infty$ (Table II). [This is a significant deviation from the 55% that one would expect on the basis of level degeneracies alone, without taking Eq. (3) into account.] The detachment signals measured for this channel were in fact so small that a determination of the threshold became impossible. The $^3F_3 \rightarrow a^4F_{9/2}$ threshold, on the other hand, could be measured, as its relative intensity is clearly higher (21% at $T=\infty$). Signal levels were still small, and even after several hours of scanning the signal-to-noise ratio remained poor. A threshold value of 4475(15) cm^{-1} was measured, which translates into a $J=4-3$ fine-structure splitting of 875(15) cm^{-1}, in good agreement with Corderman, Engelking, and Lineberger's value of 910(50) cm^{-1} [34]. A further investigation of the ionic fine structure via other (including s-electron detaching) thresholds was not attempted, as the calculated threshold intensities indicated rather unfavorable signal-to-background ratios.

D. Rhodium

Rhodium is found in the same group of the Periodic Table as cobalt and also forms a stable negative ion only in the $(n-1)d^8ns^2$ electron configuration. This was established in a LPES measurement by Feigerle *et al.* [37], which is, to our knowledge, the only previous study of this system. That investigation determined a binding energy of 1.138(8) eV for the $(4d^85s^2)$ $^3F_4$ ionic ground state and $J=3-4$ and $2-3$ fine-structure splittings of 2370(65) and 1000(65) cm^{-1}, respectively. These values have been used in the schematic energy-level diagram of Rh^- and Rh shown in Fig. 11. In comparison to cobalt, the situation is simplified here due to the different order of energy levels in the atom. The $(n-1)d^7ns^2\,^4F$ term, which gave rise to the manifold of weak Co^- thresholds, is located above the $4d^85s\,^3F$ term of Rh. Hence the low-energy region of the photodetachment cross section of Rh^- is characterized by only six (s-electron detaching) thresholds.

An initial investigation of the cross section in the vicinity of the EA-defining $^3F_4 \rightarrow {}^4F_{9/2}$ threshold revealed a clean p-wave threshold, but the signal-to-noise ratio was poor due to a surprisingly low ion-beam current. The beam current in the UHV interaction chamber was only 6 nA. Based on a comparison of the Co^-, Ni^-, and Pd^- currents obtained here with the ion currents reported by Middleton [42], a substantially higher Rh^- current of ~50 nA was expected. We are unable to provide a satisfactory explanation for this poor performance of the ion source, which was also observed for the transition metals chromium and molybdenum [43].

Nevertheless, after scanning the $^3F_4 \rightarrow a^4F_{9/2}$ threshold for several hours, a p-wave fit to the final data yielded a

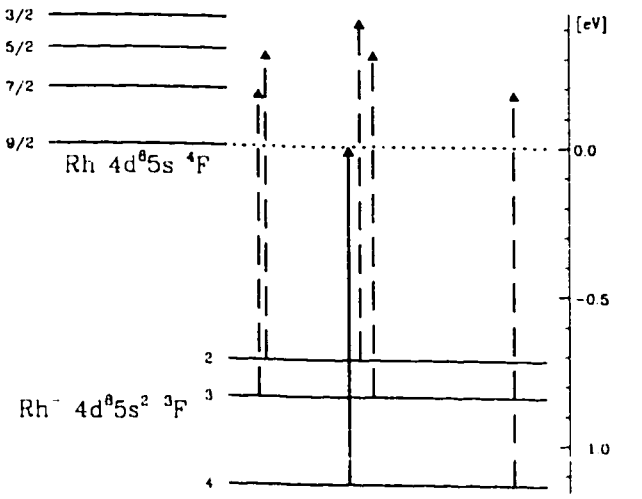

FIG. 11. Schematic energy-level diagram of Rh^- and Rh. Arrows indicate the first six detachment thresholds of which only the EA-defining $^3F_4 \rightarrow {}^4F_{9/2}$ threshold was measured (solid arrow).

threshold energy of 9218.0(15) cm^{-1} [1.142 89(20) eV]. This result for the EA of rhodium is in good agreement with the value of 1.138(8) eV found by Feigerle *et al.* [37], but constitutes a 40-fold improvement in accuracy. In light of the small ion-beam current, special care was taken in optimizing the position of the sputter cathode for a high effective temperature. Still, the detachment signal measured below the EA threshold remained small. This signal must be attributed to detachment from the two upper fine-structure levels. It was simply too small for an accurate determination of the actual thresholds, namely, $^3F_3 \rightarrow a^4F_{7/2}$ and $^3F_2 \rightarrow a^4F_{5/2}$, which are expected at photon energies of approximately 8330 and 8400 cm^{-1}, respectively. Provided that better Rh^- currents can be obtained, it should at least be possible to measure the first of these two thresholds. For a hot ion source this threshold would appear with ≈5% of the intensity of the EA threshold, which is comparable to the situation found for Ni^- (Sec. III A). The second of the two thresholds has a relative intensity of only 0.5%, and will probably always be obscured by the detachment signal of the first threshold.

E. Summary and outlook

Table III summarizes the results of our infrared LPT studies of the Co^-, Ni^-, Rh^-, and Pd^- negative ions, and also gives the values obtained in previous LPES studies for comparison. As can be seen, improvements in accuracy of up to two orders of magnitude were realized for both electron affinities and ionic fine-structure splittings. Infrared LPT spectroscopy has thus proven to be a valuable tool for the study of negative ions that exhibit multiple p-wave thresholds. However, the experiments have also indicated some of the limitations of the technique. The limitations mostly result from the fact that the present experimental setup utilized neutral particle detection to monitor the photodetachment process. Neutral atoms produced via different photodetachment channels cannot be separated, i.e., only the total cross section for photodetachment is measured. Consecutive channels thus appear as a "cascade" of thresholds in the neutral particle signal of an LPT study, as opposed to the series of

TABLE III. Summary of measured binding energies and fine-structure splittings.

Ion	Level	Binding energy (meV) This work	Previous works	Ref.
Co^-	$^3F_4$	663.3(6)	662(3)	[41]
Ni^-	$^2D_{5/2}$	1157.16(12)	1157(10)	[34]
Rh^-	$^3F_4$	1142.89(20)	1138(8)	[37]
Pd^-	$^2S_{1/2}$	562.14(12)	558(8)	[37]
	$^2D_{5/2}$	422.4(5)	422(8)	[37]

Ion	Levels	Fine-structure splitting (cm^{-1}) This work	Previous works	Ref.
Co	$^3F_2-^3F_1$	875(15)	910(50)	[34]
	$^3F_3-^3F_2$	[a]	650(50)	[34]
Ni^-	$^2D_{5/2}-^2D_{3/2}$	1485(3)	1470(100)	[34]
Rh^-	$^3F_4-^3F_3$	[a]	2370(65)	[37]
	$^3F_3-^3F_2$	[a]	1000(65)	[37]

[a]Could not be measured in the present study.

individual peaks observed in the electron spectrum of a LPES measurement. This is not necessarily a limitation in the case of s-wave detachment, but, for p-wave channels, the detachment signal at threshold is notoriously small. The present study has shown that only the two or three strongest thresholds within a sequence of cascaded p-wave thresholds can be measured with an accuracy that is clearly superior to accuracies achieved with LPES. In cases such as Co^-, where a large number of thresholds is present, most thresholds cannot be resolved, as their strength relative to the photodetachment background is too small. In such cases an unambiguous interpretation of the LPT spectrum has to rely on previous LPES results in addition to calculated threshold strengths. Fortunately, the EA's of most of the remaining transition-metal negative ions that could be studied in LPT experiments have been previously measured via LPES, so the average term energies are known.

The limitations described above could be removed by implementing techniques for a channel-selective detection of the photodetachment products. An approach which seems particularly promising was used in the LPT study of alkali negative ions with visible light [9]. There the photodetached electrons were monitored through an electron spectometer as the laser was tuned. Electrons resulting from different detachment channels then appear as separated peaks in the spectrum, and the dependency of a particular peak on the photon energy is directly proportional to the partial cross section of the respective detachment channel. Hence a combination of this detection scheme with the infrared LPT techniques demonstrated here should in principle allow a resolution of dense threshold manifolds as found in Co^-. In practice, ion-beam energies higher than those used here would probably be required in order to provide threshold electrons with sufficient energy for detection. If necessary, the signal-to-noise ratio could always be improved by using an interaction region with collinear rather than crossed laser and ion beams. Resonant ionization spectroscopy (RIS) constitutes an alternative approach for state-selective detection. In recent years, this technique has been very successfully applied to the study of alkaline-earth negative ions [3]. The excellent signal-to-noise ratio achievable with RIS enables the detection of even the weakest detachment channels. On the other hand, the atomic energy-level structure of the element under investigation must provide for a practical resonant ionization scheme, which might not be the case for some transition metals.

A very different approach to the study of the fine structure of transition-metal negative ions could involve two-photon rather than single-photon threshold spectroscopy. The observation of two-photon detachment thresholds has been reported for three main group negative ions, namely, H^- [44], Cl^- [45], and Si^- [33]. This detachment scheme is particularly interesting for transition-metal negative ions, as their two-photon thresholds follow the Wigner s wave law with its characteristic sharp onset. Cascades of even closely spaced s-wave thresholds have proven to be an accurate measure of ionic fine structure [11]. The threshold shifts that are inevitable with the high laser intensities necessary for the two-photon process would likely be the same for all fine-structure thresholds, and thus the splitting would remain unchanged.

Both LPT and LPES studies depend on an initial population of the ionic levels to be investigated. Hence, for a "thermal" ion source, bound states that lie more than $\sim$0.5 eV above the ionic ground state typically remain undetected. A study of such high-lying bound ionic states would have to employ a "nonthermal" ion source (e.g., a charge-exchange chamber) or resonant multiphoton schemes in the detachment process. Resonant multiphoton detachment from atomic negative ions was only recently demonstrated. These experiments located the excited state under investigation via a laser-driven two-photon electric-dipole [5] or single-photon magnetic-dipole [6] transition from the (same parity) ionic ground state. (There is yet no experimental evidence that any atomic negative ion would exist in two stable configurations of opposite parity [46].) Although the present study of the Pd^- ion was unsuccessful in the attempt to drive the ^2D fine-structure transition, we still believe that multiphoton techniques are very promising for further investigations of transition-metal ions. In several systems an accurate fine-structure determination seems possible via a 2(Raman)+1 photon detachment scheme, as it was used in a study of Se^- and Te^- [20]. In addition, the near degeneracy of $(n-1)d^m$, $(n-1)d^{m-1}ns$, and $(n-1)d^{m-2}ns^2$ configurations found in most transition-metal atoms suggests that the respective ions may exist in more than one stable electron configuration. However, Pd^- is the only experimentally proven case thus far. A single-photon transition between two such configurations will be of electric quadrupole nature and therefore extremely weak, but a two-photon transition might be sufficiently strong in some cases.

IV. CONCLUSION

This paper has described photodetachment threshold experiments on transition-metal negative ions possessing more than one stable state. A case study of the Co^-, Ni^-, Rh^-, and Pd^- ions has resulted in significantly improved values for the electron affinities of these elements, and in most cases has also provided accurate measurements of ionic fine-

structure splittings. The experimental approach was based on a tunable infrared laser source, and is believed to be applicable to most of the remaining transition-metal negative ions. The limitations of the technique, as well as possible improvements and alternative detachment schemes, have been discussed.

ACKNOWLEDGMENTS

We gratefully acknowledge the Natural Science and Engineering Research Council of Canada (NSERC) for support of this work. We are also thankful to J. D. Garrett for manufacturing the various sputter cathodes.

[1] D. R. Bates, Adv. At., Mol., Opt. Phys. **27**, 1 (1991); T. Andersen, Phys. Scr. **T34**, 234 (1991).

[2] S. J. Buckmann and C. W. Clark, Rev. Mod. Phys. **66**, 539 (1994).

[3] T. Andersen, H. H. Andersen, P. Balling, P. Kristensen, and V. V. Petrunin, J. Phys. B **30**, 3317 (1997).

[4] C. Blondel, Phys. Scr. **T58**, 31 (1995).

[5] P. Kristensen, H. Stapelfeldt, P. Balling, T. Andersen, and H. K. Haugen, Phys. Rev. Lett. **71**, 3435 (1993).

[6] J. Thøgersen, M. Scheer, L. D. Steele, H. K. Haugen, and W. P. Wijesundera, Phys. Rev. Lett. **76**, 2870 (1996).

[7] M. Scheer, H. K. Haugen, and D. R. Beck, Phys. Rev. Lett. **79**, 4104 (1997).

[8] H. Hotop and W. C. Lineberger, J. Phys. Chem. Ref. Data **14**, 731 (1985).

[9] J. Dellwo, Y. Liu, D. J. Pegg, and G. D. Alton, Phys. Rev. A **45**, 1544 (1992).

[10] D. Feldmann, Z. Phys. A **277**, 19 (1976).

[11] M. Scheer, R. C. Bilodeau, and H. K. Haugen, Phys. Rev. Lett. **80**, 2562 (1998).

[12] M. Scheer, R. C. Bilodeau, J. Thøgersen, and H. K. Haugen, Phys. Rev. A **57**, R1493 (1998).

[13] E. P. Wigner, Phys. Rev. **73**, 1002 (1948).

[14] H. Hotop and W. C. Lineberger, J. Phys. Chem. Ref. Data **4**, 539 (1975).

[15] R. J. Zollweg, J. Chem. Phys. **50**, 4251 (1969).

[16] O. P. Charkin and M. E. Dyatkina, Zh. Strukt. Khim. **6**, 422 (1965) [J. Struct. Chem. (USSR) **6**, 397 (1965)].

[17] J. M. Garcia de la Vega, Phys. Rev. A **51**, 2616 (1995).

[18] E. Clementi, Phys. Rev. **135**, A980 (1964); Y. Guo and M. A. Whitehead, Phys. Rev. A **38**, 3166 (1988); J. M. Garcia de la Vega, J. Phys. B **27**, L447 (1994).

[19] R. Middleton, Nucl. Instrum. Methods Phys. Res. **214**, 139 (1983).

[20] J. Thøgersen *et al.*, Phys. Rev. A **53**, 3023 (1996).

[21] J. R. Nestor, Appl. Opt. **21**, 4154 (1982).

[22] L. Minnhagen, J. Opt. Soc. Am. **63**, 1185 (1973).

[23] W. K. Bischel and M. J. Dyer, Phys. Rev. A **33**, 3113 (1986); E. C. Looi, J. C. Stryland, and H. L. Welsh, Can. J. Phys. **56**, 1102 (1978), and references therein.

[24] P. Rabinowitz, B. N. Perry, and N. Levinos, IEEE J. Quantum Electron. **22**, 797 (1986).

[25] W. Heuer and H. Zacharias, IEEE J. Quantum Electron. **24**, 2087 (1988).

[26] H. Bryant, K. Sentrayan, and V. Kushawaha, Spectrosc. Lett. **25**, 1387 (1992).

[27] J. Thøgersen, L. D. Steele, M. Scheer, C. A. Brodie, and H. K. Haugen, J. Phys. B **29**, 1323 (1996).

[28] N. D. Gibson, B. J. Davies, and D. J. Larson, J. Chem. Phys. **98**, 5104 (1992).

[29] J. W. Farley, Phys. Rev. A **40**, 6286 (1989); T. F. O'Malley, Phys. Rev. **137**, A1668 (1964).

[30] H. Hotop and W. C. Lineberger, J. Chem. Phys. **58**, 2379 (1973).

[31] P. A. Cox, in *Structure and Bonding*, edited by J. D. Dunitz *et al.* (Springer-Verlag, Berlin, 1975), Vol. 24, pp. 59–81.

[32] P. C. Engelking and W. C. Lineberger, Phys. Rev. A **19**, 149 (1979).

[33] M. Scheer, R. C. Bilodeau, C. A. Brodie, and H. K. Haugen, Phys. Rev. A (to be published).

[34] R. R. Corderman, P. C. Engelking, and W. C. Lineberger, J. Chem. Phys. **70**, 4474 (1979).

[35] D. Feldmann, R. Rackwitz, E. Heinicke, and H. J. Kaiser, Z. Phys. A **282**, 143 (1977).

[36] E. R. Cohen and B. N. Taylor, Rev. Mod. Phys. **59**, 1121 (1987).

[37] C. S. Feigerle, R. R. Corderman, S. V. Bobashev, and W. C. Lineberger, J. Chem. Phys. **74**, 1580 (1981).

[38] J. R. Fuhr, W. C. Martin, A. Musgrove, J. Sugar, and W. L. Wiese, http//:physics.nist.gov

[39] *Atomic Energy Levels*, edited by C. E. Moore, Natl. Stand. Ref. Data Ser., No. 35 (U.S. GPO, Washington, DC, 1971).

[40] M. Scheer, R. C. Bilodeau, and H. K. Haugen, J. Phys. B **31**, L11 (1998).

[41] D. G. Leopold and W. C. Lineberger, J. Chem. Phys. **85**, 51 (1986).

[42] R. Middleton (unpublished).

[43] R. C. Bilodeau, M. Scheer, and H. K. Haugen, J. Phys. B (to be published).

[44] C. Y. Tang *et al.*, Phys. Rev. Lett. **66**, 3124 (1991).

[45] R. Trainham, G. D. Fletcher, and D. J. Larson, J. Phys. B **20**, L777 (1987).

[46] M. Scheer *et al.*, Phys. Rev. Lett. **80**, 684 (1998).

Paper 7

Observation of the magnetic-dipole fine-structure transition in the tellurium negative ion.

Michael Scheer, René C Bilodeau and Harold K Haugen.

Journal of Physics B **31**, L11-5 (1998).

J. Phys. B: At. Mol. Opt. Phys. 31 (1998) L11–L15. Printed in the UK PII: S0953-4075(98)88895-0

LETTER TO THE EDITOR

Observation of the magnetic-dipole fine-structure transition in the tellurium negative ion

Michael Scheer, René C Bilodeau and Harold K Haugen†

Department of Physics and Astronomy, McMaster University, Hamilton, Ontario, L8S 4M1, Canada

Received 31 October 1997

Abstract. Two-colour two-photon detachment of $Te^-(5p^5\ ^2P_{3/2})$ via the $^2P_{3/2} \rightarrow {}^2P_{1/2}$ magnetic dipole transition has yielded an accurate value for the fine-structure splitting of the ion: 5005.36(10) cm^{-1} (0.620 586(13) eV). The work clearly demonstrates the applicability of forbidden transitions in the study of the structure of negative ions. One-photon detachment from the $Te^-(5p^5\ ^2P_{1/2})$ level also provided a threshold value which, in combination with the well known $^2P_{3/2}$ binding energy, served as an independent measurement of the fine-structure splitting.

Multiphoton techniques have been applied to the study of negative ion structure only quite recently [1–5]. With regard to bound energy levels, stable atomic negative ions typically only exhibit terms and fine structure corresponding to the ground electronic configuration [6, 7]. Hence, the study of bound levels most often reduces to a study of levels of the same parity. The binding of these levels can be determined by single-photon detachment experiments based on electron spectrometry or tunable laser photodetachment threshold spectroscopy [7]. Electron spectrometry experiments do not achieve the same ultimate accuracy as tunable laser spectroscopy. Also, single-photon detachment experiments exhibit serious limitations in cases where the levels are closely spaced, particularly for thresholds other than Wigner s-wave features, and in cases where the levels are not effectively populated in the ion source [5]. Multiphoton approaches utilizing pulsed laser technology can largely overcome these problems. Three-photon detachment via resonantly enhanced stimulated Raman processes has been demonstrated as a superior approach in determining the fine-structure splittings of Se^- and Te^- [2, 5]. In the two-photon stimulated Raman process, the transition between levels of the same parity is electric-dipole allowed. The application of (electric-dipole) 'forbidden' transitions to the study of negative ions was also reported recently [4]. In that work, magnetic dipole transitions between fine-structure levels of Ir^- and Pt^- were discussed, but some uncertainty in the interpretation remained due to the fact that signals could neither be obtained for the corresponding 2 + 1 Raman process, nor for single-photon detachment from the excited levels. The failure of the 2 + 1 Raman experiment might well be explained by small cross sections for such processes in these species, and the lack of single-photon detachment from the excited level is readily explained by the fact that the highly excited levels are essentially unpopulated in species derived from the sputter ion

† Also with the Department of Engineering Physics, the Brockhouse Institute for Materials Research and the Center for Electrophotonic Materials and Devices, McMaster University.

0953-4075/98/010011+05$19.50

source, but some uncertainty remains. In contrast, in the present experiment on Te^-, the fine structure is very well known from a number of earlier experiments incorporating (2 + 1)-photon Raman approaches and single-photon detachment schemes [2, 5, 8]. Therefore there can be no doubt in this case as to the interpretation of the experiment, which involved photodetachment of Te^- via (1 + 1)-photon absorption, with a magnetic dipole transition between the fine-structure levels as the first step. The situation is depicted in figure 1, a simplified energy level diagram of Te^- and the ground state of Te. In addition, in order to verify the fine-structure splitting, a standard single-photon detachment experiment was conducted from the upper fine-structure level. We did not measure the binding energy of the lower level (EA of Te) as it was recently determined by Haeffler *et al* with very high accuracy: 15 896.18(5) cm^{-1} (1.970 876(7) eV) [9].

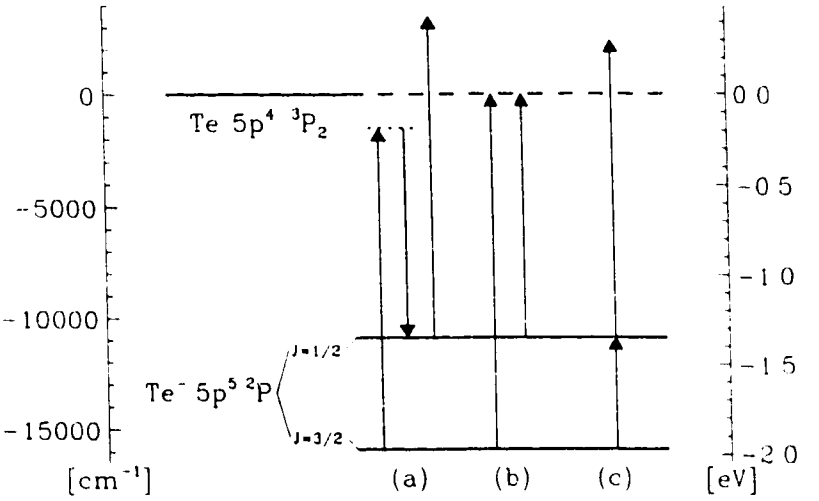

Figure 1. Schematic energy level diagram of Te^- and Te. Different photodetachment schemes aimed at a determination of the fine-structure splitting are indicated by arrows: (a) three-photon detachment via the two-photon Raman E1 resonance; (b) one-photon detachment thresholds; (c) two-photon detachment via the one-photon M1 resonance.

The details of our experimental approach are described elsewhere [5, 10]. Laser pulses of nanosecond duration at a wavelength of ≈751 nm, emitted from a 10 ns duration Q-switched Nd:YAG laser pumped dye laser, and the corresponding second Stokes light at ≈1998 nm, obtained from an H_2 Raman shifter, were utilized in the 1 + 1 photodetachment experiment. The infrared beam (1998 nm) drives the magnetic dipole (M1) transition, while the dye laser light (751 nm) ensures the subsequent detachment from the excited $J = \frac{1}{2}$ level. Infrared pulse energies were ≈2 mJ at 2 μm. The single-photon detachment threshold of $Te^-(^2P_{1/2})$ was obtained by employing the output of the pulsed dye laser directly. Routine calibrations of the dye laser set-up were conducted using an optogalvanic cell, which was also used in a direct measurement of the Raman shift yielding 4155.20(2) cm^{-1}. Rigorous comparisons of the wavelength of the second Stokes light with known ionic energy intervals have also been performed. Various tests indicate that the second Stokes wavelength calibration is reliable to at least 0.2 cm^{-1}. A 12 keV Te^- beam was extracted from a Cs sputter ion source, magnetically mass-analysed, and then charge-state analysed in an ultra-high vacuum chamber, where the Te^- beam currents were typically about 150 nA. There the ion beam was crossed at 90° with the two coaxial and focused laser beams, or the collimated dye laser

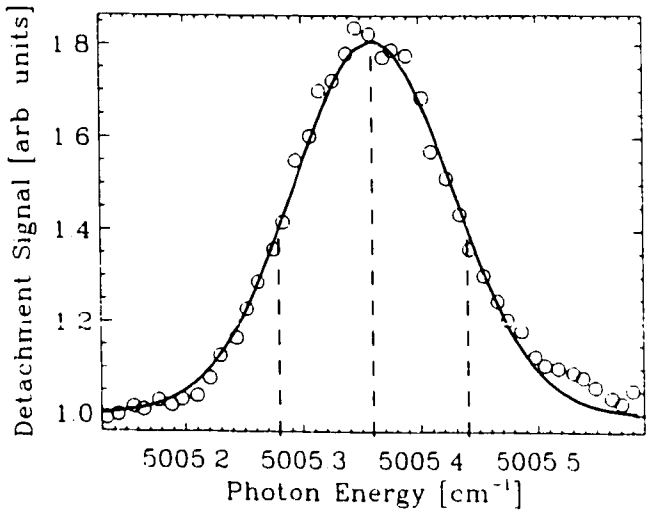

Figure 2. Two-colour two-photon detachment signal versus infrared laser photon energy in the vicinity of the magnetic-dipole fine-structure resonance. The full curve represents a Gaussian fit.

beam in the case of single-photon detachment. The photodetached neutral atoms impinged on a discrete dynode electron multiplier which was operated in an (linear) analogue regime. Data collection involved a gated integrator and boxcar averager.

Laser wavelength scans of the region expected to yield the 1 + 1 (M1) photodetachment resonance were carried out by eliminating from the Raman cell output all components except the residual dye laser and second Stokes beams and then focusing the light on the ion beam utilizing a 60 cm focal length lens. An example of the resonant signal is shown in figure 2. The sharp resonant feature is seen to be 0.16(2) cm^{-1} wide and the signal-to-background ratio is about 1:1. The resonance is clearly resolved and exhibits a high signal-to-noise ratio. The background level is primarily due to one-photon detachment of the excited $Te^-(5p^5\ ^2P_{1/2})$ ions since the thermal population from the sputter ion source leads to an initial population of this level of $\sim$1%. The resonance position is found to be 5005.36(10) cm^{-1} (0.620 586(13) eV). The uncertainty is attributed largely to a combination of the uncertainty in the second Stokes wavelength calibration and a possible systematic error due to a Doppler shift. This new value for the fine-structure splitting can be compared with the earlier values of Slater and Lineberger, 5008(5) cm^{-1} [8]; Kristensen *et al*, 5004.7(2) cm^{-1} [2] and Thøgersen *et al*, 5004.6(5) cm^{-1} [5]. Although the values are close and misinterpretation of the resonance in figure 2 can be ruled out, the present value differs from that of [2] by about three standard deviations and from that of [5] by 1.5 standard deviations of the earlier measurements, respectively. Although the differences are not large, the discrepancy with [2] was of concern, given the fact that we assume that an accuracy of $\approx$0.2 cm^{-1} can be routinely obtained in our respective pulsed laser measurements. Hence, numerous checks were conducted on the laser calibration and other experimental parameters in the present work. In order to further investigate the source of the difference, we conducted a careful measurement of the single-photon detachment threshold from the upper Te^- level. While earlier investigations [5] had not obtained high accuracy signals from the $J = \frac{1}{2}$ level of the ion, improvements in the experimental parameters combined with greatly increasing the number of laser wavelength scans allowed a highly

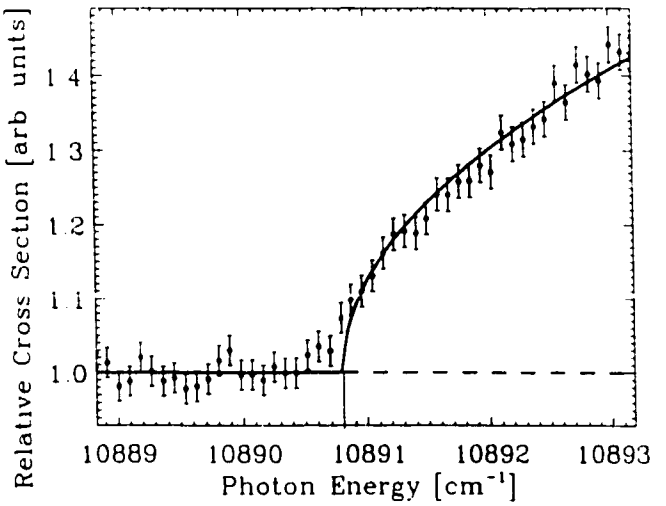

Figure 3. Relative cross section versus laser wavelength for single-photon detachment from the $J = \frac{1}{2}$ level of $Te^-(5p^5\ ^2P)$. Error bars were estimated on the basis of counting statistics. The full curve represents a Wigner s-wave fit.

accurate binding energy to be obtained from the detachment scan of the excited level. The results of the scan are shown in figure 3. The binding energies obtained for the $J = \frac{1}{2}$ level is 10890.80(15) cm^{-1} which, if subtracted from the EA of Te (15896.18(5) cm^{-1} [9]), yields an energy difference of 5005.38(16) cm^{-1}, in excellent agreement with the new value extracted from the (1 + 1)-photon detachment measurement. Subsequently, it was realized [11] that a calibration error probably existed in the earlier Te^- (2 + 1)-photon detachment experiment [2], leading to a minor systematic error not accounted for by the error bars. Various considerations indicate that the present value for the Te^- fine-structure splitting should be adopted.

The clear demonstration of a two-photon detachment via a 1 + 1 magnetic dipole resonance in a case where the interpretation is perfectly clear verifies the perspectives which were outlined in [4]. The M1 transition in Te^- is expected to be of moderate strength [12], having an Einstein A coefficient of $\approx 2\ s^{-1}$, estimated on the basis of isoelectronic extrapolation from neutral I [13, 14] by accounting for the difference in wavelength. The fact that atomic negative ions generally possess fine structure which might be studied using 'forbidden transitions' suggests that the present approach may be extensively utilized in the future. Indeed, in a very recent study of the negative ion of antimony we were able to investigate previously unobserved structure through the incorporation of magnetic dipole transitions [15]. Developments in laser technology (e.g. through infrared optical parametric oscillators) leading to perhaps two orders of magnitude more infrared light intensity than in the present case, would serve to greatly increase available signal levels. Backgrounds, due to single-photon detachment from the excited level as in the present work, could be reduced in the future. This might be achieved via an ion source with a much lower effective temperature, via novel charge-exchange-based ion-beam preparation, or probably most effectively by a scheme to *selectively* pre-deplete the ions in the upper level or levels via saturated laser-induced photodetachment prior to the actual multiphoton detachment of the ground level.

In summary, we have measured the $Te^-(5p^5\ ^2P_J)$ fine-structure splitting via a magnetic-dipole $(1+1)$-photon detachment scheme. The experiment clearly establishes the feasibility of such experiments, under typical negative ion beam and pulsed laser conditions, in a case where the interpretation of the resonance is beyond question. In addition, a minor systematic error in an earlier stimulated-Raman $(2+1)$-photon detachment measurement of the same splitting has been noted. Perspectives for future developments have also been briefly discussed.

We gratefully acknowledge the Natural Science and Engineering Research Council of Canada (NSERC) for support of this work. T Andersen and V V Petrunin are also thanked for their comments on the manuscript.

References

[1] Stapelfeldt H and Haugen H K 1992 *Phys. Rev. Lett.* **69** 2638
[2] Kristensen P, Stapelfeldt P, Balling P, Andersen T and Haugen H K 1993 *Phys. Rev. Lett.* **71** 3435
[3] Petrunin V V, Volstad J D, Balling P, Kristensen P, Andersen T and Haugen H K 1995 *Phys. Rev. Lett.* **75** 1911
[4] Thøgersen J, Scheer M, Steele L D, Haugen H K and Wijesundera W P 1996 *Phys. Rev. Lett.* **76** 2870
[5] Thøgersen J, Steele L D, Scheer M, Haugen H K, Kristensen P, Balling P, Stapelfeldt H and Andersen T 1996 *Phys. Rev.* A **53** 3023
[6] Bates D R 1991 *Adv. At. Mol. Opt. Phys.* **27** 1
Andersen T 1991 *Phys. Scr.* T **34** 23
Buckmann S J and Clark C W 1994 *Rev. Mod. Phys.* **66** 539
Blondel C 1995 *Phys. Scr.* T **58** 31
[7] Hotop H and Lineberger W C 1985 *J. Phys. Chem. Ref. Data* **14** 731
[8] Slater J and Lineberger W C 1977 *Phys. Rev.* A **15** 2277
[9] Haeffler G, Klingmuller A E, Rangell J, Bezinsh U and Hanstorp D 1996 *Z. Phys.* D **38** 211
[10] Thøgersen J, Steele L D, Scheer M, Brodie C A and Haugen H K 1996 *J. Phys. B: At. Mol. Opt. Phys.* **29** 1323
[11] Andersen T and Petrunin V V Private communication
[12] Garstang R H 1964 *J. Res. Natl. Bur. Stand. Sect.* A **68** 61
[13] Hohla K and Kompa K L 1976 *Handbook of Chemical Lasers* ed R W F Gross and J F Bott (New York: Wiley)
[14] Hess W P, Kohler S J, Haugen H K and Leone S R 1986 *J. Chem. Phys.* **84** 2143
[15] Scheer M, Haugen H K and Beck D R 1997 *Phys. Rev. Lett.* **79** 4104

Paper 8

Two-Photon Detachment of Negative Ions via Magnetic Dipole Transitions.

J. Thogersen, M. Scheer, L. D. Steele, H. K. Haugen, and W. P. Wijesundera.

Physical Review Letters **76**, 2870-3 (1996).

Two-Photon Detachment of Negative Ions via Magnetic Dipole Transitions

J. Thogersen, M. Scheer, L. D. Steele, and H. K. Haugen*
Department of Physics and Astronomy, McMaster University, Hamilton, Ontario, Canada L8S 4M1

W. P. Wijesundera
Department of Physics, University of Toronto, Toronto, Ontario, Canada M5S 1A7
(Received 24 October 1995)

Two-photon detachment spectroscopy of the Ir$^-$ $(5d^86s^2\,{}^3F_4)$ and Pt$^-$ $(5d^96s^2\,{}^2D_{5/2})$ ions is conducted using laser intensities $\sim 10^{10}$ W/cm^2. Sharp resonances in the two-photon detachment yields, attributed to magnetic dipole transitions, are observed at photon energies of 7087.3 ± 0.4 and 9740.9 ± 0.5 cm^{-1} for Ir$^-$ and Pt$^-$, respectively. Multiconfiguration Dirac-Fock calculations predict fine structure splittings of 6671 and 9535 cm^{-1} for Ir$^-$ (J = 4-3) and Pt$^-$ (J = 5/2-3/2), and A coefficients of 7 and 14 s^{-1}, respectively, for the upper fine structure levels of the ions.

PACS numbers: 32.80.Gc, 32.80.Dz, 32.80.Rm

The study of negative ions has been an area of considerable interest over the last few decades [1]. More recently multiphoton studies have attracted considerable attention since the negative ion species, with their short range potentials, represent qualitatively different targets for strong-laser-field studies [2]. In addition to the study of fundamental optical phenomena, multiphoton experiments are beginning to play a role in the elucidation of negative ion structure. Multiphoton Raman experiments have been directed to the very accurate determination of ionic fine structure [3,4]. In addition, the study of Stapelfeldt *et al.* [5] has illustrated the application of multiphoton studies to resonant structure in the continuum of negative ion species. Since the bound states of negative ions almost exclusively refer to the terms and fine structure levels of the same (ground) electronic configuration, the study of states below the first detachment limit most often reduces to a study of states of the same parity. Hence two-photon absorption, in an allowed electric dipole scheme, is useful in elucidating ionic structure via Raman or other 2 + 1 photon absorption schemes [3,4]. However, "forbidden" transitions—in particular, of magnetic dipole ($M1$) or electric quadrupole ($E2$) character—could also be applicable to such investigations. In these cases, a single-photon resonant absorption process would be required between states of the same parity [6]. In the present Letter, we demonstrate 1 + 1 photon detachment processes in Ir$^-$ and Pt$^-$, where the resonant enhancements in the detachment yields are attributed to $M1$ transitions. This would be the first application of forbidden transitions in negative ions in an optical regime [7] and many prospective applications exist for negative ions of intermediate and heavy mass. In addition, we present calculations on the fine structure splittings and theoretical results on Einstein coefficients for fine structure levels of negative ions.

The experimental setup is described in detail elsewhere [4]. A 10 Hz Q-switched Nd:YAG laser with an associated dye laser is employed in the work. The output of the dye laser is converted to tunable near-infrared radiation via first and second Stokes generation using stimulated Raman scattering in a single-pass high pressure hydrogen cell, and infrared laser pulse energies are only ~1 mJ. The negative ion beam is derived from a sputter ion source, and the ions are accelerated to a final kinetic energy ~6–10 keV. A magnet with a maximum field ~6 kG deflects the ions through 30°. The ion beam subsequently travels through a differential pumping region and is then charge state analyzed by electric field deflection through an angle of 10°. The beam then propagates through a field-free region and is crossed perpendicularly with a focused infrared laser beam with focal intensity ~10^{10} W/cm^2. Subsequent charge-state analysis separates the photodetached neutral atoms which then impinge on a discrete-dynode electron multiplier. Analog data collection is achieved using a gated integrator and boxcar averager.

Schematic energy level diagrams of the negative ions of iridium and platinum are shown in Fig. 1. Ir$^-$ $(5d^86s^2\,{}^3F_4)$ has a binding energy of 12 622(41) cm^{-1} [8] with respect to Ir $(5d^76s^2\,{}^4F_{9/2})$. The J = 4-3 fine structure splitting of Ir$^-$ was predicted to be 7600(1500) cm^{-1} on the basis of isoelectronic extrapolation [8]. Pt$^-$ has a $5d^96s^2\,{}^2D_{5/2}$ ground state [9] and the J = 5/2-3/2 splitting of the ^2D term has been predicted, also on the basis of isoelectronic extrapolation, to be 10 000(1000) cm^{-1} [10]. The binding energy of Pt$^-$ is 17 141(4) cm^{-1} with respect to Pt $(5d^96s\,{}^3D_3)$ [4,11], so that absorption of a second photon at the resonant $M1$ transition energies for both the Ir$^-$ and Pt$^-$ ions can lead to photodetachment via 1 + 1 photon absorption processes.

Sharp resonances in the neutral atom yields are observed, as shown in Fig. 2. The Ir$^-$ resonance is found at an energy of 7087.3(4) cm^{-1} while for Pt$^-$, the energy is 9740.9(5) cm^{-1}. The energy uncertainties are associated with possible calibration errors, in particular,

 0031-9007/96/76(16)/2870(4)$10.00

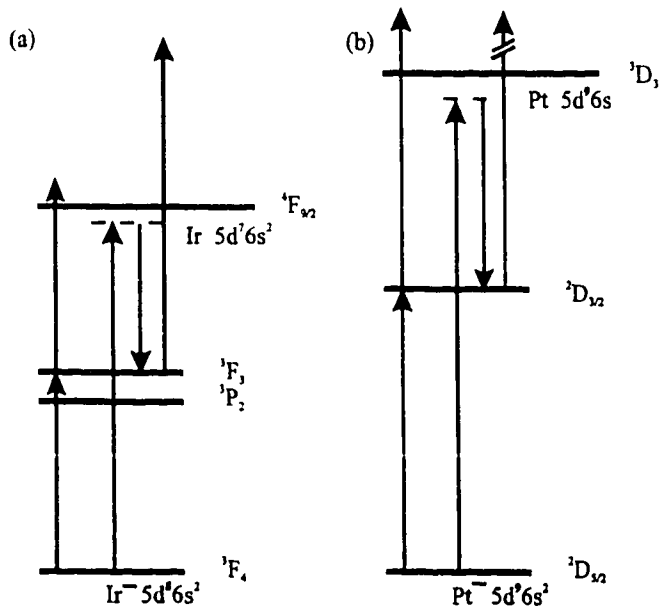

FIG. 1. Schematic energy level diagrams of (a) Ir$^-$ and (b) Pt$^-$ showing the 1 + 1 $M1$ resonant photon absorption and the 2 + 1 Raman absorption schemes. The ordering of the levels in the Ir$^-$ ion follows the current calculations (see text). Only the 1 + 1 photon absorption scheme has been observed experimentally in the present work.

due to a potential residual Doppler shift [3,4]. The background signals are attributed to a combination of nonresonant two-photon detachment processes, collisional detachment, and possibly photodetachment of weak molecular ion impurity beams. The peaks illustrated in Fig. 2 exhibit widths $\sim$0.2 cm^{-1}, which is mainly due to a combination of the Doppler widths expected from the effects of the divergences of the ion and laser beams, and the bandwidth of the laser light. The photon energy scan regions for Ir$^-$ and Pt$^-$ are, respectively, 5895–9234 and 8328–10951 cm^{-1}. Experimental

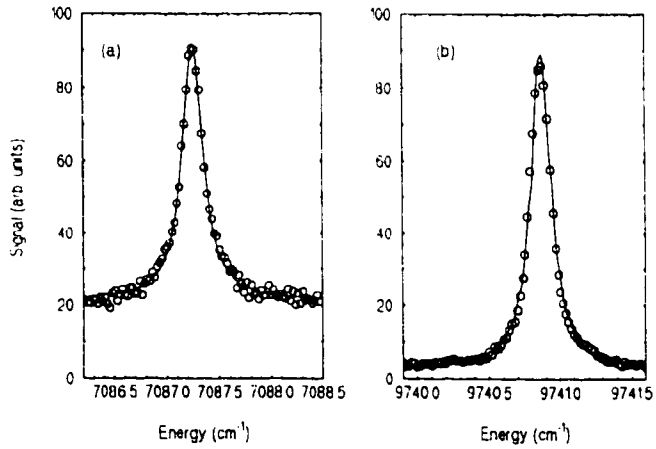

FIG. 2. The resonances in the two-photon detachment yields for (a) Ir$^-$ and (b) Pt$^-$.

scans below the current lower photon energy limit are much more difficult, given the present nonlinear optical conversion scheme. Moreover, below 6311 cm^{-1} in Ir$^-$ and 8571 cm^{-1} in Pt$^-$, a 1 + 1 absorption process is not possible, and a second fixed photon energy which is sufficiently energetic would have to be incorporated in order to maintain a second order process. The intensity dependence of the Pt signal is found to scale as $\sim I^{1.7}$ (where I is the laser intensity), which supports the proposed 1 + 1 absorption scheme under only moderate saturation. Attempts to observe a 2 + 1 detachment process in a Raman coupling regime [3,4] are also made by utilizing two laser beams, a tunable red dye laser beam (which is Raman converted for Ir$^-$), and the first Stokes output of a (H_2) Raman-converted Nd:YAG fundamental beam at a wavelength of 1.9 μm. These efforts to obtain resonances via this second technique, which provides for the allowed two-photon electric dipole transition between the J levels, are unsuccessful to date. This might be explained by the increased complexity of the Ir$^-$ and Pt$^-$ Raman experiments, and smaller cross sections for the 2 + 1 photon absorption processes as contrasted with earlier work on Se$^-$ and Te$^-$ [3,4,12].

The GRASP92 multiconfiguration Dirac-Fock (MCDF) program [13] is used to perform extended optimal level (EOL) [14] calculations to determine relevant energy differences in the Ir$^-$ and Pt$^-$ ions. The EOL procedure is utilized since it provides a common set of wave functions for all the levels considered. All levels are thus treated in a consistent manner. Our approach allows the correlation energy among valence electrons to be accounted for in both the ground and excited states. For the Ir$^-$ ion, the $6s$, $6p$, $5d$, $7s$, $7p$, $6d$, and $5f$ orbitals are included. For the Pt$^-$ ion, the same orbitals are included, with the extra addition of the $5g$ orbital. Calculated wave functions are used to obtain A coefficients for $M1$ transitions. A detailed description of our method is provided in Ref. [15]. the ground state of Ir$^-$ is found to be the $5d^86s^2$, $J = 4$ level and is of ^3F character . A $5d^86s^2$, $J = 2$ level of ^3P character is the first excited level, and it lies 5920 cm^{-1} above the ground state. The $5d^86s^2$, $J = 3$ level is the second excited level and it is found to lie 6671 cm^{-1} above the ground state, which is close to the previous estimate of 7600(1500) cm^{-1} [8]. The third excited level, at an energy of 12861 cm^{-1}, is found to be a $5d^86s^2$, $J = 2$ level of ^3F character, and a fourth excited level ($J = 0$) is found at an energy of 14653 cm^{-1}. The energy of the second $J = 2$ level is close to that obtained earlier, 12000(1200) cm^{-1}, derived from isoelectronic extrapolation [8]. It is therefore expected to be unbound on the basis of our calculations [8]. The A value for the $M1$ transition between the $J = 3$ and $J = 4$ levels is calculated to be 7 s^{-1}. The ground state of the Pt$^-$ ion is found to be the $5d^96s^2$, $J = 5/2$ level. The $J = 3/2$ level is the first excited level and it lies 9535 cm^{-1}

above the ground state. This is also close to the previous estimate of 10000(1000) cm^{-1} [10]. The A value for the $M1$ transition between these levels is found to be 14 s^{-1}. The $5d^{10}6s$, $J = 1/2$ level is found to be the second excited state, and it lies 11301 cm^{-1} above the ground state. Previous work [10] predicted this $^2S_{1/2}$ level to lie 12850 cm^{-1} above Pt^- ($^2D_{5/2}$). The accuracy of the energy level calculations cannot be readily derived from first principles, but comparisons with known values indicate a level of accuracy of a few percent (see below).

The arguments supporting the current $M1$ interpretation of the resonances are now considered. The present calculations on the $M1$ transition probabilities are in qualitative agreement with values taken from neutral atom species of comparable mass [16], and the energies of the isolated resonances are very close to the theoretical values. The observed intensity dependence for the Pt^- case also supports the conclusions. Indeed, our computer simulations of the laser-ion interaction—which incorporate Gaussian functions for the temporal, spectral, and spatial variations of the laser pulse—indicate that the 1 + 1 photon detachment process via an $M1$ resonance should be readily observable under the present experimental conditions. The signal simulations are based on the calculated values for the A coefficients and order-of-magnitude values for the single-photon detachment cross section of the excited $^2D_{3/2}$ level. Some saturation of the signal is clearly predicted, such that the slope for signal-versus-intensity relationship is less than 2, but the many uncertainties in the various experimental parameters do not warrant detailed deductions from this first work. We also performed additional calculations on the fine structure splittings in neutral Au and I, as well as Te^-, in order to further evaluate the likelihood of the present $M1$ interpretation being correct. Our calculated value for the $5d^96s^2\,^2D$ $J = 5/2$-$3/2$ splitting for Au is found to be 11987 cm^{-1}, compared with a literature value of 12274 cm^{-1} [17]. The ground state fine structure splittings for I and Te^- are found, respectively, to be 7445 and 4879 cm^{-1}, which can be compared with literature values of 7603 [17] and 5005 cm^{-1} [3]. The calculated values lie below experimental values to an extent which is comparable to that described above for Ir^- and Pt^-, which lends further support for the $M1$ interpretation of the observed peaks.

The possible role of other states should be considered. If the Pt^- energies are shifted downward from the theoretical values, it is possible that the $^2D_{3/2}$ level lies below our lower (two-photon detachment) scanning range of 8571 cm^{-1}, and that the $^2D_{5/2}$-$^2S_{1/2}$ transition is observed instead. However, given the fact that this would be an electric quadrupole transition, the much lower transition probability [6,16] would suggest that this explanation is unlikely. Similarly, in the Ir^- case, a single photon $J = 4$-2 transition (for either $J = 2$, of ^3P or ^3F character) is assumed to be too weak for our present experiment to detect. A scan aimed at detection of a 1 + 1 photon detachment resonance via the second $J = 2$ level is conducted on Ir^- in the range of 11042–12539 cm^{-1}, but no peak is observed. Either the $E2$ transition is too weak or the second $J = 2$ level is unbound, as our calculations suggest. The failure of the 2 + 1 photon Raman experiment could suggest that the excited state is of the opposite parity to the ground state. However, an allowed electric-dipole transition should then lead to an enormous single-photon absorption probability, and this is not the case here. This conclusion might be modified for a strongly spin-forbidden electric-dipole transition, but no states of this character are expected in these energy regions. Resonant enhancement after two-photon absorption via a state embedded in the continuum of the ion is also possible. Narrow continuum states have been observed previously (see, e.g., Refs. [5] and [18]). We consider this prospect more relevant to Ir^- where there are more levels. A two-photon transition at the resonant Ir^- energy would lie at 14175 cm^{-1} which is 478 cm^{-1} below our calculated $J = 0$ level, but a two-photon transition from the ground $J = 4$ level would be precluded in this case. Similarly, twice the resonant energy is 1314 cm^{-1} above the second calculated $J = 2$ level, which represents about a 10% energy difference—a significantly larger difference than seen in the above comparisons with well-known experimental values. Moreover, our current understanding does not support a long-lived (hence narrow) $J = 2$ level in the continuum. Finally, the possibility of ions, other than the ground Ir^- and Pt^- species, leading to the observed resonance can be considered. Excited levels can be ruled out on the basis that, for excitations of ~5000 cm^{-1} and above, the thermal population in these other levels is so low that it can be neglected [4] in these two-photon experiments. The isolated and sharp resonances observed are also not expected to be associated with weak molecular impurity ions. The negative ions of iridium and platinum are highly prolific from a sputter ion source and the observed signal strengths are very reproducible over long periods of time.

The observation of electric-dipole-forbidden transitions in an optical regime is of course not uncommon in neutral atoms and positive ions. They play a very important role in astronomical and astrophysical phenomena, and form the basis of some of the more powerful lasers [19]. Multiphoton processes involving electric-dipole-forbidden transitions can greatly improve the knowledge of fine structure in negative ions. In addition, the $M1$ pumping scheme might provide values for the lifetimes of excited fine structure levels of some atomic negative ions for the first time, provided that the intensity and other experimental conditions can be accurately calibrated in future work. Alternatively, novel preparation techniques for highly excited levels, together with ion storage schemes, may be required to obtain some first experimental knowledge of these lifetimes [20]. Lifetimes of ~100 ms, as suggested

by the current experimental and theoretical effort, are accessible to accurate measurement via storage rings [21]. Analogous studies of a number of other negative ions of intermediate and heavy mass in the regime of tunable two-photon detachment could reveal as-yet-unknown aspects of negative ion structure. Moreover, new optical parametric oscillator technology will yield laser pulse energies 2 orders of magnitude higher than utilized in the present work. Finally, species such as Ir^- and Pt^- could provide model targets for strong-laser-field studies on atomic species which exhibit only a single resonant interaction.

In summary, the possibilities for resonant multiphoton detachment of negative ions via magnetic dipole transitions have been outlined. Experiments conducted on both Ir^- and Pt^- are used to support the $M1$ interpretation of the resonances observed in the present work. Our theoretical calculations on the ionic properties and computer simulations on the expected experimental signals further support the magnetic dipole interpretation and indicate that such resonances should be readily observed under typical experimental conditions with pulsed laser sources and keV ion beam technology.

We thank the Natural Sciences and Engineering Research Council of Canada (NSERC) for support of this work. The inputs of T. Andersen, P. Balling, and H. Stapelfeldt during various stages of the work is also greatly appreciated. A. F. Starace has provided helpful guidance on some of the theoretical questions.

*Also with the Department of Engineering and Physics, the Institute for Materials Research, and the Center for Electrophotonic Materials and Devices, McMaster University.

[1] See H. Hotop and W. C. Lineberger, J. Phys. Chem. Ref. Data **14**, 731 (1985); D. R. Bates, Adv. At. Mol. Phys. **27**, 1 (1991); and T. Andersen, Phys. Scr. **T34**, 23 (1991).
[2] M. D. Davidson, H. G. Muller, and H. B. van Linden van den Heuvell, Comments At. Mol. Phys. **29**, 65 (1993).
[3] P. Kristensen *et al.*, Phys. Rev. Lett. **71**, 3435 (1993).
[4] J. Thogersen *et al.*, Phys. Rev. A (to be published); J. Thogersen *et al.*, J. Phys. B (to be published).
[5] H. Stapelfeldt *et al.*, Phys. Rev. A **50**, 1618 (1994).
[6] See A. Corney, *Atomic and Laser Spectroscopy* (Oxford University, New York, 1977).
[7] Radiofrequency spectroscopy has been applied to fine structure determinations in the helium negative ion; D. L. Mader and R. Novick, Phys. Rev. Lett. **29**, 199 (1972).
[8] C. S. Fiegerle, R. R. Corderman, S. V. Bobashev, and W. C. Lineberger, J. Chem. Phys. **74**, 1580 (1981).
[9] H. Hotop and W. C. Lineberger, J. Chem. Phys. **58**, 2379 (1973).
[10] R. J. Zollweg, J. Chem. Phys. **50**, 4251 (1969).
[11] N. D. Gibson, B. J. Davies, and D. J. Larson, J. Chem. Phys. **98**, 5104 (1993).
[12] A. F. Starace (private communication).
[13] F. A. Parpia, C. Froese Fischer, and I. P. Grant, Comput. Phys. Commun. (to be published).
[14] I. P. Grant, in *Computational Chemistry*, edited by S. Wilson (Plenum, New York, 1988); K. G. Dyall *et al.*, Comput. Phys. Commun. **55**, 425 (1989).
[15] W. P. Wijesundera, S. H. Vosko, and F. A. Parpia, Phys. Rev. A **51**, 278 (1995).
[16] R. H. Garstang, J. Res. Natl. Bur. Stand. Sect. A **68**, 61 (1964).
[17] See *Atomic Energy Levels*, edited by C. E. Moore, National Standard Reference Data Series (U.S. National Bureau of Standards, Washington, DC, 1971), Vol. III.
[18] A. Stintz *et al.*, Phys. Rev. Lett. **75**, 2924 (1995).
[19] K. Hohla and K. L. Kompa, in *Handbook of Chemical Lasers*, edited by R. W. F. Gross and J. F. Bott (Wiley, New York, 1976); W. P. Hess *et al.*, J. Chem. Phys. **84**, 2143 (1986).
[20] C. Desfrancois, H. Abdoul-Carime, N. Khelifa, and J. P. Schermann, Phys. Rev. Lett. **73**, 2436 (1994); T. Andersen *et al.*, Phys. Rev. A **47**, 890 (1993).
[21] P. Balling *et al.*, Phys. Rev. Lett. **69**, 1042 (1992).

Paper 9

Fine-structure measurements for negative ions: Studies on Se^- and Te^-.

J. Thogersen, L. D. Steele, M. Scheer, H. K. Haugen, P. Kristensen, P. Balling, H. Stapelfeldt, and T. Andersen.

Physical Review A **53**, 3023-8 (1996).

Fine-structure measurements for negative ions: Studies of Se^- and Te^-

J. Thøgersen, L. D. Steele, M. Scheer, and H. K. Haugen*
Department of Physics and Astronomy, McMaster University, Hamilton, Ontario, Canada L8S 4M1

P. Kristensen, P. Balling, H. Stapelfeldt,† and T. Andersen
Institute of Physics and Astronomy, University of Aarhus, DK-8000 Aarhus C, Denmark

(Received 10 October 1995)

This paper comprises a comparison of experimental methods used for determining fine-structure splittings in negative atomic ions. The comparison is based on experimental data for the fine-structure splittings of the $4p^5\ ^2P$ term of Se^- and $5p^5\ ^2P$ term of Te^- obtained by single-photon detachment and three-photon detachment in a Raman coupling scheme. The result for the $J=\frac{3}{2}-\frac{1}{2}$ splitting in Se^- is found to be 2278.2(2) cm^{-1}, while the $J=\frac{3}{2}-\frac{1}{2}$ splitting in Te^- is 5004.6(5) cm^{-1}. A variety of experimental approaches to fine-structure measurements are briefly discussed. In many atomic negative ions the perspectives for improvements in the determination of fine-structure splittings are in the range of two to three orders of magnitude.

PACS number(s): 32.10.Fn, 32.80.Fb, 32.80.Rm, 32.80.Dz

INTRODUCTION

The spectroscopy of negative ions has been a topic of considerable interest for the past two decades (for recent reviews, see Refs. [1–3]), stimulated by the fact that negative ions exhibit qualitatively different properties from those of neutral atoms and positive ions. The additional electron of a negative ion is bound by a short-range potential rather than by a Coulomb potential. This implies that most negative ions only exist in one bound electronic configuration as opposed to the infinity of Rydberg states present in neutral atoms and positive ions. Progress in the knowledge of negative-ion structure has primarily been achieved from laser-ion interaction experiments and from *ab initio* calculations. In particular, tunable laser photodetachment spectroscopy has been used extensively to determine binding energies, the position and width of autoionizing states in the continuum, and properties of bound electronic configurations such as term or fine-structure splittings [4,5]. The determination of the energy of bound levels has mainly been accomplished by measuring the threshold energy of the transition from the negative-ion level either to the ground level or to an excited level of the corresponding neutral atom. However, this technique may not be well suited for studies in which the fine-structure or term splittings exceed many hundred cm^{-1} due to the typically very low populations in the higher-lying excited states. Recently we demonstrated a method for accurate determination of fine-structure splitting in ions which does not rely on the initial population of the excited level [6]. This technique is based on population transfer from the lower-lying to the upper-lying fine-structure level via stimulated Raman transitions induced by two strong laser fields (see Fig. 1).

This paper addresses tunable laser techniques used to determine term and fine-structure splittings in negative ions. The experimental efforts involve collaborative studies between the University of Aarhus and McMaster University. Both single-photon detachment studies and multiphoton Raman experiments are conducted. Single-photon detachment studies are conducted on the ground and excited levels of Se^- and Te^-. The results are compared with the three-photon Raman results, and the advantages and disadvantages of the techniques are analyzed. A broader discussion of the current status of knowledge of fine-structure splittings in atomic negative ions is also given, and additional experimental prospects such as direct multiphoton absorption experiments are outlined briefly. These alternative techniques are also under development in the laboratories at the University of Aarhus and at McMaster University and will be reported in detail separately.

EXPERIMENTAL SETUPS

The experimental setups involved in the efforts at the University of Aarhus and McMaster University are conceptually identical. In the following, the experimental setups are described, and the differences are noted later, where significant. Only the Se^- Raman experiments are performed at the University of Aarhus, while the Te^- Raman result and all the single-photon results stem from the McMaster University setup.

The experimental setup at the University of Aarhus (as seen in Fig. 2) consists of a fast ion beam crossed perpendicularly with two focused laser beams. The Se^- ions are produced in an ANIS (Aarhus Negative Ion Source) sputter source with a selenium-based cathode. A beam is then created by extracting and accelerating the ions to a final energy of 30 keV. The beam is mass analyzed in a magnetic field, and prior to the interaction region is deflected by a set of electrostatic plates in order to remove any neutral atoms which are produced by collisions between the negative ions

*Also with the Department of Engineering Physics, the Institute for Materials Research, and the McMaster Accelerator Laboratory of McMaster University.

†Present address: Steacie Institute for Molecular Sciences, National Research Council of Canada, Ottawa, Ontario, Canada K1A 0R6.

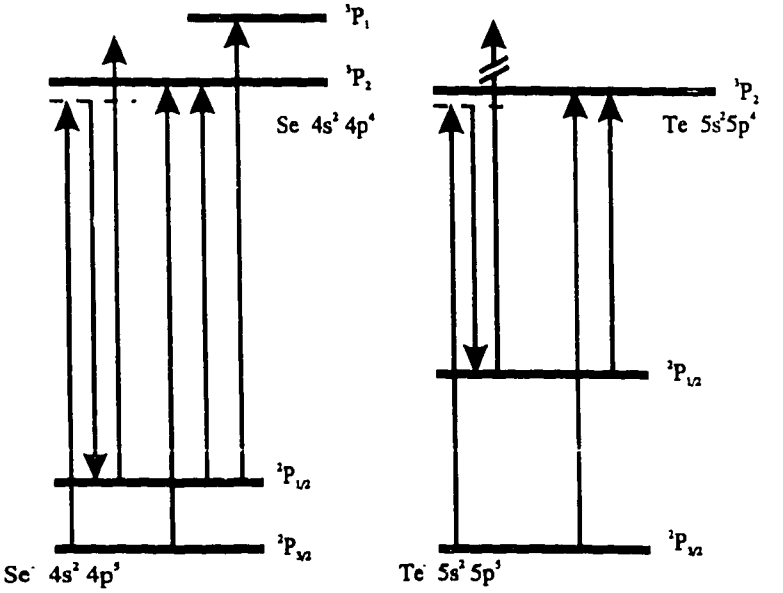

FIG. 1. Schematic energy-level diagram of Se^- and Te^- illustrating the three-photon and single-photon detachment leading to production of neutral Se and Te.

and the residual gas. The beam is charge-state analyzed just after the interaction region by a second set of deflection plates. The laser-detached neutral atoms are then detected by a discrete dynode electron multiplier in a fixed time window after each laser pulse, corresponding to the time it takes the neutral atoms to reach the detector. The open electron multiplier which is used for detection of the neutral atoms takes advantage of the large linear dynamic range and the data are acquired by a boxcar integrator. The laser system for the Se^- Raman work consists of two dye lasers—one operated around 714 nm with a bandwidth of 0.1 cm^{-1} and another around 614 nm with a bandwidth of 0.3 cm^{-1}, both pumped by the second harmonic of the same Q-switched YAG (yttrium-aluminum-garnet) laser which operates at a repetition rate of 10 Hz. The laser beams are focused with a 40-cm focal-length lens and are crossed at 90° with the ion beam, although a small angle of 2.2° exists between the laser beams. An optical delay line ensures optimum temporal overlap between the two laser beams.

The experimental setup at McMaster University is very similar to the Aarhus apparatus. A Middleton sputter ion source provides the negative-ion beams which are typically run at ~10 keV energy. The resolution of the magnet (~5%) is lower than the one in Aarhus, but this is not a limitation where the ions are prolific and the spectral features are unambiguous. The Nd:YAG laser is operated at 10 Hz and has a pulse length of 8 ns and a linewidth of 1.1 cm^{-1}. A pulsed dye laser with a linewidth of ~0.03 cm^{-1} and a pulse length of 6 ns is utilized alone or together with a Raman conversion cell with high-pressure hydrogen gas at 17–21 bar of pressure. At this pressure the Raman shift in H_2 is 4155.20(4) cm^{-1} [7]. Finally, the laser-ion interaction regions in both the Aarhus and the McMaster setups are operated at pressures of $\sim 10^{-8}$ mbar. Therefore collisional detachment within the time-gated window of the boxcar integrator (~50 ns) is almost entirely negligible.

RESULTS

Energy level splitting between the fine-structure levels of Se^-: Raman experiment

Since a detailed description of the technique for the determination of the fine structure was given in a previous paper [6], our presentation here is brief. The yield of Se atoms is recorded while scanning the wavelength of the red laser around 714 nm. The wavelength of the orange laser is fixed at 614.476 nm. The pulse energies of the red and the orange laser beams are 36 and 2.8 mJ, respectively, and the pulse duration of both lasers is ~8 ns. The result is shown in Fig. 3. The strong resonance observed at 714.529 nm corresponds to the wavelength at which the Raman condition for coupling the two fine-structure components of Se^- is fulfilled $[E(^2P_{3/2}) + \hbar\omega_{\text{orange}} - \hbar\omega_{\text{red}} = E(^2P_{1/2})]$ (see Fig. 1). The photon energy of the orange laser is chosen such that single-photon detachment of the $^2P_{3/2}$ ground level of Se^- cannot

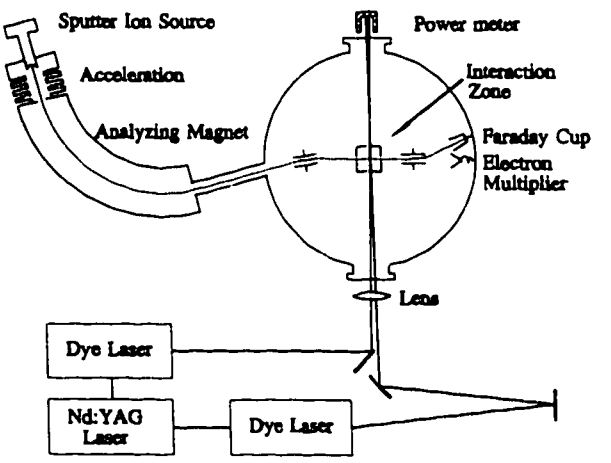

FIG. 2. Experimental setup in the Aarhus experiments. The McMaster apparatus is entirely analogous.

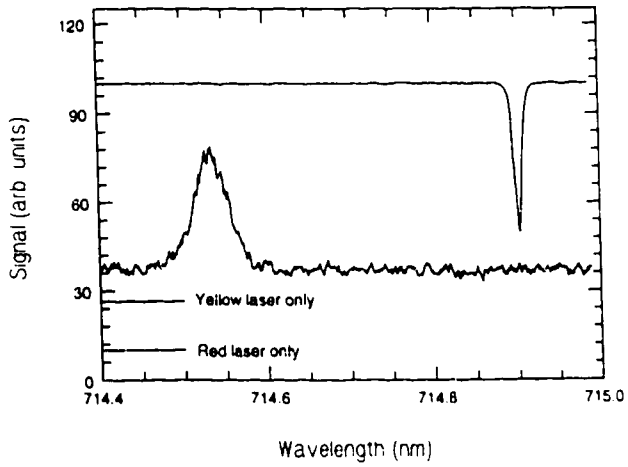

FIG. 3. Plot of the neutral Se signal obtained in the Raman-based experiment versus wavelength of the red laser (~714) nm is shown in the lower trace. The wavelength of the second laser is fixed at 614.476 nm. See Fig. 1 for a schematic illustration of the Raman experiment. Signal from optogalvanic calibration lamp is shown in the upper trace.

occur, but sufficiently large to allow single-photon detachment of the upper $^2P_{1/2}$ level. Thus the peak is the result of population transfer from the lower to the upper fine-structure level by a stimulated Raman process followed by single-photon detachment by the orange laser. Away from resonance, a fraction of the background can be attributed to two-photon detachment of the ground level ($2\hbar\omega_{\text{red}}$, $2\hbar\omega_{\text{orange}}$, $\hbar\omega_{\text{red}}+\hbar\omega_{\text{orange}}$). However, since a small fraction of the ions ($\leq 5\%$) exists in the $^2P_{1/2}$ upper fine-structure level, the direct single-photon detachment by the orange laser is believed to be another significant contribution to the background signal. Considering the three-photon nature of the Raman peak, it might seem surprising that this process is at least as efficient in detaching the ground level as the lower-order processes contributing to the background. The reason is that the lower-order processes are nonresonant two-photon processes whereas the Raman peak results from a resonant two-photon process followed by a strongly saturated one-photon detachment process. As evident from the Raman condition, the position of the peak will give information about the fine-structure splitting if the wavelengths of the two laser fields at the resonance are known. Absolute calibrations of the two wavelengths are performed using optogalvanic discharge cells. The position of the Raman peak is found to appear at a wavelength $\lambda_{\text{red}}=714.529(10)$ nm. Consequently, the fine-structure splitting of Se^-, when correcting for the angle between the two laser beams, can then be determined to be $E(^2P_{3/2})-E(^2P_{1/2})=2278.3(3)$ cm^{-1}. This value improves the accuracy by a factor of 6 in comparison with the previous reported value [2279(2) cm^{-1}] [8]. The main contribution to the uncertainty of the fine-structure splitting in this case is the uncertainty in the angle between the two laser beams. It is clearly possible to reduce this error source, so the uncertainty can be diminished by a factor of 2.

Fine-structure splitting in Se^-: Single-photon detachment experiment

An initial set of measurements is made using the negative ion of sulphur. The binding energy of the fine-structure levels

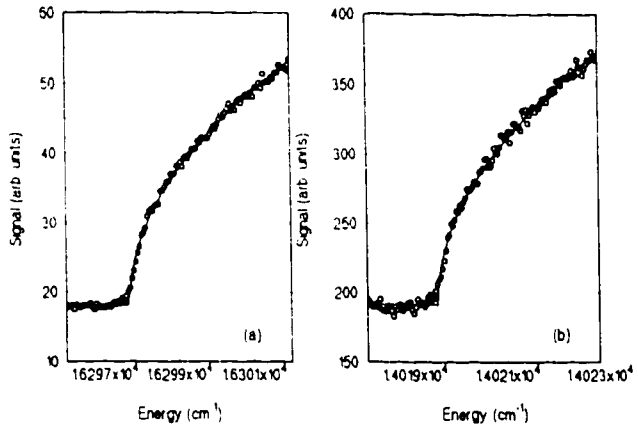

FIG. 4. Plot of the neutral Se signal from single-photon detachment of (a) the ground level $4p^5\ ^2P_{3/2}$ and (b) the excited level $4p^5\ ^2P_{1/2}$ of Se^- fitted with a Wigner s-wave threshold.

in S^- are very well known and the S^- study is conducted to search for possible systematic errors in the McMaster single-photon detachment studies. The experimental value obtained for the electron binding energy of S^- is 16 753.1(6) cm^{-1}, which is in good agreement with the previously known value of 16 752.966(8) cm^{-1} [4]. No unexpectedly large systematic effects are evident from the S^- calibration.

The binding energy of the $4p^5\ ^2P_{3/2}$ and $^2P_{1/2}$ levels of Se^- are determined by tunable laser photodetachment spectroscopy. The fine-structure splitting is then determined as the difference between the respective binding energies. A scan in the region of the ground-level detachment threshold is shown in Fig. 4(a). The measurements are done with a sufficiently low laser-pulse intensity such that saturation of the laser-ion interaction is negligible, and the data are then fitted to the appropriate Wigner threshold. The fit is restricted to a region sufficiently close to threshold such that the limits of applicability of the Wigner law are found to be satisfied empirically. The dye laser is calibrated via use of an optogalvanic cell. The electron affinity is measured at two different kinetic energies of the ion (8.5 and 12 kV) in order to investigate the possible influence of Doppler effects. (If the ion and laser beams do not cross at exactly 90°, the Doppler effect will lead to a systematic error.) The two results are identical within the experimental uncertainty, and the final result for the binding energy of the ground $^2P_{3/2}$ level is 16 297.7(4) cm^{-1}. This result is in excellent agreement with the electron affinity of 16 297.8(2) cm^{-1} reported by Mansour *et al.* [9]. A scan in the region of the excited-level electron detachment threshold is shown in Fig. 4(b). The small deviation near the foot of the s-wave threshold results from the finite resolution of the experiment due to the Doppler width and the bandwidth of the pulsed laser. Two separate runs and fits to the excited-level detachment data yield binding energies of 14 019.67 and 14 019.50 cm^{-1}. The final result is 14 019.6(4) cm^{-1}. Thus the fine-structure splitting becomes 2278.1(3) cm^{-1}. A separate measurement of the photodetachment of $Se^-(^2P_{1/2})$ is conducted in the vicinity of the $Se(^3P_1)$ threshold. Since the thermal population in Se^- ($^2P_{1/2}$) is low, and since the detachment to $Se(^3P_2)$ is substantial in this region, the signal-to-noise is rather poor. A value of 16 009.7(20) cm^{-1} is obtained for the transition en-

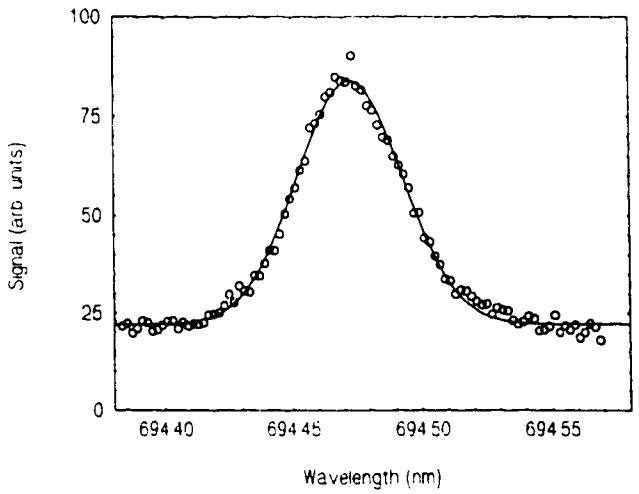

FIG. 5. Plot of the neutral Te signal obtained in the Raman-based experiment versus wavelength of the dye laser. The fixed frequency laser is the Nd:YAG laser fundamental beam (1064.43 nm). See Fig. 1 for a schematic illustration of the Raman experiment.

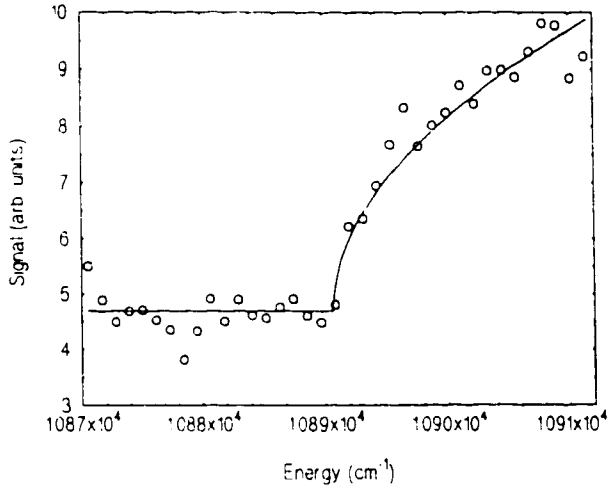

FIG. 6. Plot of the neutral Te signal from the single-photon detachment process $Te^-(5p^5\ ^2P_{1/2}) \rightarrow Te(5p^4\ ^3P_2)$ fitted with a Wigner s-wave threshold.

ergy. By taking into account the known fine-structure energy splitting ($^3P_2$-$^3P_1$) in the selenium atom of 1989.45(1) cm^{-1} [10], one obtains a binding energy for $Se^-(^2P_{1/2})$ with respect to $Se(^3P_2)$ of 14 020.3(17) cm^{-1}. This is consistent with the more accurate results above, and reflects the limitations due to low population in the excited level, and due to accessing an excited level threshold of the neutral atom.

Fine-structure splitting in Te^-: Raman experiment

A three-photon Raman experiment is conducted at McMaster University with the negative tellurium ion. An energy level diagram is shown in Fig. 1. An analogous experiment on Te^- has been performed previously at the University of Aarhus [6], and a fine-structure splitting of 5004.7(2) cm^{-1} was obtained. The McMaster University experiment serves to establish the accuracy which can be readily achieved in such work, and provides a comparison of results for totally independent, yet technically analogous systems. In the McMaster experiment, the main technical difference (versus the Aarhus Te^- and above Se^- work) is that the two laser beams are in this case overlapped collinearly via a dichroic mirror and focused with an 18-cm focal-length lens. Approximately 100 nA of Te^- current is employed in the ultrahigh-vacuum section of the apparatus. Using a 15-mJ dye laser beam where the photon energy is calibrated via an optogalvanic lamp, and 30 mJ of the fundamental Nd:YAG laser beam, we find a Raman resonance with a center wavelength of 694.472 nm (vacuum) as shown in Fig. 5. The Nd:YAG laser (vacuum) wavelength is measured to be 1064.43(5) nm with a pulsed laser wavemeter. This leads to a value of the fine-structure splitting of 5004.6(5) cm^{-1}. This is in very close agreement with the earlier result from Aarhus [6] of 5004.7(2) cm^{-1}, and the previous best result of 5008(5) cm^{-1} [11]. The scan shows a 3:1 signal-to-background ratio. The background is attributed to two-photon nonresonant processes and one-photon detachment from the excited electronic state, as discussed already for Se^-.

Fine-structure splitting in Te^-: Single-photon detachment experiment

Single-photon detachment experiments are conducted to measure the ground- and excited-level energies of the $5p^5\ ^2P$ term. As in the case of Se^-, saturation effects are avoided and the computer fits to the data are restricted to a region close to threshold, where the Wigner threshold law is expected to apply. A high signal-to-noise ratio is achieved on the single-photon detachment experiment on the ground-state ions, as in the case for Se^-. The binding energy of the $^2P_{3/2}$ level is found to be 15 896.9(4) cm^{-1}, which is in good agreement with the literature value of 1.9708(3) eV, or 15 895(2) cm^{-1}. The excited-level data, displayed in Fig. 6, shows a low signal-to-noise ratio due to the low excited-level population. The small population also results in a low signal-to-background ratio, since photodetachment of impurity ions contribute substantially to the detected signal. This reflects the key point in the limitation for single-photon experiments in the present regime. Also only a relatively low laser power is available in this case, ~0.9–1.6 mJ per pulse, due to the low Raman conversion in this wavelength regime. The binding energy is found to be 10 890.8(20) cm^{-1}. This value together with the binding energy of the ground level [15 896.9(4) cm^{-1}], gives a fine-structure splitting of 5006(2) cm^{-1}.

DISCUSSION

Comparison of Raman and single-photon detachment results in Se^- and Te^-

The results of the three-photon Raman and single-photon experiments for Se^- and Te^- can now be compared directly. In the case of Se^-, the two techniques yield results which are mutually consistent and are of the same level of accuracy. Since the fine-structure splitting in Se^- is still not too large, a serious limitation on the single-photon work is not encountered. The situation is very different in Te^-.

In this case, the Raman approach is clearly superior. The population of the upper $^2P_{1/2}$ level is sufficiently low that this clearly affects the accuracy which can be obtained with

the single-photon technique. The McMaster Raman experiment on Te^- is not pushed to the limit of accuracy that is possible (as illustrated in the earlier Aarhus work), and in this current instance is limited by the wavemeter calibration on the Nd:YAG laser wavelength, and not by factors intrinsic to the technique. Thus the level of accuracy which can be readily obtained (~ 0.2 cm^{-1}) with the Raman work can be compared with the uncertainty of the single-photon study in this case, which is 2 cm^{-1}.

It is instructive to consider the implications of a Boltzmann temperature distribution for the populations in various fine-structure levels. Although level populations cannot be rigorously associated with a thermodynamic temperature, for assumed ion-source temperatures in the range of 1000–1500 K, the level populations are expected to drop off very rapidly for fine-structure splitting greater than ~ 1000 cm^{-1}. Thus the Se^- splitting is in the range of 2–3 kT, while the splitting in Te^- is about twice that, which explains the poor signal-to-noise in the Te^- single-photon data. This aspect is further illustrated by single-photon detachment studies on the negative ions of Si^-, Ge^-, Sn^-, and Pt^-, which will be reported separately [12]. As discussed further below, the higher-lying terms and higher-lying fine structure levels in these species are in the range of ~ 6500–$10\,000$ cm^{-1} above the respective ground levels. In our single-photon work, aimed at improving the electron affinity (EA) values for these species [12], we have not yet been successful in observing adequate single-photon signals from the higher-lying states.

The most significant sources of experimental uncertainty in the present work stem from possible Doppler shifts, and the effects of the finite linewidth of the laser sources and possible errors in their calibration. Even in transverse geometry, the characterization of Doppler effects could be improved at least by a factor of 2 or 3, and pulsed laser sources with somewhat narrower linewidth could be utilized in future work. With a further increase in accuracy, yet other effects should be taken into account. Possible complications from hyperfine splitting should be considered at the level of 0.1 cm^{-1} [13] and transit-time broadening can be important for the Raman work with pulsed laser beams [14]. For the present experimental conditions, the transit-time effect alone contributes a width <0.1 cm^{-1}, but for higher beam energies and strong focusing conditions, this effect may not be negligible. The main thrust of the paper, however, is not to suggest improvements beyond the present level of accuracy. Rather, we suggest experimental schemes for the very substantial improvement of negative-ion data, as is outlined in the following section.

General perspectives for fine-structure measurements in atomic negative ions

The pioneering work of Hotop and Lineberger [4] and others provided an excellent overview of the EA's of the elements, and Lineberger's group has conducted selected single-photon detachment experiments with cw lasers of very high spectral resolution. Other species have been measured via electron spectrometry, while still other results rely on isoelectronic extrapolations. The binding energies of the ground levels of selected negative species such as hydrogen, oxygen, and sulphur are known to very high accuracy and some fine-structure splittings are also very well determined. However, the fine-structure splittings of many atomic negative-ion species are poorly determined including many intermediate mass and heavy species. Not only the fine-structure splittings, but also the EA's of many rare-earth species are unknown. Heavy species such as Ir^- and Pt^- have large uncertainties in the energy of various terms as well as for the fine-structure splittings of specific terms. For example, the $J=\frac{5}{2}-\frac{1}{2}$ splitting of the ^2D state of Pt^- is given as 10 000(1000) cm^{-1} [15,16].

It was seen via the Se^- and the Te^- studies that the three-photon Raman technique could be very useful in cases where there is limited population in the excited level of the negative ion, and where the laser wavelengths required can be conveniently obtained. In addition, the Raman experiment yields a sharp peak as opposed to a Wigner threshold. Thus there is a potential additional advantage of the Raman approach over the single-photon case even where all states are fairly well-populated, especially where p-wave thresholds would be obtained in the single-photon detachment as opposed to s-wave thresholds. In transition-metal ions, where there are many fine-structure states which are relatively closely spaced, the Raman approach may therefore be quite attractive. There are limitations of the Raman approach beyond the wavelength issues noted above. Focused laser beams are required in the multiphoton experiments and therefore a much smaller target volume is involved as contrasted with single-photon experiments. In addition, the signals depend in part on the cross sections for the Raman process, and these cross sections are not known at present. Therefore precise extrapolations beyond the Se^- and Te^- cases are not possible. For higher-lying levels which are very weakly bound with respect to the neutral-atom ground state, the Raman technique would require access to midinfrared laser-based sources. If a Raman experiment is attempted with photon energies such that the virtual level is lying in the continuum, the ion can be photodetached directly from the ground level via absorption of a single-photon. The three-photon Raman signal is then expected to be lost in an enormous background due to single-photon absorption, especially for long (nanosecond) laser pulses. A similar wavelength restriction would exist for single-photon studies if detachment to the ground state of the neutral atom is required. However, wavelength restrictions might be solved if the single-photon detachment is conducted to an excited-state threshold of the corresponding neutral atom. The limitations of this variation of single-photon work, as well as a possible solution, are noted below.

Negative-ion species where the greatest advances in the accuracy of data are possible typically involve very weakly bound states. With most negative-ion production techniques, both the single-photon and Raman approaches encounter difficulties in these cases. This comprises ions where all levels are weakly bound as in the alkaline-earth species such as Ca^-, and those in which only the higher-lying levels are weakly bound such as in Si^-, Sn^-, and Ir^-. Si^- is known to possess several levels which are bound: a $^4S_{3/2}$ level bound by 1.385(5) eV; a ^2D term bound by 0.523(5) eV and a ^2P term bound by 0.029(5) eV [17]. Both the ^2D and the ^2P terms would be weakly populated in a beam extracted from a sputter source exhibiting near-thermodynamic-equilibrium conditions. Even the ^2D term would require a substantial IR

laser capability in order to conduct Raman experiments or single-photon threshold laser experiments to the ground state of the corresponding neutral atom. The ^2P term would be ruled out in this context. The situation is worse in the analogous case of Sn^- where the corresponding uncertainties are much larger [4,18]. Cases such as Ir^- are also difficult in the context of the two techniques outlined in this paper. The binding energy of Ir^- is 1.565(8) eV or 12 622(65) cm^{-1}, and the fine-structure splittings of the ^3F term are given, via isoelectronic extrapolation, as $J=4-3$, 7600(1500) cm^{-1}; $J=3-2$, 4400(900) cm^{-1}, and $J=4-2$, 12 000(1200) cm^{-1} [19]. The $J=4-3$ splitting may be amenable to a Raman experiment, but the single-photon work is likely not feasible.

There exist techniques which can greatly extend and complement those which are utilized in the present work. The approaches presented here are (1) multiphoton experiments in a more general context, (2) application of resonant ionization spectroscopy (RIS), and (3) selective charge-transfer mechanisms. The above examples of Si^-, Sn^-, and Ir^- might be addressed by alternative multiphoton studies. The ^2D term in Sn^- could be explored via a 2+1 photon-absorption experiment in a spin-changing absorption process from the ground ^4S term. An analogous 2+1 photon-absorption experiment is possible in Ir^- $^3F(J=4-2)$ with no spin change. Other multiphoton schemes using relatively intense fields may be applied in other cases. For very weakly bound species such as Ca^- and many rare-earth ions the EA's can be determined by performing detachment spectroscopy to excited states of the corresponding neutral atom, thereby facilitating use of favorable laser wavelengths. However, this typically leads to a very small threshold feature on top of a large background. Very recently the application of resonant ionization spectroscopy to negative ions has pointed toward substantial solutions for these cases [20]. By detecting positive ions in a RIS arrangement, sensitive and selective monitoring of the population in the excited states of the neutral atom is provided. Finally, it should be noted that one could populate excited levels by selective charge-exchange mechanisms, such that thermodynamic equilibrium mechanisms are not limiting. Many charge-exchange mechanisms may be of interest in populating highly excited states in negative ions since these collisional processes may offer advantages over the pseudo-thermal-equilibrium distribution which is associated with the sputter ion sources.

CONCLUSIONS

The accuracy of the fine-structure splitting as well as the electron affinities in Se and Te have been improved by a combination of tunable laser spectroscopic studies in both single-photon and multiphoton absorption regimes. The pulsed laser techniques, along with associated nonlinear optical conversion mechanisms, provide a means to achieve very substantial progress for a large number of atomic negative-ion species. The pulsed laser experiments often facilitate improvements in data by one to three orders of magnitude, readily access new wavelength regions in the IR, and allow for multiphoton as well as single-photon experiments. Finally, some of the techniques discussed here may also find applications in the future for work with negatively charged molecules and clusters.

ACKNOWLEDGMENTS

This work has been supported by Aarhus Center for Advanced Physics, the Carlsberg Foundation, and the Natural Science and Engineering Research Council of Canada.

[1] D. R. Bates, Adv. At. Mol. Phys. **27**, 1 (1991).
[2] T. Andersen, Phys. Scr. **T34**, 23 (1991).
[3] S. J. Buckman and C. W. Clark, Rev. Mod. Phys. **66**, 539 (1994).
[4] H. Hotop and W. C. Lineberger, J. Phys. Chem. Ref. Data **14**, 731 (1985).
[5] V. A. Esaulov, Ann. Phys. (Paris) **11**, 493 (1986).
[6] P. Kristensen, H. Stapelfeldt, P. Balling, T. Andersen, and H. K. Haugen, Phys. Rev. Lett. **71**, 3435 (1993).
[7] W. K. Bischel and M. J. Dyer, Phys. Rev. A **33**, 3113 (1986).
[8] H. Hotop, T. A. Patterson, and W. C. Lineberger, Phys. Rev. A **8**, 762 (1973).
[9] N. B. Mansour, C. J. Edge, and D. J. Larson. Nucl. Instrum. Methods Phys. Res. Sect. B **31**, 313 (1988).
[10] C. E. Moore, *Atomic Energy Levels* (U.S. GPO, Washington, D.C., 1971), Vol. 35.
[11] J. Slater and W. C. Lineberger, Phys. Rev. A **15**, 2277 (1977).
[12] J. Thøgersen, L. D. Steele, M. Scheer, C. A. Brodie, and H. K. Haugen, J. Phys. B (to be published).
[13] A. Corney, *Atomic and Laser Spectroscopy* (Oxford University Press, Oxford, 1977).
[14] W. Demtröder, *Laser Spectroscopy, Basic Concepts and Instrumentation* (Springer-Verlag, Berlin, 1982).
[15] H. Hotop and W. C. Lineberger, J. Chem. Phys. **58**, 2379 (1973).
[16] R. J. Zollweg, J. Chem. Phys. Lett. **50**, 4251 (1969).
[17] A. Kasdan, E. Herbst, and W. C. Lineberger, J. Chem. Phys. **62**, 541 (1975).
[18] T. M. Miller, A. E. S. Miller, and W. C. Lineberger, Phys. Rev. A **33**, 3558 (1986).
[19] C. S. Feigerle, R. R. Corderman, S. V. Bobashev, and W. C. Lineberger, J. Chem. Phys. **74** 1580 (1981).
[20] V. V. Petrunin, J. D. Voldstad, P. Balling, P. Kristensen, T. Andersen, and H. K. Haugen, Phys. Rev. Lett. **75**, 1911 (1995).

Paper 10

Electron affinities of Si, Ge, Sn and Pt by tunable laser photodetachment studies.

J. Thogersen, L. D. Steele, M. Scheer, C. A. Brodie, and H. K. Haugen.

Journal of Physics B **29**, 1323-30 (1996).

J. Phys. B: At. Mol. Opt. Phys. 29 (1996) 1323–1330. Printed in the UK

Electron affinities of Si, Ge, Sn and Pt by tunable laser photodetachment studies

J Thøgersen, L D Steele, M Scheer, C A Brodie and H K Haugen†

Department of Physics and Astronomy, McMaster University, Hamilton, Ontario, Canada L8S 4M1

Received 17 October 1995

Abstract. The electron affinities of silicon, germanium, tin and platinum are measured by tunable laser photodetachment spectroscopy via detection of the neutral atomic species. The binding energy values obtained for Si^-, Ge^- and Sn^- (electron configuration np^3 with $n = 3$ to 5) are 11 207.0(5) cm^{-1}, 9942.6(4) cm^{-1} and 8969.6(5) cm^{-1}, respectively. The improvements in accuracy over the existing values in the literature for these three species lie between one and two orders of magnitude. The binding energy of the $5d^96s^2\ ^2D_{5/2}$ ground level of Pt^- is found to be 17 141(6) cm^{-1}. This result is in relatively good agreement with the two existing results in the literature. Finally, the prospects for further studies of atomic negative ions are briefly discussed.

1. Introduction

Negative ions have been the topic of considerable study in the past two decades due to both their fundamental and practical implications. One decade ago, Hotop and Lineberger reviewed the existing data on atomic negative ions [1]. Since that time, progress has continued on atomic negative ions, but much effort has been directed to molecular and cluster species [2, 3]. Although most elements form negative ions, many electron affinities, electron configurations and quantum states are either poorly known or totally unknown. The situation is most notable for species of medium and heavy mass and particularly where very weakly bound states are involved. A substantial improvement in the knowledge of the atomic negative ions will require input from a variety of complementary experimental techniques.

In the present paper, we report the electron affinities of silicon, germanium, tin and platinum. The first three species form negative ions with an np^3, $n = 3$–5 outer subshell configuration. The measured electron affinities of these species can be improved considerably by utilizing tunable laser photodetachment spectroscopy in the near infrared region of the spectrum. Nonlinear optical conversion of the visible light from a pulsed dye laser via stimulated Raman processes is employed to probe the ionic species. The Wigner threshold law [4] provides for an s-wave behaviour at the photodetachment threshold in the case of Si^-, Ge^- and Sn^-, and a very accurate determination of the threshold is possible. The electron affinity of platinum is also reported and the Wigner p-wave behaviour associated with photodetachment of Pt^- provides a distinct contrast with the above three

† Also with the Department of Engineering Physics, the Institute for Materials Research and the Center for Electrophotonic Materials and Devices at McMaster University, Hamilton, Ontario, Canada.

0953-4075/96/071323+08$19.50

ions. Some broader perspectives for further work in these and other atomic negative ion species are briefly discussed.

2. Experimental technique

A schematic of the McMaster University set-up is shown in figure 1. A sputter ion source provides beams of the required negative ions. Si^-, Ge^-, Sn^- and Pt^- are all prolific ions from this source and this greatly reduces beam contamination issues. The ions are accelerated to an energy of ~8–12 keV and are subsequently charge and mass analysed by a magnet with a bending angle of 30° and a magnetic field restricted to a maximum of ~0.6 T. The ion beam then passes through a differential pumping section which provides for a differential vacuum of between two and three orders of magnitude. The beam then enters an ultra-high vacuum (10^{-9}–10^{-8} mbar) section where the beam is first charge-state analysed via electric field deflection through an angle of ~10°. The ion beam is then subsequently crossed perpendicularly with the pulsed laser beam. Another set of electric field deflection plates separates the charge states. The residual negative ion beam is monitored in a Faraday cup, while the photodetached neutral atoms are monitored via a discrete dynode electron multiplier of wide dynamic range.

The basic laser system is comprised of a pulsed Nd:YAG laser operating at 10 Hz and an associated dye laser. The frequency-doubled output of the Nd:YAG laser at 532 nm pumps the dye laser which has a linewidth of ~0.03 cm^{-1} and a tuning range from 540–730 nm. The linearity of the dye laser wavelength scan is determined with an optogalvanic cell containing neon [5] to be 0.02 nm over a range from 589–725 nm (i.e. a slope of ~0.15 pm nm^{-1}). In a separate experiment the reproducibility of the wavelength scan is tested by measuring an optogalvanic line in neon in a 2 nm wide scan 15 times. The result shows that the reproducibility of the scan (and therefore the error introduced by adding several scans) is within a fraction of the dye laser linewidth. In every measurement presented below, the dye laser is calibrated with at least one optogalvanic line close to the detachment threshold. In much of the current work the output of the dye laser must be Raman shifted in order to obtain laser light in the infrared region. The first and second Stokes outputs of the stimulated Raman conversion in a high pressure hydrogen cell are utilized for this purpose. The cell is 86 cm long and operates at a H_2 pressure of ~20 bar. At this pressure the Raman shift is 4155.20(4) cm^{-1} [6]. A dispersion prism or filter system is used to separate the wavelengths exiting the Raman cell. Typically a few mJ of

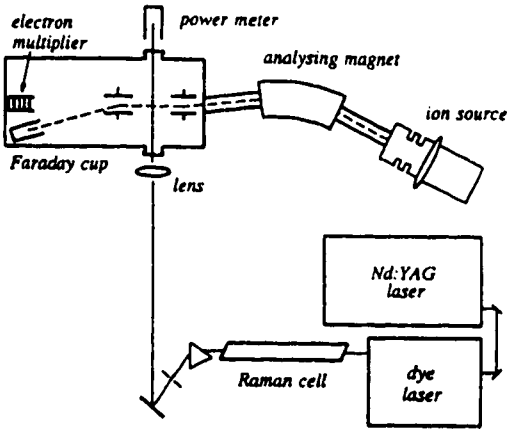

Figure 1. Experimental set-up.

first Stokes Raman output is obtained from the nonlinear optical conversion, but the amount of light utilized in the experiment is also dictated by saturation considerations, as discussed further below. The laser beams are utilized in the ultra-high vacuum chamber as collimated beams with a cross sectional area of ~0.25 cm^2. The accuracy of the electron affinity data is determined in part by the bandwidth of the laser light as well as the absolute calibration of the laser wavelength. Since the wavelength is calibrated via the optogalvanic cell, the fact that a fast ion beam is employed requires extra considerations due to the possible influence of Doppler effects. The geometry of the set-up is arranged such that the laser and ion beams cross at 90°, and as outlined below, checks are done on the possible magnitude of systematic errors due to residual Doppler effects.

The data acquisition is based on a boxcar averager and gated integrator, combined with a personal computer and associated software. The time delay for data acquisition is adjusted to account for the flight time of the neutral atoms between the laser–ion interaction and their detection at the electron multiplier, and it is time gated with an acquisition window such that the signal from all the photodetached neutral atoms is collected. The pulsed laser experiment facilitates a large signal-to-noise ratio despite the fact that the vacuum in the UHV section is above 10^{-9} mbar, since the majority of the collisional detachment events in the UHV section do not enter the data collection window. The voltage on the electron multiplier detector is adjusted such that the analogue pulse which is obtained from the device is proportional to the number of photodetached neutral atoms impinging on the detector The required limitation on the gain of the detector, as well as further restrictions on the laser light intensity such that the light–ion interactions are far from saturation, ensure that the behaviour of the cross section versus wavelength is not compromised due to technical aspects.

The accuracy of the experimental approach is evaluated by conducting electron affinity (EA) measurements on a very well known ion. The negative ion of sulphur is chosen for this calibration as the electron affinity of S has been previously determined to be 16 752.966(8) cm^{-1} [1]. This value was determined by CW laser photodetachment threshold spectroscopy under very well determined kinetic and geometric conditions. In the current experimental effort, a calibration run is conducted utilizing a 12 keV S^- beam. From a computer-based fit to the Wigner s-wave behaviour [4], the binding energy of S^- ($^2P_{3/2}$) is found to be 16 753.1(6) cm^{-1}, which is in excellent agreement with the literature. The light S^- ion has a relatively large Doppler shift compared with the other species, so it provides a good test for unexpected systematic errors. In addition, the excellent agreement between new data from a parallel effort [7] on the fine structure of Se^- and Te^-, and the corresponding literature values, further serves to indicate that the experimental uncertainties are well represented by the associated error bars.

3. Results

3.1. Si^-

An energy level diagram for the photodetachment experiment in Si^- is shown in figure 2. In addition to the ground $^4S_{3/2}$ level, Si^- also has excited ^2D and ^2P terms. The latter two terms are predicted to be bound by 0.523(5) eV and 0.029(5) eV, respectively [1, 8]. The corresponding Wigner s-wave threshold fit to the experimental data is shown in figure 3. The fit to the data is made using an analytical function which satisfies the Wigner threshold law, plus a linear slope to allow for possible linear changes in the background. Different regions for the fits are chosen and the accuracy of the fits is noted. The fit is restricted to

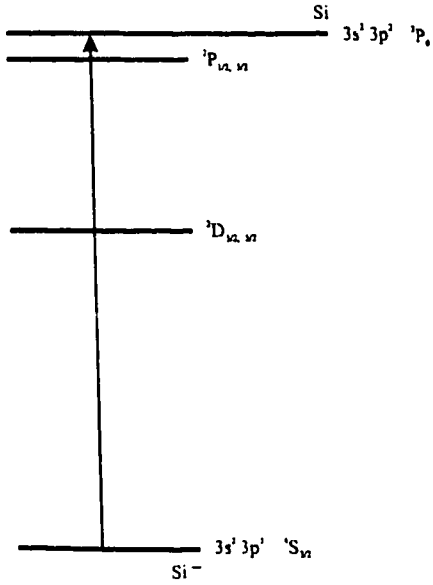

Figure 2. Energy level diagram for Si^-.

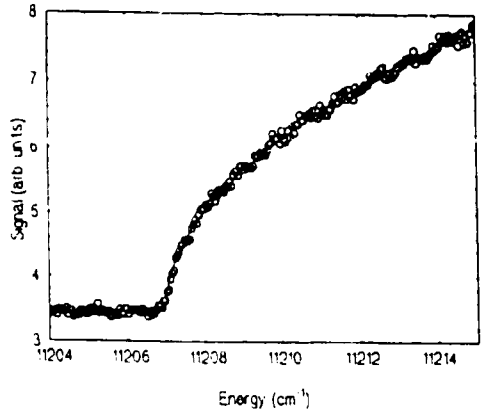

Figure 3. Photodetachment signal of Si^- fitted with Wigner s-wave detachment law.

a sufficiently small region near threshold such that the Wigner threshold law is found to be satisfied empirically. The finite resolution of the experiment is mainly determined by the laser linewidth and the Doppler width and shows up as a 'foot' close to the detachment threshold. The error made by using the Wigner threshold law without including the finite experimental resolution is estimated by comparing this fit with the convolution of a Gaussian response function and the Wigner threshold law. The result shows that the error is less than $\frac{1}{20}$ of the width of the response function and therefore negligible in this context. In addition, considerations are given to the potential saturation issues which have been discussed above. The computer fit gives a value of the EA of 11 207.0(5) cm^{-1}, which compares favourably with the previous value of 11 170(40) cm^{-1} [1, 8], but is considerably more accurate. The background signal in figure 3 is attributed to collisionally detached neutral atoms, thermal population in the excited states of Si^- ions, electronic noise, and to the possibility of molecular ion contamination. The latter may stem from species such as AlH^- since the Si source material is contained in an Al cathode. The background is sufficiently small to be of little consequence, and molecular impurity ions are expected to lead to complications only if the contaminant beam is large and if the photodetachment threshold associated with this impurity beam happens to fall in the region of the desired threshold.

3.2. Ge^-

The relevant energy level diagram of Ge^- is very analogous to Si^- and is not shown here. In addition to the ^4S ground term, Ge^- possesses a ^2D term which is bound by 0.4(2) eV [1]. It is assumed that the ^2P term is likely to be not bound. A scan of the threshold region reveals a distinct s-wave character. The signal-to-noise is almost identical to that of Si^-, with a slightly lower background yield. The measurement utilized the first Stokes output of the Raman-shifted dye laser scanned in the region around 709 nm. The final computer fit is found to yield an EA of 9942.6(4) cm^{-1} (with respect to $Ge(^3P_0)$), which compares

well with the previous value of 9945(24) cm^{-1} [1,9]. A second experiment is conducted in the region of the $^3P_1$ threshold in the neutral atom as opposed to the $^3P_0$ threshold. A weak threshold signal is observed which is consistent with the above interpretation of the first signal corresponding to the Ge^- (^4S)–$Ge(^3P_0)$ transition, given that the fine structure splitting of $Ge(^3P_0–^3P_1)$ is 557.1 cm^{-1}.

3.3. Sn^-

The energy levels of Sn^- are strictly analogous to the Ge^- case. Again, an excited ^2D term is reported to be bound by 0.4(2) eV [1], and the ^2P term is assumed to be unbound. A scan in the region of the Wigner threshold, with a computer fit to the s-wave behaviour, is shown in figure 4. The measurement employs the second Stokes output of the dye laser scanned in the region around ~579 nm. The final result of the computer fit yields an EA of 8969.6(5) cm^{-1} which is much more accurate than the previous value of 8969(32) cm^{-1} [1,9]. The background signal is very low in the case of Sn^-. This may be attributed to a smaller population of the ^2D term as opposed to Si^- and Ge^-, or to a much lower level of molecular ion contamination, or both.

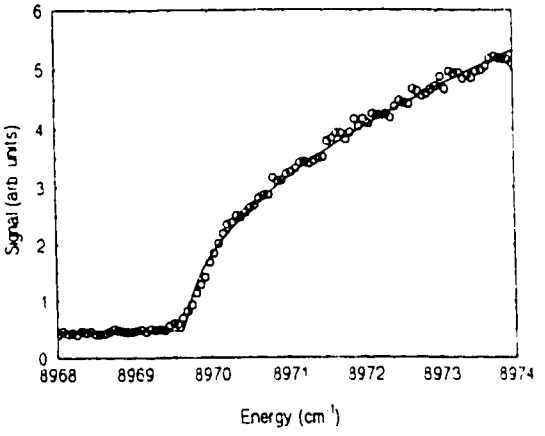

Figure 4. Photodetachment signal of Sn^- fitted with Wigner s-wave detachment law.

3.4. Pt^-

An energy level diagram for the Pt^- experiment is shown in figure 5. The ground level is $5d^96s^2\ ^2D_{5/2}$, and the fine structure splitting for $J = \frac{5}{2}$ to $J = \frac{3}{2}$ is predicted to be 10000(1000) cm^{-1} [1, 10, 11]. In this case, as opposed to those reported above, a p-wave threshold behaviour is expected and observed. A wide scan of 10 nm is taken in order to measure a large section of the p-wave detachment region and this is illustrated in figure 6. A high background is observed and is expected to be due to molecular ion contamination. The resolution of the magnet is such that, for such a heavy mass, a spread of a few mass units in the transmitted beam is expected. We do not believe that the population in the excited $^2D_{3/2}$ level contributes significantly to the background signal. For a fine structure splitting of ~10000 cm^{-1}, the thermal population in the excited state for typical ion source 'temperatures' is expected to be negligible [7]. The final result of the computer fit is 17 141(6) cm^{-1} which is intermediate in value between the result of Gibson *et al* who determined a value of 17 125(9) cm^{-1} [10] and Hotop and Lineberger who quote 17 160(16) cm^{-1} [11].

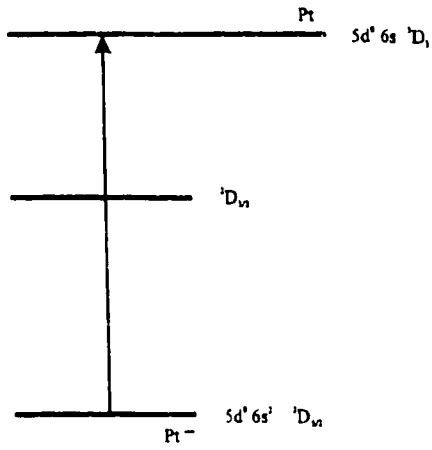

Figure 5. Energy level diagram for Pt^-.

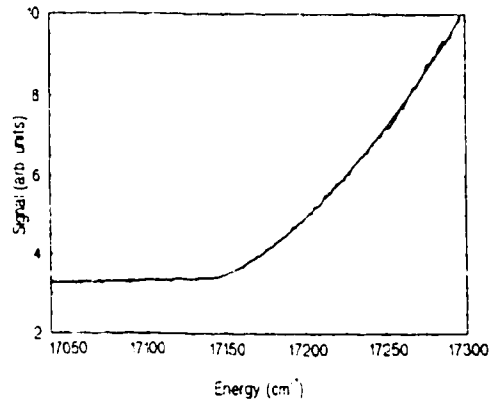

Figure 6. Photodetachment signal of Pt^- fitted with Wigner p-detachment law.

4. Discussion

The electron affinities of silicon, germanium, tin and platinum are improved in the present work by utilizing pulsed laser techniques and associated nonlinear optics. The structure of Si^- was relatively well determined before the present work but our value for the EA of Si represents a factor of 80 improvement over the previous value of Kasdan *et al* [8] who used laser photodetachment electron spectrometry. The present work, however, does not yield information on the excited states of Si^-, while the photoelectron spectroscopy work of [8] also obtained results for the ^2D and ^2P levels. In the case of Ge^- and Sn^-, the application of Raman conversion to access the near-infrared regime provides an improvement in the experimental uncertainty of the associated EAs by a factor of 60. However, the excellent agreement between the present Ge^- and Sn^- results with those of Miller *et al* [9] indicates that the experiment of [9] is likely to be more accurate than the error bars would indicate. Neither the present work nor the study of [9] report on excited states of Ge^- and Sn^-. There remain very large uncertainties regarding the binding energy of the ^2D term in these two species, as well as whether the ^2P term is bound or unbound [1]. The present result for the electron affinity of Pt is more accurate than the previous two measurements, and our value lies almost exactly between the previous two values. All three experiments use tunable laser photodetachment threshold spectroscopy.

The limits of accuracy are dictated by a number of factors including possible residual Doppler effects, the spectral width of the laser beam, the calibration and resetting of the laser scans, and the accuracy of the computer fits. The residual Doppler shift is one of the more significant factors. The laser and ion beams cross nominally at 90°, but there is some uncertainty in this crossing angle. We estimate a worst case of ±2°, which with the typical ion beam energy of ~10 keV, translates into ±0.2–0.3 cm^{-1}. There is also a Doppler width, but this is expected to be less than the shift and the relevant spectral features are expected to be determined to a small fraction of the width. The laser linewidth of the direct dye laser output is ~0.03 cm^{-1}, while the widths for the first and second Stokes converted light are determined to be 0.3 and 0.5 cm^{-1}, respectively. As in the case of the Doppler width, only a fraction of these values enters directly into the error estimation. The calibration errors are typically very small in comparison to the other factors. Finally, the uncertainties in the

computer fits are also significant, particularly in the case of the p-wave detachment. The fits are restricted to regions where the Wigner threshold law is found to hold, and the size of the region is varied such that it is clear when the accuracy of the fit is no longer adequate. The deviation from the Wigner law can, in principle, reflect the behaviour of the light–ion interaction cross section as well as the possibility of saturation effects. As noted previously, steps are taken to ensure that saturation due to experimental aspects does not occur in the region of interest. A more serious concern is the possible influence of background due to other ionic species, including isobaric (or near isobaric) molecular species. Since all the species studied here represent very prolific ions from a sputter ion source, and since the basic properties were already well established, the issue is not possible misidentification, but rather the fact that the background can have a finite slope. The impurity species are expected to be weak but where the laser–ion interaction occurs well above the threshold, the cross section can be large, and a finite slope can influence the accuracy of the computer fit. This is almost a negligible consideration in the present work for fits to the s-wave behaviour, but can be a more important issue for the p-wave detachment. Hence the rather large uncertainty bars for Pt^- reflect a conservative estimate on the accuracy of the computer fit.

The present work on Ge^- and Sn^- illustrates the major improvements in EA determinations which are still possible with atomic negative ions, even for those which are relatively strongly bound. There exist opportunities for the application of tunable infrared light to a variety of species, in particular to ions of intermediate and heavy mass. Further examples taken from the very near infrared region of the spectrum are illustrated by Ru^- [$4d^7 5s^2\ ^4F_{9/2}$] which has a binding energy of 1.05(15) eV [12], and Sb^- [$5p^4\ ^3P_2$] which has a binding energy of 1.07(5) eV [13]. When atoms with substantially smaller EAs are considered, the required wavelengths for tunable laser photodetachment spectroscopy to the first detachment threshold requires wavelengths further into the infrared regime. It may then be preferable to consider other techniques, such as, for example, detachment to an excited state of a neutral atom, accompanied by resonant ionization spectroscopy (RIS) on the neutral atom product in order to ensure very sensitive and selective detection [14]. A discussion of detachment to excited states (plus RIS), and other techniques for accurately determining fine structure splittings in negative ions, is given in a separate paper [7]. The application of pulsed lasers and multi-keV ion beams readily facilitates the determination of several EA values to a level of a few tenths of a wavenumber. With substantially more effort, the current results could be improved—with the present experimental approach—by about a factor of two or three. The status of the theory does not warrant such additional efforts at this time.

5. Conclusions

Substantial improvements in the determination of the electron affinities of Si, Ge, Sn and Pt are obtained via tunable laser photodetachment threshold spectroscopy. Even with atomic species, there still exist substantial opportunities for the improvement of EAs via utilization of nonlinear optical conversion of laser light to the infrared spectrum, as well as by the application of RIS in the study of negative ions.

Acknowledgments

We thank the Natural Sciences and Engineering Research Council of Canada for their support of this work. The comments of T Andersen are also appreciated.

References

[1] Hotop H and Lineberger W C 1975 *J. Phys. Chem. Ref. Data* **4** 539; 1985 *J. Phys. Chem. Ref. Data* **14** 539
[2] Bates D R 1991 *Adv. At. Mol. Phys.* **27** 1
[3] Andersen T 1991 *Phys. Scr.* T **34** 23
[4] Wigner E P 1948 *Phys. Rev.* **73** 1002
[5] Nestor J R 1982 *Appl. Opt.* **21** 4154
[6] Bischel W K and Dyer M J 1986 *Phys. Rev.* A **33** 3113
[7] Thøgersen J, Steele L D, Scheer M, Haugen H K, Kristensen P, Balling P, Stapelfeldt H and Andersen T *Phys. Rev.* A in press
[8] Kasdan A, Herbst E and Lineberger W C 1975 *J. Chem. Phys.* **62** 541
[9] Miller T M, Miller A E S and Lineberger W C 1986 *Phys. Rev.* A **33** 3558
[10] Gibson N D, Davies B J and Larson D J 1993 *Phys. Rev.* A **47** 1946
[11] Hotop H and Lineberger W C 1973 *J. Chem. Phys.* **58** 2379
[12] Feigerle C S, Cordermann C C, Bobashev S V and Lineberger W C 1981 *J. Chem. Phys.* **74** 1580
[13] Feldmann D, Rackwitz R, Heinecke E and Kaiser H 1977 *Z. Phys.* A **282** 143
[14] Petrunin V V, Voldstad J D, Balling P, Kristensen P, Andersen T and Haugen H K 1995 *Phys. Rev. Lett.* **75** 1911

Paper 11

Infrared laser photodetachment of transition metal negative ions: Studies on Cr^-, Mo^-, Cu^- and Ag^-.

René C Bilodeau, Michael Scheer and Harold K Haugen.

Journal of Physics B **31**, 3885 (1998).

J. Phys. B: At. Mol. Opt. Phys. 31 (1998) 3885–3891. Printed in the UK PII: S0953-4075(98)92940-6

Infrared laser photodetachment of transition metal negative ions: studies on Cr^-, Mo^-, Cu^- and Ag^-

René C Bilodeau, Michael Scheer and Harold K Haugen†

Department of Physics and Astronomy, McMaster University, Hamilton, Ontario, L8S 4M1, Canada

Received 1 April 1998, in final form 8 June 1998

Abstract. Photodetachment threshold spectroscopy on the negative ions of chromium, molybdenum, copper and silver has yielded values for the electron affinities of 5451.0(10), 6027(2), 9967.2(3) and 10521.3(2) cm^{-1}, respectively. The results agree well with previous measurements, with an improvement in the accuracy of up to a factor of 300.

1. Introduction

Negative ions play an important role in a number of areas of pure and applied physics. For example, negative ions form the basis for ultrasensitive detection of atoms and isotopes in accelerator mass spectrometry [1, 2]. Also, the short-range potential in which the excess electron is bound gives rise to structure fundamentally different from that found in the neutral atom or positive ions, which are bound in a Coulomb potential. Hence negative ions are also interesting from a purely fundamental viewpoint. As a result, negative ion research is currently an active area of study [3]. Although many improvements to the measured electron affinities (EAs) have been presented since the 1985 review of Hotop and Lineberger [4], the EAs of many species remain relatively poorly known or, in some cases, totally unknown. This is particularly true for the transition metal elements, which generally form weakly bound ions. Presented in this paper are the results of photodetachment threshold spectroscopy measurements on the negative ions of chromium, molybdenum, copper and silver, using tunable infrared laser light. The EAs were measured with improvements in accuracy over the previous values ranging from a factor of about 10 (for Mo) to 300 (for Ag). To our knowledge, this is the first time that atomic negative ions of transition metals have been studied with infrared laser threshold spectroscopy.

2. Methodology

The experimental set-up is illustrated in figure 1. The dye laser is pumped by the second harmonic of a 10 Hz pulsed Nd:YAG laser. Near-infrared laser dyes are utilized to produce $\approx$8 ns laser pulses, tunable over the region of 680–980 nm with a bandwidth of 0.1–0.06 cm^{-1}. The dye-laser beam is focused into a 120 cm long high-pressure Raman cell

† Also with: the Department of Engineering Physics, the Brockhouse Institute for Materials Research and the Center for Electrophotonic Materials and Devices, McMaster University, Hamilton, Ontario, L8S 4M1, Canada.

0953-4075/98/173885+07$19.50

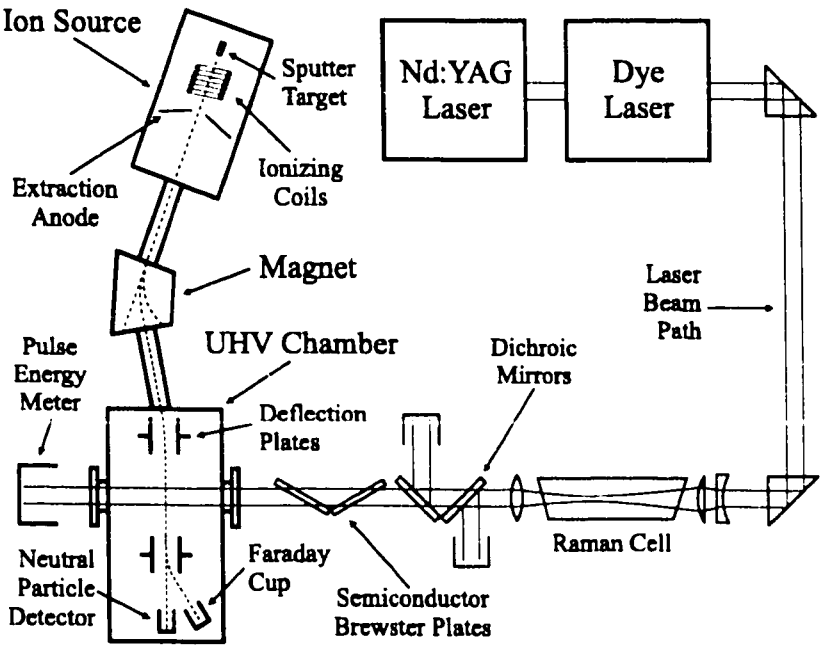

Figure 1. Schematic of the experimental apparatus, see text for details.

filled with H_2, where the dye-laser light is Raman shifted into the first and second Stokes laser beams. The first Stokes Raman shift has been directly measured against optogalvanic lines of Ar to be 4155.197(20) cm^{-1}, which agrees well with the literature value of 4155.187(5) cm^{-1} [5] for a cell pressure of 22(1) bar. After the Raman cell, the beam is recollimated and then passed through dichroic mirrors to remove the undesired anti-Stokes wavelengths as well as the residual pump wavelength with an efficiency of $\approx 90\%$. The light is then further filtered with silicon or germanium semiconductor plates arranged at Brewster's angle, and paired in order to eliminate beam walking as the laser is tuned. This system allows for the production of tunable infrared laser light over the region of 1–5 μm (see figure 2). The laser light is finally passed through a CaF_2 viewport into the ultra-high vacuum interaction chamber where it crosses the ion beam at 90°. A pulse-energy meter located after the exit port of the chamber serves to monitor the laser light. The optics table, including the pulse-energy meter assembly, can be sealed and flushed with dry nitrogen to effectively eliminate absorption of the infrared light in air.

Negative ion beams are produced with a caesium sputter source and accelerated to an energy of 16–19 keV. The ions are mass selected by bending the beam through an angle of 30° with a magnetic field of $\leqslant 5.2$ kG. The ion beam is then passed through a differential pumping section and into the ultra-high vacuum (UHV) chamber with background pressures of $\sim 10^{-8}$ mbar. The beam is further charge-state-analysed with a pair of electrostatic deflection plates, which produces a deflection of $\approx 10°$. The ions then interact with the collimated, pulsed laser. The residual negative ions are deflected into a Faraday cup by a second pair of electrostatic deflection plates, while the photodetached neutral atoms are detected with a discrete-dynode electron multiplier operating in the analogue regime. The voltage on the detector is adjusted so as to ensure that the output signal is linear with respect to the number of incident neutrals over the dynamic range of interest. Finally, the

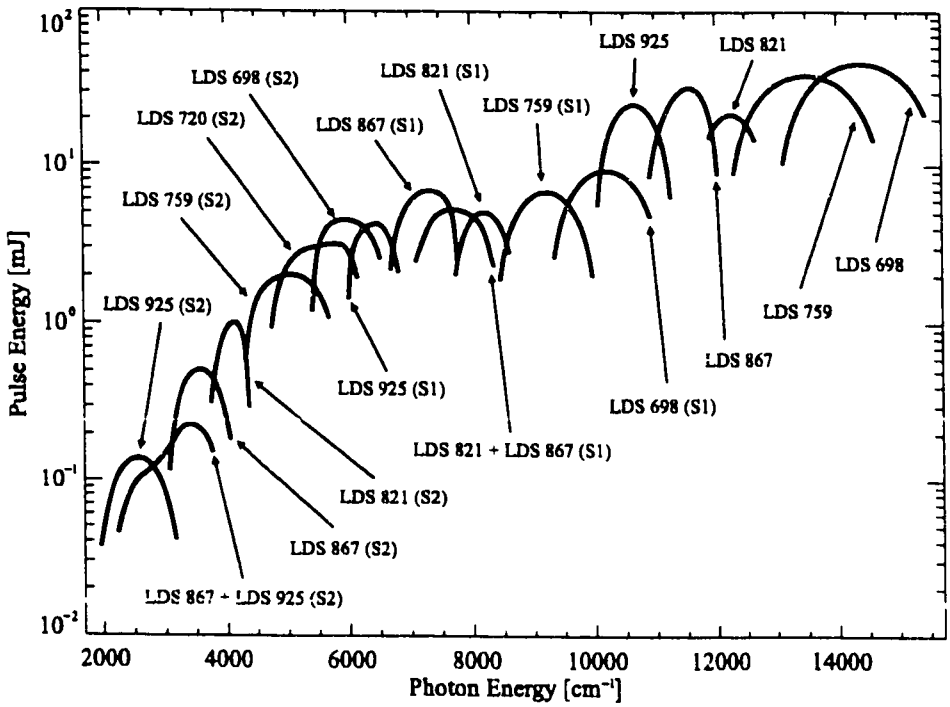

Figure 2. Approximate pulse energies realizable in the 1-5 μm tuning range with our experimental set up. For clarity of presentation, only a selected set of laser dyes are presented. The laser dyes themselves operate up to ≈ 1 μm. For longer wavelengths, the first Stokes or second Stokes are utilized (indicated by (S1) or (S2), respectively, in the figure labels). See the text for a more detailed discussion.

output signal of the neutral particle detector is preamplified to minimize line noise, and is integrated with a boxcar averager. The boxcar gate is triggered by the laser pulse with a time delay adjusted to compensate for the time of flight of the neutral particles from the interaction region to the detector, typically ≈ 2 μs. The width of the boxcar acquisition window is adjusted so as to collect all the neutral particles produced during the pulse. In this way, an effective discrimination between the collisional background detachment events and the photodetachment signal can be achieved, allowing for an excellent signal-to-noise ratio. The integrated signal for each pulse (or the average of a number of pulses) is then collected and recorded by a personal computer.

The binding energy of a negative ion state is extracted by fitting a Wigner threshold law behaviour to the data. The Wigner threshold law states that for a photon energy ε and binding energy ε_0, the cross section for photodetachment is 0 for $\varepsilon < \varepsilon_0$, and is proportional to $(\varepsilon - \varepsilon_0)^{\ell+1/2}$ for $\varepsilon > \varepsilon_0$, where ℓ is the angular momentum of the detached electron. Therefore, if the detached electron carries no angular momentum (i.e. an s-wave electron) a square root behaviour is expected, while if the detached electron carries one unit of angular momentum (a p-wave electron) a $\frac{3}{2}$ power law is expected. The cross section for a p-wave threshold thus increases much more slowly than that for an s-wave threshold. It is comparatively much more difficult to extract the binding energy of the negative ion in the case of a p-wave threshold behaviour, especially if a baseline signal is present (see the discussion in section 4).

The negative ions of Cr, Mo, Cu and Ag are not expected to have any bound excited states or terms. Therefore only two energy levels are relevant in these systems: the negative ion ground state and the neutral atom ground state. For Cr and Mo, the negative ion state is the $^6S_{5/2}$ level of the $(n-1)d^5ns^2$ configuration and the neutral atom state is the $^7S_3$ level of the $(n-1)d^5ns$ configuration. On the other hand, for Cu and Ag the negative ion ground state is $(n-1)d^{10}ns^2\ ^1S_0$ and the neutral ground state is $(n-1)d^{10}ns\ ^2S_{1/2}$. (Note that $n=4$ for Cr and Cu, while $n=5$ for Mo and Ag.) As a result, in all four cases an s-electron is removed in the detachment process and the detached electron carries one unit of angular momentum, stemming from the absorbed photon. Hence, a p-wave threshold behaviour is expected for all the negative ions reported in the present paper.

3. Results

3.1. Cu^- and Ag^-

Copper is a very prolific negative ion from the caesium sputter source. The ≈450 nA currents obtained in the interaction region of the UHV section allowed for excellent statistics. Although a factor of 4 less ion current was obtained for silver, much more laser light could be produced at wavelengths near the threshold region (21 mJ as opposed to 8.5 mJ for the wavelengths needed for Cu, see figure 2) and so, low statistical noise could be achieved for Ag as well. Figure 3 is a plot of the neutral particle yield in the Ag^- photodetachment experiment over a range of 11 cm^{-1}, where each point represents the sum of the detachment yields from 2000 laser pulses. As can be seen by the full curve, the data agree very well with the expected p-wave behaviour discussed above. The fit to the data gives an electron affinity for Ag of 10 521.3(2) cm^{-1} (1.304 47(2) eV, using 8065.5410(24) cm^{-1} eV^{-1} [6]),

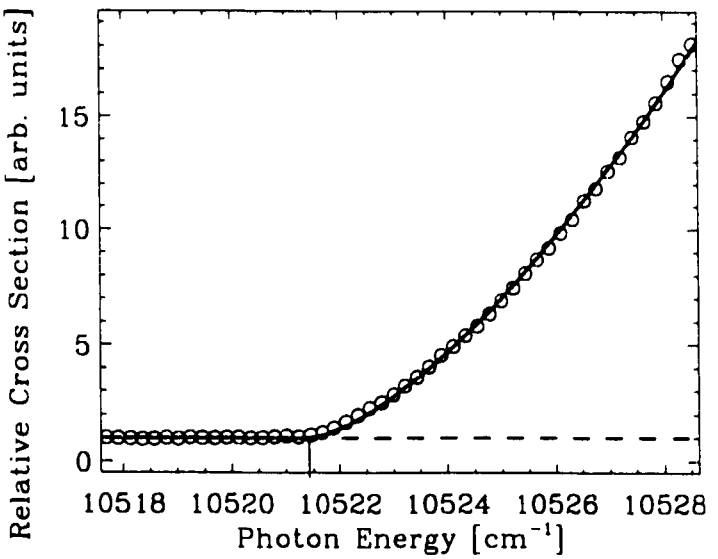

Figure 3. Relative cross section for the $^1S_0 \rightarrow {}^2S_{1/2}$ detachment threshold of Ag^-. The fitted Wigner p-wave is represented by the full curve. The vertical line indicates the best fit location of the threshold.

where the uncertainty represents one standard deviation and includes possible systematic errors (see section 4 below). This value represents a significant improvement over the previously measured value by Hotop *et al* of 1.302(7) eV [7] (after recalibration [4]). A similar experiment on Cu^- gives an EA of 9967.3(3) cm^{-1} (1.235 79(4) eV) for copper, which agrees well with the Leopold *et al* value of 1.235(5) eV [8]. These experimental values also compare well with the theoretical EAs of Cu and Ag of 1.236 and 1.254 eV, respectively, recently calculated by Neogrády *et al* using quasi-relativistic one-component approximations to the Dirac–Coulomb Hamiltonian [9].

3.2. Cr^- and Mo^-

Unlike copper and silver, the negative ions of chromium and molybdenum are not very prolific from a Cs sputter source. Currents of only about 2.5 nA of Cr^- and 0.5 nA of Mo^- are obtained in the interaction region. A low beam current naturally gives rise to a poorer signal-to-noise ratio. It also often results in a poorer signal-to-background ratio as the background count does not necessarily scale with the beam current (see section 4 below). This effect can be compensated to some extent by increasing the scan range, but a larger uncertainty in the fit to the data is inevitable. The detachment yield for Cr^- versus photon energy is shown in figure 4 over a region of $\approx$100 cm^{-1}. A Wigner p-wave threshold fit yields a value of 5451.0(10) cm^{-1} (0.675 84(12) eV) for the electron affinity of Cr. This agrees well with, and is a substantial improvement over, the value of Feigerle *et al* of 0.666(12) eV [4, 10]. Likewise, from a scan over $\approx$ 200 cm^{-1} around the threshold of Mo^- we obtain an electron affinity of 6027(2) cm^{-1} (0.7472(2) eV), in good agreement with the previous result of 0.748(2) eV [11].

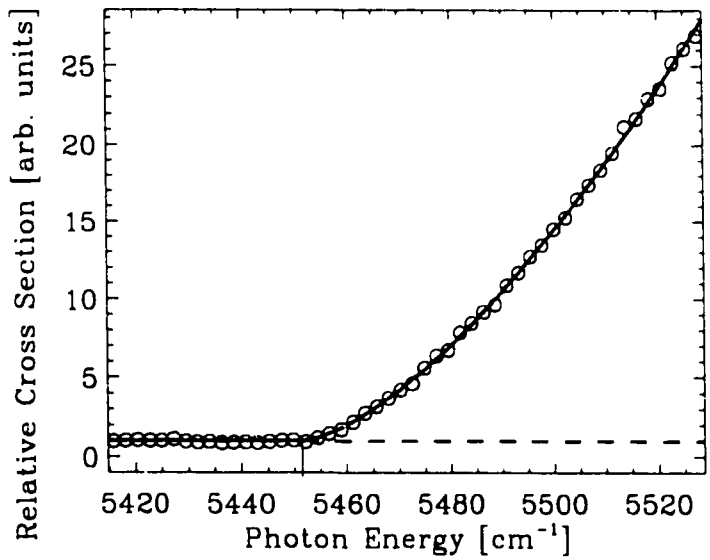

Figure 4. Plot of the relative detachment yields in the $^6S_{5/2} \rightarrow {}^7S_3$ photodetachment experiment on Cr^-. The full curve represents a fitted p-wave threshold law. The best-fit value of the threshold is indicated by a vertical line.

4. Discussion

The results of this work are summarized in table 1 (errors are given to one standard deviation); included for comparison are the results of previous works [4, 7, 8, 10, 11]. The excellent agreement of all the EAs with previous works, suggests that the previous values were likely to be more accurate than indicated by the error bars. All of the previous experiments were based on photodetachment electron spectrometry. In this technique, fixed energy photons are used to detach the electron, and the binding energy is deduced from the measured energy of the detached electrons. As a result, the accuracy of these measurements is limited by that of the electron spectrometer. In contrast, the main contribution to the final error in our experiments is typically the uncertainty in the fit. Aside from pure counting statistics, the accuracy of the fit can also be limited due to a large, and possibly sloped, photodetachment background. Populated bound excited states of the negative ion can produce such photodetachment backgrounds. If the fractional population in the excited state is sufficiently large, the binding energy of the excited state can be determined from its photodetachment threshold, analogous to the determination of the ground state binding energy. This approach works well for s-wave threshold features [12], but can be very challenging for p-wave thresholds, which is the subject of a parallel study on the transition metal ions Co^-, Rh^-, Ni^- and Pd^- [13]. If the population in the excited state is not sufficient, then more sophisticated techniques can be used to study the bound excited states, such as resonant multiphoton detachment [14]. However, the negative ions of Cr, Mo, Cu and Ag are not expected to possess bound excited states. The small photodetachment background seen in figures 3 and 4 is likely due to very small amounts of mass-coincident or nearly mass-coincident impurity molecules, such as hydrides. Finally, the laser bandwidth also limits the accuracy to which the threshold can be fitted. The bandwidth produces a broadening that can be more easily seen in s-wave thresholds [15]. The error introduced by this broadening is only a small fraction of the actual bandwidth and is typically insignificant relative to the statistical uncertainties involved.

Table 1. Summary of measured electron affinities.

Element	This work	Previous works	Reference
Cr	0.675 84(12) eV	0.666(12) eV	[10]
Mo	0.747 2(2) eV	0.748(2) eV	[11]
Cu	1.235 81(4) eV	1.235(5) eV	[8]
Ag	1.304 47(2) eV	1.302(7) eV	[7]

In addition to statistical noise and the laser bandwidth, there are possible systematic errors which limit the accuracy of the experiment. The dye laser is frequently calibrated against known optogalvanic resonance lines of low-pressure Ar gas [16]. Lines that lie near the scan wavelength ranges are selected and yield a calibration error of no more than ± 0.05 cm^{-1}. Comparing values obtained from a number of such lines reveals that the laser tuning deviates from linearity by less than 1 part in 1000, which is negligible over the scan ranges presented here. Peak pulse intensities of less than 10^8 W cm^{-2} were produced in the experiments; therefore threshold shifts due to intense laser fields are expected to be insignificant [17]. In a separate experiment, we have verified that this effect is indeed negligible by measuring photodetachment thresholds at various laser intensities. As noted previously, uncertainties of ± 0.02 and ± 0.04 cm^{-1} are assigned to the first and second Stokes shifts, respectively. Finally, the largest contribution to possible systematic errors

comes from possible Doppler shifts caused by any deviation of the laser–ion crossing angle from 90°. Careful measurements ensure that this angle can be realized with an accuracy of $\approx 0.5°$, which translates into a possible Doppler shift of $\leqslant 0.07$ cm^{-1} for the ions studied here. Therefore, the total of the systematic contributions to the error is less than ± 0.1 cm^{-1}, assuming that the error sources are independent. Previous measurements with this system have indicated that no other significant systematic errors are present [15].

5. Conclusions

The results of the infrared threshold photodetachment experiments on the negative ions of the transition metals yield substantial improvements for the electron affinities of Cr, Mo, Cu and Ag. The work demonstrates that highly accurate values for electron affinities can be obtained using this method, even if the negative ions are only weakly bound and detach with a p-wave threshold behaviour, as is the case for nearly all the transition metals.

Acknowledgments

We are grateful to the Natural Sciences and Engineering Research Council of Canada (NSERC) for their support of this work. We would also like to thank J D Garrett for manufacturing the cathodes used in the experiments.

References

[1] Litherland A E 1980 *Ann. Rev. Nucl. Part. Sci.* **30** 437
[2] Kutschera W and Paul M 1990 *Ann. Rev. Nucl. Part. Sci.* **40** 411
[3] Bates D R 1991 *Adv. At. Mol. Opt. Phys.* **27** 1
Andersen T 1991 *Phys. Scr.* T **34** 23
Buckmann S J and Clark C W 1994 *Rev. Mod. Phys.* **66** 539
Blondel C 1995 *Phys. Scr.* T **58** 31
[4] Hotop H and Lineberger W C 1985 *J. Phys. Chem. Ref. Data* **14** 731
[5] Bischel W K and Dyer M J 1986 *Phys. Rev.* A **33** 3113
Looi E C, Stryland J C and Welsh H L 1978 *Can. J. Phys.* **56** 1102 and references therein
[6] Cohen E R and Taylor B N 1987 *Rev. Mod. Phys.* **59** 1121
[7] Hotop H, Bennett R A and Lineberger W C 1973 *J. Chem. Phys.* **58** 2373
[8] Leopold D G, Ho J and Lineberger W C 1987 *J. Chem. Phys.* **86** 1715
[9] Neogrády P, Kellö V, Urban M and Sadlej A J 1997 *Int. J. Quantum Chem.* **63** 557
[10] Feigerle C S, Corderman R R, Bobashev and Lineberger W C 1981 *J. Chem. Phys.* **74** 1580
[11] Gunion R F, Dixon-Warren St J and Linberger W C 1996 *J. Chem. Phys.* **104** 1765
[12] Scheer M, Bilodeau R C, Thøgersen J and Haugen H K 1998 *Phys. Rev.* A **57** R1493
Scheer M, Bilodeau R C and Haugen H K 1998 *Phys. Rev. Lett.* **80** 2562
[13] Scheer M, Brodie C A, Bilodeau R C and Haugen H K *Phys. Rev.* A at press
[14] Scheer M, Haugen H K and Beck D R 1997 *Phys. Rev. Lett.* **79** 4104
Thøgersen J, Scheer M, Steele L D and Haugen H K 1996 *Phys. Rev. Lett.* **76** 2870
Kristensen P, Stapelfeldt H, Balling P, Andersen T and Haugen H K 1993 *Phys. Rev. Lett.* **71** 3435
[15] Thøgersen J, Steele L D, Scheer M, Brodie C A and Haugen H K 1996 *J. Phys. B: At. Mol. Opt. Phys.* **29** 1323
[16] Minnhagen L 1973 *J. Opt. Soc. Am.* **63** 1185
[17] Trainham R, Fletcher G D, Mansour N B and Larson D J 1987 *Phys. Rev. Lett.* **20** 2291